



LUND UNIVERSITY

Sensitivity-Enhanced Raman Spectroscopy and High-Speed Fluorescence for In Situ Gas-Phase Diagnostics

Kim, Haisol

2022

[Link to publication](#)

Citation for published version (APA):

Kim, H. (2022). *Sensitivity-Enhanced Raman Spectroscopy and High-Speed Fluorescence for In Situ Gas-Phase Diagnostics*. [Doctoral Thesis (compilation), Faculty of Engineering, LTH]. Department of Physics, Lund University.

Total number of authors:

1

General rights

Unless other specific re-use rights are stated the following general rights apply:

Copyright and moral rights for the publications made accessible in the public portal are retained by the authors and/or other copyright owners and it is a condition of accessing publications that users recognise and abide by the legal requirements associated with these rights.

- Users may download and print one copy of any publication from the public portal for the purpose of private study or research.
- You may not further distribute the material or use it for any profit-making activity or commercial gain
- You may freely distribute the URL identifying the publication in the public portal

Read more about Creative commons licenses: <https://creativecommons.org/licenses/>

Take down policy

If you believe that this document breaches copyright please contact us providing details, and we will remove access to the work immediately and investigate your claim.

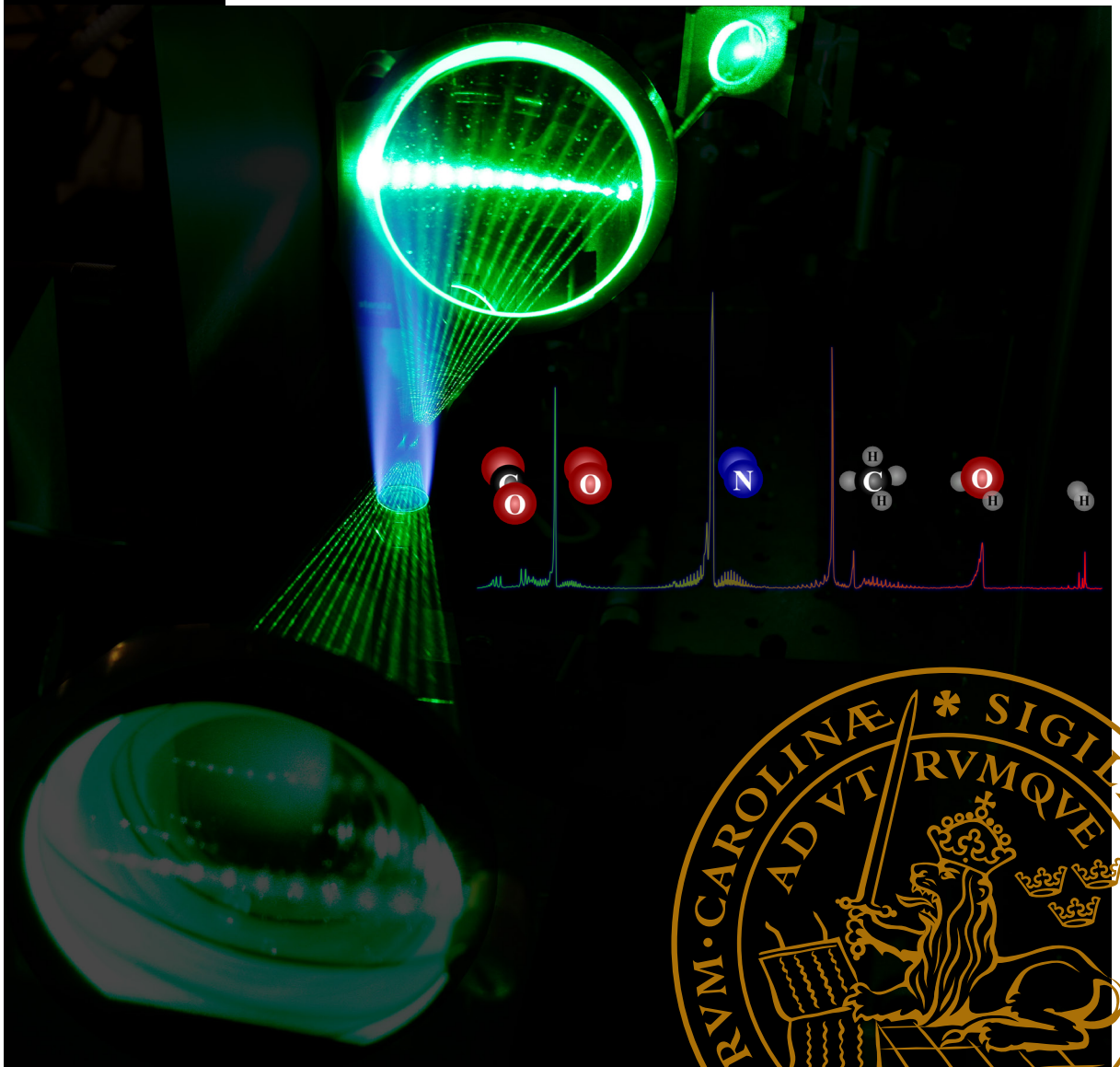
LUND UNIVERSITY

PO Box 117
221 00 Lund
+46 46-222 00 00

Sensitivity-Enhanced Raman Spectroscopy and High-Speed Fluorescence for *In Situ* Gas-Phase Diagnostics

HAI SOL KIM

DIVISION OF COMBUSTION PHYSICS | FACULTY OF ENGINEERING | LUND UNIVERSITY



Sensitivity-Enhanced Raman Spectroscopy and High-Speed Fluorescence for *In Situ* Gas-Phase Diagnostics

Haisol Kim



LUND
UNIVERSITY

DOCTORAL DISSERTATION

by due permission of the Faculty of Engineering, Lund University, Sweden.
To be defended in Rydberg Hall at the Department of Physics, Professorsgatan 1,
Lund. 18th of March 2022, at 13:15.

Faculty opponent

Dr. Wolfgang Meier, German Aerospace Center (DLR), Germany

Cover photo by Haisol Kim and Shen Li

pp i-74 © Haisol Kim

Paper 1 © Siemens Energy AB

Paper 2 © Optica Publishing Group

Paper 3 © Optica Publishing Group

Paper 4 © by the Authors (Published by Elsevier Inc.)

Paper 5 © by the Authors (Manuscript under review)

Division of Combustion Physics
Department of Physics

ISBN 978-91-8039-161-0 (print)

ISBN 978-91-8039-162-7 (pdf)

ISSN 1102-8718

ISRN LUTFD2/TFCP-243-SE

Lund Reports on Combustion Physics, LRCP-243

Printed in Sweden by Media-Tryck, Lund University
Lund 2022



Media-Tryck is a Nordic Swan Ecolabel
certified provider of printed material.
Read more about our environmental
work at www.mediatryck.lu.se

MADE IN SWEDEN 

*To my mom and dad, who always tell me
"You can do it. Do whatever you want."*

항상 걱정과 조언이 마르지 않지만, 그럼에도
“너의 삶을 살아라” 하시며 믿고 응원해주시는 부모님께.

Abstract

In this work, combustion and thermal decomposition processes were studied employing laser-based diagnostic techniques, and the techniques were improved and demonstrated to achieve enhanced detection sensitivity. Raman spectroscopy was employed to study flames under elevated and atmospheric pressures with various fuels, such as methane, hydrogen-enriched methane, DME, ethylene, and ammonia. Raman spectra of major chemical species in flames were identified and converted into mole fractions. In addition, the Raman spectrum of nitrogen was utilized to obtain temperatures. The quantitative results are intended to serve for model development and validation. In this study, however, the ethylene flame was challenging to study with Raman spectroscopy due to soot particles emitting a laser-induced incandescence (LII) signal, much stronger than Raman scattering signal. Therefore, improving the diagnostic technique to solve this issue was motivated.

In studies of thermal decomposition processes, emitted gas components by biomass were of interest. Raman spectroscopy served as a good technique, detecting hydrocarbons, carbon dioxide, and water released while heating. With Raman spectra, the quantity of the components was analyzed with the heating time and temperature. The limitation of the study was that the Raman signals are close to undetectable at high temperatures due to the strong laser-induced fluorescence (LIF) signal emitted from volatile hydrocarbons released during the decomposition process.

Raman spectroscopy was thus improved to enhance detection sensitivity. A multi-pass concept was employed to optimize laser excitation, and filtering techniques were implemented to reject unwanted backgrounds and competing signals. The multi-pass concept enhanced the excitation by a factor of 45, enabling the detection of formaldehyde, a minor intermediate species in a DME flame. The so-called Periodic Shadowing filtering spatially rejected stray light and multiple scattering, offering narrower and clearer Raman peaks in spectra. A polarization lock-in filtering (PLF) technique was developed to reject competing laser-induced signals such as LII and LIF, solving the issues mentioned above while employing Raman spectroscopy. Therefore, with these filtering techniques, a sooting ethylene flame and biomass decomposition at high temperature could be studied by employing PLF-combined Raman spectroscopy.

Another laser-based technique, planar laser-induced fluorescence (PLIF), was employed to study an actual-scale gas turbine burner and combustion characteristics. PLIF measurements at 2 kHz repetition enabled high-speed imaging of hydroxyl (OH) radical in turbulent flames for a fuel-flexibility study of the burner supplied with natural gas, hydrogen-enriched natural gas, and pure hydrogen as a fuel. The results provided useful information to understand flame characteristics when switching fuel from natural gas to hydrogen. In addition, PLIF imaging with higher laser repetition rates at 3 and 5 kHz was tested, and correlation between consecutive images was observed from the 5 kHz case, where flame image velocimetry technique can be employed for flow dynamics study.

Popular Science Summary

A laser is a familiar device for many people, and it is used around us for various purposes, such as pointing at a presentation screen or stars in the night sky. The word LASER is an acronym for "Light Amplification by the Stimulated Emission of Radiation." It can be inferred from the name that light builds up the intensity (amplification) in the device through a process (stimulated emission) that makes the emitted light directional. Therefore, light from a laser is directional, unlike a light bulb. Since the laser beam diverges little, the high intensity of the light is conserved during the propagation. It is why a laser pointer with a power of 5 mW can damage the eyes, while we can look at a 500 mW light bulb without any problem.

Apart from indicating a screen or processing materials, a laser can be employed for various scientific measurements since a laser beam exchanges its energy with molecules on the way. For example, when a beam passes a molecule, the molecule can absorb a part of the energy from the beam. Therefore, if one investigates the beam intensity at the source and the end, the type and quantity of molecules can be measured. Similarly, various laser-based diagnostic techniques have been developed to measure different properties, such as temperature and velocity, in all four states of matter: solid, liquid, gas, and plasma.

Non-intrusiveness is an important advantage of employing laser-based techniques over conventional probing methods. For example, if one wants to measure the temperature of a candlelight, an easy way is to insert a thermometer into the flame. However, the shape of the flame deforms as soon as the thermometer is inserted. It can be due to the cold surface of the thermometer or the change of volume by introducing the thermometer. Therefore, it is questioned if the temperature measured by the thermometer is the actual temperature of the flame that we wanted to know. On the other hand, temperature measurements by laser-based techniques do not interfere with the flame. The beam interacts with the atoms and molecules to emit signals, but does not affect the shape of the flame. Therefore, the non-intrusive technique can provide more accurate measurements.

Two laser-based diagnostic techniques are employed to study various reaction processes in this study. One is Raman spectroscopy, and the other is laser-induced Fluorescence (LIF). For illumination with a laser beam, so-called Raman scattering gives emitted light of different wavelengths for different types of molecules. Detection of this light results in simultaneous detection of multiple chemical

species. In addition, the signal strength is proportional to the number of molecules, so Raman spectroscopy is useful to study species composition in the probe volume.

Raman spectroscopy was employed in this study to detect various species and analyze their quantity in flames of various fuels: methane, hydrogen-enriched methane, ethane, ethylene, dimethyl ether (DME), and ammonia. The analyzed data sets were provided to improve models used for predicting the combustion process with computations. In addition, developing techniques to improve Raman spectroscopy is another important part of this study.

Raman scattering is a weak process, and efficient use of the laser light is thus necessary for measurements with sensitive detection of chemical species. Therefore, two mirrors were employed in this study to encapsulate and reflect the laser beam back and forth through the probe volume, which increases the signal by a factor equal to the number of passes. In this study, the signal amplification was 45 times that achieved with the single beam. As a result, formaldehyde, a species of minor concentration in an intermediate step of combustion, could be measured in a flame.

Another approach to improve Raman scattering signals is by removing other types of signals and background. If other strong signals, such as fluorescence and luminosity, are emitted from the probe volume, the weak Raman scattering signals are easily overwhelmed. Therefore, two filtering techniques to remove the unwanted components are introduced in this study. Periodic Shadowing (PS) is a spatial filtering technique employed to minimize data contamination by stray light, reflections and scattered light that can arise in the probe volume and its surroundings. The filtering is done by blocking a part of the signal using a glass plate with a stripe pattern imprinted. Due to the blockage, the pattern appears in the signal registered on the camera, and the signal appears as dashed lines in Figure 1. Stray light contribution is detected in the region between the lines, and it can be filtered out with mathematical signal processing methods.

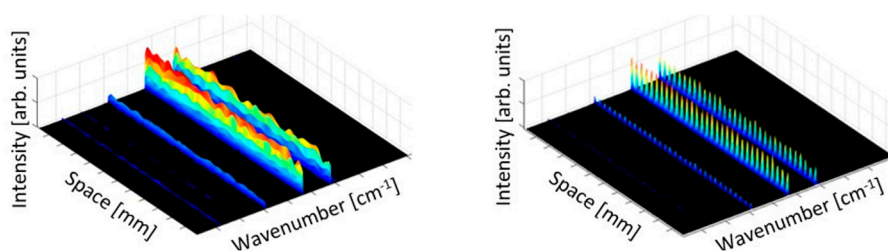


Figure 1. Normal spectral data (left) and PS-modulated spectral data (right), edited from [1].

¹ M. Gong, H. Kim, J. Larsson, T. Methling, M. Aldén, E. Kristensson, C. Brackmann, T. Eschrich, M. Jäger, W. Kiefer, Fiber-based stray light suppression in spectroscopy using periodic shadowing, *Opt Express* 29 (2021) 7232-7246.

Another filtering technique is polarization lock-in filtering (PLF). It is developed to reject competing signals that arise in the same probe volume as the Raman signal. Similar to the PS technique, this method is also based on modulation of the signal and post-processing. The PLF method is, however, based on continuous change of the laser polarization instead of spatial blocking of the signal. Since the Raman scattering is polarization dependent, the Raman signal varies with changes in laser polarization over time, while competing signals are recorded all the time.

These two filtering techniques were simultaneously applied to study sooting flames and thermal decomposition processes. The sooting flame was difficult to investigate without the filtering technique due to soot particles that emit blackbody radiation resulting in yellow light from the flame, as well as strong laser-induced incandescence (LII) signals due to additional heating by the laser. The PLF technique efficiently suppressed the LII signal, and the concentrations of the major species in the flame could be analyzed. In the thermal decomposition study, a biomass pellet was heated up to study gas emissions. A strong fluorescence signal was an obstacle to employing Raman spectroscopy, but the PLF technique removed the fluorescence signal effectively, and further analyses of the Raman spectra for evaluation of species concentrations were carried out.

Fluorescence signals have been considered troublesome competing signals in Raman measurements, but fluorescence itself is a useful laser-based technique for measurement of chemical species. As one could guess from the previous paragraphs, the LIF signal is relatively strong, so even a chemical species of low concentration can be detected with this method. However, the LIF technique requires a specific wavelength of laser light determined by the specific species of interest and is therefore mostly limited to measurement of one species at a time. For LIF measurements in flame, species that give useful information to understand the flame characteristics are selected. For example, hydroxyl radical, formed in the so-called reaction zone at the edge of the flame. Therefore, detecting hydroxyl radicals in flames using the LIF technique gives a clear picture of the flame shape.

This work includes some hydroxyl radical measurements carried out with the LIF technique in a gas turbine test rig in collaboration with Siemens Energy AB. The goal was to study the flame behavior for different mixtures of natural gas and hydrogen in the fuel since fuel-flexibility of gas turbines is of relevance for efficient use of fuel sources and combustion with reduced carbon dioxide emission in the future.

Populärvetenskaplig Sammanfattning

En laser är ett välbekant hjälpmedel för många människor som används för en mängd olika ändamål, till exempel för att peka på en presentationsskärm eller på stjärnor på natthimlen. Ordet LASER är en förkortning av "Light Amplification by the Stimulated Emission of Radiation." Av namnet kan man inse att intensiteten förstärks (amplification) i enheten genom en process (stimulated emission) som gör det utsända ljuset riktat. Till skillnad från ljuset från en glödlampa, som sänds ut i alla riktningar från lampan, är laserns ljus därför riktat i en stråle och en hög intensitet bevaras under utbredningen. Därför kan en laserpekare med en effekt på 5 mW skada ögonen, medan vi kan titta på en 500 mW glödlampa utan problem.

Förutom att indikera på en skärm eller bearbeta material, kan en laser användas för en mängd olika vetenskapliga mätningar eftersom en laserstråle kan utbyta sin energi med molekyler på vägen. Till exempel, när en stråle passerar en molekyl, kan molekylen absorbera en del av energin från strålen. Därför, om man jämför strålens intensitet vid källan och slutet, kan typen och mängden av olika molekyler i strålen mätas. På liknande sätt har olika laserbaserade diagnostiska tekniker utvecklats för att mäta olika egenskaper, såsom temperatur och hastighet, i materiens alla fyra tillstånd: fast, flytande, gas och plasma.

Beröringsfrihet är en viktig fördel med att använda laserbaserade tekniker jämfört med konventionella mätmetoder. Om man till exempel vill mäta temperaturen i ett levande ljus är ett enkelt sätt att sätta in en termometer i lågan. Lågans form deformeras dock så fort termometern sätts in, antingen beroende på termometerns kalla yta eller volymförändring då den förs in. Därför ifrågasätts om temperaturen som termometern visar är den faktiska temperaturen för lågan som man ville veta. Temperaturmätning med laserbaserade tekniker stör däremot inte lågan. Strålen växelverkar med atomer och molekyler för att avge signaler, men påverkar inte lågans form. Därför kan den beröringsfria laserbaserade tekniken ge mer tillförlitliga mätningar.

Två laserbaserade diagnostiska tekniker används för att studera olika reaktionsprocesser i denna studie. Den ena är Raman-spektroskopi och den andra är laserinducerad fluorescens (LIF). Vid belysning med en laser ger så kallad Raman-spridning utsänt ljus av olika våglängd för olika typer av molekyler. Detektion av detta ljus innebär att olika kemiska ämnen kan detekteras samtidigt. Signalstyrkan

är proportionell mot antalet molekyler, så Raman-spektroskopi är en användbar teknik för att studera den kemiska sammansättningen i laserstrålens mätområde.

Ramanspektroskopi användes i denna studie för att detektera och mäta koncentrationer av kemiska ämnen i flammor för olika bränslen: metan, väteberikad metan, etan, eten, dimetyleter (DME) och ammoniak. Resultaten tillhandahölls för att förbättra modeller som används för att förutsäga förbränningsprocessen med beräkningar. Dessutom är utveckling av tekniker för att förbättra Raman-spektroskopi en annan viktig del av denna studie.

Ramanspridning är en svag process och effektiv användning av laserljuset är således nödvändig för mätningar med känslig detektion av kemiska ämnen. Därför används i dessa studier två speglar för att kapsla in och reflektera laserstrålen fram och tillbaka genom mätområdet, vilket ökar signalen proportionellt mot antalet passager. I denna studie uppnåddes 45 gångers förstärkning jämfört med signalen för en passage av laserstrålen. Som ett resultat av detta kunde vi mäta formaldehyd, en förening som bildas i lägre koncentrationer i ett delsteg i förbränningskemin.

Ett annat sätt att förbättra signaler Raman-spektroskopi är genom att ta bort andra typer av signaler och bakgrunder. Om andra starka signaler, såsom laserinducerad fluorescens och ljus från en flamma sänds ut från mätvolymen, överträffas de svaga Raman-spridningssignalerna lätt. Därför introduceras två filtreringstekniker för att ta bort oönskade bakgrunder i denna studie. Periodic shadowing (PS) är en filtreringsteknik som används för att minimera störningar från så kallat ströjljus, reflexer och spritt ljus som kan uppstå i mätregionen och dess omgivning. Filtringen görs genom att blockera en del av signalen med hjälp av en glasplatta med ett streckmönster. Blockeringen medför att det streckade mönstret finns med i signalen som registreras på kameran, så som visas i figur 1. Ströjlusbidrag detekteras i området mellan linjerna och kan vidare filtreras bort genom matematisk signalbehandling.

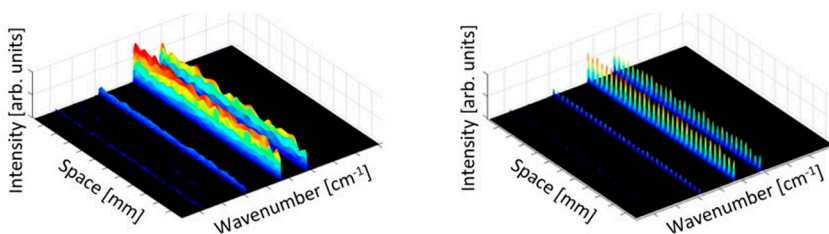


Figure 1. Spektraldata från mätning med Raman-spektroskopi, normal mätning (vänster) och PS-modulerad mätning för filtrering av ströjljus (höger), figur modifierad från referens [1].

¹ M. Gong, H. Kim, J. Larsson, T. Methling, M. Aldén, E. Kristensson, C. Brackmann, T. Eschrich, M. Jäger, W. Kiefer, Fiber-based stray light suppression in spectroscopy using periodic shadowing, *Opt Express* 29 (2021) 7232-7246.

En annan framtagen filtreringsteknik är polarization lock-in filtering (PLF). Den är utvecklad för att undertrycka andra optiska signaler som uppstår i samma mätregion som Raman-signalen. Liksom PS-tekniken baseras även denna metod på modulering av signalen och matematisk signalbehandling. PLF-metoden baseras emellertid på kontinuerlig ändring av laserns polarisation istället för rumslig blockering av signalen. Då Raman-spridningen beror på strålens polarisation varierar Raman-signalen med polarisationsförändringen över tiden, medan konkurrerande signaler (till exempel fluorescens) registreras oförändrade hela tiden.

Dessa två filtreringstekniker tillämpades samtidigt för att studera sotande flammor och pyrolys/förgasning av biomassa. En sotande flamma är svår att undersöka p.g.a. av svartkroppsstrålning från sotpartiklar, dels direkt ifrån flammen vilket ger gult ljus, dels genom ytterligare upphettning av sotpartiklar vid belysning med laser för mätningar. PLF-tekniken undertryckte effektivt dessa bakgrundssignaler och koncentrationen av kemiska ämnen i flammen kunde bestämmas. I studier av pyrolys och förgasning av biomassa uppstod en stark fluorescenssignal vilket utgjorde ett hinder för mätningar med Raman-spektroskopi. Dock tog PLF-tekniken bort fluorescenssignalen effektivt och analyser av Raman-signaler för bestämning av koncentrationer kunde genomföras.

Vid Raman-mätningar utgör fluorescenssignaler en störande bakgrund, men laser-inducerad fluorescens är i sig även en användbar teknik för mätning av kemiska ämnen. Som man kan gissa utifrån föregående stycken är LIF-signalen relativt stark, så även kemiska ämnen av låga koncentrationer kan detekteras med denna metod. Dock kräver tekniken laserljus av en viss våglängd som bestäms av det kemiska ämne man önskar mäta och är därför oftast begränsad till mätning av ett ämne i taget. Flamm-mätningar med laserinducerad fluorescens görs på ämnen som ger användbar information för att förstå flammans karakteristik, till exempel hydroxylradikalen (OH) som bildas i den så kallade reaktionszonen vid flammans kant. Att detektera hydroxylradikaler med hjälp av LIF-tekniken kan därför ge en tydlig bild av flammans form.

Detta arbete inkluderar vissa mätningar av hydroxylradikalen genomförda med LIF-tekniken i en anläggning för gasturbinbrännare och i samarbete med Siemens Energy AB. Målet var att studera flammans beteende för olika sammansättningar av naturgas och vätgas i bränslet då bränsleflexibilitet för gasturbiner är relevant för effektivt utnyttjande av olika bränsleresurser och förbränning med minskade emissioner av koldioxid i framtiden.

알기 쉬운 요약

레이저(Laser)는 많은 사람들에게 익숙한 도구로, 발표 화면이나 특정한 물체를 가리키는데 자주 사용된다. Laser 는 사실 "복사의 유도 방출 과정에 의한 빛의 증폭 (Light Amplification by the Stimulated Emission of Radiation)"에서 첫 글자를 따 만들어진 단어이며, 이를 통해 빛이 이 장치 안에서 특정한 과정을 통해 증폭됨으로써 직진성을 가지게 된 것으로 유추할 수 있다. 그렇기에 레이저에서의 빛은 일반 전구와는 달리 한 방향으로 나아가는 성질을 가진다. 이것이 5 밀리วัต 세기의 레이저 포인터로는 사람의 눈을 다치게 할 수 있지만 500 밀리وات 세기의 전구는 바라보아도 아무 문제가 없는 이유이다.

레이저는 어떤 물체를 가리키는 것 외에도 다양한 과학적 실험에 활용할 수 있다. 예를 들어, 광선이 어떤 분자를 통과할 때, 그 분자는 광선이 가지고 있는 에너지의 일부를 흡수한다. 그렇기 때문에, 처음과 나중의 광선 에너지를 비교함으로써 광선이 지나간 분자의 종류 또는 양을 계산할 수 있다. 이러한 원리를 이용해 다양한 레이저 기반 계측법들이 개발되었고, 이를 이용해 온도나 속도 등 물질의 다양한 특성을 고체, 액체, 기체, 그리고 플라스마 상태에서 계측할 수 있다.

비침습성은 레이저 기반 계측법이 가지는 매우 중요한 장점이다. 예를 들어, 촛불의 온도를 측정하고자 할 때, 간단하게 생각할 수 있는 방법은 온도계를 화염에 넣어 눈금을 읽는 것이다. 하지만, 온도계를 화염에 넣는 순간 그 촛불의 형태는 변하게 된다. 이것은 온도계의 차가운 표면 온도 때문일 수도 있고, 온도계의 부피 때문에 촛불의 연소과정이 영향을 받아서일 수도 있다. 그렇기 때문에, 온도계를 이용해 측정한 촛불의 온도는 기존에 알고자 했던 화염의 온도와 같을 수 없다. 반면에, 레이저 기반 계측법을 활용하면 화염 자체의 성질을 바꾸지 않고 보다 정확한 온도를 측정할 수 있다. 광선이 화염 안에 있는 원자 또는 분자와 상호작용해 신호를 만들어낸 후 즉시 원래 상태로 돌아가 화염을 그대로 유지하기 때문이다. 그래서 비침습 기법을 활용하면 보다 정확한 계측이 가능하다.

본 논문에서는 다양한 반응 과정을 연구하기 위해 두 가지 종류의 레이저 기반 계측법이 활용되었다. 하나는 라만 분광 (Raman spectroscopy) 기법이고, 다른 하나는 레이저 유도 형광 (Laser-induced Fluorescence, LIF) 기법이다. 라만 분광법은 레이저 광선을 계측하고자 하는 지점에 조사하고, 그곳에서 발생하는 빛을 검출한다. 라만 산란 신호는 그 신호를 발생시킨 분자의 종류에 따라 다른 색을 나타내는 특징을 가지고 있어, 다양한 종류의 분자를 동시에 측정할 수 있는 특징이 있다. 게다가 산란 신호의 세기는 분자의 양에 선형적으로 비례하는 특성이 있어, 측정하는 지점에서의 분자량과 분포를 연구하는 데에 유용하다.

본 논문에서는 다양한 종류의 화염에서 화학종의 분포와 그 양을 분석하기 위해 라만 분광법을 활용하였다. 메탄, 수소 혼합 메탄, 에탄, 에틸렌, 디메틸 에테르, 암모니아 화염이 그 대상이었으며, 그 안에 분포하는 주 화학종과 온도를 화염 내 다양한 위치에서 측정하였다. 측정된 데이터는 컴퓨터 기반의 화염 시뮬레이션 모델 개선을 위해 검증 데이터로 쓰였다. 추가로, 라만 분광법의 계측 감도를 높이기 위한 기법 개선 또한 본 논문의 중요한 부분이다.

라만 산란은 약한 세기를 가지는 프로세스로, 레이저 광선을 효율적으로 활용하는 것이 매우 중요하다. 그래서 본 논문에서는 한 쌍의 거울을 활용해 빛을 가두고 광선이 계측 지점을 여러 번 왕복하도록 만들었다. 광선이 여러 번 계측 지점을 통과할수록 신호의 세기는 비례하여 강해졌고, 본 논문에서는 하나의 광선 대비 45 배 증폭된 신호를 얻을 수 있었다. 그 결과, 디메틸 에테르 화염에 극소량 존재하는 포름알데히드를 계측할 수 있었고, 화염 내 위치에 따른 분포를 확인하였다.

라만 산란 신호를 개선하기 위한 다른 방법은 라만 산란 이외의 신호나 간섭을 제거하는 것이다. 만약 계측 지점에서 형광 신호와 같은 다른 강한 신호가 발생한다면 상대적으로 약한 라만 산란 신호는 감지하기 어렵다. 따라서, 이러한 불필요한 신호를 제거하기 위해 두 종류의 필터링 기법이 적용되었다. 주기 음영법(Periodic Shadowing, PS)은 공간적으로 신호를 필터링하는 방법으로, 난반사에 의한 신호 간섭을 효과적으로 제거한다. 줄무늬가 인쇄된 유리판을 이용해 신호의 모양을 변형하고, 그 결과 검출기에 기록된 신호는 Figure 1에서와 같은 무늬를 갖게 된다. 이때 난반사에 의한 신호는 줄무늬로 가려진 부분에서도 항상 검출되며, 수학적 기법을 활용하면 신호 전체에서 난반사의 영향을 제거할 수 있다.

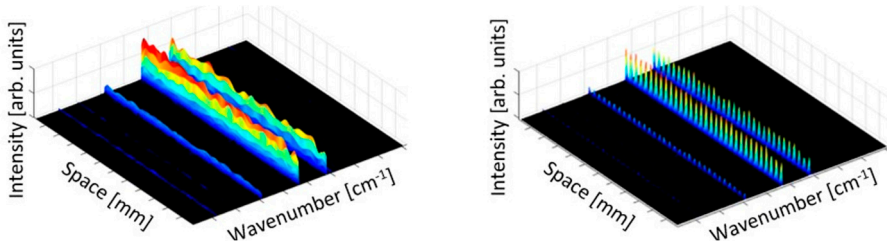


Figure 1. 일반적인 라만 산란 신호와 (좌) PS 기법으로 줄무늬가 새겨진 라만 산란 신호 (우), [1]에서 편집.

다른 필터링 기법은 편광 락인 필터링 (Polarization Lock-in Filtering, PLF) 기법이다. 이 기법은 계측 지점에서 발생하는 다른 종류의 강한 신호들을 제거하기 위해 본 논문에서 개발되었으며, 원리와 후처리는 PS 기법과 유사하다. PS 기법은 공간적으로 신호를 변조하는 반면, PLF 는 레이저 광선의 편광을 이용해 시간적으로 신호를 변조한다. 레이저 광선의 편광을 주기적으로 변환하면, 이에 민감한 라만 산란 신호는 그 세기가 주기적으로 변하지만, 형광 신호와 같은 다른 종류의 신호들은 이에 반응하지 않는다. 따라서, 이렇게 주기적으로 변조한 신호에 앞서 적용한 수학적 기법을 적용하면 라만 산란 신호만을 남기고 모두 제거할 수 있다.

이 두 가지 필터링 기법을 동시에 적용하여 숲을 동반한 화염 또는 바이오매스 열분해 과정 계측에 라만 산란 기법을 활용할 수 있었다. 숲을 동반한 화염의 경우, 숲 입자들에서 발생하는 레이저 유도 백열 발광 신호 때문에 라만 분광법을 적용하기 어렵다고 알려져 있었다. 하지만 PLF 기법을 활용해 이 간섭을 효과적으로 제거하였다. 열분해 연구에서는 바이오매스가 가열될 때 방출되는 물질들을 라만 분광법으로 계측하고자 하였으나 높은 온도에 이르렀을 때 방출되는 휘발성 탄화수소 성분들이 강한 레이저 유도 형광 신호를 발생했고, 라만 분광법 적용에 어려움이 있었다. 이 역시 PLF 기법을 통해 효과적으로 제어되어 라만 분광법을 이용한 방출 물질 분석이 가능하게 되었다.

앞서 형광 신호는 라만 분광법을 적용하는 데에 장애물로 설명되었다. 하지만 다양한 환경에서 레이저 유도 형광 (LIF) 신호는 유용한 정보를 제공한다. 레이저 유도 형광

¹ M. Gong, H. Kim, J. Larsson, T. Methling, M. Aldén, E. Kristensson, C. Brackmann, T. Eschrich, M. Jäger, W. Kiefer, Fiber-based stray light suppression in spectroscopy using periodic shadowing, *Opt Express* 29 (2021) 7232-7246.

기법은 분석하고자 하는 특정한 종을 계측하는데 유용한데, 앞서 언급했듯이 그 강한 세기로 인해, 극소량으로 존재하는 종 또한 용이하게 계측할 수 있다. 하지만 레이저 유도 형광 기법은 레이저 광선의 색을 계측하고자 하는 종이 흡수하고자 하는 색으로 맞춰주어야 하는 불편함도 있다. 화염 연구에서는, 화염의 특성을 잘 나타내는 특정한 종을 계측하기 위해 레이저 유도 형광 기법을 적용하곤 한다. 예를 들어, 히드록실 라디칼(Hydroxyl radical, OH radical)은 화염 안 연소 반응이 일어나는 지점에서 아주 잠시 존재하는 물질로, 레이저 유도 형광 기법을 이용해 이 라디칼을 계측하면 화염의 모양을 촬영하는 데에 용이하다.

본 논문은 레이저 유도 형광 기법을 적용해 가스터빈 연소기에서 히드록 실라디칼을 계측한 연구를 포함한다. 연소 연구 분야에서 주목받고 있는 가스터빈 연소기의 연료 유연성 연구를 위해 Siemens Energy사와 협력하여 연구했으며, 연구 결과 연료를 천연가스에서 수소로 점진적으로 변환해갈 때 드러나는 화염 특성 변화에 대한 유용한 정보를 얻을 수 있었다.

List of Papers

- I. A. A. Subash, H. Kim, S.-I. Möller, M. Richter, C. Brackmann, M. Aldén, A. Lantz, A. Lindholm, J. Larfeldt, and D. Lörstad, Investigation of Fuel and Load Flexibility in a Siemens Gas Turbine-600/700/800 Burner Under Atmospheric Pressure Conditions Using High-Speed Hydroxyl-PLIF and Hydroxyl Radical Chemiluminescence Imaging.
ASME Journal of Engineering for Gas Turbines and Power 143 (8): 081009, 2021.
- II. M. Gong, H. Kim, J. Larsson, T. Methling, M. Aldén, E. Kristensson, C. Brackmann, T. Eschrich, M. Jäger, W. Kiefer, and A. Ehn, Fiber-based stray light suppression in spectroscopy using periodic shadowing.
Optics Express 29: 7232-7246, 2021.
- III. H. Kim, M. Aldén, and C. Brackmann, Suppression of unpolarized background interferences for Raman spectroscopy under continuous operation.
Optics Express 29: 1048-1063, 2021.
- IV. H. Kim, M. Gong, E. Kristensson, A. Ehn, M. Aldén, and C. Brackmann, Time-resolved polarization lock-in filtering for background suppression in Raman spectroscopy of biomass pyrolysis.
Combustion and Flame 224: 219-224, 2021.
- V. H. Kim, A. Zubairova, M. Aldén, and C. Brackmann, Signal-enhanced Raman spectroscopy with a multi-pass cavity for quantitative analysis of formaldehyde in a one-dimensional laminar DME/air flame.
Combustion and Flame (under review)

Related Works

- VI. R. C. Rocha, S. Zhong, L. Xu, X. S. Bai, M. Costa, X. Cai, H. Kim, C. Brackmann, Z. Li, M. Aldén, Structure and laminar flame speed of an ammonia/methane/air premixed flame under varying pressure and equivalence ratio.
Energy & Fuels 35: 7179–7192, 2021

The Author's Contributions

Paper I

Investigation of Fuel and Load Flexibility in a Siemens Gas Turbine-600/700/800 Burner Under Atmospheric Pressure Conditions Using High-Speed Hydroxyl-PLIF and Hydroxyl Radical Chemiluminescence Imaging

A. A. Subash, H. Kim, S.-I. Möller, M. Richter, C. Brackmann, M. Aldén, A. Lantz, A. Lindholm, J. Larfeldt, and D. Lörstad. *ASME Journal of Engineering for Gas Turbines and Power* 143 (8): 081009, 2021.

Experimental investigations were performed using a standard third-generation dry low emission (DLE) burner under atmospheric pressure conditions to study the effect of central and pilot fuel addition, load variations, and hydrogen (H₂) enrichment in a natural gas (NG) flame. High-speed 2 kHz planar laser-induced fluorescence (PLIF) of OH radicals and imaging of OH chemiluminescence were employed to investigate the flame stabilization, flame turbulence interactions, and flame dynamics. The effects of hydrogen addition on combustion characteristics have been observed and analyzed.

I have largely contributed to the experimental setup and data collection process, as well as data analysis and writing. The entire laser and detection system was brought to and installed at the Siemens test facility, and the measurements continued for several weeks. All the lasers and cameras had to be set by Arman and me. Active discussions during the measurements made the data collection more efficient, and I have learned through the data evaluation process. I have contributed to the publication by writing and commenting on others' work.

Paper II

Fiber-based stray light suppression in spectroscopy using periodic shadowing

M. Gong, H. Kim, J. Larsson, T. Methling, M. Aldén, E. Kristensson, C. Brackmann, T. Eschrich, M. Jäger, W. Kiefer, and A. Ehn. *Optics Express* 29: 7232-7246, 2021.

A fiber-based stray-light suppression method is developed and implemented in an experimental setup with a high-power high-repetition-rate laser system used for Raman measurements in different room-temperature gas mixtures and a premixed

flame. The method is referred to as fiber-based periodic shadowing. The Raman spectroscopy results in combustion have shown that employing the fiber-based PS method reduces the stray-light level by up to a factor of 80. Therefore, better molecular species identification, as well as concentration and temperature evaluation, were performed. The results show that the method is feasible and efficient in practical use and can be employed as a general tool for improving spectroscopic accuracy.

I have mainly contributed to the experimental setup, data collection, and data evaluation in this work. The project was a part of Miaoxin's thesis work, and I was partly in charge of the supervision as well. The fiber-based periodic shadowing concept was tested for the first time in the lab, and therefore, we experienced many errors during the study. Therefore, various approaches and creative ideas were shared by the co-authors and tested in the lab.

Paper III

Suppression of unpolarized background interferences for Raman spectroscopy under continuous operation

H. Kim, M. Aldén, and C. Brackmann. *Optics Express* 29: 1048-1063, 2021.

A time-resolving filtering technique, called Polarization Lock-in Filtering (PLF), was developed to improve background suppression in Raman spectroscopy. The technique enables the separation of signal contributions via their polarization dependency. As a result, background interferences of broadband laser-induced fluorescence and incandescence were effectively suppressed from Raman spectra. The method was tested for measurements in a sooting flame accompanying laser-induced incandescence signals. The technique resulted in a 200-fold decrease of the background and allowed for quantitative analyses of concentrations and temperatures from the filtered data.

After validating the concept of the filtering technique, I suggested this follow-up study to optimize the technique. I have prepared the measurements by installing new apparatus for controlling parameters and increasing reproducibility. Data evaluation and the writing were driven by me as well.

Paper IV

Time-resolved polarization lock-in filtering for background suppression in Raman spectroscopy of biomass pyrolysis

H. Kim, M. Gong, E. Kristensson, A. Ehn, M. Aldén, and C. Brackmann. *Combustion and Flame* 224: 219-224, 2021.

This work is a part of the developing Polarization Lock-in Filtering (PLF) technique. The method was tested to reject laser-induced fluorescence signals on a continuous operation of Raman spectroscopy for a biomass pyrolysis process. The result showed good filtering abilities for the fluorescence signals by suppressing up to a factor of 50. The released species during the biomass pyrolysis process were identified in the Raman spectra, and their amounts were quantified. The technique revealed the potential to increase the general applicability of Raman spectroscopy under conditions where interfering signals present a challenge and a limiting factor.

I initiated this work after finding a necessity to handle interference signals properly to improve Raman spectra. I realized the idea in the lab and validated its applicability. Measurement designing and data evaluation were driven by me with the help of Marcus and Christian. I was the main person in charge of writing with full support from the co-authors.

Paper V

Signal-enhanced Raman spectroscopy with a multi-pass cavity for quantitative analysis of formaldehyde in a one-dimensional laminar DME/air flame

H. Kim, A. Zubairova, M. Aldén, and C. Brackmann. *Combustion and Flame (under review)*

This work reports a signal enhancement scheme to amplify the signal strength of Raman scattering. A multi-pass cavity enhanced the signal intensity by a factor of 45, and therefore, formaldehyde was quantitatively analyzed in a DME/air flame. The detection limit of the improved Raman spectroscopy setup was computed to 40 ppm. Formaldehyde quantity and temperatures in the flame were obtained from the analyses of the Raman spectra, and the results were compared with modeling results.

I have contributed to the experiment preparation, beam aligning in the multi-pass, data collection, evaluation, and writing. Experimental works were mostly shared with Alsu, and I got much help from Marcus and Christian through discussions.

Table of Contents

| | |
|--------------------------------------------------------------------------|-------------|
| Abstract | i |
| Popular Science Summary | iii |
| Populärvetenskaplig Sammanfattning | vii |
| 알기 쉬운 요약 | xi |
| List of Papers | xv |
| Related Works | xvi |
| The Author's Contributions | xvii |
| 1 Introduction | 1 |
| 1.1 Motivation | 1 |
| 1.2 Objectives | 2 |
| 1.3 Thesis outline | 2 |
| 2 Fundamentals | 3 |
| 2.1 Raman spectroscopy and quantitative data analysis | 3 |
| 2.2 Laser-Induced Fluorescence (LIF) | 8 |
| 2.3 Combustion and various types of flames | 10 |
| 2.4 Gasification and pyrolysis of biomass | 12 |
| 3 Experimental Equipment | 15 |
| 3.1 High-repetition-rate and high-power lasers | 15 |
| 3.2 Dye laser | 16 |
| 3.3 Spectrometers and Cameras | 17 |
| 3.4 High-pressure chamber | 19 |
| 3.5 Burners, heating cells, and gas turbine rig | 20 |
| 4 Results – Combustion and Pyrolysis Studies | 25 |
| 4.1 Fuel-flexibility study, PLIF studies | 25 |
| 4.2 Atmospheric pressure combustion, Raman spectroscopy studies | 27 |
| 4.3 Elevated pressure combustion, Raman spectroscopy studies | 31 |
| 4.4 Biomass pyrolysis and gasification, Raman spectroscopy studies | 37 |

| | | |
|----------|----------------------------------------------------------------|-----------|
| 5 | Signal Enhancement Techniques | 41 |
| 5.1 | High-repetition-rate laser and multiple data accumulation..... | 41 |
| 5.2 | Multi-pass cavity | 42 |
| 6 | Background Suppression Techniques | 47 |
| 6.1 | Periodic Shadowing (PS) with a grating and fiber optics..... | 47 |
| 6.2 | Development of Polarization Lock-in Filtering (PLF)..... | 51 |
| 7 | Results with Improved Raman Spectroscopy | 57 |
| 7.1 | Multi-pass Raman spectroscopy | 57 |
| 7.2 | Grating-based PS combined Raman spectroscopy | 59 |
| 7.3 | Fiber-based PS combined Raman spectroscopy | 60 |
| 7.4 | PS and PLF combined Raman spectroscopy | 61 |
| 8 | Summary | 65 |
| | References | 67 |
| | Acknowledgments..... | 71 |

1 Introduction

1.1 Motivation

Since ancient history, combustion has been serving as a source of heat and energy production. However, only a few centuries back, the process started to be properly studied and characterized. The industrial revolution accelerated the use of combustion all over society, and thus the necessity of understanding and better utilization increased.

The knowledge on combustion has been piling up step by step for a few centuries and is a valuable resource to achieve recent needs in increasing combustion efficiency and reducing emissions. Nevertheless, the complicated chemical processes that can include hundreds of reactions and species are far from fully understood, e.g., for complex renewable fuels increasingly used for energy supply. Therefore, a series of works in this thesis was done to understand combustion more, hoping it helps in taking one more step forward, supporting the efforts in society having the purpose of benefiting humanity by saving natural resources and keeping our planet sustainable while supplying a sufficient amount of energy in demand.

A way to contribute is to develop proper methods to measure the reaction processes, which directly benefits the understanding and improvement. Laser-based diagnostic techniques are accurate and sophisticated methods to study combustion and other thermal reaction processes. In addition, they are widely employed in various research fields, so developing a powerful laser-based technique can benefit many other fields as well. Therefore, improving laser-based combustion diagnostic techniques as carried out in the work of this thesis is also motivated.

Moreover, the studies of combustion and development of laser-based diagnostic techniques can be mutually beneficial. Combustion processes are accompanied by large temperature gradients and abrupt changes in chemical composition, conditions which sets requirements and serves as benchmarks for the development of laser-based techniques. On the other hand, the data obtained by the improved techniques are utilized to understand combustion better and improve the process, e.g., as input for the development and validation of computational models.

1.2 Objectives

Combustion, pyrolysis, and gasification processes were studied with the laser-based techniques: Raman spectroscopy and planar laser-induced fluorescence (PLIF). Measurements to understand combustion processes were made under various conditions, e.g., at elevated pressure and on carbon-free fuels (hydrogen and ammonia) with Raman spectroscopy and in turbulent premixed flames with the PLIF imaging. The data obtained from Raman spectroscopy were intended to validate and develop computational models, and some limitations of Raman spectroscopy were recognized, motivating the development of the technique for measurements under harsh conditions where strong competing signals are emitted.

Improved Raman spectroscopy with enhanced sensitivity for minor species detection and suppression of competing background signals was desired. Therefore, the detection sensitivity enhancement was studied by improving the laser excitation scheme and beam arrangement as well as by employing filtering techniques. A spatial filtering technique was demonstrated to suppress multiple scattering and stray light, and a temporal filtering method was developed to separate vibrational Raman scattering signals from competing background signals.

1.3 Thesis outline

Chapter 2 is an overall introduction to the laser-based techniques employed in the thesis work, Raman spectroscopy and PLIF, as well as thermal reaction processes, i.e., combustion, pyrolysis, and gasification.

Chapter 3 presents experimental equipment employed in measurements.

Chapter 4 presents measurement results obtained with PLIF and Raman spectroscopy in studies of premixed flames and biomass pyrolysis/gasification. PLIF was employed to investigate hydroxyl (OH) radicals in turbulent flames operated under gas-turbine-like conditions, and Raman spectroscopy was employed in studies of premixed flames of various fuels at atmospheric and elevated pressure as well as biomass thermal decomposition.

Chapter 5 introduces signal enhancing techniques combined with Raman spectroscopy to detect chemical species at low concentrations.

Chapter 6 introduces filtering techniques for Raman spectroscopy to suppress competing signals and backgrounds. Periodic shadowing (PS) was demonstrated to reject multiple scattering and stray light, and the polarization lock-in filtering (PLF) method was developed to suppress polarization-independent signals, e.g., laser-induced fluorescence (LIF) and laser-induced incandescence (LII).

Chapter 7 presents results from flames and biomass decomposition with improved Raman spectroscopy combined with the signal enhancing and filtering techniques.

2 Fundamentals

2.1 Raman spectroscopy and quantitative data analysis

Raman spectroscopy is a technique of analyzing inelastically scattered photons from a probe volume using spectroscopic methods. In this section, different kinds of scattering are briefly introduced to understand the Raman scattering process, and descriptions of detailed detection and quantification process follow.

Light scattering is the emission of photons from atoms and molecules as well as larger particles or droplets as a result of their interaction with photons of incident light. For example, when photons pass through, a molecule can absorb the photon and transfer itself into an excited state corresponding to the amount of energy the photon possesses. However, if the photon energy does not correspond to the molecule's excited states, the molecule is considered to be de-excited immediately within a time (τ) allowed by the Heisenberg Uncertainty principle in Equation 2.1 [1]. Most of these temporarily excited molecules are de-excited back to the original state, and the energy is released by photons emitted in dipole radiation pattern. This kind of scattering is called elastic scattering and is referred to as Rayleigh scattering for atoms or molecules in the gas phase.

$$\tau\Delta E \sim h/4\pi \tag{2.1}$$

However, there exists an inelastic scattering process as well. It means that the molecule is de-excited to another energy level than its initial level before absorbing the photon. Raman scattering is an example of inelastic light scattering, and it occurs when the molecule is de-excited to a different rotational or vibrational level than the original one. In this case, the scattered photon has altered energy from the excitation photon, and scattered light is observed at a wavelength shifted from that of the excitation light and the elastic scattering. The scattered light is divided into Stokes and anti-Stokes Raman scattering depending on whether the molecule gains or loses energy, respectively. The Jablonski energy-level diagram in Figure 2.1 illustrates the processes and their difference by showing the transitions between molecular energy levels.

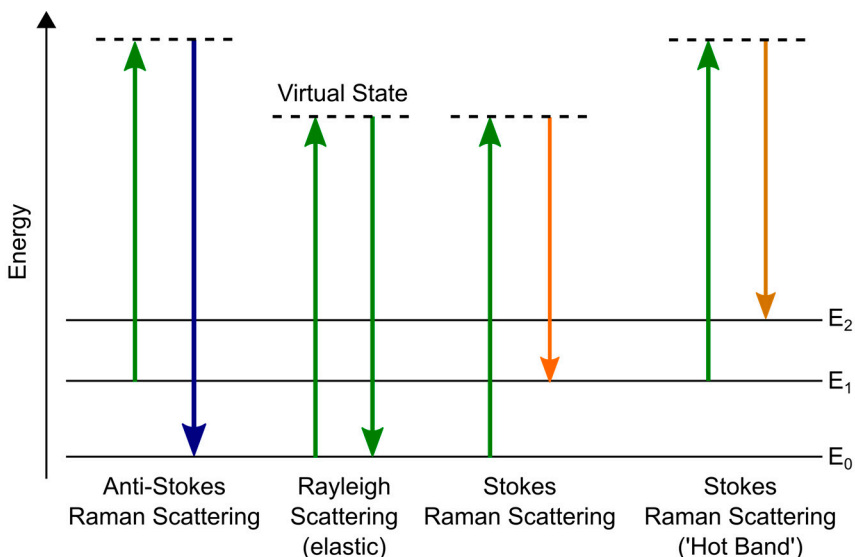


Figure 2.1. A Jablonski diagram of elastic scattering and Raman scattering processes. The hot band is observed when the molecule is already excited due to the high temperature. All the dashed lines are virtual states.

From this energy diagram, some important characteristics of Raman scattering can be understood. At first, the molecule is excited to a so-called virtual state, which means that the amount of energy to excite the molecule does not match that required for a transition to a real excited state. In other words, Raman scattering occurs for an arbitrary wavelength of the excitation light that can be chosen freely experimentally, which enables simultaneous detection of Raman scattering of various species, known or unknown beforehand, with a single excitation source. It is the same for the elastic scattering process, and the lifetime (τ) of the virtual state can be estimated using Equation 2.1 with the difference between the photon energy and that of a real excited state as a measure of ΔE . For the 532 nm beam in this study, the lifetime in the virtual state is $\sim 10^{-14}$ seconds, i.e., ~ 10 fs. Therefore, the process can be considered instantaneous [2].

Second, the energy differences between the ground state and the excited states play an important role. The Raman scattered photons have altered energy from the excitation, and the difference in photon energy is determined by the separation between the initial and final state, mostly between the ground and the first excited state at room temperature. Therefore, the Raman photons can be selectively detected by removing the signals emitted at the excitation wavelength. Furthermore, the separation between the energy levels is species-dependent. Therefore, Raman scattering from different molecules is emitted at different wavelengths, i.e., with a different so-called Raman shift expressed in wavenumbers relative to the excitation

wavelength. For this reason, spectroscopic methods implemented in studies with Raman scattering provide specific measurements of multiple species simultaneously.

Another important feature in the energy diagram is the energy difference between the excited states of the molecule. The spacing between energy levels is not identical, and therefore, the transition from the ground state to the first excited state gives a different Raman shift compared with a transition from the first excited state to the second excited state. In a Raman spectrum, Raman signals from transitions between excited states reside next to the fundamental Raman signal corresponding to transitions from the ground state. The Raman signals from the excited states are more pronounced at high temperatures, at which condition more molecules are thermally excited to the upper states. These Raman signals are therefore referred to as "hot bands," and analyzing the intensities of the hot bands gives temperature information of the gas containing the molecules in the probe volume.

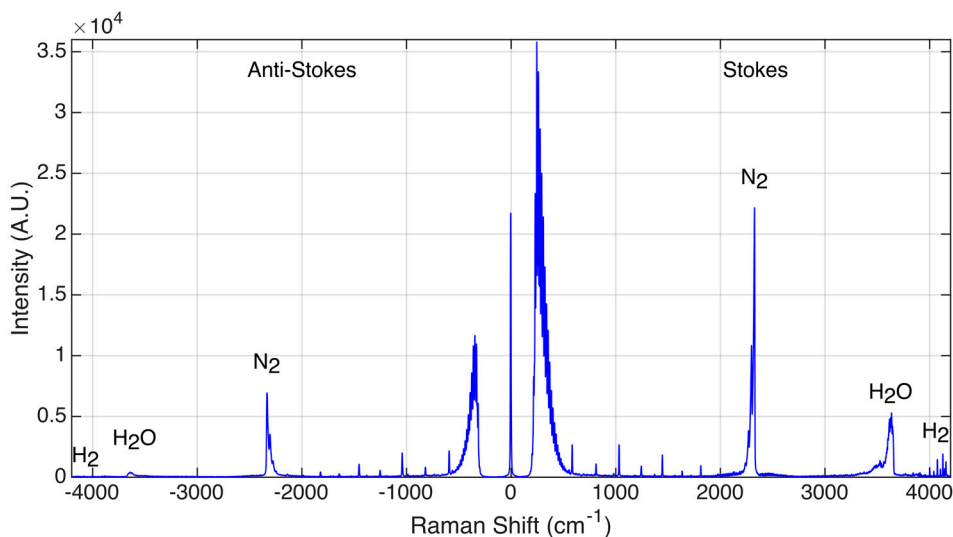


Figure 2.2. A sample spectrum with Raman peaks of the products in an ammonia/air flame, covering anti-Stokes and Stokes Raman signal. Bands and peaks close to the laser line at zero are pure rotational Raman signals. Low detector sensitivity at the left of the spectrum needs to be considered.

The characteristics of the Raman spectroscopy mentioned above are observed in the sample spectrum presented in Figure 2.2. The spectrum is recorded in the product zone of an ammonia/air flame where nitrogen, water, and hydrogen exist. The signal was scanned from the anti-Stokes to the Stokes region. Various species are detected simultaneously with their rotational and vibrational Raman signals, and all the peaks could be identified by referring to the literature or calculating energy levels with molecular constants.

The vibrational Raman signal strength of a diatomic gas is given by Equation 2.2 [3]. N is the number density of molecules, ν values are for the frequencies of the excitation laser (0) and molecular vibrational resonances (k), m is the molecular mass, ω_e is the vibrational frequency, a' is the polarizability, γ' is the anisotropy of the polarizability tensor, I is the excitation intensity, and h , c , k are universal physical constants. The polarizability-related terms make the vibrational Raman signal dependent on laser polarization, and these terms are different for rotational Raman scattering [4]. Therefore, different responses to polarization change could be utilized to separate vibrational Raman signals from rotational Raman signals in Paper 3. The Raman cross-section on the right-hand side of Equation 2.2 is defined by grouping the molecular-specific components together and is a quantity often used to account for the response of different molecules. Equation 2.2 implies that the signal intensity is linearly proportional to the number density in the probe volume, which makes a quantitative study using Raman spectroscopy straightforward. In addition, the signal is proportional to the excitation intensity, I , and signal enhancement with arrangements for increased laser intensity will be discussed in Chapter 5.2, Multi-pass cavity.

$$I_{\text{Raman}} = N \frac{h(\nu_0 - \nu_k)^4}{8mc^4\nu_k[1 - e^{-hc\omega_e/kT}]} [(a')^2 + \frac{4}{45}(\gamma')^2] I = N \left(\frac{\partial \sigma}{\partial \Omega} \right) I \quad (2.2)$$

Another quantity used to group the molecular-specific properties is the so-called Raman scattering activity, consisting of the last two polarizability terms and the degree of degeneracy (g_j) [5]. In Paper 5, the Raman scattering activity value of formaldehyde was used to convert the signal intensity into mole fraction since a Raman cross-section value was missing in the literature. A more detailed explanation is presented in the paper.

A high temperature in the probe volume is indicated with the appearance of several peaks for nitrogen around 2331 cm^{-1} , so-called hot bands (see Figure 2.1). The relative population of molecules in excited vibrational states is determined by the Boltzmann distribution and expressed as Equation 2.3, where ν is a vibrational quantum number, h is Planck constant, k is Boltzmann constant, and T is the absolute temperature [6]. At higher temperatures, excited states are increasingly populated, and the strength of the hot bands' peaks increases. Therefore, the accurate temperature could be derived by fitting the nitrogen spectrum with hot bands to theoretical spectra at high temperatures. Similarly, the anti-Stokes Raman signal of nitrogen at -2331 cm^{-1} is pronounced at high temperatures. An alternative approach for temperature evaluation is to compare the intensity ratio between the Stokes and anti-Stokes peaks.

$$N_\nu/N = e^{-\nu hc\omega_e/kT} (1 - e^{-hc\omega_e/kT}) \quad (2.3)$$

In this study, the hot bands of nitrogen are utilized to estimate flame temperatures since air is supplied for an oxidizer, and nitrogen is detected in all positions of flames. Model spectra of various temperatures were generated in PGOPHER software with molecular constants [7]. By fitting the measured nitrogen Raman spectra to the model spectra, the temperature could be obtained. The method was cross-checked with previous works [8, 9].

Even though the Raman scattering has many advantages to study various species simultaneously and quantitatively, the weak intensity of the signal has been a limitation for many applications. An example of this can be seen in Figure 2.2, studying the signal observed at 0 cm^{-1} . A notch filter with an optical density of 6 was installed to block the inelastic scattering, and it also cuts off the rotational Raman signals around the laser wavelength (at 0 cm^{-1}). However, even with the attenuation by the filter, a peak of strong intensity remains at 0 cm^{-1} , comparable to the nitrogen signal intensity at 2331 cm^{-1} . It gives an idea of how strong other competing signals could be compared with Raman scattering signals. The inelastic scattering could be blocked by optical filters, but spectrally broad competing signals, overlapping with the Raman peaks, impose challenges to Raman spectroscopy.

This work includes applications of Raman spectroscopy and developments of add-on techniques to improve the applicability of the method. Raman signal intensities have been amplified by employing a high-repetition-rate and high-power laser in combination with accumulating signals from multiple pulses over time. This method increases the signal intensity and signal-to-noise ratio of the Raman signals, but the temporal resolution of the data has been lowered. Another method of installing an optical cavity around the measurement volume and sending a laser beam through the measurement volume multiple times has been demonstrated. This method amplified the signal intensity significantly, and the loss of the temporal resolution was negligible. The details are described in Chapter 5, Signal Enhancement Techniques.

In Chapter 6, Background Suppression Techniques, Spatial and temporal filtering techniques are introduced to suppress unwanted laser-induced signals. Both techniques are based on the lock-in amplification method. The spatial filtering method cleared stray light and multiple-scattered photons in the detector, while the temporal filtering method removed other laser-induced signals that do not respond to the polarization change of the excitation beam, e.g., laser-induced fluorescence and incandescence. Therefore, improved Raman spectra in luminous or fluorescent reaction phenomena could be obtained.

2.2 Laser-Induced Fluorescence (LIF)

In this section, the laser-induced fluorescence (LIF) technique is introduced. It is one of the most-used laser-based diagnostic techniques to study flames, and it was employed in this study to investigate turbulent flames on burners for gas turbine applications. The fluorescence process is different from the scattering process, as presented in Figure 2.3, and some aspects of it will be described and compared with the scattering processes.

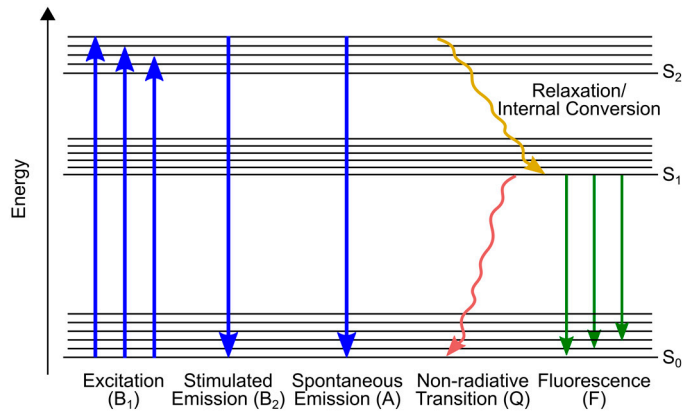


Figure 2.3. A Jablonski diagram of the simplified laser-induced fluorescence process.

The energy diagram shows that the process is more complicated than the scattering processes. The first thing to discuss is the absence of the virtual state. While the scattering processes were considered instantaneous due to the short lifetime of the virtual state, the fluorescence process involves real states and a relaxation process that results in a delayed signal emission. The excitation to a real molecular state requires the energy of the incident photons to match the energy of the excited state for the target species. Therefore, laser wavelength tuning is often required to conduct LIF studies.

Another factor to consider in the fluorescence process is the relaxation after the excitation. For example, when a molecule has absorbed a photon and is excited to a certain state, it loses a part of the gained energy through relaxation/internal conversion processes (cf., Figure 2.3) before it is de-excited to the ground state emitting the fluorescence signal. This results in the fluorescence emission having a different wavelength than the excitation. In addition, collisions with other molecules result in de-excitation without emission of radiation, which competes with the fluorescence. The overall process is affected by many factors, and the fluorescence intensity is related to the factors in Equation 2.4 [3], valid for low excitation intensity, I_v . B_1 , B_2 , A , and Q are denoted in Figure 2.3, and they are rates of

absorption, stimulated emission, spontaneous emission, and non-radiative transition, respectively. N is the total population of the ground state and excited states. Constants A and B are molecule-dependent that can be found in the literature, but Q varies with temperature, pressure, and composition, i.e., even within a specific flame. Therefore, obtaining Q for various flame conditions is challenging. For that reason, LIF is a challenging technique for quantitative measurements, in contrast to Raman spectroscopy, based on a scattering process that is instantaneous, so energy loss is negligible.

$$F \sim N \frac{B_1 I_\nu A}{A+Q} \quad (2.4)$$

Nevertheless, the involvement of actual states in the fluorescence process increases the transition probability, and fluorescence gives stronger signals in general than Raman scattering for the same amount of laser excitation. Therefore, the LIF technique is often employed to detect a specific intermediate species in flame, e.g., hydroxyl (OH) radicals, which can characterize the flame shape based on the distribution of the species.

In addition, the strong signal intensity of fluorescence makes planar imaging possible, and this version of the technique is called planar laser-induced fluorescence (PLIF). A laser beam is then stretched to form a laser sheet for this method, inducing fluorescence from the probed species distributed in the plane. Detecting OH radicals with the PLIF technique helps identify the flame-front because the OH is a radical in the reaction process (see Figure 2.4). The signal strength of PLIF is also sufficient to conduct single-shot imaging of the radicals, and therefore, the PLIF technique is often employed to study turbulent flames.

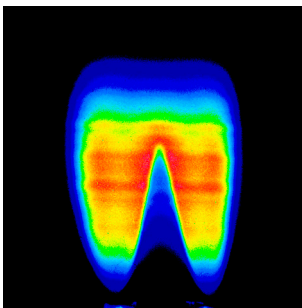


Figure 2.4. A sample PLIF image of OH radicals in a Bunsen flame.

An example of PLIF measurements to investigate combustion characteristics of turbulent hydrogen-enriched methane flames is presented in Paper 1. A high-repetition-rate laser was employed to characterize the turbulent flame properties and instabilities with an actual scale burner for SGT-600 (25 MW), SGT-700 (33 MW),

and SGT-800 (62 MW) industrial gas turbines. The high-frequency fluctuations of the flame were recorded by detecting OH radicals using the PLIF technique and chemiluminescence imaging, both at a 2 kHz data sampling rate. The high-repetition-rate laser was essential to investigate the full cycle of pressure oscillations in the combustion chamber, and some characteristic frequencies of different modes were derived from a set of images. The results are discussed in Chapter 4.1, Fuel-flexibility study, PLIF.

2.3 Combustion and various types of flames

Combustion is one of the most important processes for energy production. Since the industrial revolution, it has been playing an important role in society for various purposes, including generating electricity and operating vehicles. Nevertheless, the complicated process involving interactions between chemical kinetics, fluid dynamics, and heat transfer is not understood enough to optimize the processes fully. Enormous efforts have been put into combustion studies to improve the processes, and every achievement has contributed to more efficient and thus more sustainable energy production.

However, the concerns about combustion in society are increasing. Pollutants are formed in the combustion process, and it has been affecting the environment negatively. Many studies and reports on climate change claim that greenhouse gas emissions, primarily carbon dioxide (CO_2), must be reduced to net-zero levels to keep the planet livable [10], and the governments of many countries jointly set the goal to achieve this by the year 2050. For example, passenger vehicles with internal combustion engines are rapidly replaced by electric cars, and governments encourage this shift by offering subsidies and building infrastructure.

This rapid movement in society often gives a misconception that combustion only has disadvantages and will be completely replaced with other means in a future energy supply. Its share will probably be substantially reduced in some sectors like passenger vehicles, but replacing combustion entirely with other energy sources is not yet possible within the goal currently set. According to the Net-Zero Emission by 2050 scenario (NZE) reported by International Energy Agency, about 21% of the total energy supply will be from fossil fuels, and more than 60% of the fossil fuel use will be based on combustion [11]. In addition, renewable biomass can be considered CO_2 neutral in a long-term perspective, and if this is also combusted to produce energy, about 30% of the total energy supply will still rely on combustion. With the help of the carbon capture, utilization, and storage (CCUS) schemes, as well as relatively new and clean combustion concepts such as metal and ammonia combustion, combustion will be continuously used to fulfill society's energy demand while reducing its environmental impact.

Therefore, a better understanding and improvement of the combustion process is increasingly important to meet the energy demand and reduce emissions. The improvements in the combustion process will benefit society for the next decades, and it would support achieving net-zero emissions within the goal.

In this study, combustion processes were investigated by means of experimental studies. Non-intrusive laser diagnostic techniques have played an important role to study combustion for decades due to their ability to provide non-intrusive measurements of key parameters of the process. Compositions of major species and temperatures were measured in flames, and the experimental data were made available to validate numerical models developed by colleagues. Computational models are highly valuable as cost-efficient tools to gain an increased understanding of the development and optimization of combustion processes.

Various flames of interest investigated in this study are presented in Figure 2.5. The first photo is a Bunsen-type flame in a high-pressure chamber, and characteristics of hydrogen-enriched methane flames under elevated pressure conditions were studied. The other photos show flames stabilized on porous-plug McKenna burners. The McKenna burner was chosen for atmospheric pressure measurements since it can offer well-defined one-dimensional flames, of which composition and temperature information are useful for model development and validation. A sooting ethylene/air flame, which shows strong backgrounds due to natural soot luminosity and laser-induced incandescence, was investigated to test a newly developed filtering technique to suppress background and enable Raman spectroscopy. In addition, ammonia flames were studied due to their carbon-free nature and show strong yellow luminescence (cf., Figure 2.5) and fluorescence from NH_2 and NO_2 that makes applying some optical techniques challenging.

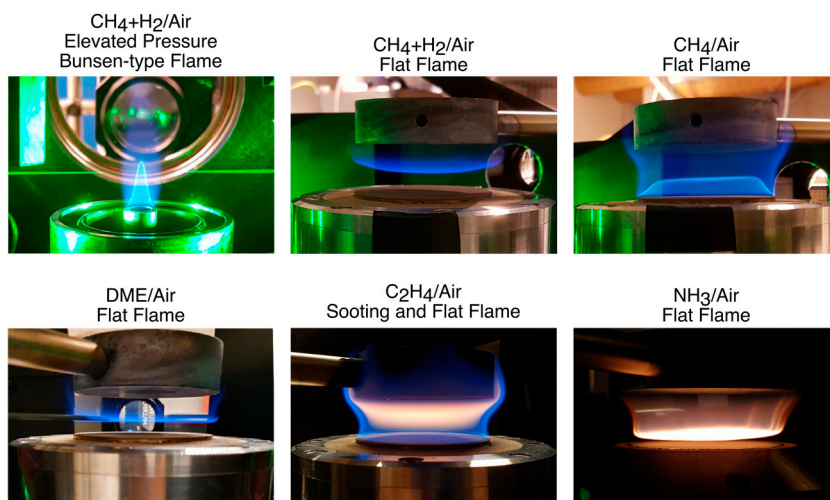


Figure 2.5. Photographs of the flames investigated in this study.

Moreover, combustion is a good target for developing laser-based diagnostics since it accompanies challenging environments such as high temperature and rapid composition changes from abrupt reactions. For example, the gas temperature measured in a premixed McKenna burner flame (cf., Figure 2.5) increases from room temperature to 1700 K within 5 mm height. Therefore, high spatial resolution and measurement sensitivity is required to resolve the abrupt change. Furthermore, the flame-front region of premixed flames, indicated by the luminous region in the photos of Figure 2.5, contains many short-living minor species, which are challenging to detect and quantify with conventional measurement techniques. Improved detection sensitivity can be validated by measuring those minor species in flames. Paper 5 is an example of improving the detection limit of Raman spectroscopy. In the study, the Raman signal of formaldehyde was captured in the preheat region near the flame-front and quantified to mole fractions up to 2000 ppm. The detection limit of the species with the setup was computed to be 40 ppm.

2.4 Gasification and pyrolysis of biomass

Thermal decomposition is one way to convert biomass into liquid and gaseous biofuels for use in sustainable energy production, e.g., biomass oil is obtaining great interest as having the potential to be a renewable energy source to replace fossil fuels [12]. The importance of understanding the process increases with the concerns about the impact of energy production on the environment and climate because biomass is a renewable fuel source that can be considered CO₂ neutral.

The energy production using biomass involves a complicated sequence due to its complex composition and structure. Therefore, investigating the components emitted from the biomass pellets during the decomposition process would help understand the detailed process of the energy conversion and the following combustion. In addition, biomass can be produced from various sources with different processes. Therefore, characterizing different pellet structures during the thermal decomposition using *in situ* measurements will provide essential information to understand the process.

Pyrolysis is one type of thermal decomposition, which can be achieved by heating while oxygen access to the biomass is prohibited, in contrast to gasification that allows a limited supply of oxygen. In practice, pyrolysis is also part of the gasification process, e.g., in the formation of syngas, of which the main components are H₂ and CO. Syngas is of interest as a fuel for gas turbines, which in turn can present components in a future flexible energy supply. Understanding the formation and the chemical reactions involved in pyrolysis and gasification makes it possible to optimize the product yields and reduce the amount of undesirable gases, such as HCl [13].

Much experimental research on biomass pyrolysis and gasification has been carried out using sampling methods, e.g., gas chromatography and mass spectrometry [14]. However, these methods have a limitation in that the gas cannot be measured *in situ*. *In situ* measurements of the gas compositions using Fourier transform infrared spectroscopy (FTIR) [14] and diode-laser-based absorption spectroscopy [15] have been reported, but both techniques are restricted to line-of-sight measurements. In addition, homonuclear diatomic molecules such as H₂, O₂, and N₂ are not detectable with infrared absorption, and multi-species detection with absorption spectroscopy may require multiple laser sources.

In this work, Raman spectroscopy was developed and employed to investigate pyrolysis and gasification of biomass. Since the gas composition is unknown and consists of multiple components, Raman spectroscopy was considered an advantageous technique for such studies. Even though there was a challenge of suppressing a competing fluorescence signal, its ability to detect multiple species simultaneously and quantitatively was a great benefit for the purpose of the study. Results obtained with conventional and improved Raman spectroscopy are separately presented in the following chapters.

3 Experimental Equipment

3.1 High-repetition-rate and high-power lasers

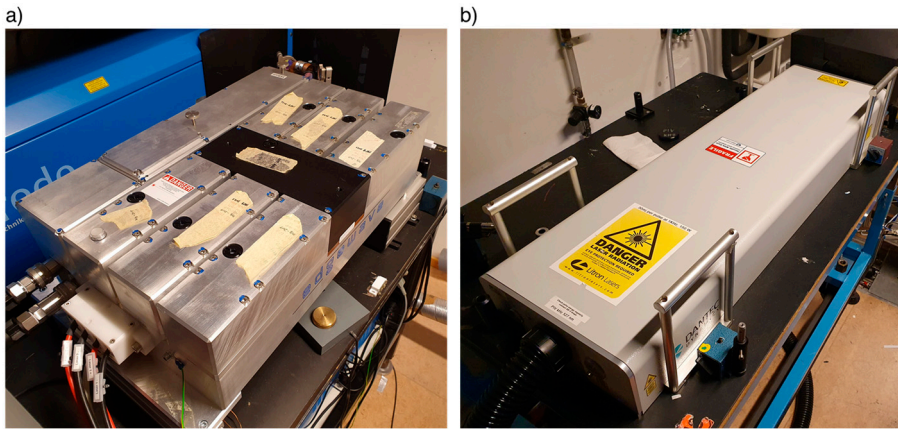


Figure 3.1. Photographs of (a) an Edgewave Nd:YAG laser (HD40I-OE) and (b) a Litron Nd:YLF laser (LDY304), employed in this study.

Two lasers, shown in Figure 3.1, were used in this study: an Edgewave Nd:YAG laser (HD40I-OE) and a Litron Nd:YLF laser (LDY304). The Nd:YAG laser can be operated between 2 and 10 kHz repetition rate, and the average power of the output beam is up to 100 W at 532 nm. The pulse duration is 12 ns, and the wavelength is selectively chosen by installing different harmonic-generation modules, e.g., 1064, 532, 355, and 266 nm. Most of the work in this thesis employed the frequency-doubled wavelength at 532 nm.

While the Nd:YAG laser was used for the published works, some experiments were made with the Nd:YLF laser. The laser is operated at 1 kHz, and the maximum average power and pulse energy are 30 W and 30 mJ, respectively. The operating power and pulse energy of the Nd:YAG laser were often in practice also limited to 30 W and 10 mJ, respectively, to avoid laser-induced breakdown, so the lower maximum power of the Nd:YLF laser was not necessarily a disadvantage. The Nd:YLF laser has a relatively long pulse width of ~ 150 ns, reducing the risk for laser-induced breakdown, and the wavelength is 527 nm.

These high-repetition-rate lasers were employed in the studies because they significantly benefit Raman spectroscopy and allow high-speed PLIF measurements. The details will be discussed in Chapter 5.1, High-repetition-rate laser and multiple data accumulation.

3.2 Dye laser

As discussed in Chapter 0, the fluorescence technique normally requires wavelength tuning for the excitation of the species selected for investigation. Depending on experimental conditions and purposes, various approaches to tune the wavelength exist, e.g., using an optical parametric oscillator or a dye laser. For the study presented in Paper 1, the need for high-speed LIF imaging required a dye laser optimized for use with the Nd:YAG laser. The dye laser (Sirah Credo) employed for the PLIF measurements of turbulent flames is presented in Figure 3.2.

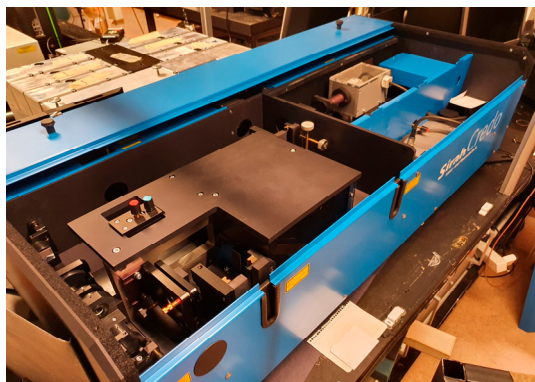


Figure 3.2. A photograph of a dye laser (Sirah Credo) employed for the PLIF measurements of turbulent flames.

For the measurements in Paper 1, the previously introduced Nd:YAG laser was used to pump the dye laser, and a 566 nm beam was generated from the fluorescence of the Rhodamine 590 dye. The beam was frequency-doubled and tuned to match the OH radical $Q_1(8)$ transition of the $A^2\Sigma^+(1) \leftarrow X^2\Pi(0)$ band at 283.55 nm.

The wavelength-tuned beam was stretched to form a sheet using an $f=40$ mm cylindrical concave lens and an $f=500$ mm spherical convex lens. The width of the laser sheet was 50 mm, and pulse energy was between 1.75 and 1.9 mJ. The repetition rate of 2 kHz was set for main measurements, and 3 and 5 kHz were tested for one experimental condition.

3.3 Spectrometers and Cameras

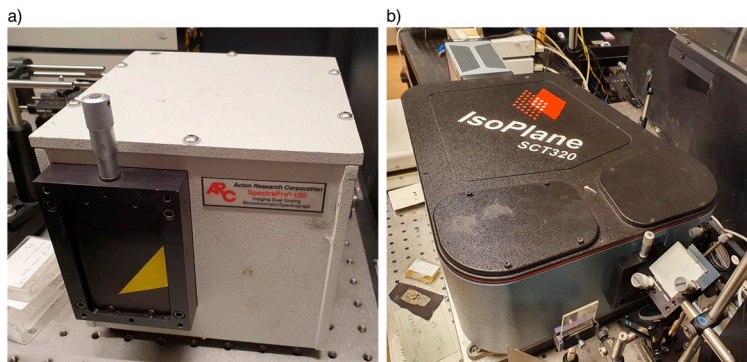


Figure 3.3. Photographs of (a) a Czerny-Turner type spectrometer (Acton, Spectrapro-150) and (b) a Schmidt-Czerny-Turner type spectrometer (Princeton Instrument, SCT-320) employed in this study.

A spectrometer is one of the essential pieces of equipment for Raman spectroscopy, and the quality of the data depends heavily on the spectrometer's specifications and gratings therein. The first spectrometer used in this study is an astigmatism-corrected Czerny-Turner type of focal length $f=150$ mm (Spectropro-150, Acton), with a grating of 1200 lines/mm installed. It is a simple and compact spectrometer that is easy to install and operate, but the so-called Bowing effect has been a typical issue with the Czerny-Turner type spectrometers [16]. The signal, i.e., the image of the spectrometer slit on the camera sensor that is supposed to be straight along the vertical direction, was bent on the sensor, as presented in Figure 3.4.

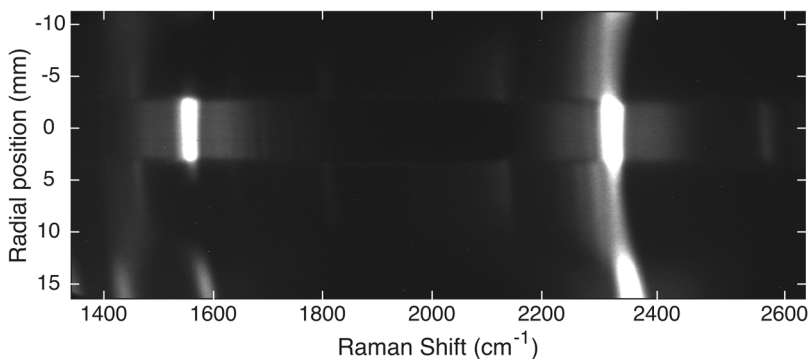


Figure 3.4. A sample spectral image of a dispersed signal by a Czerny-Turner type spectrometer. The lower part of the signal is dislocated toward the larger Raman shift due to the Bowing effect. The image was measured across a Bunsen-type flame, and radial position of 0 mm corresponds to the center of the flame.

For Raman spectroscopy, binning multiple image pixels vertically is one way to increase the signal-to-noise ratio of the measurement. However, the Bowing effect makes it difficult to devise such a method since the signals at different heights of a sensor are imaged with different amounts of horizontal dislocation. Therefore, an additional process is required to correct the distorted signals when a Czerny-Turner type spectrometer is employed.

The spectrometer employed the most in this study is a Schmidt-Czerny-Turner type spectrometer of focal length $f=320$ mm (IsoPlane SCT-320, Princeton Instruments). This type of spectrometer has solved problems with astigmatism and reduced coma and spherical aberration compared with the former type of spectrometer. Due to the improved equipment, no additional broadening of peaks due to the imaging defects of the spectrometer was observed. Three gratings of 600, 1800, and 2400 lines/mm were installed in the turret, and therefore, Raman spectroscopy measurements could be carried out with various spectral resolutions depending on interest.

An intensified charge-coupled device (ICCD) camera (PI-MAX 4: 1024×256, Gen III HbF intensifier, Princeton Instruments) was mounted on the spectrometers to record dispersed signals. The intensifier offered a short gate width down to a few nanoseconds, and the recording timing was synchronized with the laser pulses. Therefore, continuous background signals were minimized, e.g., ceiling light and flame chemiluminescence.

The intensifier has different quantum efficiency to signals of different wavelengths, where the maximum is ~50% near 500 nm. In addition, signal relaying optics and spectrometers are also wavelength sensitive, so an intensity calibration for different wavelengths is required. A broadband reference signal from a temperature-controlled black-body radiation source was recorded with a given measurement setup and compared with a reference intensity curve. This provided a calibration spectrum to correct signal intensities for the detector response at various wavelengths.

For the PLIF measurements, another camera was required for 2-dimensional imaging since the ICCD camera for Raman spectroscopy had a wide rectangular-shaped sensor (1024×256) optimized for spectroscopic use and relatively slow image acquisition. A high-speed CMOS camera (FASTCAM SA5, Photron) coupled with a two-stage image intensifier (HiCATT, Lambert) was employed for the high-speed PLIF imaging, and another CMOS camera (Phantom V7.1, Vision Research) mounted with a gated image intensifier (Hamamatsu) was employed for high-speed chemiluminescence imaging. The PLIF recording was synchronized with laser excitation at 2 kHz repetition. Chemiluminescence images were recorded at the same sampling rate but slightly delayed to avoid laser-induced signals in the images.

3.4 High-pressure chamber

A high-pressure chamber presented in Figure 3.5 was employed to investigate flame characteristics under elevated pressure conditions. The internal volume of the chamber is 25 liters, and the maximum operating pressure is 35 atm. It has four windows for optical access that enabled investigation with various optical diagnostic techniques. The windows are made of sapphire glass, which is anti-reflection coated for wavelengths from 250 to 430 nm and also around 560 nm. The windows are kept warm with heating bands to prevent condensation of water. The detailed design and operating specifications of the chamber were reported by Joo et al. [17].

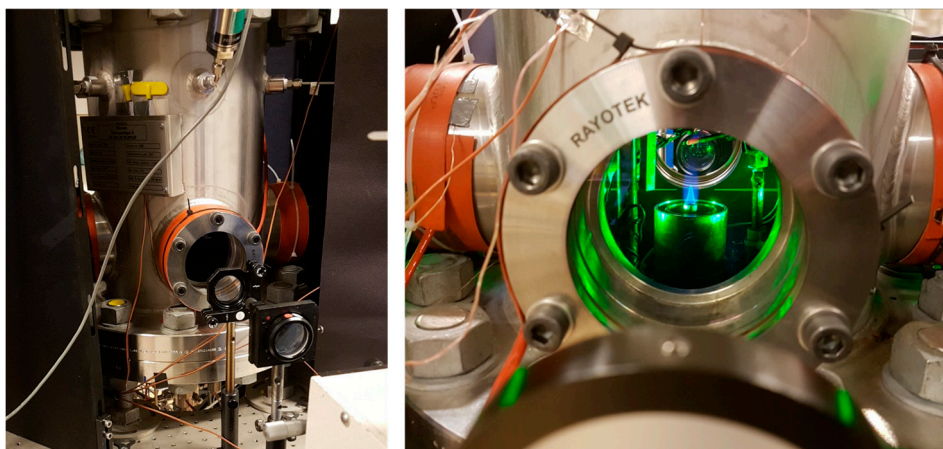


Figure 3.5. Photographs of a high-pressure chamber with four windows for optical access. A Bunsen-type flame is located at the center of the chamber, where a green laser beam is introduced through one of the windows. Two windows perpendicular to the laser path are utilized for signal collection.

A Bunsen burner is installed in an interchangeable burner module at the bottom of the chamber. Therefore, the tube diameter of the burner could be selected depending on interest, and a tube of 7 mm inner diameter was employed in this study. A larger tube is co-axially mounted around the burner tube, and an air co-flow was introduced in this outer tube to stabilize the flame.

The high-pressure chamber opens up a new dimension in the study of flame characteristics, but the current facility also has some points to improve in the future. At first, the inefficient ventilation of the product gases sometimes limits the running time of continuous measurement. For example, a large amount of water vapor was accumulated and detected in the ambient gas after around 30 minutes of ammonia flame operation. Therefore, a complete shutdown of the facility and purging the chamber were required from time to time.

So far, only Bunsen-type flames have been studied in the high-pressure chamber as such configurations can be installed relatively easily. However, considering that the experimental results are intended as input to understanding and predicting flame characteristics using computational models, flame stretch at the tip of Bunsen-type flames is challenging to model. While this has been achieved for some of the cases investigated for combustion of ammonia/methane/air mixtures [18], detailed modeling of other investigated conditions for flames of ammonia/methane/air and hydrogen-enriched methane/air remain to be carried out to utilize experimental results fully. A stagnation-plane burner for operation in a high-pressure vessel resulting in one-dimensional flames similar to the ones illustrated in Figure 2.5 has been presented by Versailles et al. [19], and a version of this burner has recently been designed for installation in the high-pressure chamber at Lund University for future studies in flames better suitable for computational modeling.

At last, the operating pressure of the chamber was limited due to unstable flame behaviors. Such instabilities are an intrinsic property of premixed flames as the reaction zone becomes progressively thinner at elevated pressure [20, 21]. Studies of hydrogen-enriched methane/air flames and ammonia/methane/air flames are presented in this study, and the maximum pressure conditions were 5 and 3 atm, respectively. In the previous investigations, including results reported by Joo et al. [17], methane/air premixed flames were maintained up to 20 atm at fuel-rich conditions. However, this required strong preheating of the burner, and it was achieved for flame heights less than 10 mm, resulting in a stable flame for a short period of time.

In the studies of the current work, the acquisition of Raman spectra required the flames to be stable for a longer time, and the flame cones were larger than 15 mm, which reduced the stability under elevated pressures. The relation between burner size, flame height, and preheating to achieve flame stability at higher pressures could be further investigated. Nevertheless, the intrinsic instability mechanism of premixed combustion sets a limit on the maximum pressure that can be achieved.

3.5 Burners, heating cells, and gas turbine rig

McKenna burner flames, as shown in Figure 2.5, were employed for the main atmospheric combustion studies with Raman spectroscopy. Increasing the detection sensitivity of the laser technique was one of the goals, so minor and intermediate species were targeted in laminar flames stabilized on the burner. From the combustion perspective, the goal was to experimentally obtain accurate composition and temperature profiles to serve model development. For these purposes, one-dimensional flames on McKenna burners were adequate.

A small oven and heating cells were employed in studies of the thermal decomposition processes of biomass pellets. In the first measurements, an oven with four arms was employed (Figure 3.6). The oven was built with a cross-shaped chamber wrapped with a heating band and insulation material. The end opening of the four arms could be closed with windows. Two tube fittings on the chamber allowed for continuous purging with argon and a fixed amount of oxygen to obtain a pyrolysis or gasification environment.

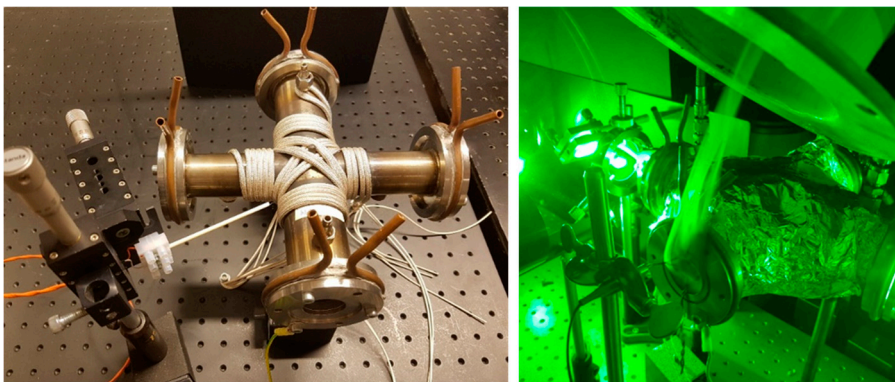


Figure 3.6. An oven for studies of thermal decomposition process of biomass pellets.

The temperature inside the oven went over 700 K after 15 minutes of continuous heating, but the heating band could not bear the high temperature and broke several times. In addition, the purging could not prevent volatile hydrocarbons from condensing on the windows, which caused beam and signal attenuation over time and required replacement several times. The small solid angle of detection, limited by the size of the window, was another downside of the oven. Therefore, a new type of heating cell was devised.

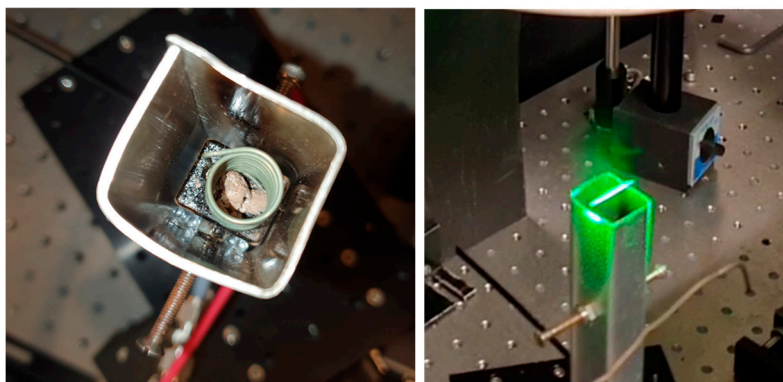


Figure 3.7. Photographs of a heating cell for gasification of biomass pellets.

Instead of using the oven, another tube-type heating cell for gasification was introduced (Figure 3.7). A small heating coil was installed inside a tube where argon and oxygen mixture continuously flows. The temperature increase was much faster than that of the oven, reaching 700 K in 40 seconds and 970 K in 200 seconds. The heating rate and temperature increase were measured to be reproducible for repeated measurements.

The pellet was inserted inside the coil resulting in more efficient heating, which induced a faster thermal decomposition. Measurements of emitted gases and volatiles were made immediately above the opening of the cell (see Figure 3.7), which offered better optical access not affected by condensation of volatile hydrocarbons on windows. Only the gasification process could be studied with the cell because a large amount of argon flow to meet the pyrolysis condition was not feasible due to heat losses obtained at the high flow required to maintain inert conditions. Nevertheless, the new heating device was helpful to test the fluorescence background suppression technique, discussed in Chapter 6.2, Development of Polarization Lock-in Filtering (PLF).

An atmospheric gas turbine test rig at the Siemens Energy AB facility was used in a fuel-flexibility study of full-scale gas-turbine burners. A schematic of the test rig from Paper 1 is presented in Figure 3.8. The fuel supplied was a mixture of natural gas and hydrogen, which was mixed with combustion air in a mixing tube of the burner, see Figure 3.9. Pressure transducers and an emission probe were used to monitor combustion characteristics, including possible combustion instabilities in real time. The combustion chamber had three large-size windows for optical access located around the burner tip, allowing a horizontal sheet to be arranged in front of the burner and the emitted signals to be viewed from below (cf., Figure 3.8).

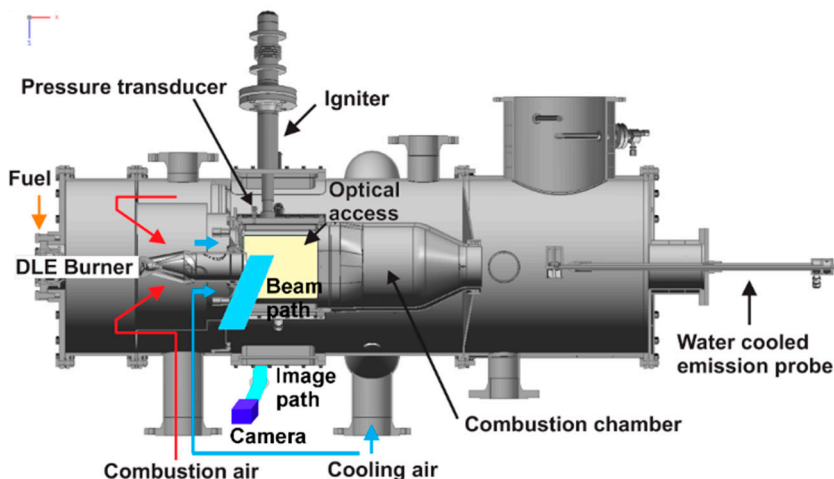


Figure 3.8. A schematic of the atmospheric pressure combustion test rig at Siemens Energy AB with light paths for optical diagnostics indicated [22, 23].

The Nd:YAG and dye laser formed a laser sheet wavelength-tuned for hydroxyl (OH) PLIF. The sheet was approximately 50 mm wide, and it investigated the region from the burner tip to 50 mm downstream, passing the axis of the burner, as presented in Figure 3.9 from Paper 1. The sheet was passing two pilot outlets on the burner tip.

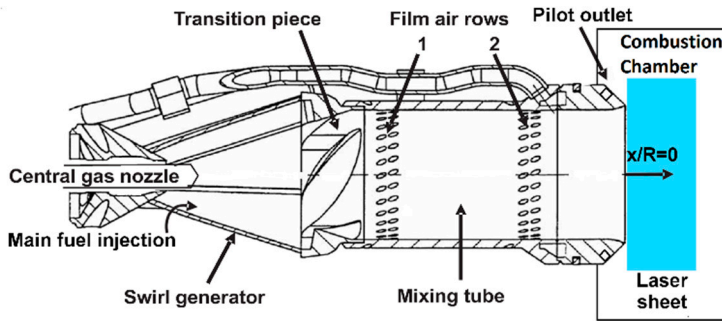


Figure 3.9. A schematic of the Siemens 3rd generation DLE burner [23, 24].

4 Results – Combustion and Pyrolysis Studies

4.1 Fuel-flexibility study, PLIF studies

High-speed PLIF and chemiluminescence imaging were done on turbulent flames using the actual scale burner and test rig at Siemens Energy AB facility, see Figure 3.8 and Figure 3.9. OH radicals were the target for both imaging techniques to detect the location and shape of the flame-front. PLIF images provided the OH radical distribution in an axial cross-section downstream the burner, OH* chemiluminescence showed a line-of-sight flame image with a larger field of view. Natural gas served as a base fuel, while the hydrogen enrichment was varied, and the flame behavior was investigated. Thus, measurements were made ranging from pure natural gas to 30%, 60%, 80% hydrogen mixing, and also for pure hydrogen.

In addition, fuel splitting was varied to test the burner performance. The effect of 3% of the total fuel sent to pilot channels was investigated, and 2% to a central fuel channel was also tested. Changes in flame shape and location with the operating condition were measured with the imaging techniques at 2 kHz acquisition rate. Sequences of 2728 PLIF images were saved on the camera since the number of images was limited by the memory capacity. The images were post-processed in order to extract useful information. For example, background luminosity from the PLIF images below a threshold was removed, and gradient mapping revealed the flame-front location and boundary layers. A mathematical approach called proper orthogonal decomposition (POD) was used to derive characteristic frequencies of the flame movement from the series of images. POD is an efficient method to find dominant modes from a set of images where fluctuations of various frequencies are superimposed in the set. For the results and detailed explanations, readers are referred to Paper 1.

The OH radical imaging successfully investigated flame behavior under various conditions. Especially, the differences between the natural gas flame and hydrogen flame were apparent. However, additional information from the sequences of high-speed single-shot images was limited. For example, flame image velocimetry (FIV) is a technique for obtaining flame propagation velocity by correlating the shape and location of the flame-front in two images. The 2 kHz sampling rate was expected to

enable this technique, but it was not fast enough to trace the flame-front in consecutive images. Therefore, one of the operation conditions was selected, and laser repetition and sampling rate were raised to 3 kHz and 5 kHz. Series of the PLIF images at the increased repetition rates are presented in Figure 4.1.

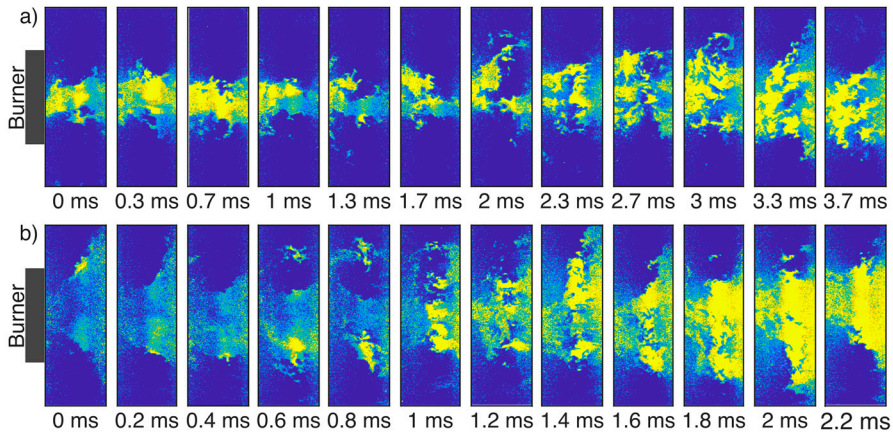


Figure 4.1. High-speed PLIF images in sequence at (a) 3 kHz and (b) 5 kHz repetition and sampling rate. The images are taken near the burner tip.

For the 3 kHz image set displayed in the upper panels, it is difficult to correlate between consecutive images. For example, small flame structures separated at the top of the 2 ms image disappear in the next image. However, the 5 kHz results shown in the bottom panels enable a rough estimation of how the flame evolves between images. The circulation at the upper part of the 0.6 ms image remains in the next two frames, and the detachment of a region at the upper part of the 1.6 ms image is traceable in the next image. The test and results provide valuable information to estimate the required temporal resolution to trace the flame-front propagation in turbulent combustion studies in the future.

4.2 Atmospheric pressure combustion, Raman spectroscopy studies

As described in Chapter 3.5, one-dimensional flames on McKenna burners were measured at atmospheric pressure. This chapter presents an investigation of methane flames with Raman spectroscopy. A simple setup is an advantage of Raman spectroscopy, which is found in Figure 4.2. There are two special features in the setup. One is the laser beam sent back to the measurement region with mirrors, so-called double-pass alignment, and the other is the spherical mirror located on the opposite side of the spectrometer, as going to be discussed in Chapter 5.2, Multi-pass cavity. Each of these components doubled the signal strength.

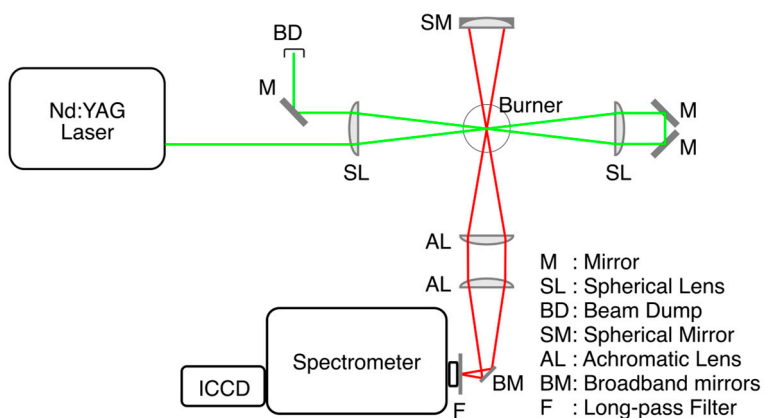


Figure 4.2. A schematic of Raman spectroscopy setup for flat flame studies. The green line is for the laser beam path, and the red lines indicate the signal collection path.

A methane/air flame of equivalence ratio $\Phi=1.4$ was measured with Raman spectroscopy. Additional nitrogen dilution levitated the flame a few millimeters, and the burner height was controlled with a lab jack to measure at various heights. Measurements were made at 23 heights above the burner (HAB) equidistant from 1 to 12 mm and at 3 additional heights at 15, 18, and 20 mm, covering from reactant zone to product zone. A stagnation plate was located at 21 mm HAB.

Some Raman spectra of the selected heights are presented in the top panel of Figure 4.3. For each displayed spectrum, 400 spectra were accumulated on the detector for 80 ms to enhance the signal, and eight spectra acquired at different spectrometer center wavelengths were stitched into one spectrum covering the entire spectral range of interest: from 200 to 4400 cm^{-1} . A grating of 1800 lines/mm employed for this measurement offered a good spectral resolution to resolve individual rotational lines located as close as 5 cm^{-1} .

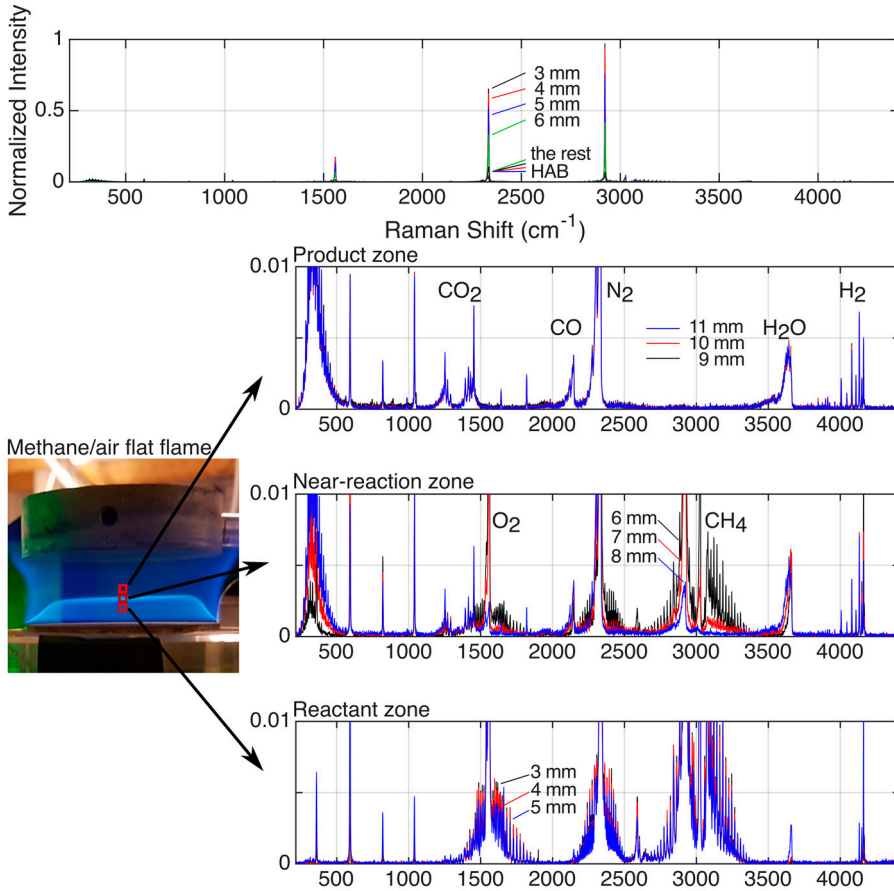


Figure 4.3. Raman spectra of methane/air flame at equivalence ratio $\Phi=1.4$. Measurement heights are scanned from 1 to 20 mm above the burner (HAB), while the flame-front is located around 8 mm HAB. 3 spectra are grouped and separately presented in the lower panels.

According to the ideal gas law, the number of molecules decreases with the temperature increase, i.e., the height increase in the flame. Therefore, only spectra with strong signal acquired at lower heights are visible in the top panel, and the spectra are separately presented in the three lower panels, magnifying the intensity. The signal intensity is normalized to the global maximum intensity: the methane signal intensity at 1 mm HAB.

The major species in the methane/air flame are oxygen (O_2), nitrogen (N_2), methane (CH_4), and hydrogen (H_2) in the reactant zone and carbon dioxide (CO_2), carbon monoxide (CO), nitrogen, water (H_2O) in the product zone. All the species are detected in the Raman spectra at wavenumbers 1285 and 1388 cm^{-1} for CO_2 , 1550 cm^{-1} for O_2 , 2145 cm^{-1} for CO , 2331 cm^{-1} for N_2 , 2915 cm^{-1} for CH_4 , 3657 cm^{-1} for

H₂O, and 4160 cm⁻¹ for H₂. The first six spectra in the bottom and middle panel present the O₂ peak while the top panel does not have it. Therefore, the flame-front can be expected to be located between 8 and 9 mm HAB.

The other peaks in the spectra can be identified in another set of spectra from the same measurement presented in Figure 4.4. Six acquired spectra near the flame-front with a step of 0.5 mm are selected. Therefore, the upper panel shows spectra on the product side, and the lower panel is from the reactant side.

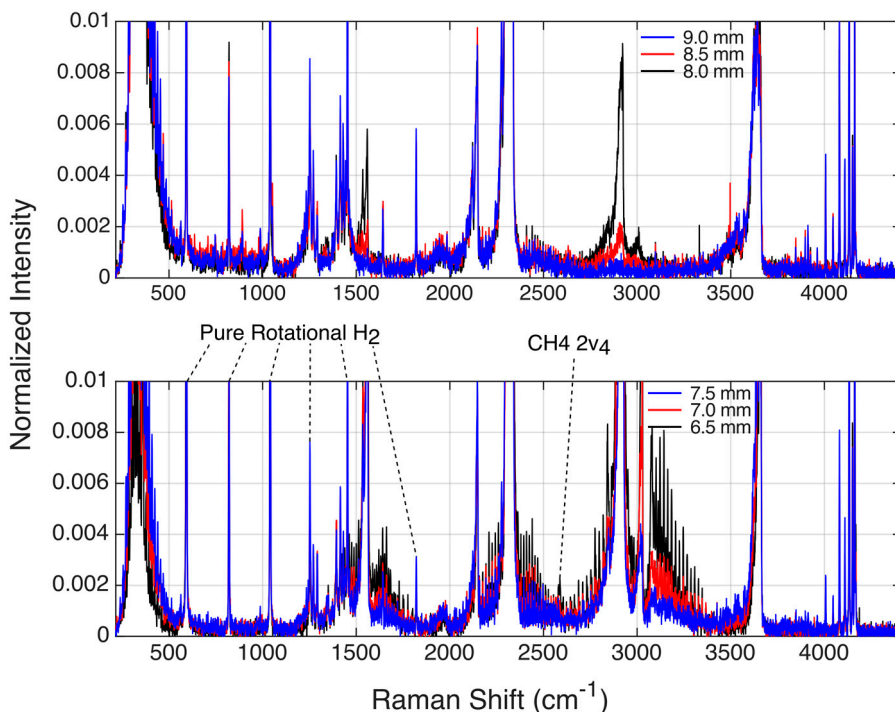


Figure 4.4. Raman spectra of methane/air flame at equivalence ratio $\Phi=1.4$. Measurement heights are scanned near the flame-front, and the y-axis is rescaled to search for minor species in the flame.

Quantifying Raman signals to number densities of the major species was carried out by integrating signal intensities in channels defined by spectral regions covering each peak and taking Raman cross-sections into account. Raman cross-sections of the major species have been collected and listed by Eckbreth [3]. Since all the major species are detectable, mole fractions of each species at measured heights were obtained and can serve for model validation.

The relatively simple quantification process could be employed thanks to the high spectral resolution achieved by 1800 lines/mm grating. When the spectral resolution is insufficient, signal interference between multiple channels can lower

measurement accuracy, so-called cross-talk. In such conditions, a smart approach using pre-measured or calculated cross-talk effect between different channels is reported to mitigate its effect on quantification processes [25]. The accuracy of quantified results is reportedly good. However, it was not employed in this study due to the lack of pre-measured cross-talk data and added complexity when a Raman signal of new species is detected.

The Raman spectra from the measurement were useful for the quantification and model validation, but minor species detection was still challenging. In order to detect intermediate minor species in combustion, peaks appearing only at a few heights were searched. A small peak between two CO₂ peaks at 1343 cm⁻¹ appeared at a few heights near the reaction zone, and it is speculated to be from ethylene (C₂H₄) [26]. However, the signal could not be enhanced to a level that can be quantified, and no other signal of minor species could be resolved with the given signal-to-noise ratio. Some additional spectra, acquired employing a 2400 lines/mm grating with a better spectral resolution, were not useful either due to reduced signal strength.

The limitation of the setup on detecting minor species was analyzed, and it was concluded that signal enhancement is necessary. Increasing the number of accumulations on the sensor could enhance the signal strength, but the longer recording time reduced the temporal resolution. Even though laminar flames were studied, the height of flames fluctuated due to the unsteady mass flow control units and airflow in the lab. Therefore, averaging more spectra of a fluctuating flame resulted in a lowered spatial resolution, reducing the chance of detecting signals from intermediate species. To solve this issue, signal enhancement techniques while keeping or improving the temporal resolution were studied and tested in Chapter 5, Signal Enhancement Techniques.

4.3 Elevated pressure combustion, Raman spectroscopy studies

Flames under elevated pressures were studied employing a high-pressure chamber and Raman spectroscopy. Premixed Bunsen-type flames with hydrogen-enriched methane (CH_4/H_2) and air were one of the first measurements with the smaller Czerny-Turner type spectrometer. A flame photograph is presented in Figure 2.5, and the experimental setup resembles that of the atmospheric pressure measurements shown in Figure 4.2.

The burner was a co-flow arrangement with a central tube of an inner diameter of 7 mm. The co-flow air was introduced in the axial direction through an outer tube of 35 mm in diameter. A fuel mixture of 65% CH_4 and 35% H_2 was premixed with air before entering the burner tube. Measurements were made in flames of equivalence ratio $\Phi=1.3$ at pressures of 1, 2, 3, and 5 atm.

The height of the flames was set the same, while the laser beam passed 7.5 mm above the burner tip, approximately at the center height of the flame. Six spectral images at different center-wavelengths were recorded, cf., Figure 3.4, and stitched to cover the entire spectral range from pure rotational Raman signals to vibrational hydrogen Raman signals, i.e., Raman shifts from 400 to 4200 cm^{-1} . Signals from the flame reactant and product zone were separately binned to get Raman spectra, and the result is presented in Figure 4.5.

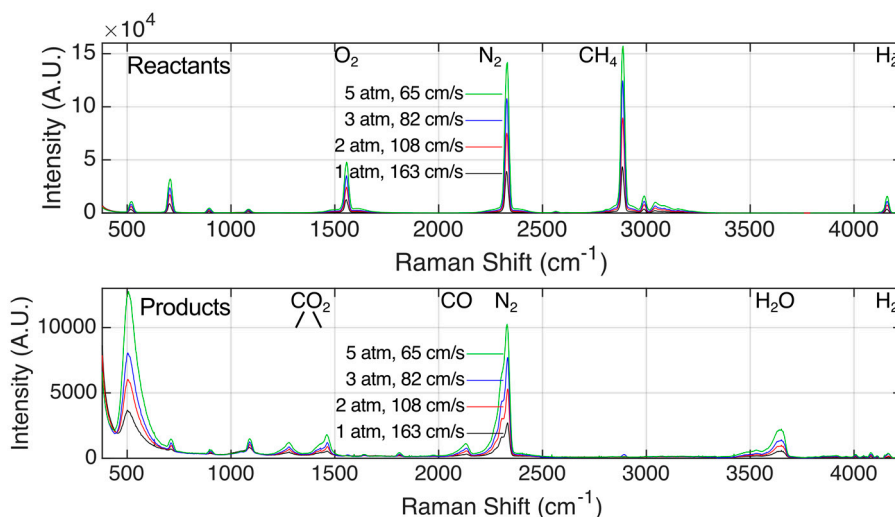


Figure 4.5. Raman spectra of a hydrogen-enriched methane/air flame at an equivalence ratio $\Phi=1.3$, under various pressure conditions. Spectra of reactant zone and product zone are presented in separate panels. Flow speed varied to keep the flame height the same over the different pressure conditions.

Increased signal strength is observed at elevated pressures due to the higher number density of the gas. However, the signal strength is not completely proportional to the pressures because of flow rate change and line broadening at high pressures. The major species discussed in the previous section are detected with Raman spectroscopy also here: O₂, N₂, CH₄, and H₂ in the reactant zone and CO₂, CO, N₂, H₂O, and H₂ in the product zone. The diagnostic goal of this measurement to test the Raman spectroscopy setup and investigate Raman signal quality at elevated pressures was well achieved, and the peaks of each species were integrated and quantified to mole fractions, presented in Figure 4.6.

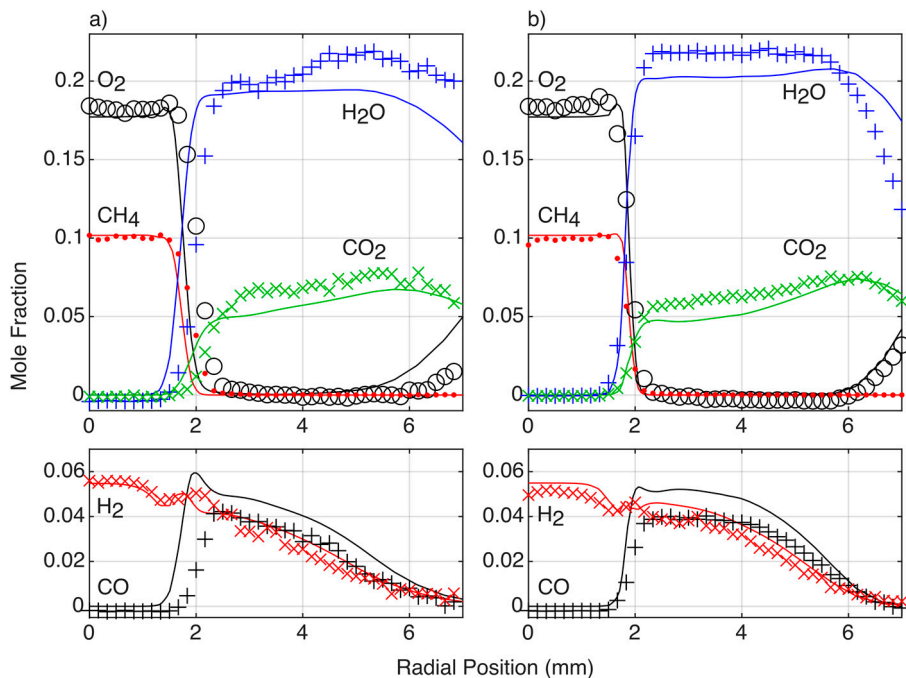


Figure 4.6. Mole fractions of major species in a hydrogen-enriched methane/air flame at an equivalence ratio $\Phi=1.3$, under pressure conditions of (a) 1 and (b) 5 atm. Markers are experimental data, and lines are simulated results.

In the figure, flame composition profiles under 1 and 5 atm conditions are compared with simulation results obtained using a reduced chemical kinetic mechanism implemented with computational fluid dynamics. The trends of each component's profile show good agreement between the experiment and simulation, especially at the 5 atm case. Radial shifts are observed in some cases, and it might be attributed to an error in the calculation of flame thickness. With these results, Raman spectroscopy was proved to be a strong technique to investigate flames under high-pressure conditions.

Ammonia (NH_3) combustion was also studied in the high-pressure chamber. Preheated ammonia mixed with methane and air was supplied to the burner. With different ammonia mixture fractions, pressures, and equivalence ratios, various flames were investigated with Raman spectroscopy and laser-induced fluorescence. The Schmidt-Czerny-Turner type spectrometer was employed in this study, and eight spectral images with different center wavelengths were stitched, as presented in Figure 4.7. The straight signal observed in the vertical direction of the image shows the improvement in imaging with the new type of the spectrometer compared with the spectral image in Figure 3.4.

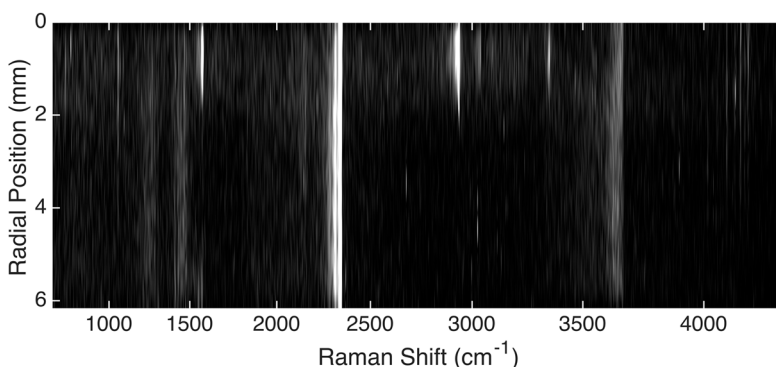


Figure 4.7. A sample Raman spectral image of ammonia(20%)-methane(80%)/air flame at an equivalence ratio $\Phi=1.2$ under 2 atm. The radial position of 0 mm is the center of the Bunsen-type flame.

Strong Raman signals of the major species identified for the hydrogen-enriched methane flames appear again, and the NH_3 signal at 3334 cm^{-1} is the additional peak in this spectrum. Even though CO_2 , CO , and H_2 are not present in reactants, they are detected in this region, corresponding to radial positions 0-1 mm, possibly due to diffusion. Another thing to note is the broadband fluorescence detected across the entire spectral range for radial positions between 0 and 2 mm. The broadband signal is detected at all Raman shifts, and it has been an obstacle to accurate Raman-based quantification.

Raman spectra of the flames with various NH_3 fractions at 3 atm are presented in Figure 4.8. The upper panel shows the species detected at the 1 mm radial position of the flame (reactant zone), and the lower panel shows the spectra at 2 mm away from the flame center (product zone), see Figure 4.7. The signal strength is normalized to the nitrogen signal intensity to compare the mole fraction of ammonia at various conditions. The spectra in the lower panel have been smoothed with a span of 5 pixels for a better visualization due to the noisy background from the fluorescence interference.

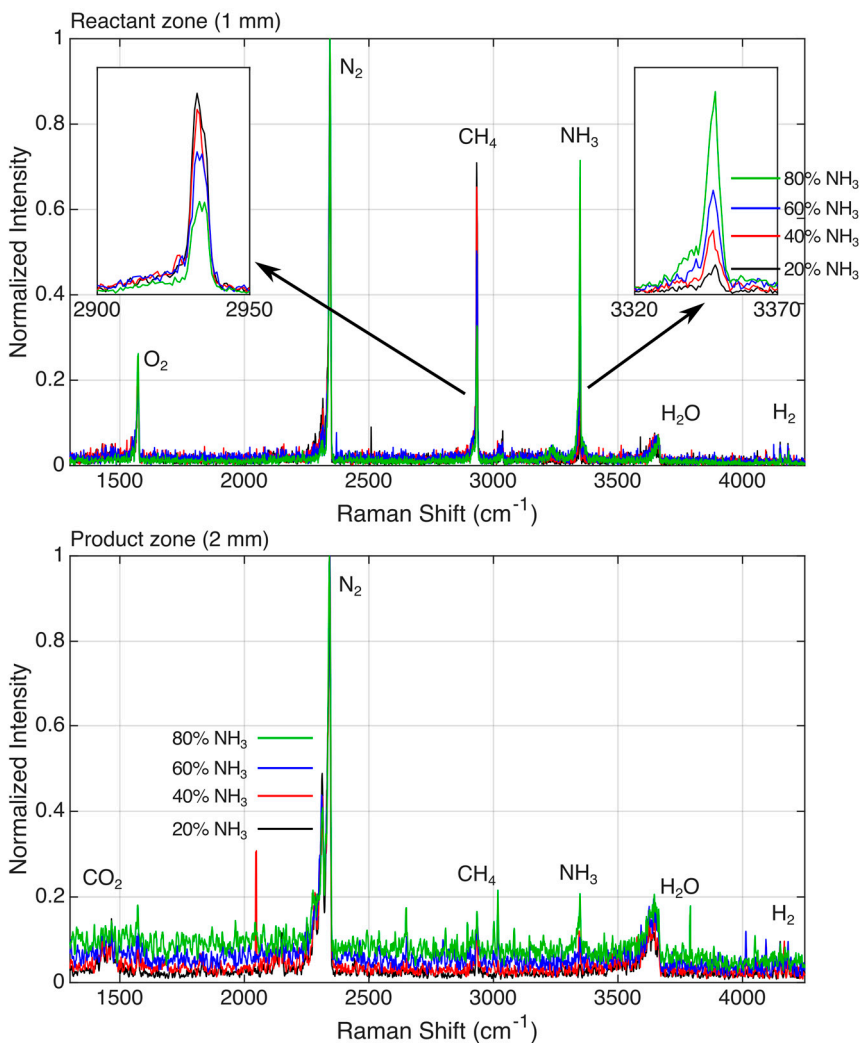


Figure 4.8. Raman spectra of ammonia-methane/air flame with different fuel mixtures at equivalence ratio $\Phi=1.2$ and 3 atm. Ammonia fractions varied from 20 to 80%. The upper panel shows Raman spectra at 1 mm radial position (reactant zone), and the lower panel shows Raman spectra at 2 mm radial position (product zone).

On the insets of the upper panel, CH_4 and NH_3 peak intensities change according to the flame conditions, while other peaks do not respond to it so much. In the lower panel showing the product zone, CH_4 and NH_3 are consumed, so their peaks are hard to compare, but the CO_2 peak appears in low NH_3 fraction cases, where the relative amount of CH_4 is higher. The different background level of the spectra is mainly due to the broadband fluorescence from NH_2 in the reaction zone. Therefore, a higher background level is observed from larger NH_3 fraction cases.

Similarly, spectra at pressure conditions of 1, 2, and 3 atm are compared in Figure 4.9. The equivalence ratio and ammonia fraction in the fuel mixture were fixed to $\Phi=1.0$ and 20%, respectively. Again, the spectra in the lower panel are smoothed with a span of 5 pixels to mitigate fluorescence interference. Absolute intensities are compared between the cases.

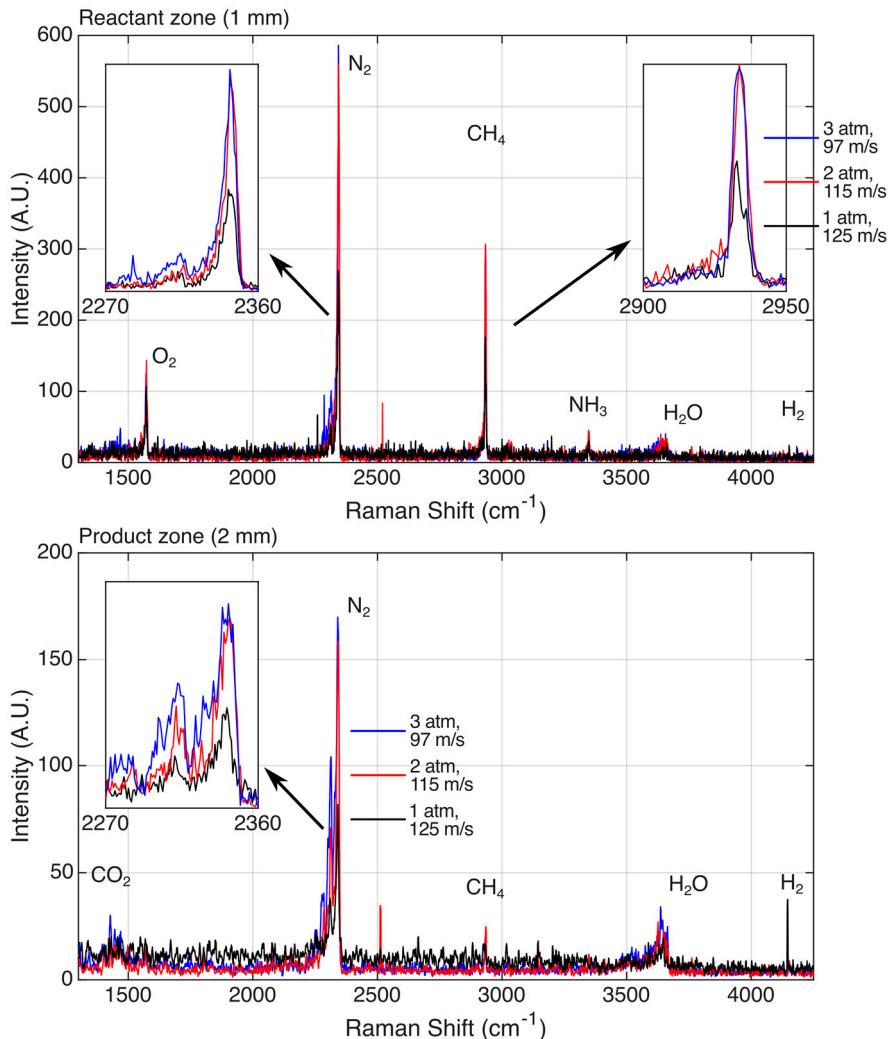


Figure 4.9. Raman spectra of ammonia(20%)-methane(80%)/air flame under various pressure conditions at equivalence ratio $\Phi=1.0$. Chamber pressure varied from 1 to 3 atm, and jet velocity was altered accordingly to keep the same flame height. The upper panel shows Raman spectra at 1 mm radial position (reactant zone), and the lower panel shows Raman spectra at 2 mm radial position (product zone).

On the insets of the upper panel, the signal increases with pressure, but the 3 atm case does not follow the trend. A similar trend has been observed in other equivalence ratio cases, that the signal strength for high-pressure cases does not increase from a certain pressure level. This issue might be attributed to the accumulated water vapor in the chamber, which attenuates the laser beam and lower the excitation efficiency over time. A continuous run of ammonia combustion produces a large amount of water, and more frequent laser-induced breakdown observed at the later part of measurements supports this speculation.

In Figure 4.9, nitrogen hot bands are presented in the insets of each panel. The relative intensity of hot bands is difficult to compare between cases in the lower panel, but the stronger intensity at 3 atm is observed in the upper panel. Temperatures based on the fit of the nitrogen spectra, explained in Chapter 2.1, are obtained and presented in Figure 4.10.

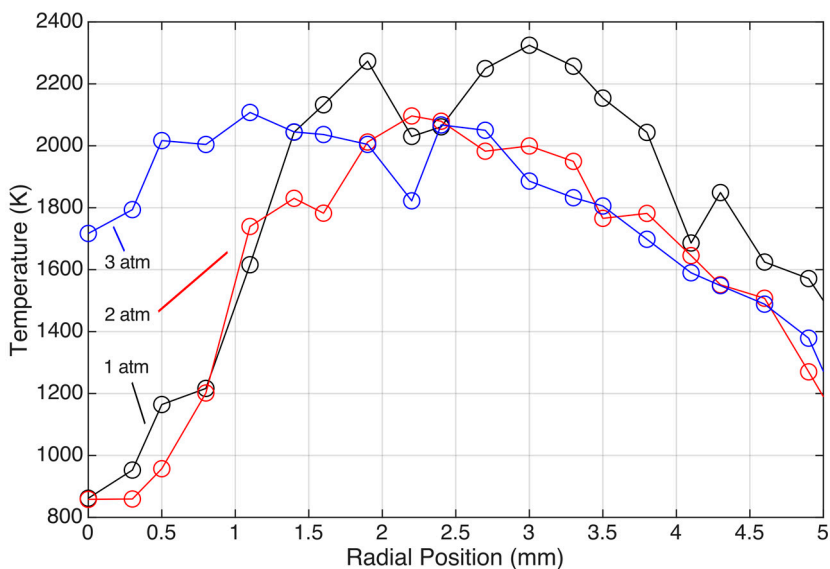


Figure 4.10. Thermometry using Raman spectra of ammonia(20%)-methane(80%)/air flame under various pressure conditions at equivalence ratio $\Phi=1.0$. Chamber pressure varied from 1 to 3 atm.

Higher temperature at the center of the flame where reactants are present is observed for the 3 atm case, consistent with the stronger hot band peak observed at 1 mm radial position for the 3 atm case spectrum (see Figure 4.9). On the other hand, 2 and 3 atm cases show similar profiles in the product zone, while the 1 atm case has a large fluctuation, potentially attributed to its largest noise level observed in Figure 4.9.

Even though Raman spectroscopy on ammonia flames under elevated pressures was challenging due to the broadband LIF interference and water accumulated in the chamber, the temperature data obtained from the Raman spectra were valuable for model validation and development. Furthermore, difficulties of obtaining Raman spectra in ammonia flames were recognized, and it started the search for effective ways to suppress the competing signals.

4.4 Biomass pyrolysis and gasification, Raman spectroscopy studies

In the earlier biomass pyrolysis and gasification studies, the oven with four windows was employed, cf., Figure 3.6. The measurement setup is similar to the one employed for flame measurements, and its schematic is presented in Figure 4.11.

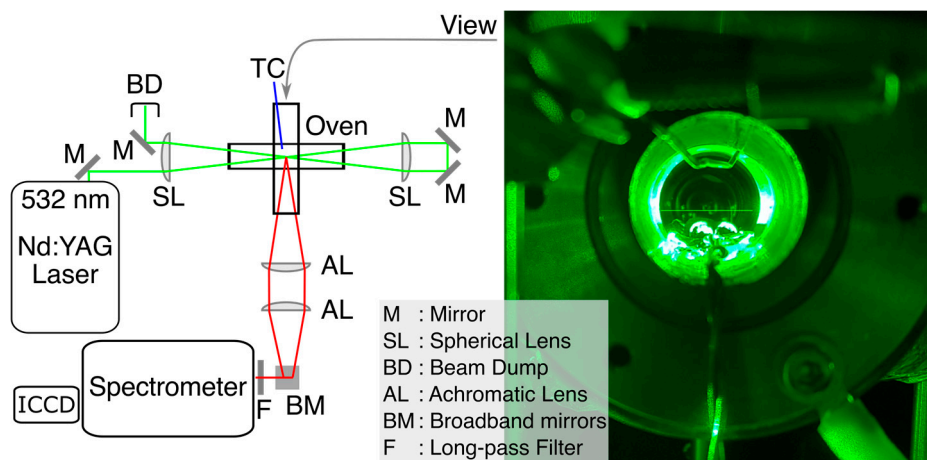


Figure 4.11. A schematic of biomass pyrolysis and gasification measurement setup. The green line is for the laser beam path, and the red lines indicate the signal collection path. The photograph at right is a view inside the oven from the thermocouple side.

The openings of the oven were closed with windows except at the one opposite the spectrometer, which was kept open for temperature measurements using a thermocouple and biomass pellet insertion. The ambient condition in the oven was controlled by purging with an argon and oxygen mixture with no oxygen for pure pyrolysis and a limited amount of oxygen for gasification. The signal was recorded continuously during oven heating until almost no gases were driven out from pellets anymore. It took about 25 minutes for each case, and the maximum temperature was between 650 and 750 K. The sampling rate of the spectra was about 1 Hz, where the

repetition rate of the laser was 2.5 kHz, and 2000 shots were accumulated on the detector.

Pyrolysis and gasification of various types of pellets were measured with Raman spectroscopy, and two pyrolysis results showing distinctive differences are selected for discussion here. Before looking at the Raman spectra, the total measured signal versus the oven temperature is presented in Figure 4.12. One thing to note here is that the temperature did not increase linearly with time, and heating duration is indicated at the top of the plot.

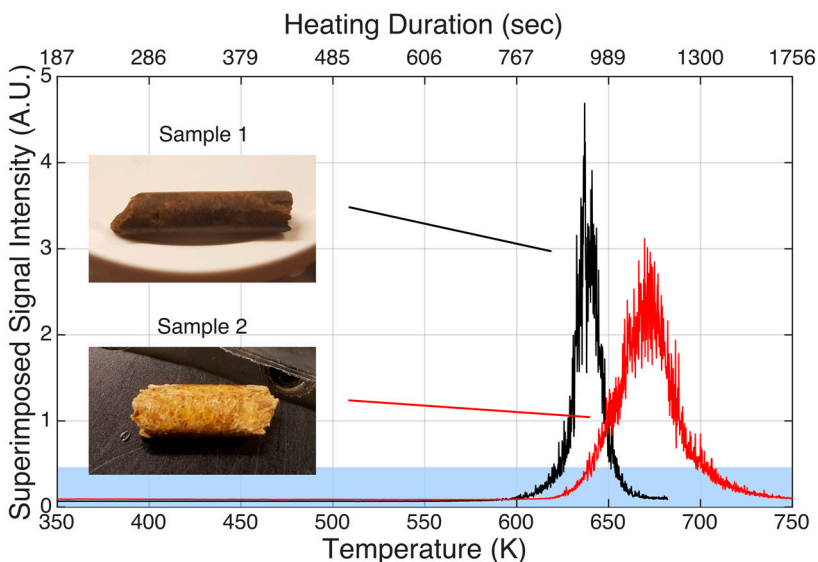


Figure 4.12. Overall superimposed signal intensity versus temperature of the biomass pyrolysis process. The processes of the two pellets are compared. Heating duration averaged from the two cases is written at the top.

The strong signal appearing around 650 K in the figure is dominated by laser-induced fluorescence (LIF) of volatile hydrocarbons. When the volatiles were released, a large amount of condensed smoke could be observed, cf., the right panel of Figure 3.6. The strong LIF signal serves as a good indication of hydrocarbon release from biomass pellets, but Raman scattering signals cannot be clearly distinguished due to their relatively weak intensity and appear as small peaks superimposed on the fluorescence background in the acquired spectra. Therefore, only the part of the total signals, shaded blue in Figure 4.12, could be attributed to Raman spectra and analyzed by estimating the LIF background with segmented polynomial fittings, as shown in Figure 4.13.

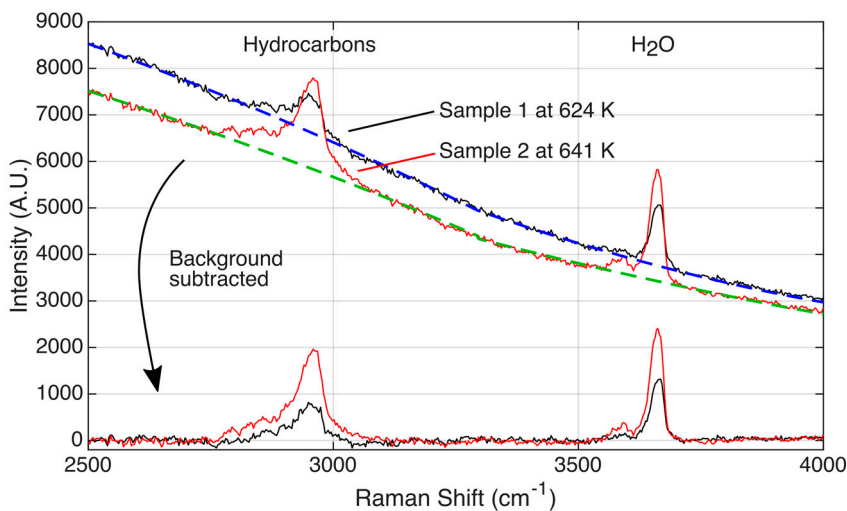


Figure 4.13. Sample Raman spectra at the early stage of volatile hydrocarbon release in pyrolysis processes of different samples. Background fluorescence signals are fitted to second-degree polynomial functions in two segments. Fifty spectra over time are averaged, equivalent to a 10 K increase, to reduce noise.

The spectra presented in Figure 4.13 were taken at temperatures when the LIF signal is about to increase significantly, cf., 624 K for sample 1 and 641 K for sample 2 in Figure 4.12. Fifty spectra were averaged for each curve during a 10 K temperature increase. At this point, the LIF strength was 2 to 9 times stronger than the Raman scattering peaks. The LIF background was fitted with second-degree polynomial functions segmented at 3293 cm^{-1} . Background subtraction by fitting results in artifacts of negative intensities at some Raman shifts, but the essentially flat zero-level background obtained offers a more intuitive and quantitative intensity comparison between peaks.

Raman scattering signals of hydrocarbons and water are detected at 2950 and 3660 cm^{-1} , respectively. In the hydrocarbon spectrum around 2950 cm^{-1} , a signal shape and intensity change with time was observed at higher temperatures. It might be attributed to the presence of different hydrocarbons since various hydrocarbon peaks are located around 3000 cm^{-1} . However, the background suppression based on fitting is inaccurate in resolving weak intensity peaks. Similarly, oxygenated hydrocarbon peaks were observed for measurements on a gasification process of sample 2, but a more sophisticated method to suppress the LIF background signal at high temperatures was required.

The release of water could be detected with Raman spectroscopy from the earlier stage when no volatile hydrocarbons emitting LIF signals were present, and it showed an interesting release profile in the process. As presented in Figure 4.14, the release of water from the biomass pellets happened in two steps. The first step

finished before releasing the fluorescent hydrocarbons, and then a larger amount of water was driven out together with hydrocarbon volatiles.

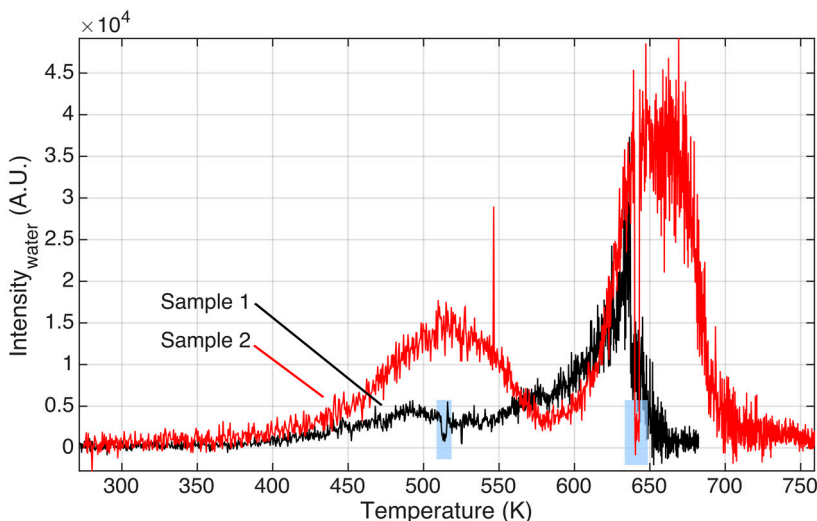


Figure 4.14. Signal intensity of water channel with heating biomass pellets. Fluorescence background is subtracted by fitting with second-degree polynomial functions. Signal drops indicated with blue shades are due to the manipulation of laser beam polarization, and proper background subtraction would show the signal dropping to 0.

The first water peak in the figure was interpreted as a drying process with the release of water absorbed by the pellets when stored at room condition, while the later release is interpreted as a result of progressive thermal decomposition. The substantial LIF interference could have influenced the water signal intensity in the second step, so a validation parameter was devised in the measurement.

The laser beam polarization was temporarily rotated during the measurement and resulted in a signal decrease at positions indicated with blue shades in Figure 4.14. Since vibrational Raman scattering signals are highly polarized, the weak signal intensity originally positioned on top of the strong LIF signal responded to the polarization change. Moreover, the signal in Figure 4.14, background-subtracted by fitting, dropping close to zero in the blue shades means a properly suppressed LIF contribution and that the profiles indeed show true H₂O Raman signals. This method, which came up during these measurements, was further developed and devised to improve Raman spectroscopy measurements under conditions with fluorescence background; this is introduced in Chapter 6.2, Development of Polarization Lock-in Filtering (PLF).

5 Signal Enhancement Techniques

5.1 High-repetition-rate laser and multiple data accumulation

A high-repetition-rate and high-power laser is employed for most of the measurements in this study. Specifications, including the repetition rate and power, are given in Chapter 3.1. This section will discuss the advantages of such lasers for Raman spectroscopy.

Raman scattering is a weak process, so high-fidelity diagnostics require a strong excitation source to achieve sensitive detection. Proper selection of laser equipment can improve the excitation part of the technique so that it can be used in more applications with enhanced detection sensitivity. In general, powerful lasers are required for Raman spectroscopy in the gas phase due to the low molecular number density and thus weaker Raman signal. The laser beam is often tightly focused on the center of the probe volume to achieve good spatial resolution and efficient signal collection to the spectrometer. Moreover, pulsed lasers are preferred for measurements with high temporal resolution and for combination with time-gated detection under conditions with high background luminosity.

However, there is a downside to employing a powerful laser with high pulse energy. The laser-induced breakdown is a phenomenon where the beam with high energy changes the medium drastically by ionization and induces strong white-light emission from a generated plasma. At ambient conditions in the laboratory air, where dust particles are present, the breakdown was observed occasionally from the laser pulse energy of 50 mJ focused in the probe volume corresponding to an intensity on the order of $5 \cdot 10^{11}$ W/cm² [27]. The white light from the breakdown is observed with the naked eye, and therefore, it saturates the sensitive detector, already optimized to collect weak Raman signals. Therefore, this phenomenon limited the maximum applicable pulse energy of the laser for measurements.

One method to avoid breakdown problems in Raman measurements is using a so-called pulse stretcher, a concept to redistribute the pulse energy temporally by stretching the pulse duration. The stretcher consists of beam splitters and multiple optical loops. Separate beams split from the main beam are sent to different loops, which result in different time delays for the pulses of the beams. The delayed beams are then recombined, resulting in a beam with temporally stretched pulses that is

guided toward the probe volume. With the beam stretcher concept, lasers with high pulse energy could be successfully employed for Raman spectroscopy by many researchers [28-30]. The stretchers reportedly expand ~10 ns pulse duration by a factor of 15 with a 10-fold decrease in peak intensity. However, installing the beam stretcher is a complicated and time-consuming task since it requires very delicate control of multiple optical components.

In this study, the laser-induced breakdown issue with high pulse energy was avoided by employing the high-repetition-rate laser. The maximum operating average power of the laser is 100 W, but the power is distributed between two to ten thousand pulses per second, which results in pulse energies less than 50 mJ. Therefore, the risk of optical breakdown at the center of the probe volume could be significantly lowered even though the laser beam was focused.

Another advantage of employing the high-repetition-rate laser is efficient data accumulation. Even though the energy is distributed over multiple pulses, so the single-pulse energy is rather low, signals from multiple pulses can be accumulated on the chip, in principle, until the detector's dynamic range is optimally utilized. Since the signals from many pulses are added up, this approach is a trade-off between signal strength and temporal resolution, but a critical shortcoming of Raman spectroscopy is substantially improved using this function. The combination is very useful when studying steady-state phenomena, and therefore, an on-chip accumulation function was utilized in all measurements in this study to a different extent. The typical accumulation setting for flame measurements with 20 W laser power and 10 kHz repetition rate was 500 to 5000 accumulations to optimize the 16-bit dynamic range, depending on the concentration of target molecules. Accumulating signals of 5000 laser pulses for one spectrum is equivalent to a recording time of 500 ms. Thus, this type of acquisition also allows following slowly varying processes in time, e.g., biomass pyrolysis and gasification.

5.2 Multi-pass cavity

A concept of reusing the beam many times in a cavity, a so-called multi-pass cavity, was employed for the measurements in the studies of Paper 2 and 5. The cavity concept to enhance the intensity of Raman scattering was reported firstly by Hill and Hartley in 1974 [31]. Ever since that study was conducted, there have been further studies on signal enhancement in Raman spectroscopy by devising various kinds of multi-pass cavities [9, 32-34]. However, the detailed settings and practical considerations of the multi-pass cavity for these studies had to be validated and learned through tests, and therefore, the concept was investigated during the series of measurements.

The multi-pass cavity consists of two concave mirrors with a focal length and a diameter of 10 cm. The surface coating for high reflectivity at the laser wavelength of 532 nm gives 95.4% reflectance. The two mirrors face each other and are placed approximately 40 cm apart to form a near-concentric configuration, for which the mirror arrangement is presented in Figure 5.1 with one mirror drawn in the horizontal plane for illustration of the beam spot pattern on the surface. The near-concentric configuration can provide a good spatial resolution in measurements due to the small probe volume at the center, where the incident beam passes through a focusing lens prior to entering the cavity. The repeated passes of the laser beam through the cavity in both directions also remain focused in the region at the center.

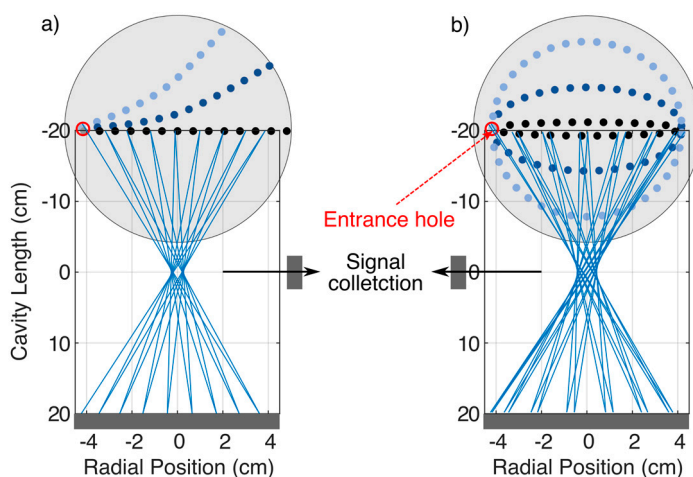


Figure 5.1. Two modes of concentric cavity configuration. Multi-pass beamlines and reflection patterns on the mirror are overlaid for (a) two-point and (b) envelope mode. The pattern with different colors on the mirrors is achieved for different entrance beam angles.

By adjusting the cavity length, two modes of the multi-pass cavity could be obtained for the near-concentric cavity. A two-point mode is obtained by reducing the cavity length by a few millimeters from the concentric configuration. When the mode is properly aligned, a reflection pattern of multiple passes on the mirrors is aligned consecutively, straight from an edge of the mirror to the opposite end, and two focused intersection points are observed at the center of the cavity, as presented in Figure 5.1a. The two points lie in parallel to the mirror surfaces, on the optical axis of the signal collection lenses, and are spaced 3 mm apart. The number of passes can be controlled by adjusting the direction of the incident beam, and the maximum gain is limited by the number of reflections that fit on the mirror surface, which in turn is determined by the gap between the beam entrance and the first reflection point on the same mirror.

Another mode, the so-called envelope mode of the cavity, is obtained with a shorter cavity length than for the two-point mode. When the cavity length is shortened from the two-point mode, the intersection points of the beams move away from the optical axis of the cavity in opposite directions, and the space between the points is filled with displaced beam paths. Gradually, the common intersections cease to exist, and the beams are distributed equidistantly, forming an envelope at the cavity center (see Figure 5.1b). The shape of the envelope depends on the angle of the incident beam to the cavity, and it can be altered from a circle to an ellipse approaching a plane. The reflection pattern behaves differently from that of the two-point mode. Instead of traveling from one end of the mirror to the other, the beam can be reflected nearly uncountable times, continuously filling the gap between the reflection spots from the previous passages around the mirror perimeter. Due to this characteristic, an entrance hole on one of the cavity mirrors is a requirement to form this mode. In practice, the beam reflects as many times as it can until it falls on and escapes through the entrance hole.

The measurements in Paper 2 and 5 required an efficient signal collection scheme, and envelope mode and two-point mode were employed, respectively. The signal was enhanced by a factor of 32 and 45, respectively. Later, it was found that the two-point mode has some advantages over the envelope mode. Tightly focused intersections at the center of the cavity enable measurements with good spatial resolution, crucial for measurements where there are concentration gradients, e.g., in premixed flames. This scheme also ensures efficient signal collection. For example, when one of the intersection points is in focus by the signal-collection optics, all the beams passing the point are in focus. Another benefit of employing this mode is the easy handling of the exit beam experimentally. Since the beam exits the cavity on the opposite side to the entrance, it can simply be guided toward a beam dump.

The envelope mode is beneficial to measure across a larger area with the spread beam passes. The envelope can be flattened to a plane aligned horizontally or vertically for measurements at various positions. When the plane is horizontally oriented, the amplification of the signal can be as efficient as the two-point mode. However, careful handling of the exit beam is required for the envelope mode. As presented in Figure 5.2a, when the envelope of the passes is arranged in a circle shape, the beam escapes the cavity at an angle equal in magnitude to the incident but on the opposite side of the surface normal. In such a configuration, the exit beam can be readily blocked.

On the other hand, when the beam passes are flattened by sending the incident beam horizontally into the cavity (see Figure 5.2b), the exit beam is directed back to the laser head, overlapped with the incident beam. The more beam passes arranged for enhanced signal generation, the closer the exiting beam is sent back toward the excitation source, potentially damaging the laser. It can happen anytime during the

optimization of the multi-pass alignment, and the consequence could be critical. A Faraday isolator can be a means to avoid such events.

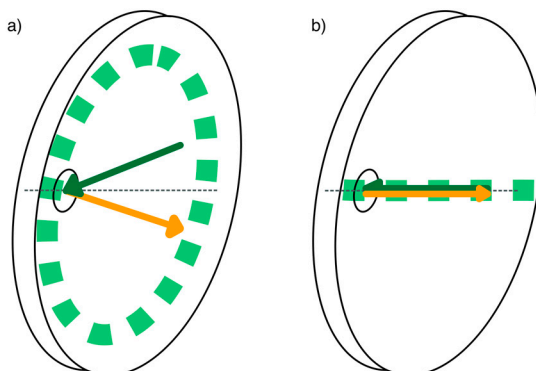


Figure 5.2. Drawings of entrance and exit beam directions for (a) ring envelope mode and (b) flat envelope mode of multi-pass alignment. The flat envelope mode is desired for measurements with good spatial resolution, but the exit beam can direct back to the excitation source, potentially damaging the laser.

A photo of the Raman spectroscopy setup with multi-pass alignment is shown in Figure 5.3, and three spherical mirrors in the setup related to signal enhancement are marked. One of them, marked with a red circle, has an 80 mm diameter and is aluminum-coated for broadband wavelength range reflection and is located on the opposite side of the detector. Raman scattering signals propagate in both directions, and the mirror on the opposite side sends a portion of the signals back to the detector side, increasing signal strength by a factor of 2. The other two mirrors, marked with blue circles, form the multi-pass cavity, facing each other with the measurement volume at the center.

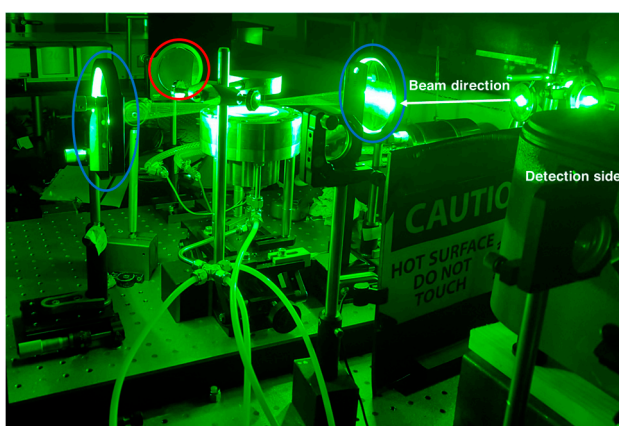


Figure 5.3. Photo of a Raman spectroscopy setup with multi-pass arrangement. A mirror on the opposite side of the detector is marked with a red circle, and multi-pass cavity mirrors are marked with blue circles.

The multi-pass cavity is an efficient way of enhancing the Raman scattering signal, but there are a few points to be taken care of to optimize the benefit of the cavity and not enhance interference signals. Proper handling of stray light and multiple scattering is one of them. Since the cavity mirrors are installed near the measurement volume, the chance of signal contamination by stray light from the extra optics could increase. Therefore, proper filtering of light at the laser wavelength is necessary.

Another source of interference is a continuous background signal, such as flame luminosity. The time for the beam to travel between the cavity mirrors needs to be considered when setting the gate width of the detector. The laser beam travels the cavity length of 40 cm in approximately 1.3 ns, and therefore, the gate width is broadened by tens of nanoseconds, proportional to the number of the passes, which enhances contributions of continuous background signals by the same factor. For example, a 20 ns gate width was used for single-pass measurements with a margin, but it was widened to 150 ns for multi-pass alignment with ~ 50 passes. The continuous background was not an issue in the presented measurements, but employing the technique to luminous samples requires attention.

Beam steering effects can add complexity to measurements and data analysis when a large temperature gradient exist in the measurement volume. For example, vertical displacements of some spots at the center of the reflection pattern were observed on the mirrors while measuring at positions near the flame-front in a premixed flame. Therefore, the gain of the cavity is not conserved between different positions. In other words, direct comparison of the absolute signal strengths between different heights could be inaccurate under such conditions. However, it was not an issue for the data analyses of the presented works since relative quantities and the spectral shape of the signals at each position were studied.

Nevertheless, the multi-pass cavity provides a substantial benefit that outstrips the costs and drawbacks. The improved detection limit of the Raman spectroscopy to tens of parts per million (ppm) for gas-phase diagnostics is an example. Minor species in various flames could be studied, and the quantification of formaldehyde in a DME/air flame is presented in Paper 5.

The measurements currently continue to detect nitrogen oxides (NO_x) in ammonia/air flames using the signal enhancement technique. For example, signal enhancement by multi-pass arrangement have enabled nitric oxide (NO) detection and quantification in a laminar premixed ammonia/air flame. The detection limit of NO was estimated to 1500 ppm in the flame product zone.

6 Background Suppression Techniques

The previous chapter was about increasing the signal intensity of the Raman scattering using specific kinds of lasers and signal-enhancing schemes. This chapter is about how to increase the detection sensitivity by removing background and interference signals. Specifically, spatial and temporal filtering techniques were devised and tested.

6.1 Periodic Shadowing (PS) with a grating and fiber optics

Periodic Shadowing (PS) is a spatial filtering technique to remove stray light and multiple-scattered signals in spectroscopy. It resembles structured illumination, which has been actively employed in microscopy to suppress stray light and improve image contrast [35]. The structured illumination was employed in spray imaging with the SLIPI technique by Kristensson et al. and Berrocal et al. [36-38], and its performance to reject multiple scattering and stray light was outstanding.

The application of structured illumination was expanded to flame studies, and the PS technique was developed by Kristensson et al. for the spectroscopic techniques [39]. Both structured illumination and PS are based on lock-in amplification, but PS spatially modulates the signal, while structured illumination spatially modulates the incident laser sheet.

PS was demonstrated for various optical diagnostic techniques by Kristensson et al. [39], and their investigation also included Raman spectroscopy. In particular, the analysis of the filtering performance focused on cleaning elastic scattering and stray light to improve the signals of pure rotational Raman scattering located near the laser wavelength. The purpose of the measurement was to validate the PS technique, so they demonstrated it by measuring spectra of ambient air.

Follow-up studies to investigate the filtering performance for practical applications were conducted. With the PS combined Raman spectroscopy, one-dimensional laminar flames, biomass pyrolysis and gasification processes, and ambient air were

measured. In the studies, both rotational and vibrational Raman signals were investigated in detail, and the improved spectra are presented in Paper 2, 3, and 4.

For the PS technique in its original configuration, a Ronchi grating needs to be located at a focal plane of the collected signals. Therefore, the grating was attached to the entrance slit of the spectrometer, where the Raman probe volume was imaged. The stripe pattern on the grating blocks a portion of signals and imprints a modulation pattern on the recorded image, as presented in Figure 6.1a.

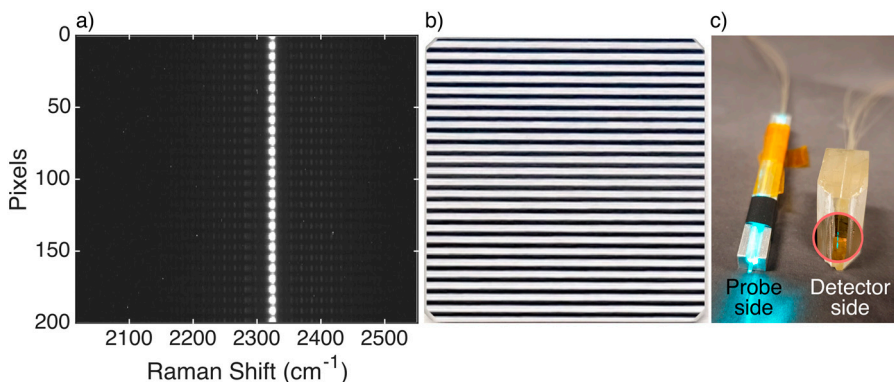


Figure 6.1. (a) Spatially resolved nitrogen Raman spectrum with a grating-based periodic shadowing (PS). (b) Ronchi grating for the grating-based PS. (c) Optical fiber bundle for the fiber-based PS.

The line pair frequency on the grating determines the modulation frequency, and it can be chosen depending on the detector pixel resolution and the spatial scale and desired resolution of the investigated phenomenon. It was reported that the loss of spatial resolution is inversely proportional to the spatial frequency of the Ronchi grating [39]. On the other hand, a series of tests with PS combined Raman spectroscopy in this study showed no strong relation between the line frequencies and binned signal intensity after the filtering. Therefore, a Ronchi grating with a 5 lines/mm spatial frequency was chosen for all the measurements presented in the studies.

The technique has also been further developed by employing an optical fiber bundle instead of grating to broaden the applicability of the PS Raman spectroscopy. A customized array of optical fibers was devised to implement the PS technique. Paper 2 contains the validation of the fiber-based PS technique and its practical applications.

A bundle of fiber optics customized for the PS application was manufactured by Leibniz IPHT and cladded by Heraeus Comvance company (see Figure 6.1c). The bundle consists of 19 identical multimode fibers. One end of the bundle for collecting the signals is shaped circularly, with an outer ring of 12 fibers and an inner ring of 6 fibers with 1 at the center. Each fiber has a numerical aperture of

0.22, and the fiber core diameter is 114 μm . Altogether, the proving tip has a diameter of ~ 1.61 mm, including the coating. The other end of the bundle directed toward the spectrometer is arranged straight, relaying the signals to the entrance slit. There are gaps between each fiber on the detector side, so the signal is naturally modulated spatially.

Unlike the grating, which blocks a part of the signals and reduces the overall signal intensity on the detector chip, the fiber-based PS technique fully utilizes the signal intensity collected on the probing end. Therefore, it could be more beneficial to employ the fiber-based approach when sensitive detection is required. On the other hand, the optical fibers can be a limitation for some measurements where spatial resolution is required. Since the signal collected on a circular end is rearranged to a linear array on the other end, the signal is not spatially resolved on the detector. Nevertheless, employing optical fibers gives large freedom of aligning and locating the detector so that the fiber-based PS technique could broaden the applicability of the Raman spectroscopy for more complicated systems with limited optical access.

The same data acquisition and processing scheme is used for both methods, using the Ronchi grating and the fiber bundle. Signal recording in two-dimension is required to resolve the modulation, so slower recording speed and a chance of noise accumulation are potential downsides of the method. However, the improvement of spectra through filtering is significant. For example, the detector image in Figure 6.1a shows a vertical, spatially modulated line corresponding to an N_2 Raman signal imaged on the slit. In addition, a background level intensity between the spots of the vertically aligned signal pattern is observable, and it is brighter than the actual background level at the left or right end of the image. It implies that unwanted signals reach the sensor through unintended light paths or multiple reflections spatially broaden the signal inside the spectrometer. These false signals would be filtered out through a series of steps in the following filtering process.

The series of plots in Figure 6.2 from Paper 2 visualizes the data processing steps for the filtering technique very nicely, and its mathematical expressions are explained in the work by Kristensson et al. [39]. If we follow the steps in the figure, the two-dimensional spectral data with the modulated signal is Fourier-transformed along the modulation direction (Figure 6.2i and a). The modulation frequency could be obtained from the transformed data (Figure 6.2a), and a band-pass filter is applied to select the component with the modulation frequency (Figure 6.2c and d). The selected component is then restored to a filtered spectrum through the inverse Fourier transform.

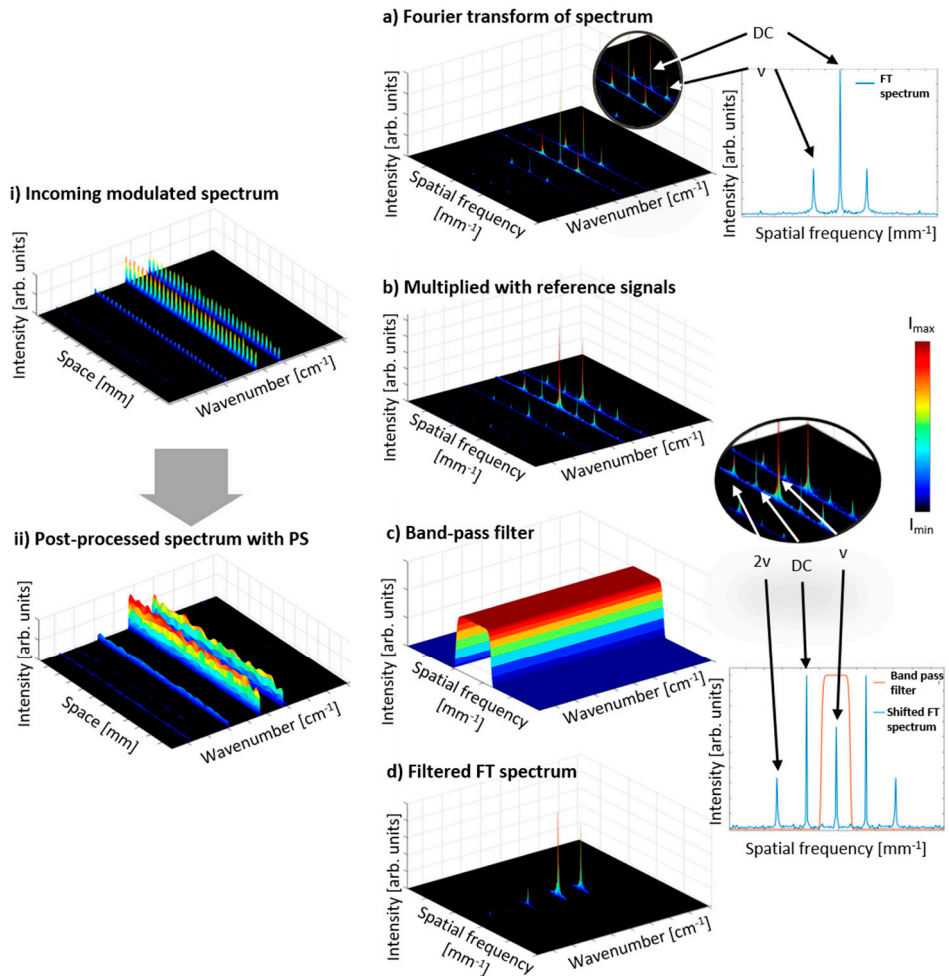


Figure 6.2. The procedure of Periodic Shadowing post-process with sample spectral data [40].

In the post-process, the proper band-pass filter size is important to optimize the filtering quality. The effect of the filter size is presented in Figure 6.3. An M6 bolt in the lab has been imaged with the PS setup, and the spectrometer set for imaging with the grating positioned in the zeroth-order. Six filter widths were tested, and the top left panel has the narrowest filter while the bottom right is for the widest. It is clear that finer details of the bolt thread appear with broader filters, but using a too broad filter preserves the modulation pattern resulting in image artifacts. The optimum size of the filter can be selected in a calibration measurement, and the same size could be used for the rest of the experiment unless the modulation frequency alters.

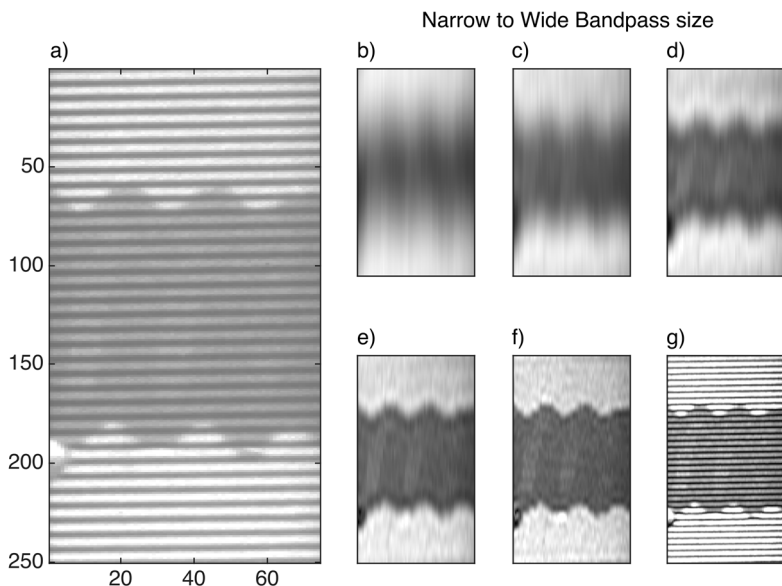


Figure 6.3. The effect of bandpass filter size on the filtering quality. (a) A part of an M6 bolt is imaged with periodic shadowing, and the size of the band-pass filter varied from (b) the narrowest to (g) the widest in the post-process. The image is taken at the zeroth-order diffraction setting of the spectrometer.

The PS technique significantly improves both rotational and vibrational Raman spectra by suppressing the background signals of stray light and multiple scattering. A broadening effect of the Raman signals was also significantly reduced in the results. The effect was quantized by fitting the spectra to modeled spectra using the PGOPHER software [7], and the Lorentzian broadening factor in the model was reduced to near zero after the filtering. Paper 2 contains the validation of the fiber-based PS technique and its practical applications.

6.2 Development of Polarization Lock-in Filtering (PLF)

While the PS technique effectively filters out stray light reaching the detector through unintended paths, other types of laser-induced signals originating from the probe volume of the Raman signal cannot be removed with the technique. Laser-induced fluorescence (LIF) and incandescence (LII) are examples of competing signals that impose difficulty on resolving Raman scattering signals and quantification. For example, during this study, the LII signal deters Raman spectroscopy to be employed for sooting flame measurements, and the LIF signal

from the gasification process of a biomass pellet was an obstacle to employing Raman spectroscopy.

A photograph of the sooting ethylene(C_2H_4)/air flame is presented in Figure 2.5. The flame is luminous due to the existence of soot particles, and the soot particles emit strong LII signals when heated by the laser beam. In Figure 6.4a, the Raman and LII signal intensities are compared. The small peak observed at 2331 cm^{-1} is the vibrational Raman signal of nitrogen, normally one of the strongest Raman peaks in premixed flames. However, the LII background is ~ 20 times stronger than the peak. Therefore, it is challenging to distinguish and quantify Raman scattering peaks with the LII background.

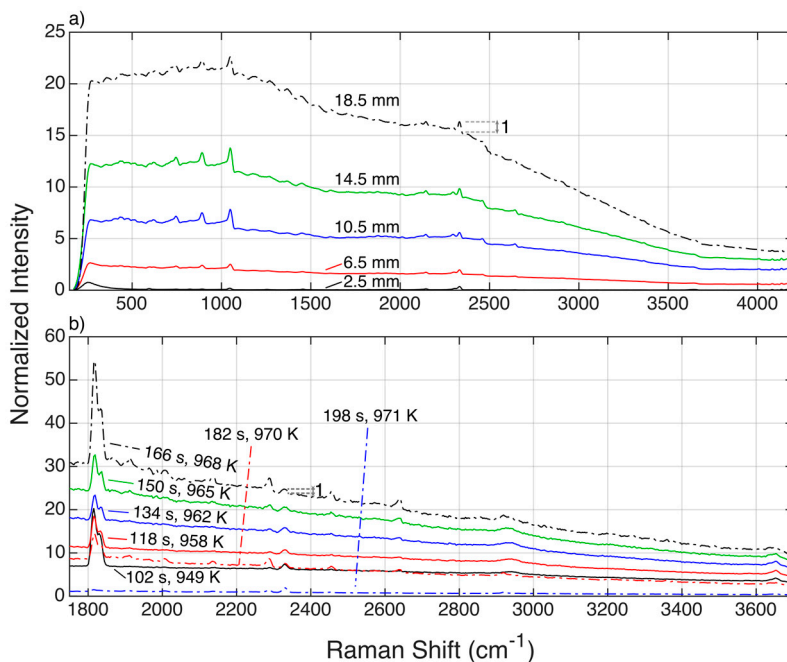


Figure 6.4. Raman spectra with competing signals. Intensities are normalized to the maximum nitrogen Raman signal intensity. (a) is from a sooting flame accompanying laser-induced incandescence. (b) is from released gas of biomass gasification accompanying laser-induced fluorescence.

LIF signal interference to experimental spectra is also problematic, as presented in Figure 4.13 and Figure 6.4b for biomass pyrolysis and gasification processes, respectively, when a large number of volatile hydrocarbons are released at high temperatures. In the spectra of Figure 6.4b, Raman peaks are located at 2331 , 2922 , and 3653 cm^{-1} , from nitrogen, hydrocarbons, and water, respectively. The LIF signal is much stronger than the nitrogen Raman peak by a factor of ~ 30 . Fitting the broadband background and subtracting it from spectra was tried as presented in Chapter 4.4, but it leaves a concern about the accuracy of fitting the background.

Therefore, a filtering technique was developed to reject these competing signals and named Polarization Lock-in Filtering (PLF).

The PLF technique is based on the lock-in amplification used in the PS technique. While the PS technique requires spatial modulation of signals on the detector, the PLF technique utilizes the laser beam's polarization and temporal modulation. Vibrational Raman signals are highly polarized, so the signal intensity depends on the excitation beam's polarization orientation. The beam polarization is altered repeatedly between p- and s-polarization while continuously recording the spectra. As a result, vibrational Raman signals are modulated while other signals, e.g., LIF and LII, are not affected. The 2-dimensional spectral images obtained from measured data are filtered according to the same process as the PS technique, cf., Figure 6.2, and only vibrational Raman signals remain in the result.

The PLF technique requires the alternation of polarization, and a half waveplate, a Pockels cell, or a photoelastic modulator (PEM) can be employed for the purpose. The component for polarization modulation can be chosen for the desired range of frequency modulation. For example, rotation mounts provide a maximum modulation frequency of about 2 Hz, while PEMs have a much faster operation in the order of 10 kHz. In this study, a half waveplate attached to a rotation mount was placed in the beam path. A schematic of the setup is presented in Figure 6.5.

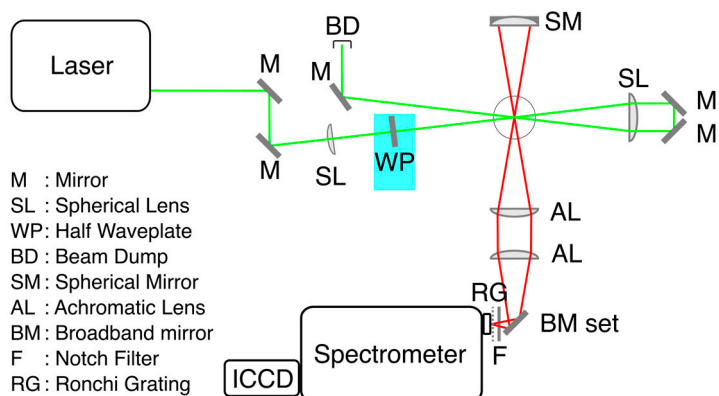


Figure 6.5. A schematic of Raman spectroscopy setup with the polarization lock-in filtering technique. The half waveplate (blue-shaded) is an addition to the conventional setup.

One thing to note here is that it is beneficial to install the waveplate close to the probe volume since some optical components have different performances, e.g., reflectance and transmittance, for different polarizations of the beam.

The signals from the probe volume are recorded while the beam polarization is continuously alternating. The spectra over time can be presented in 2-dimension, and Figure 6.6 is the sample spectral image of a sooting ethylene/air flame.

Vibrational Raman signals are modulated over time due to the polarization change, but the other signals are recorded as solid lines since they are not polarized. The figure resembles the spectral image of the PS technique presented in Figure 6.1a, but the PLF utilizes temporal modulation while PS requires spatial modulation; therefore, the y-axes of Figure 6.1 and Figure 6.6 are different. The next filtering step follows the same routine as the spatial filtering technique (cf., Figure 6.2).

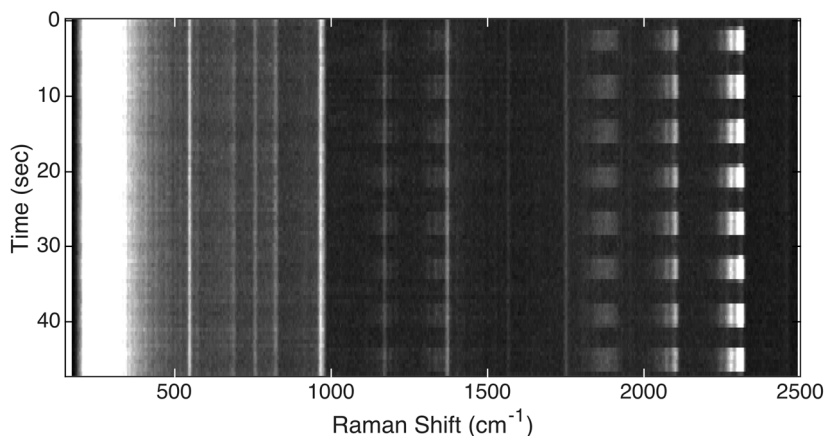


Figure 6.6. Raman spectral image with temporally modulated vibrational Raman signals for the PLF technique.

The laser beam intensity at the probe volume can vary depending on the location of the waveplate in the setup and laser specification. Therefore, the effect needs to be considered before the Fourier transform step. For example, the laser beam energy at two polarizations was measured, and the difference was within 10%. Depolarized signals serve as a good reference for the calibration, e.g., rotational Raman signals. Since Raman signal intensity is linearly proportional to the incident laser energy, cf., Equation 2.2, the variation of the depolarized signals can be compared to the beam energy variation under different polarizations.

Installing a component to modulate polarization is straightforward. However, determining the modulation frequency related to the laser repetition and data recording requires some considerations similar to selecting an appropriate grating for the periodic shadowing concept. Therefore, the effect of some setting parameters on the filtering quality was studied and reported in Paper 3.

The controlled parameters were the period of modulation, the number of data accumulations, and the total recording time. The period of modulation was altered between 3 and 9 seconds. The number of accumulations setting was between 1000 and 4000 shots, where the larger number of accumulations gains the signal intensity while losing temporal resolution. The recording duration was varied between 45 and 53 seconds, and the purpose of investigating this parameter was to understand how

the modulation phase matching of the first and the last signal affects the data reconstruction, i.e., matching the phase of the first and the last row in Figure 6.6.

The repetition rate of the laser should be considered when setting the parameters. For example, the laser repetition rate was 5 kHz in the study presented in Paper 3. Therefore, a data sampling rate of 2 frames per second (fps) was expected for the 2500 accumulations setting. However, an extra addition of data readout processing time on the detector resulted in the sampling rate of 1.58 fps instead. In such a case, too fast polarization modulation cannot be fully resolved with the sampling rate.

In addition, there is a limitation to increasing the sampling rate as well. If the signal is accumulated for 1000 pulses, the sampling rate raises to 3.02 fps. However, the signal intensity of the Raman scattering would decrease in consequence. Therefore, the setting of the different parameters needs to be done by considering various aspects, and it often requires a user to make a trade-off.

The parameter study in Paper 3 was done by investigating vibrational Raman scattering signals in the presence of acetone fluorescence. Acetone was vaporized in a container by flowing air through the liquid, and the acetone-seeded air was supplied to a McKenna burner without a flame, as presented in Figure 6.7. Raman and fluorescence signals generated by laser beams of 266 and 532 nm were measured close to the burner surface, and the fluorescence strength could be controlled either by varying the flow rate of the air or changing the intensity of the 266 nm beam. During the series of measurements, the flow rate was fixed.

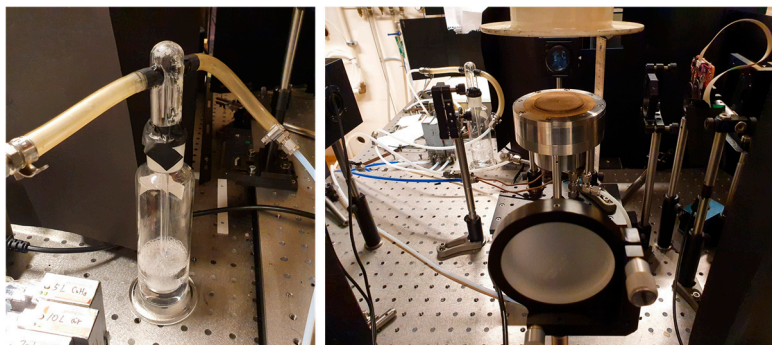


Figure 6.7. Acetone-seeded airflow to a Raman spectroscopy setup for a parameter study.

The parameter study result shows that the filtering performance is not much affected by the variation of the tested parameters. On the other hand, the background level of the raw data is strongly related to the noise level in the filtered result. In addition, the test was done only at the steady-state condition, so the faster modulation would increase the temporal resolution in unsteady measurements, corresponding to the previous study that spatial resolution after PS increases for higher grating frequency [39].

7 Results with Improved Raman Spectroscopy

7.1 Multi-pass Raman spectroscopy

The principle of the multi-pass concept was discussed in Chapter 5.2. Combining the multi-pass concept with Raman spectroscopy, formaldehyde, an intermediate species in a premixed DME/air flame (see Figure 2.5), was detected, as presented in Paper 5. It represents an improvement compared with the results presented in Chapter 4.2.

The multi-pass cavity presented in Paper 5 increased the Raman signal strength by a factor of 45, and therefore, signal amplification at the formaldehyde Raman channel at 2781 cm^{-1} was possible. On-chip accumulation of 50 shots gave 1.67 frames per second sampling rate, which was short enough to mitigate the averaging effect from the long-term fluctuation of the flame. The multi-pass alignment is shown in Figure 7.1.

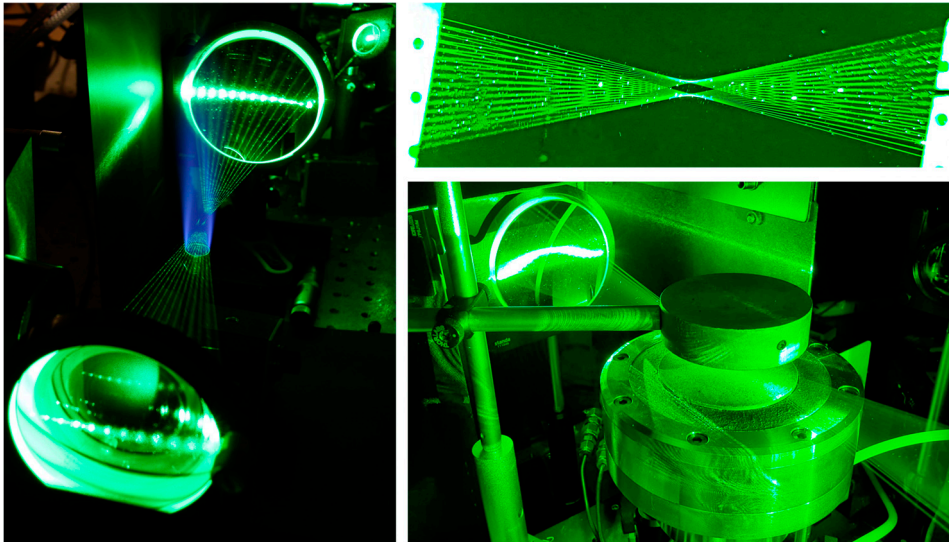


Figure 7.1. A photograph of the multi-pass concept employed for flame investigation using Raman spectroscopy.

The burner height was scanned to measure the entire flame preheat region where formaldehyde is present. It was from the flame-front height to 2.24 mm above, equivalent to heights between 5 and 7.24 mm above the burner (HAB). Beam steering was observed at the height just below the flame-front due to the large temperature gradient. The multi-pass alignment was affected by this, and a curved line pattern was observed on the cavity mirrors, see Figure 7.1. Therefore, absolute signal strength between different heights could not be compared. However, the steering effect did not affect the evaluation of relative mole fractions of the detected species, and the result is plotted in Figure 7.2 together with simulation results using Zhao and Aramco kinetic reaction mechanisms [41-48]. The formaldehyde detection limit with the setup was computed to be 40 ppm. More results, including thermometry and further discussions, are presented in Paper 5.

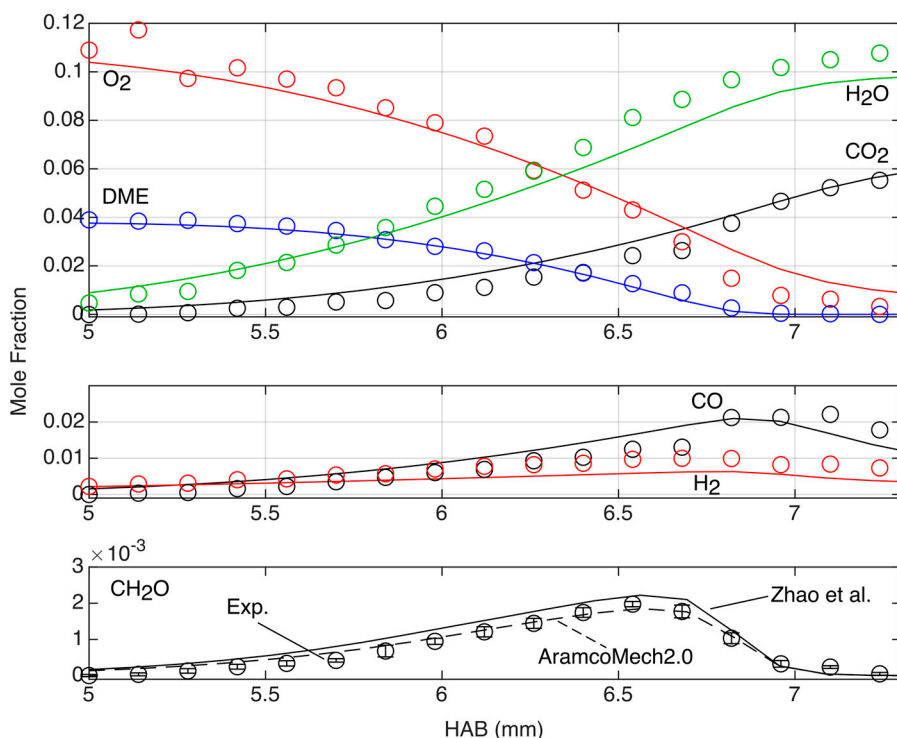


Figure 7.2. Mole fractions of major species and formaldehyde with height in a laminar fuel-lean DME/air flame. The nitrogen profile is excluded. Mole fractions converted from Raman spectra (markers) are plotted with simulation results (lines) using the kinetic reaction mechanism by Zhao et al. [41]. In the bottom panel, formaldehyde mole fractions from Raman spectra (markers) and simulation results (lines) using kinetic reaction mechanisms by Zhao et al. and AramcoMech 2.0 are plotted [41-48]. The maximum mole fraction of formaldehyde from the experiments is ~2000 ppm.

7.2 Grating-based PS combined Raman spectroscopy

For studies of vibrational Raman signals in flames, the introduction of the PS technique helped minimize stray light as well as the effect of cross-talk between adjacent peaks. For example, cross-talk of vibrational nitrogen Raman signal on carbon monoxide signal has been an issue at flame temperatures. Populated rotational levels at higher temperature give O-branch lines of the nitrogen signal that overlap with the carbon monoxide signal, and such a broadening of the nitrogen signal imposes an additional negative effect on the quantification of carbon monoxide.

Figure 7.3a shows the cross-talk of nitrogen O-branch peaks ($1940\text{--}2331\text{ cm}^{-1}$) on carbon monoxide peaks (2145 cm^{-1}) for a spectrum measured in a hydrogen-enriched methane and air flame, where the PS technique suppresses the background level. This is important for quantification of signals with weak intensities, and for example, the maximum amount of carbon monoxide in a stoichiometric methane/air flame was calculated 14% higher after the filtering than the value before the filtering: from 0.77% to 0.87%.

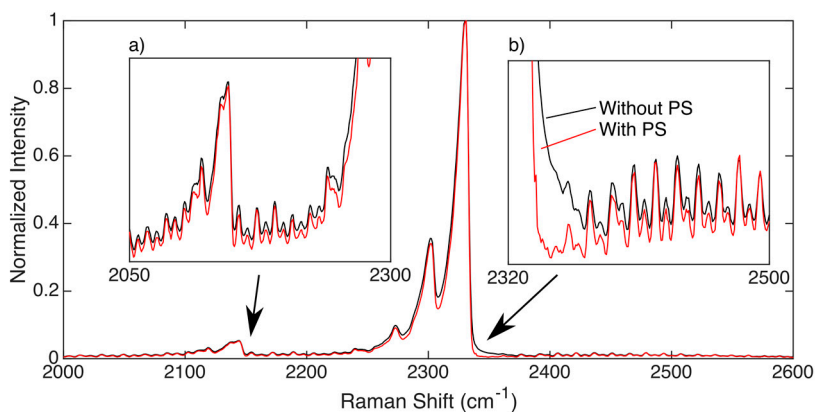


Figure 7.3. An improved Raman spectrum of fuel-rich methane/air flame with periodic shadowing (PS) method. The ratio of nitrogen peaks at 2331 and 2300 cm^{-1} changes after applying PS. (a) Nitrogen-carbon monoxide cross-talk can be handled better by reducing signal broadening. (b) Some S-branch peaks are revealed with the PS method, and reduced broadening of the Q-branch gives more accurate intensities of the S-branch peaks.

The filtering technique also affects the result of Raman-based thermometry, which utilizes vibrational Raman signals. The narrowing of the strong nitrogen peaks altered the ratio between its fundamental peak and hot bands, as presented in Figure 7.3. Therefore, the temperature values changed about 20 K after applying the filtering technique. In addition, the fitting process became more straightforward since only the Gaussian broadening had to be considered.

A few more S-branch peaks of the vibrational nitrogen Raman signals are detected with the reduced broadening effect of the Q-branch signal in Figure 7.3b. Therefore,

the accuracy of the thermometry can be improved by fitting the Q-branch hot bands and S-branch lines simultaneously.

7.3 Fiber-based PS combined Raman spectroscopy

In Paper 2, improved Raman signals of a methane/air flame with the fiber-based PS enabled Raman-based thermometry not only with vibrational Raman signals but also with pure rotational Raman signals. At room temperature, pure rotational Raman signals appear close to the laser wavelength, i.e., within 200 cm^{-1} , and those are often contaminated by elastic scattering signals. However, clear identification of the pure rotational signals and their intensities could be carried out by suppressing the elastic scattering with the filtering presented in Figure 7.4 from Paper 2. Therefore, the spectra could be fitted to theoretical spectra, and temperatures were obtained.

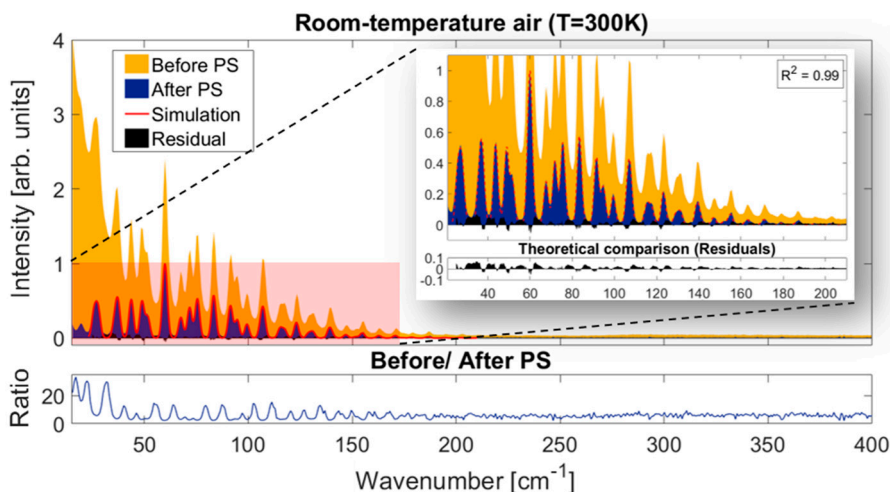


Figure 7.4. Improved pure rotation Raman signals close to laser wavelength by fiber-based PS method [40]. The signals are from ambient air, and therefore, pure rotational Raman peaks of nitrogen and oxygen are superimposed.

In the figure, the strong signal at 20 cm^{-1} is effectively cleared with the fiber-based PS method, and interference-free pure rotational Raman signals of nitrogen and oxygen are obtained also at shorter Raman shifts. The strong intensity is speculated to be broadened elastic scattering signal due to multiple scattering and stray light. The PS method successfully filtered out the undesired signals, and it mitigates a shortcoming of Raman spectroscopy as an incoherent optical technique, which is vulnerable to competing signals and background levels.

The effect of broadened elastic scattering on Raman signals is significant at high-temperature gas measurements, e.g., in flames. Rotational transitions between

populated levels of larger quantum numbers are induced due to the high-temperature environment, and therefore, the broader distribution of pure rotational Raman peaks is observed in spectra, e.g., in flames, so the PS method was tested on a flame.

A premixed methane/air flame on a McKenna burner was investigated. The measurement height varied from reactants to products, accompanying temperature increase. Spectra from 3 heights were chosen for discussion and are presented in Figure 7.5 from Paper 2. The lowest height at 3 mm is close to the burner surface, so reactants at room temperature were detected. Pure rotational lines are detected up to 400 cm^{-1} at higher temperatures, and the signal contamination worsens with the temperature increase.

Nevertheless, the PS method cleared the interference and provided spectra composed of only pure rotational lines. At 12 mm height, pure rotational Raman signals of carbon dioxide in the product zone are observed after the filtering. Each CO_2 line could not be resolved due to the lack of spectral resolution, but the comparison with the simulated spectrum shows good agreement.

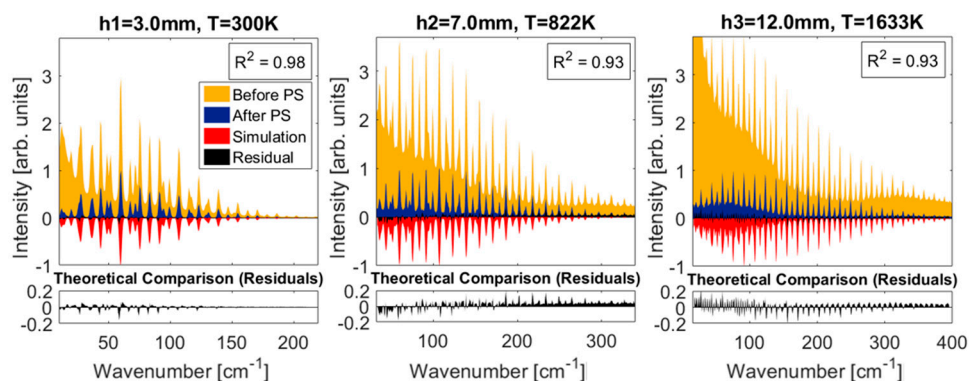


Figure 7.5. Improved pure rotation Raman signals close to laser wavelength in a methane/air flame by fiber-based PS method [40]. Three panels have different x-axis scales, and the peaks spread broader at higher temperatures. Spectra after PS are normalized to their maximum intensity of each case, and temperatures are obtained by fitting the experimental spectra to simulated spectra.

7.4 PS and PLF combined Raman spectroscopy

The PLF technique has been demonstrated for measurements under challenging conditions with Raman spectroscopy: a sooting flame with LII signals (Paper 3) and a biomass gasification process with LIF signals (Paper 4). In the first case, a premixed ethylene/air flame at an equivalence ratio of 2.0 was set on a porous-plug McKenna burner, see Figure 2.5. The measurement positions were scanned from the burner surface to the flame stabilizer 21 mm above the burner (HAB).

This study was designed to test and validate the PLF technique by investigating a steady-state flame. The raw and filtered spectra from the measurements are presented in Figure 7.6 from Paper 3. Most of all, it is promising that the LII signal with an intensity of over 20000 photon count, exceeding Raman scattering intensity by a factor of 25, was successfully suppressed, and the quantitative analyses of the Raman spectra were possible. The detailed mole fraction analyses and thermometry results are presented in Paper 3.

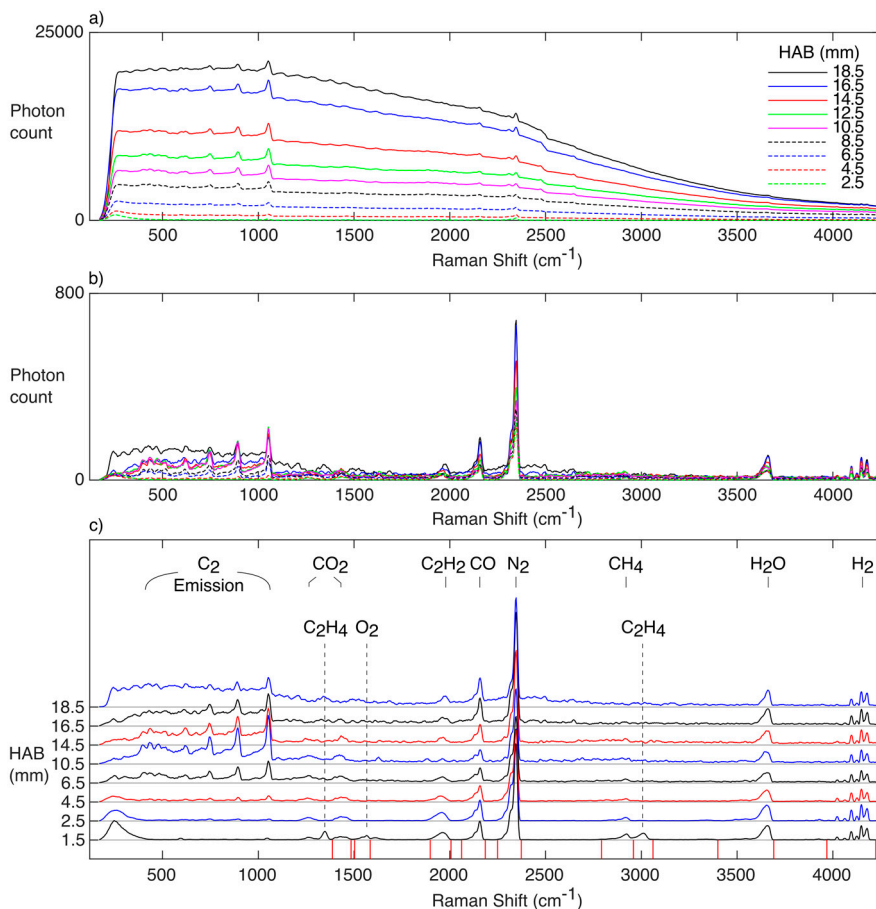


Figure 7.6. Laser-induced incandescence (LII) signal suppression by the PLF-combined Raman spectroscopy for a sooting flame study, revised from [49]. (a) Broadband LII signals are dominating all the Raw spectra at various heights. (b) The PLF technique effectively suppresses the LII signals from the spectra. (c) Some filtered spectra are presented with offset, and Raman peaks are identified.

It is good to note that the laser beam intensity variation due to the polarization change was compensated, as explained in Chapter 6.2. However, C₂ emission signals at short Raman shifts remain, indicating an artifact of the filtering technique.

It is speculated that the amount of soot particles sublimated is not linearly proportional to the laser pulse energy, so the emission signals therefore do not become completely polarization-independent.

The work presented in Paper 4 contains the results of the LIF suppression in the measurements on an unsteady process of biomass gasification. Biomass pellets placed in the heating cell, presented in Figure 3.7, were investigated with the PLF combined Raman spectroscopy. An argon flow purged the ambient air away from the probe volume above the pellet, and a limited amount of air was supplied to induce the gasification process. The cell was continuously heated with a temperature increase rate of 10.7 K/s for the first 50 seconds, and the LIF signal of hydrocarbon volatiles was first observed at 828 K. The temperature increase rate slowed down from this point, and a strong LIF signal covered Raman signals, as presented in Figure 7.7. The modulation period of the polarization was 2 seconds, and the data sampling rate was 1.86 fps.

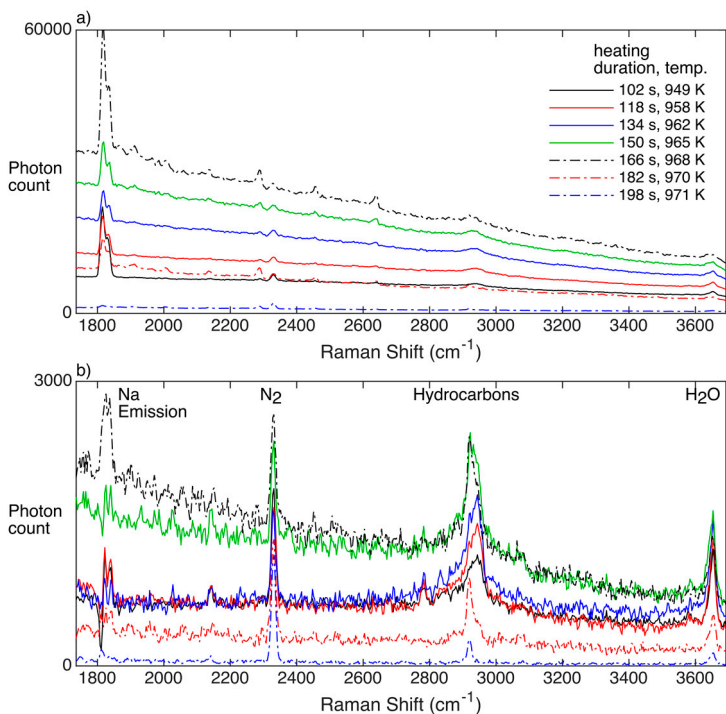


Figure 7.7. Laser-induced fluorescence (LIF) suppression by the PLF technique for a biomass gasification study using Raman spectroscopy. (a) Broadband LIF signals are dominating all the Raw spectra at various heights. (b) The PLF technique effectively suppresses the LIF signals from the spectra, and Raman peaks are revealed.

Figure 7.7 presents the spectra at various stages of the heating before and after filtering with the PLF technique. The LIF signal, 30 times stronger than the Raman

peaks, was successfully removed under the continuous measurements of the unsteady process. Raman peaks of carbon monoxide, nitrogen, hydrocarbons, and water are detected, but the exact kind of hydrocarbons could not be identified. However, the shape change of the hydrocarbon signal over time is observed, so different kinds of hydrocarbons are driven out from the pellet at different stages of the process.

The quantitative species concentrations are derived from the spectra by integrating signal intensities of each channel. The composition profiles of species are presented in Figure 7.8 from Paper 4. The smooth profiles could be attributed to the low modulation frequency and thus low temporal resolution. The faster sampling rate and modulation frequency would increase the temporal resolution and enable the investigation of unsteady phenomena on a faster scale.

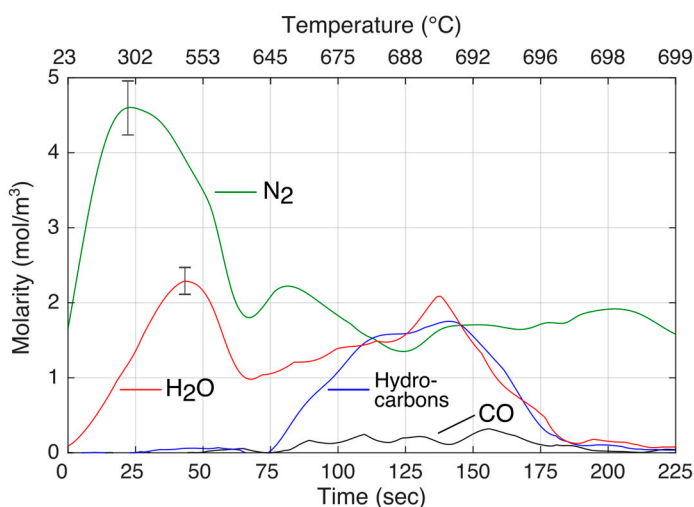


Figure 7.8. Absolute quantities of nitrogen, water, hydrocarbons, and carbon monoxide released from a biomass pellet on a gasification process of continuous heating [50].

8 Summary

Raman spectroscopy was employed to investigate laminar premixed hydrogen-enriched methane flames under various pressure conditions. Raman scattering signals of major species in flames were successfully converted to mole fractions of the species, and temperatures were obtained using nitrogen Raman signals. The results served for chemical kinetic model validation.

One-dimensional laminar premixed flames with different fuels, e.g., methane, hydrogen-enriched methane, DME, and ammonia, were studied at atmospheric pressure with Raman spectroscopy with good spatial resolution, i.e., $\sim 100 \mu\text{m}$. In addition to chemical kinetic model validation, detection of minor intermediate species in flames was another goal of the Raman spectroscopy studies, but it was challenging with the given setup due to the lack of detection sensitivity. Therefore, it was desired to improve the signal detection sensitivity of the setup.

Raman spectroscopy also investigated gas release from biomass pyrolysis and gasification. Simultaneous multiple species detection and quantified results are the advantages of employing Raman spectroscopy, and various components emitted from heated biomass were successfully detected. It demonstrated the potential benefits of employing Raman spectroscopy to study biomass thermal decomposition processes.

However, limitations of employing the technique were also recognized. For example, biomass pyrolysis spectra were dominated by laser-induced fluorescence (LIF) signals of volatile hydrocarbons released at high temperatures, and it motivated the development of a filtering technique to separate Raman scattering signals from LIF signals.

A more efficient laser excitation setup was achieved by employing a multi-pass cavity. A laser beam was reused by the number of passes formed in the cavity, and thus Raman signal intensity was amplified accordingly. Two modes of the cavity were demonstrated, and it enhanced the signal intensity by a factor of 45. The improved Raman spectroscopy was employed to investigate formaldehyde in a lean premixed DME/air flame, and the detection limit of formaldehyde was 40 ppm.

Filtering techniques to suppress background signals were studied. Periodic shadowing (PS) was employed to suppress multiple scattering and stray light contamination on Raman spectra, and the filtering results showed decreased

background level near the laser line and reduced Lorentzian broadening of Raman peaks, providing clearer spectra.

Another filtering technique named polarization lock-in filtering (PLF) was invented to suppress non-Raman signals. The filtering based on polarization modulation separated polarization-dependent and -independent signals, and therefore, vibrational Raman signals remained after the filtering, while LIF and LII signals were successfully removed. The technique was employed to study biomass gasification processes at high temperatures, and the LIF signal was effectively suppressed to enable Raman spectroscopy to study biomass gasification processes at high temperatures. The PLF technique was also demonstrated to resolve Raman signals from a sooting ethylene/air flame, where the strong LII signals dominate spectra. The LII signals, 25 times stronger than Raman scattering signals, were successfully removed, and mole fractions and temperatures of the flame could be derived from Raman spectra.

As a result, the applicability of Raman spectroscopy has been expanded to reaction processes under more harsh conditions, where it was challenging to study with Raman spectroscopy before. In addition, the filtering techniques demonstrated in this thesis can be implemented for laser-based diagnostics in other fields of study by suppressing multiple scattering or separating signals having different polarization dependence.

References

- [1] M.G. Papadopoulos, A.J. Sadlej, J. Leszczynski, Non-linear optical properties of matter, Springer, 2006.
- [2] A. Mohammed, Theoretical Studies of Raman Scattering, KTH, 2011.
- [3] A.C. Eckbreth, Laser diagnostics for combustion temperature and species, CRC press, New York, U.S., 1996.
- [4] D.A. Long, Raman spectroscopy, McGraw-Hill, New York, U.S., 1977.
- [5] W.F. Murphy, W. Holzer, H.J. Bernstein, Gas Phase Raman Intensities - a Review of Pre-Laser Data, *Appl Spectrosc* 23 (1969).
- [6] S. Svanberg, Atomic and molecular spectroscopy: basic aspects and practical applications, Springer, 2012.
- [7] C.M. Western, PGOPHER: A program for simulating rotational, vibrational and electronic spectra, *J Quant Spectrosc Ra* 186 (2017).
- [8] A. Sepman, V. Toro, A. Mokhov, H. Levinsky, Determination of temperature and concentrations of main components in flames by fitting measured Raman spectra, *Appl Phys B* 112 (2013).
- [9] K.C. Utsav, P.L. Varghese, Accurate temperature measurements in flames with high spatial resolution using Stokes Raman scattering from nitrogen in a multiple-pass cell, *Appl Optics* 52 (2013).
- [10] IPCC, 2021: Summary for Policymakers, In: *Climate Change 2021: The Physical Science Basis. Contribution of Working Group I to the Sixth Assessment Report of the Intergovernmental Panel on Climate Change*, V. Masson-Delmotte, P. Zhai, A. Pirani, S.L. Connors, C. Péan, S. Berger, N. Caud, Y. Chen, L. Goldfarb, M.I. Gomis, M. Huang, K. Leitzell, E. Lonnoy, J.B.R. Matthews, T.K. Maycock, T. Waterfield, O. Yelekçi, R. Yu: B. Zhou (Ed.), Cambridge University Press.
- [11] S. Bouckaert, A.F. Pales, C. McGlade, U. Remme, B. Wanner, L. Varro, D. D'Ambrosio, T. Spencer, IEA (2021), Net Zero by 2050, IEA, Paris <https://www.iea.org/reports/net-zero-by-2050>, pp 58-59,
- [12] Q. Zhang, J. Chang, T. Wang, Y. Xu, Review of biomass pyrolysis oil properties and upgrading research, *Energy Convers Manag* 48 (2007).
- [13] A. Molino, S. Chianese, D. Musmarra, Biomass gasification technology: The state of the art overview, *J Energy Chem* 25 (2016).
- [14] S. Wang, G. Dai, H. Yang, Z. Luo, Lignocellulosic biomass pyrolysis mechanism: a state-of-the-art review, *Prog Energy Combust* 62 (2017).
- [15] D.V. Salazar, C.S. Goldenstein, J.B. Jeffries, R. Seiser, R.J. Cattolica, R.K. Hanson, Design and implementation of a laser-based absorption spectroscopy sensor for in situ monitoring of biomass gasification, *Meas Sci Technol* 28 (2017).

- [16] J.F. James, Sternberg, Robert Siegmund, *The Design of Optical Spectrometers*, Chapman and Hall, London, U.K., 1969.
- [17] P.H. Joo, J. Gao, Z. Li, M. Aldén, Experimental apparatus with full optical access for combustion experiments with laminar flames from a single circular nozzle at elevated pressures, *Rev Sci Instrum* 86 (2015).
- [18] R.C. Rocha, S. Zhong, L. Xu, X.-S. Bai, M. Costa, X. Cai, H. Kim, C. Brackmann, Z. Li, M. Aldén, Structure and Laminar Flame Speed of an Ammonia/Methane/Air Premixed Flame under Varying Pressure and Equivalence Ratio, *Energy Fuels* 35 (2021).
- [19] P. Versailles, A. Durocher, G. Bourque, J.M. Bergthorson, Measurements of the reactivity of premixed, stagnation, methane-air flames at gas turbine relevant pressures, *J Eng Gas Turbine Power* 141 (2019).
- [20] M. Matalon, Flame dynamics, *P Combust Inst* 32 (2009).
- [21] S. Kadowaki, T. Hasegawa, Numerical simulation of dynamics of premixed flames: flame instability and vortex-flame interaction, *Prog Energ Combust* 31 (2005).
- [22] A. Lantz, R. Collin, M. Aldén, A. Lindholm, J. Larfeldt, D. Lörstad, Investigation of hydrogen enriched natural gas flames in a SGT-700/800 burner using OH PLIF and chemiluminescence imaging, *J Eng Gas Turbine Power* 137 (2015).
- [23] A.A. Subash, H. Kim, S.-I. Möller, M. Richter, C. Brackmann, M. Aldén, A. Lantz, A. Lindholm, J. Larfeldt, D. Lörstad, Investigation of Fuel and Load Flexibility in a SGT-600/700/800 Burner Under Atmospheric Pressure Conditions Using High-Speed OH-Plif and OH Chemiluminescence Imaging, *J Eng Gas Turbine Power* 143 (2021).
- [24] D. Lörstad, A. Lindholm, J. Pettersson, M. Björkman, I. Hultmark. Siemens SGT-800 industrial gas turbine enhanced to 50MW: Combustor design modifications, validation and operation experience. *Turbo Expo: Power for Land, Sea, and Air; 2013: American Society of Mechanical Engineers*.
- [25] F. Fuest, R. Barlow, D. Geyer, F. Seffrin, A. Dreizler, A hybrid method for data evaluation in 1-D Raman spectroscopy, *P Combust Inst* 33 (2011).
- [26] G. Magnotti, U. KC, P. Varghese, R. Barlow, Raman spectra of methane, ethylene, ethane, dimethyl ether, formaldehyde and propane for combustion applications, *J Quant Spectrosc Ra* 163 (2015).
- [27] R. Tambay, R.K. Thareja, Laser-Induced Breakdown Studies of Laboratory Air at 0.266, 0.355, 0.532, and 1.06 μm , *J Appl Phys* 70 (1991).
- [28] J. Kojima, Q.V. Nguyen, Laser pulse-stretching with multiple optical ring cavities, *Appl Optics* 41 (2002).
- [29] H. Lee, H. Kim, Y. Lee, Y. Yoon, Jet disintegration in supercritical environments, *Exp Therm Fluid Sci* 115 (2020).
- [30] H. Tang, C. Yang, G. Wang, T.F. Guiberti, G. Magnotti, Raman spectroscopy for quantitative measurements of temperature and major species in high-pressure non-premixed $\text{NH}_3/\text{H}_2/\text{N}_2$ counterflow flames, *Combust Flame* 237 (2022).
- [31] R.A. Hill, D.L. Hartley, Focused, multiple-pass cell for Raman scattering, *Appl Optics* 13 (1974).
- [32] X.Y. Li, Y.X. Xia, J.M. Huang, L. Zhan, A Raman system for multi-gas-species analysis in power transformer, *Appl Phys B* 93 (2008).

- [33] L. Xiao-Yun, X. Yu-Xing, H. Ju-Ming, Z. Li, Diagnosis of multiple gases separated from transformer oil using cavity-enhanced Raman spectroscopy, *Chinese Phys Lett* 25 (2008).
- [34] K.C. Utsav, J.A. Silver, D.C. Hovde, P.L. Varghese, Improved multiple-pass Raman spectrometer, *Appl Optics* 50 (2011).
- [35] J.B. Pawley, *Handbook of biological confocal microscopy*, 3rd ed., Springer, New York, U.S., 2006.
- [36] E. Kristensson, M. Richter, S.-G. Pettersson, M. Aldén, S. Andersson-Engels, Spatially resolved, single-ended two-dimensional visualization of gas flow phenomena using structured illumination, *Appl Optics* 47 (2008).
- [37] E. Kristensson, E. Berrocal, M. Richter, S.-G. Pettersson, M. Aldén, High-speed structured planar laser illumination for contrast improvement of two-phase flow images, *Opt Lett* 33 (2008).
- [38] E. Berrocal, E. Kristensson, M. Richter, M. Linne, M. Aldén, Application of structured illumination for multiple scattering suppression in planar laser imaging of dense sprays, *Opt Express* 16 (2008).
- [39] E. Kristensson, J. Bood, M. Alden, E. Nordstrom, J. Zhu, S. Huldt, P.E. Bengtsson, H. Nilsson, E. Berrocal, A. Ehn, Stray light suppression in spectroscopy using periodic shadowing, *Opt Express* 22 (2014).
- [40] M. Gong, H. Kim, J. Larsson, T. Methling, M. Aldén, E. Kristensson, C. Brackmann, T. Eschrich, M. Jäger, W. Kiefer, Fiber-based stray light suppression in spectroscopy using periodic shadowing, *Opt Express* 29 (2021).
- [41] Z. Zhao, M. Chaos, A. Kazakov, F.L. Dryer, Thermal decomposition reaction and a comprehensive kinetic model of dimethyl ether, *Int J Chem Kinet* 40 (2008).
- [42] C.W. Zhou, Y. Li, E. O'Connor, K.P. Somers, S. Thion, C. Keesee, O. Mathieu, E.L. Petersen, T.A. DeVerter, M.A. Oehlschlaeger, G. Kukkadapu, C.J. Sung, M. Alrefae, F. Khaled, A. Farooq, P. Dirrenberger, P.A. Glaude, F. Battin-Leclerc, J. Santner, Y.G. Ju, T. Held, F.M. Haas, F.L. Dryer, H.J. Curran, A comprehensive experimental and modeling study of isobutene oxidation, *Combust Flame* 167 (2016).
- [43] U. Burke, W.K. Metcalfe, S.M. Burke, K.A. Heufer, P. Dagaut, H.J. Curran, A detailed chemical kinetic modeling, ignition delay time and jet-stirred reactor study of methanol oxidation, *Combust Flame* 165 (2016).
- [44] A. Kéromnès, W.K. Metcalfe, K.A. Heufer, N. Donohoe, A.K. Das, C.-J. Sung, J. Herzler, C. Naumann, P. Griebel, O. Mathieu, An experimental and detailed chemical kinetic modeling study of hydrogen and syngas mixture oxidation at elevated pressures, *Combust Flame* 160 (2013).
- [45] S.M. Burke, W. Metcalfe, O. Herbinet, F. Battin-Leclerc, F.M. Haas, J. Santner, F.L. Dryer, H.J. Curran, An experimental and modeling study of propene oxidation. Part 1: Speciation measurements in jet-stirred and flow reactors, *Combust Flame* 161 (2014).
- [46] S.M. Burke, U. Burke, R. Mc Donagh, O. Mathieu, I. Osorio, C. Keesee, A. Morones, E.L. Petersen, W.J. Wang, T.A. DeVerter, M.A. Oehlschlaeger, B. Rhodes, R.K. Hanson, D.F. Davidson, B.W. Weber, C.J. Sung, J. Santner, Y.G. Ju, F.M. Haas, F.L. Dryer, E.N. Volkov, E.J.K. Nilsson, A.A. Konnov, M. Alrefae, F. Khaled, A. Farooq, P. Dirrenberger, P.A. Glaude, F. Battin-Leclerc, H.J. Curran, An experimental and modeling study of propene

oxidation. Part 2: Ignition delay time and flame speed measurements, *Combust Flame* 162 (2015).

[47] W.K. Metcalfe, S.M. Burke, S.S. Ahmed, H.J. Curran, A hierarchical and comparative kinetic modeling study of C1– C2 hydrocarbon and oxygenated fuels, *Int J Chem Kinet* 45 (2013).

[48] Y. Li, C.W. Zhou, K.P. Somers, K.W. Zhang, H.J. Curran, The oxidation of 2-butene: A high pressure ignition delay, kinetic modeling study and reactivity comparison with isobutene and 1-butene, *P Combust Inst* 36 (2017).

[49] H. Kim, M. Alden, C. Brackmann, Suppression of unpolarized background interferences for Raman spectroscopy under continuous operation, *Opt Express* 29 (2021).

[50] H. Kim, M. Gong, E. Kristensson, A. Ehn, M. Aldén, C. Brackmann, Time-resolved polarization lock-in filtering for background suppression in Raman spectroscopy of biomass pyrolysis, *Combust Flame* 224 (2021).

Acknowledgments

If you opened this page first when you got this thesis, it must mean our relationship is more important than the piece of work. I totally agree with the idea because I did the same whenever I got others' theses. This thesis contains lots of data sets, plots, ideas, interpretations, and achievements in the lab. However, it does not really present all that I earned from our lovely Combustion Physics group. Therefore, I agree that something really important was missing in this thesis until this page. I will try my best to sort that out in a few pages from here, which is the most important and the most-read part of theses according to my statistics.

However, please forgive me if I miss someone to mention or something worth sharing. It is not because I do not appreciate it, but because I have been rushing writing with a little bit of stress. I still appreciate all the people and moments in my journey over the last five years.

To write the list of names, I must start with **Marcus Aldén**, the founder and former head of our lovely group, and more importantly (personally), who saw the value in me and gave me the opportunity to come to Lund and start doing research. You helped my life direct this wonderful field, which I always wished. It took some time to visit your office without being extremely nervous (I am still 'okay' nervous), but I tried to discuss with you more since I always learn a lot from your comments. There are so many things I want to say, but I will keep them for later so that we can talk about them one by one from time to time.

The one that I got help at the division from the first day (until the last day) was **Christian Brackmann**, my supervisor. Thank you so much for your supervision, which has always been considerate and helpful. Everyone knows how busy you are, but you still managed to be the best supervisor of your needy student. I want to be a researcher like you enjoying lab activities and being a go-to person for colleagues having problems or questions. I should be an independent researcher by now, but I have a feeling that you might still be a go-to person for me for a while, even after leaving the division.

Thank you, **Mattias Richter**, for supervising me together with Christian and Marcus and also for lending me your laser, which was used during the entire period of my PhD study. In addition, I liked your course very much, and the same goes for **Joakim Bood**. Thanks for the opportunity of taking the Laser lab Sweden course, which broadened my knowledge and network. I also liked **Dr. Berrocal's** course on

spray imaging, which became a base for my next career. In addition, thank you, **Eduard**, for your huge support on my job application process, and I wish we can collaborate in the near future. Thank you, **Zhongshan Li**, for stimulating me with new ideas, which were not always realized but always evoked new ideas in me. Thanks, **Andreas Ehn**, for inviting me to the PS study where I could learn about the filtering technique, which became the most important part of my thesis.

When I struggled to understand the new culture, I got much help from my colleagues and friends. **Elin Malmqvist** is my first office mate who injected the Swedish mindset into me through endless conversations in the office. It is so different from Koreans', so it was almost shocking initially, impressive later, and finally agreed. I always enjoyed talking with you, making the third floor the best in the building (during that period). I thank **Kajsa Larsson** for making this possible by lending me your office while away. Later, when I got my own office, **Sebastian Pfaff** became my office mate, and you are such an energizer giving me much energy for just being around. Thank you for helping me with many small things and explaining those interesting facts that I haven't really thought about before. **Shen Li** and **Qingshuang Fan** are the ones who started PhD studies at a similar time as me and came from abroad, so naturally, we got to help each other with some paper and bureaucratic work from time to time. Thank you for helping me with those hectic works, and I hope the never-ending residence permit issues are solved soon.

Christian Binder, Ali Hosseinnia, Joakim Jönsson, Christoffer Pichler, and Xin Liu are the friends that I spent the most time with after work in the first half of my study period. You altogether kept my mentality, brain, and body being healthy through many nights in a few bars in Lund, Malmö, and Norrköping; deep science talk during breaks around the physics department, which always motivated me to learn theories related to atomic and molecular spectroscopy more; and badminton every Friday for more than a year like serious players. Thank you all for being a company and giving me good memories in Sweden, especially during those tough periods right after arriving in a new country.

In the lab, thank you, **Jinlong Gao**, from whom I learned everything about the high-pressure chamber, which was an essential facility for my PhD study. **Henrik Johansson, Jim Larsson, Miaoxin Gong, and Torsten Methling** are the first Raman team members that I really enjoyed working with. It was much more fun to work altogether than by myself, and I missed the days a lot when you all left. I learned a lot from you all, and it also helped me practice how to work as a team. Of course, after work at pool places and bars was extra fun. Now I am so excited to work with you again soon, Torsten. Thankfully, **Alsu Zubairova** joined our Raman group recently, and I tried to be a helpful senior student like how the others did to me, but I wish you could feel at least my intention to be nice since it feels that I couldn't do as good as the old guys. In any case, I can see that you will do well with the continuation of the Raman study successfully, and thanks for working with me.

Apart from the Raman activity, I could do more practical and larger combustion experiments thanks to **Arman Subash**. It was also a special experience to live in Finspång with so few people around at night. However, I could only manage it thanks to you being around. **Francesco Pignatelli**, I enjoyed doing experiments with you, but, unfortunately, it was only for a short period. You are the one that makes the lab atmosphere bright and happy even during measurements. I wish there would be some more occasions where we can work together or discuss gas turbine studies in the future.

In the second half of my study, I became more introverted and spent more time at home, and the pandemic didn't help either. However, I could do some physical activities thanks to the friends who kept inviting me to events. Thanks, **Dina Hot**, for initiating the indoor climbing gang, which I really enjoyed and looked forward to every week. It was so fun and rewarding time together with **David Sanned**, **Pengji Ding**, and **Adrian Roth** in the pre-covid era. Thanks to **Saga Bergqvist**, **Adrian Roth**, and **David Andersson**, there is the second phase of the climbing gang now, and thanks for initiating it again even though I couldn't participate so often. I enjoyed hanging out with you all so much, and it was extra fun to take pictures in the climbing center with **Ruik Bi**, **Armand Dominguez**, and **Zhiyong Wu**.

Some beer is essential to balance after doing exercise, and I have another group of friends to thank. Thank you very much **Marco Lubrano Lavadera**, **Saeed Derafshzan**, **Christoffer Pichler**, **Jundie Chen**, and **Lisa Rämisch** for inviting me and accompanying social events such as watching football, karaoke night, and some parties. I could keep myself just above the minimum requirement to be a social person, thanks to you. Otherwise, I might have turned into a couch potato by now. Thank you very much for having fun and sharing good memories with me.

I have been intentionally excluding some names while writing so far, which are **Manu Mannazhi**, **Maria Ruchkina**, and **Yupan Bao**. The reason is that I decided not to put your names in any of those categories since otherwise, all the paragraphs would start with your names. We spent so much time doing many things together, and now it is full of good memories and stupid photos of you on my phone. I am grateful to have the unique pictures of you, and I hope all the best for your future so that the pictures can be auctioned. I especially liked the combination of some spontaneous and other cautious people in this group, which I wouldn't specify which is whom. Thanks to you, I learned another attitude of living, such as being spontaneous, with proof that everything gets easier when one becomes spontaneous (still good to have a cautious person around). I must admit that it is actually a huge plus to my personality.

From the first day of joining the division, I knew that I would love this division. After about five years, I can tell how many people are putting effort into keeping this lovely atmosphere. **Per-Erik Bengtsson**, **Minna Ramkull**, **Cecilia Bille**, **Sven-Inge Möller**, **Panagiota Stamatoglou**, and **Trivselgruppen** are the representative

names I would like to express my appreciation, but I would like to thank **Everyone** at the division. Thanks to your effort, I got precious friends and memories here during my PhD study. I am so grateful to be a member of a group that has the atmosphere of doing and sharing many things together. Every member actively initiates and participates in research and social activities, so the division was not a boring workplace but a playground that I enjoyed to go every day. For example, the endless discussion during lunch was what I was waiting for every morning. Now, it's not as active as before due to the pandemic, but I hope it comes back soon. I enjoyed discussions (or lectures) with the frequent discussion members of **Alexios Matamis, Samuel Jansson, Vladimir Alekseev, Karolina Dorozynska, Sandra Török, Wubin Weng, Henrik Feuk, Sebastian Nilsson, and Simon Ek**. I learned international politics, histories, relations, movies, series, and swear words every day in the kitchen. I miss it and will miss it more.

Despite the wonderful members at work and after work, my life here must have been tougher if I didn't have my Korean friends. **Yeonjin** has been helping me from settling in Sweden to finishing my PhD. I wish you good luck with finishing your study and hope you don't get too stressed from the writing. **Su Yeong, Sungwon, Narae, Taein, Bobae, Yunjeong** are the gang of my first Korean friends in Sweden, and I still don't understand how we could talk all night until sunrise so often. Thanks to all of you, I felt like I am in Korea on national holidays and birthdays, and I still remember the warmth. Thank you, **Yoonjoo**, for helping me learn Swedish and reminding me of calculus. Now you are way better than your former teacher. Thank you, **Hyerin**, for spending time and taking care of me, especially during the hectic period of the pandemic, which could have been badly gloomy. I wish you the best for every step in your journey. A special thanks to my aurora friends, **Jaeyoung, Heejae, Debora**. Northern light was pretty and intense, but I will remember you more with your kindness and amazing personalities. Our shared memory in Lund is a couple of months, but there is much more to come. I can definitely see your flourishing future, so don't worry too much, and let's enjoy and get excited about what is coming to us.

My supportive friend **Geonhwan**, I am so happy to have a best friend like you.

To my family. 엄마 아빠, 항상 걱정해 주시고, 응원해 주시고, 믿고 지켜봐 주셔서 감사해요. 이렇게 정성껏 키워 주시고 바르게 가르쳐 주셔서 감사합니다. 그리고 다솔아, 형이 멀리 있는 동안 부모님 곁에서 장남과 막내 역할 둘 다 하느라 고생이 많아. 고맙다.

At last, I would like to thank funding organizations for supporting my PhD study and research activities. The Swedish Energy Agency (Energimyndgheten) through Center of Combustion Science and Technology (CECOST) and the Swedish Foundation for Strategic Research (SSF).

Paper I



Arman Ahamed Subash¹

Postdoc Division of Combustion Physics,
Lund University,
P.O. Box 118,
Lund SE-221 00, Sweden
e-mail: arman.subash@forbrf.lth.se

Haisol Kim

Division of Combustion Physics,
Lund University,
P.O. Box 118,
Lund SE-221 00, Sweden
e-mail: haisol.kim@forbrf.lth.se

Sven-Inge Möller

Research Administrative Director
Division of Combustion Physics,
Lund University,
P.O. Box 118,
Lund SE-221 00, Sweden
e-mail: sven-inge.moller@forbrf.lth.se

Mattias Richter

Professor
Division of Combustion Physics,
Lund University,
P.O. Box 118,
Lund SE-221 00, Sweden
e-mail: mattias.richter@forbrf.lth.se

Christian Brackmann

Division of Combustion Physics,
Lund University,
P.O. Box 118,
Lund SE-221 00, Sweden
e-mail: christian.brackmann@forbrf.lth.se

Marcus Aldén

Professor
Division of Combustion Physics,
Lund University,
P.O. Box 118,
Lund SE-221 00, Sweden
e-mail: marcus.alden@forbrf.lth.se

Andreas Lantz

Siemens Industrial Turbomachinery AB,
Finspong SE-612 83, Sweden
e-mail: andreas.lantz@siemens.com

Annika Lindholm

Siemens Industrial Turbomachinery AB,
Finspong SE-612 83, Sweden
e-mail: annika.lindholm@siemens.com

Jenny Larfeldt

Siemens Industrial Turbomachinery AB,
Finspong SE-612 83, Sweden
e-mail: jenny.larfeldt@siemens.com

Daniel Lörstäd

Siemens Industrial Turbomachinery AB,
Finspong SE-612 83, Sweden
e-mail: daniel.lorstad@siemens.com

Investigation of Fuel and Load Flexibility in a Siemens Gas Turbine-600/700/800 Burner Under Atmospheric Pressure Conditions Using High-Speed Hydroxyl-PLIF and Hydroxyl Radical Chemiluminescence Imaging

Fuel and load flexibility have been increasingly important features of industrial gas turbines in order to meet the demand for increased utilization of renewable fuels and to provide a way to balance the grid fluctuations due to the unsteady supply of wind and solar power. Experimental investigations were performed using a standard third-generation dry low emission (DLE) burner under atmospheric pressure conditions to study the effect of central and pilot fuel addition, load variations, and hydrogen (H₂) enrichment in a natural gas (NG) flame. High-speed kHz planar laser-induced fluorescence (PLIF) of OH radicals and imaging of OH chemiluminescence were employed to investigate the flame stabilization, flame turbulence interactions, and flame dynamics. Along with the optical measurements, combustion emissions were also recorded to observe the effect of changing operating conditions on NO_x level. The burner is used in Siemens industrial gas turbines SGT-600, SGT-700, and SGT-800 with minor hardware differences and the study thus is a step to characterize fuel and load flexibility for these turbines. Without pilot and central fuel injections in the current burner configuration, the main flame is stabilized creating a central recirculation zone (CRZ). Addition of the pilot fuel strengthens the outer recirculation zone (ORZ) and moves the flame anchoring position slightly downstream, whereas the flame moves upstream without affecting the ORZ when central fuel injection is added. The flame was investigated utilizing H₂/NG fuel mixtures where the H₂ amount was changed from 0 to 100%. The results show that the characteristics of the flames are clearly affected by the addition of H₂ and by the load variations. The flame becomes more compact, the anchoring position moves closer to the burner exit and the OH signal distribution becomes more distinct for H₂ addition due to increased reaction rate, diffusivity, and laminar burning velocity. Changing the load from part to base, similar trends were observed in the flame behavior but in this case due to the higher heat release because of increased turbulence intensity. [DOI: 10.1115/1.4049499]

¹Corresponding author.

Manuscript received August 31, 2020; final manuscript received September 11, 2020; published online March 31, 2021. Editor: Jerzy T. Sawicki.

Introduction

Increasing demand for utilizing a wide range of alternative and renewable fuels makes it imperative to consider operational flexibility, efficiency, fuel flexibility, and emissions when designing modern industrial gas turbine engines. One key challenge is to achieve high efficiency combined with low emissions for different liquid and gaseous fuels at load variations. Currently, stationary gas turbine engines are designed to operate under lean premixed conditions in order to reduce thermal NO_x production [1,2] by lowering the flame temperature. However, this approach can lead to undesirable instabilities, which may cause local flame extinction, thermoacoustic oscillations, and poor combustion efficiency [3]. To design an industrial gas turbine, eliminating such instabilities is a significant challenge. The inclusion of a diffusion pilot flame or a prechamber combustor can prevent the occurrence of such instabilities [4,5]. A range of alternative fuels, such as residual product gases from refineries, chemical plants, and petroleum industries, particularly renewable fuels derived from biomass, have been proposed for use in gas turbines due to a substantial cost advantage, changes in the supply and availability of traditional fuel, and minimization of the adverse effects on the environment. These fuels commonly contain a significant fraction of hydrogen (H_2) and hydrocarbons (HC). H_2 , a carbon-free energy carrier, can also be produced from renewable energy sources, such as solar and wind power, via direct thermal conversion or by electrolysis [6,7]. Several combustion relevant properties of H_2 , e.g., high diffusivity, wide flammability range, high laminar and turbulent flame speed, are significantly different from those of a conventional HC fuel and can affect the operational limits, flame stabilization, and exhaust gas emissions [8–13]. The enrichment of H_2 increases the range of flame stability and lowers the lean blowout (LBO) limit [8], while it makes the flame more sensitive to flashback by enhancing the laminar and turbulent flame speed [11]. H_2 enrichment can also affect the flame stabilization by altering the flame shape and position [12]. The DNS simulation by Hawkes and Chen [14] shows that the flame surface area can be increased due to the higher burning rate per unit area. An increase in NO_x and dynamic modes of the combustor were observed in the study by Lam and Parsania [15].

The primary objective of the current study is to experimentally investigate the effects of central and pilot fuel addition, load variations and H_2 enrichment in the natural gas (NG) flame in a Siemens standard third generation dry low emission (DLE) burner under atmospheric conditions. Although high pressure is a required condition for a real gas turbine, relevant phenomena, e.g., flame turbulence interactions and flame stabilization, can also be investigated at atmospheric pressure for fundamental understanding. In addition, it is much less challenging to evaluate designs and combustion conditions using advanced measurement tools, such as laser techniques, at atmospheric pressure in order to explain phenomena detected but not fully understood at higher pressure. High-speed OH planar laser-induced fluorescence (PLIF) and OH chemiluminescence were employed in the current investigations for temporally resolved studies of flame structure,

flame stabilization, and dynamics. The OH chemiluminescence images are useful for acquiring information about the overall size and shape of the flame while the OH-PLIF images indicate the reaction zone and postflame regions. Finally, NO_x emissions were recorded to observe the effect of changing operating conditions.

This burner is used in the industrial gas turbines SGT-600 (25 MW), SGT-700 (33 MW), and SGT-800 (62 MW) with minor hardware differences. The burner design principle is well-proven since its early development history [16] and improvements are constantly implemented [17,18]. This type of burner has been thoroughly investigated using different methods such as CFD and measurements using water rig for investigating the fuel-air mixing, atmospheric combustion rig tests for fundamental investigations with high optical access, high-pressure rig tests to include the pressure effect and engine tests for complete engine conditions and the effect of neighboring burners. More details of some of the performed investigations are presented in Refs. [17–22].

Experimental Setup

Burner and Atmospheric Combustion Test Rig. Measurements were performed in the Siemens standard third generation DLE burner and its schematic is presented in Fig. 1. The airflow enters a swirl generator consisting of four quarter cones shifted with respect to each other to create a swirling flow. The swirl generator is connected to a circular mixing tube with a secondary air inlet by means of film air rows. After main fuel injection in the swirl generator, the swirling air/fuel mixture passes through the mixing tube, after which it enters the combustion chamber where it expands in a radial direction and ignites as it mixes with hot recirculated combustion gases. The burner configuration also allows the injection of additional fuel through pilot outlets, which are equidistantly distributed at the circumference around the burner tip, and through the central gas nozzle shown in Fig. 1.

The DLE burner was mounted in an atmospheric test rig also used in previous studies [17,18,20]. The experimental setup in the atmospheric rig is shown in Fig. 2. The combustion chamber located after the burner exit consists of a convectively cooled liner. The circular cross section of the combustion chamber has a similar expansion ratio as in the real gas turbine annular combustors; however, the initial section just after the burner exit has square cross section with smoothed corners to improve measurement quality. Access for optical diagnostics in the flame region is provided through quartz windows on three sides of the liner. Before entering the plenum, the combustion air was preheated up to 693 K. The fuel flow rates to the main, pilot, and central gas injectors were controlled by means of Coriolis mass flow controllers.

Operating Conditions. The experiments were performed at atmospheric pressure conditions while inlet air temperature, burner pressure drop, and flame temperature were downscaled and altered to engine conditions by matching the reference velocity in the mixing tube (based on the mass flow) and the equivalence ratio. Three parameters were varied to study their effects on combustion: Central and pilot fuel addition, load variation, and H_2 addition. At the central fuel to total fuel ratio (CFR) = 2% setting, 2% of the total fuel amount was injected through the central gas nozzle shown at the left of Fig. 1, while at the pilot fuel to total fuel ratio (PFR) = 3% setting, 3% of the total fuel amount was guided to the pilot outlet so that small diffusion flames were introduced around the edge of the burner tip. Finally, at PFR = 0, CFR = 0 setting, only main fuel was injected in the swirl generator without supplying fuel through the pilot and central injectors. When changing the fuel route, the bulk airflow was kept constant. In addition to the effect of guiding fuel to different paths, the effects of load variations, from part load (about 80%) to base load, were studied by varying the mass flow rate of the gas mixture. Both the mass flow of the air and the mass flow of the fuel

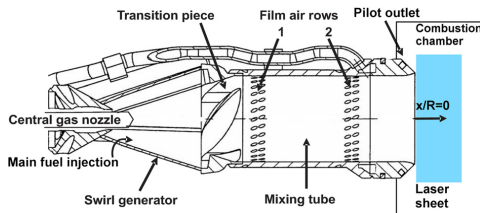


Fig. 1 Schematic of the Siemens third generation DLE burner from Ref. [19] with laser beam path and combustion chamber added

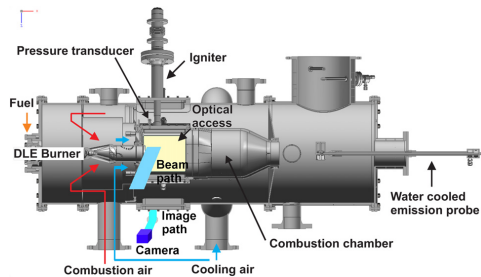


Fig. 2 Schematic of atmospheric combustion test rig assembly from Ref. [19] with laser beam path and image detection system added

were raised by a factor 1.2 to achieve the base load condition compared to the part load condition. The inlet air temperature was also increased by about 20 K at the base load condition compared to the part load. The same adiabatic flame temperature was used for all cases including the part load case. The reason for this is that the twin shaft engines SGT-600 and SGT-700 have combustor air bypass system in order to keep similar flame temperature despite reduced turbine inlet temperature. For the single shaft engine SGT-800, this is also relevant since the turbine inlet temperature is barely affected down to about 75% load using normal settings. The flame was also investigated using pure NG as well as pure H₂ fuel. In addition to the pure H₂ combustion case, H₂ enrichment where the NG fuel was enriched with 30 vol %, 60 vol %, and 80 vol % of H₂ was studied at the PFR = 3% setting. Here, the airflow was kept constant, while the mass flow rate of the fuel was adjusted at each H₂ concentration to achieve a constant global adiabatic flame temperature, which is a typical control strategy for practical gas turbines. Air-to-fuel ratio (AFR) at each flame condition is normalized by the air-to-fuel ratio at the base load (NG) case with PFR = 0, CFR = 0 (AFR0) and the normalized values are tabulated in Table 1.

Diagnostics

As optical measurement techniques, high-speed OH-PLIF, and OH chemiluminescence imaging were employed for investigating the flame at the burner exit.

OH-Planar Laser-Induced Fluorescence

High-speed (kHz) OH-PLIF measurements were performed by excitation of the $A^2\Sigma^+ - X^2\Pi$ (1-0) band of the OH radical. A frequency-doubled (532 nm) pulsed solid-state diode-pumped Nd:YAG laser (Edgewave HD401-E) was used to pump a tunable dye laser (Sirah Credo) operated with Rhodamine 590 dye. The output of the dye laser (~566 nm) was frequency-doubled and the laser wavelength was tuned to the temperature-insensitive $Q_1(8)$ transition at 283.55 nm. An approximately 50 mm wide laser sheet was formed using an $f = -40$ mm cylindrical lens and an $f = +500$ mm spherical lens and passed along the midline axis of the burner exit. The laser pulse energy varied between 1.75 mJ and 1.9 mJ during the measurements. The resulting OH fluorescence signal at wavelength ~310 nm was collected perpendicular to the laser sheet with a high-speed CMOS camera (Fastcam SA5) in combination with a two-stage image intensifier (HiCATT). The detector system was fitted with a UV sensitive lens (B. Halle, f#2, $f = 100$ mm). To suppress interference occurring from scattered laser light and background radiation, a single-band bandpass filter (315/15 nm BrightLine®) was mounted in front of the lens. The detector was set to a time gate of 40 ns to further limit background contributions from flame chemiluminescence. For each of the

flame conditions, 2728 single-shot images (using max. buffer memory of the camera) were collected at 2 kHz frequency. For compensation in the average spatial profile of the laser sheet, a cuvette with a weak dye solution was used. The scaling factor of the acquired images was 0.15 mm/pixel.

Flame Chemiluminescence. The same detector system was used to acquire line-of-sight integrated chemiluminescence images of excited OH radicals (OH*) at wavelength 310 nm. The camera was equipped with the same UV sensitive lens (B. Halle, f#2, $f = 100$ mm) and a bandpass filter centered at 310 nm. For each flame condition, 2728 single-shot images were collected at a frequency of 2 kHz and with an exposure time of 20 μ s.

Results and Discussion

Effect of Central Fuel to Total Fuel Ratio and Pilot Fuel to Total Fuel Ratio on the Main Flame. In Fig. 3, OH-PLIF images show the effects of the pilot and central fuel addition on the NG/air flame structure at a base load condition. OH-PLIF measurements were carried out to provide qualitative information of OH radical distributions in the symmetry plane through the center of the burner exit and identify the reaction zone and the postflame region. The high-intensity region indicates OH radicals that are formed in the flame front or have been convected a relatively short distance [23]. The coordinates of the images are normalized by the burner exit inner radius (R) and the flow direction is from left to right. In Figure 3, representative single shots and evaluated gradients of OH are shown in the first two rows, while probability density maps (PDMs) of the OH gradients and single shots are shown in the last two rows. The strongest gradients are good markers to indicate the approximate position of the flame front [24,25], while weaker gradients correspond to boundary layers between hot and cold gases. For each case, the PDM images were calculated by binarizing and later normalizing 2728 single shots as well as corresponding gradient images, to present the spatial distributions of OH radicals and flame fronts. A local thresholding scheme was implemented to identify the boundaries of the reaction layers and to form binarized images. For each column of pixels, 10% of the local maximum (in that column) was selected as a threshold for the signal-to-background ratio. The width of PDMs of the gradients indicates the flame front fluctuations.

Previous experimental and LES investigations [18,21] of this burner configuration showed that the main flame is stabilized downstream of the burner exit due to a central recirculation zone (CRZ) induced by the vortex breakdown process. The swirling air generated by the swirler and fuel introduced through injectors in the swirler can achieve good mixing after passing through the mixing tube and then discharge into the combustor through the burner nozzle, where it expands radially by the imposed swirl [26]. The main flame is anchored at the inner shear layer (ISL) formed by the CRZ, which brings heat and radicals from the main flame toward the burner exit and initiates reactions with the fresh fuel/air mixture. A sharp temperature and OH gradient indicate the flame front in the vicinity of the reaction zone. In the current results presented in Fig. 3, only the early portion of the NG/air flame, covered by the width of the laser sheet, is shown for three CFR and PFR settings: (a) PFR = 0, CFR = 0, (b) PFR = 3%, CFR = 0, (c) PFR = 3%, CFR = 2%. The conical shape of the OH distribution with high intensity, found at the ISL of the swirling air/fuel mixture, indicates the leading edge of the CRZ, whereas low OH signal found along the outer shear layer (OSL) indicates the outer recirculation zone (ORZ). The flame exhibits repeatedly large axial displacements with superimposed local fluctuations due to various scales of turbulence. An arbitrary cycle of the main flame fluctuation is shown in a time sequence in Fig. 4. In the sequence, the downstream propagation of the flame is clearly observed up to 0.2 ms, after which the flame is almost out of the field of view. Then, it is found to be pulled back again in the

Table 1 Fuel gas composition and normalized AFR values for different flame conditions

| Operating condition | Fuel gas composition (Vol %) | | AFR/AFR0 | Fuel splitting | | |
|----------------------------------------------------|------------------------------|----------------|----------|----------------|---------------|----------------|
| | NG | H ₂ | | AFR/AFR0 | Main fuel (%) | Pilot fuel [%] |
| Base load (NG): PFR = 0, CFR = 0 | 100 | 0 | 1 | 100 | 0 | 0 |
| Base load (NG): PFR = 3%, CFR = 0 | 100 | 0 | 1 | 97 | 3 | 0 |
| Base load (NG): PFR = 3%, CFR = 2% | 100 | 0 | 1 | 95 | 3 | 2 |
| Part load (NG): PFR = 3%, CFR = 2% | 100 | 0 | 1 | 95 | 3 | 2 |
| Base load (30% H ₂): PFR = 3%, CFR = 0 | 70 | 30 | 1.06 | 97 | 3 | 0 |
| Base load (60% H ₂): PFR = 3%, CFR = 0 | 40 | 60 | 1.21 | 97 | 3 | 0 |
| Base load (80% H ₂): PFR = 3%, CFR = 0 | 20 | 80 | 1.45 | 97 | 3 | 0 |
| Base load (100% H ₂): PFR = 0, CFR = 0 | 0 | 100 | 2.36 | 100 | 0 | 0 |

The adiabatic flame temperature was the same for all flame conditions.

frame from 0.5 ms and to propagate toward the burner exit. These repeated displacements of the flame explain why the probability values, indicating the probability for occurrence of the flame at a specific position, are small in the PDM images shown in Fig. 3IV.

Twelve pilot fuel injectors are arranged equidistantly at the circumference of the burner exit. Since the pilot fuel and co-airflow can achieve very limited mixing, the combustion occurs in a diffusion manner while interacting with the main flame. This pilot flame can be very useful to improve the LBO limit or flame stability close to the LBO conditions. Considerable effects on the flame structure were observed due to the addition of this pilot fuel. At

PFR = 3%, CFR = 0 setting, the pilot fuel intensified reactions at the ORZ, and the flame was found to be anchored attaching to the burner tip, which is consistent with the observation reported in a previous study of an older version of the burner [18]. However, the spread of the OH distribution at the ORZ was much higher and the flame attachment was much stronger in the previous burner [18] as compared to the current one. When adding the pilot fuel, the flame was also observed to be stabilized slightly downstream in the combustor as compared to the base case when neither pilot nor central fuel was added. In contrast, at the PFR = 3%, CFR = 2% setting, the stabilization of the flame moved upstream again for the additional injection of the central fuel (cf. Fig. 3(c) III/IV). The addition of central fuel enhances the CRZ, without affecting the ORZ, by increasing the fuel quantity or the local equivalence ratio in the central part of the fuel/air mixing profile upstream the main flame. For all cases with PFR = 3%, the enhancement of the ORZ was observed only in the lower part of the flame images. This effect is not related to the absorption of the laser along the beam path through the flame, which can be confirmed by the symmetric distribution of OH downstream. However, one reason could be an asymmetry in the flow distribution of the cooling air in the thin channels around the burner. It could create areas in which the local additional air would quench the neighboring pilot flames. This is more prominent when the PFR values are below 3%. Another reason could be the difference in the behavior of active pilots while the strength of the pilot flame varies over time with significantly low frequencies.

The PDMs of gradients indicate that for all cases, the flame front at the ISL fluctuates more in both axial and radial direction as compared to that at the OSL. Figure 5 presents the probability distributions of OH radicals along the radius at five different axial positions. The probability distributions also indicate that the ORZ is not symmetric at different axial positions. The axial distributions at $r/R < -0.75$ and $x/R < 0.45$ verify again the attachment of flame to the burner tip due to the addition of pilot fuel, while the radial distributions at $-1 < r/R < 1$ at different axial positions indicate that the flame moves downstream with pilot fuel injection and moves upstream with central fuel addition.

In Fig. 6, time-averaged OH chemiluminescence images, indicating the shape and position of flame, confirm the flame again to be stabilized downstream in comparison to the base case for adding 3% pilot fuel, while it moves upstream for an additional injection of 2% central fuel.

Effect of Load Variation. Figure 7 presents the effects of load variations on the NG/air flame structure. Comparison of the OH distribution at two conditions, part load and base load at PFR = 3%, CFR = 2%, indicates that the CRZ became more intense and compact for increasing the load. With increased load, keeping ϕ constant, the turbulence level and turbulent flame speed increase with the Reynolds number. The observed movement of the CRZ toward the burner exit at the base load condition indicates an increase in flame speed. At the base load, the ORZ also

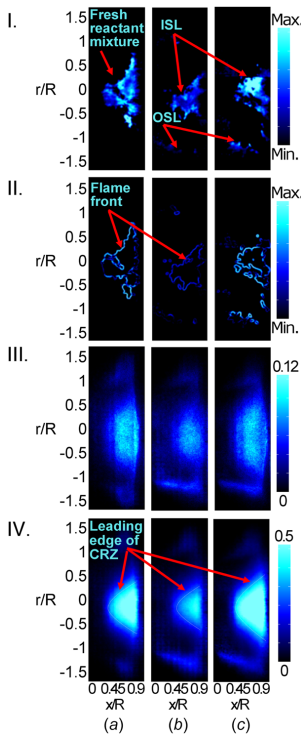


Fig. 3 OH-PLIF results of NG/air flame at base load conditions with three CFR and PFR settings: (a) PFR = 0, CFR = 0, (b) PFR = 3%, CFR = 0, and (c) PFR = 3%, CFR = 2%. I. Single-shots of OH-PLIF; II. Gradients of OH; III. PDMs of OH gradient; IV. PDMs of single-shots.

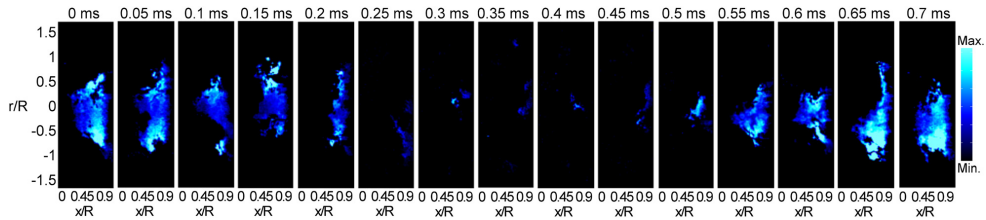


Fig. 4 The displacement of the flame is shown by OH distribution in time sequence. Base load with PFR = 0 and CFR = 0 setting.

became thinner (cf. Fig. 7(b) III) due to the faster burning rate of the pilot fuel while interacting with the relatively closer located main flame as compared to the part load case. Furthermore, the PDMs of gradients indicate that the flame front at the OSL fluctuates more in both axial and radial directions at the part load condition as compared to the base load. Like the base load case, the axial displacements of the flame including fluctuations were also observed for the part load case.

Similar to the PLIF images, time-averaged OH chemiluminescence images, shown in Fig. 8, indicate higher intensity for the flame at base load, which is attributed to a higher production rate of OH radicals from chain branching and chain propagation reactions [27]. The upstream stabilization of the base load flame is also observed in the chemiluminescence images.

Effect of H₂ Enrichment. Figure 9 presents the effects of changing fuel, from pure NG to pure H₂, on the flame structure at base load conditions with PFR=0 and CFR=0. For a pure H₂

case, the characteristics of the flame are significantly affected by the faster reaction rate, higher diffusivity, and higher burning velocity of H₂. Although the flame still follows the same stabilization mechanism as for pure NG, apparent differences are observed in the flame shape and anchoring position for the pure H₂ fuel. The higher reactivity and flame speed associated with H₂ cause the flame to be shorter and more compact. The single-shot and PDM images indicate the flame to be stabilized quite close to the burner exit. Despite that the OH signal at both the CRZ and ORZ was quite intense, the flame was not observed to be attached to the burner tip.

The PDMs of gradients suggest that the flame front at the ISL fluctuates significantly less in both axial and radial direction for pure H₂ flame as compared to the NG flame. Intensity fluctuations were also observed in the flame, which is shown in Fig. 10 by the variation of the OH signal intensity in a time sequence. Radial distributions of probability for OH at different axial positions for NG and H₂-enriched NG flames are shown in Fig. 11. It also verifies that the pure H₂ flame at PFR = 0 and CFR = 0 setting is stabilized by both CRZ and ORZ but is not attached to the burner tip.

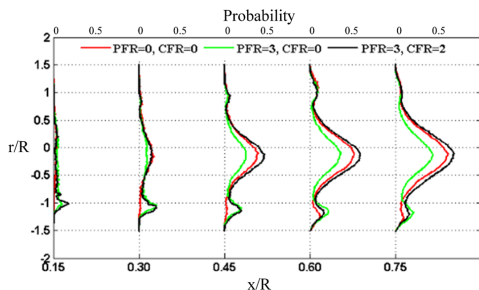


Fig. 5 Radial probability distributions of OH at five different axial positions obtained from OH-PLIF images for PFR = 0–3% and CFR = 0–2% settings

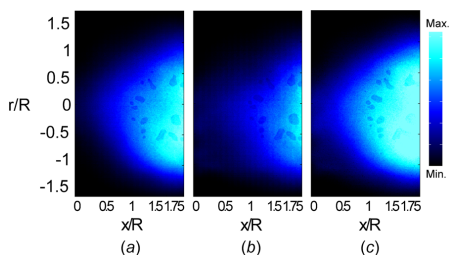


Fig. 6 Time-averaged OH chemiluminescence at three CFR and PFR settings: (a) PFR = 0, CFR = 0, (b) PFR = 3%, CFR = 0, and (c) PFR = 3%, CFR = 2% settings

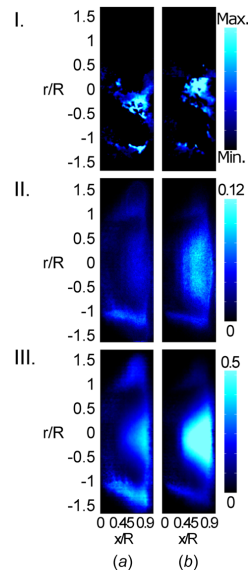


Fig. 7 OH-PLIF results of NG/air flame at different loads: (a) part load PFR = 3%, CFR = 2%, (b) base load PFR = 3%, CFR = 2%. I. Single-shots of OH-PLIF; II. PDMs of OH gradient; III. PDMs of single-shots.

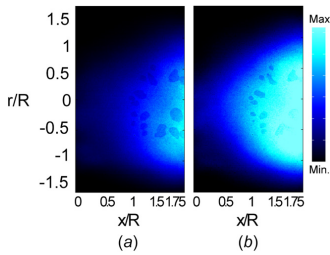


Fig. 8 Time-averaged OH chemiluminescence at different loads: (a) part load at PFR = 3%, CFR = 2% and (b) base load at PFR = 3%, CFR = 2%

The time-averaged OH chemiluminescence in Fig. 12 and single-shot OH-PLIF images in Fig. 9 show stronger OH* and OH LIF signal for the H₂ flame as compared to the NG flame, which is attributed to the higher production rate of OH for burning the more reactive H₂ fuel promoting radical formation via chain branching and chain propagation reactions [27]. The time-averaged OH chemiluminescence images also indicate that the H₂ flame is more compact and stabilized quite close to the burner exit.

At base load condition with PFR = 3% and CFR = 0 setting, the influence of H₂ enrichment (up to 80 vol %) on NG flame structure is shown in Fig. 13. The ORZ became stronger due to addition of pilot fuel and therefore, the flame was observed (cf. Fig. 10) to be anchored attaching to the burner tip. Besides the pilot fuel effects, the stabilization of the H₂-enriched NG flame followed the same mechanism as the pure H₂ flame. The flame became more compact and shorter as well as anchored closer to the burner exit with H₂ enrichment. The fact that a variety of flames (pure NG flames, H₂-enriched flames, and pure H₂ flames) could be stabilized in

this burner demonstrates the improvement and development in burner design toward fuel flexibility. In a previous study [17] with a similar burner at PFR = 0, CFR = 0, only NG flames enriched up to 80 vol % H₂ could be stabilized. Also, the flame at 80 vol % H₂ was stabilized with help of a flame attachment to the burner tip, which can cause unwanted increase of the burner surface temperature and, in worst cases, a triggering of an upstream flame propagation. Thus, the current burner design with no flame attachment to the burner tip (see Figs. 9 and 13) is more optimized for fuel flexibility operation than the one used in Ref. [17].

Flame Fluctuations. For all investigated cases, combustion fluctuations were revealed primarily by the sound of combustion and OH chemiluminescence. Proper orthogonal decomposition (POD), a statistical method, was employed on high-speed OH chemiluminescence data to study the flame dynamics. In addition to the mean field, information about the most energetic modes of flame dynamics can be acquired by employing this method [28]. POD is a procedure to decompose a given ensemble of data G (two-dimensional arrays in the present case) into a set of eigenfunctions. The details of this statistical method are not described here, but the outcome of this procedure is a certain number of orthogonal spatial eigenfunctions or modes $\Psi_i(x)$ and time coefficient $e_i(t)$ so that any snapshot $G(x,t)$ taken at a time (t) can be reconstructed with a certain number of modes M according to Eq. (1).

$$G^N(x,t) = e_0\Psi_0(x) + \sum_{i=1}^M e_i\Psi_i(x) \quad (1)$$

Here, Ψ_0 or mode 0 represents the mean field. Subsequent modes represent fluctuation and thus the dynamics. In this method, modes are a linear combination of the snapshots, and the time coefficients can be computed projecting the modes onto snapshots according to Eq. (2)

$$e_j(t) = \Psi_j(x) \times G(x,t) \quad (2)$$

For further details on the theoretical background and on the implementation, the reader is referred to Refs. [29–32].

Proper orthogonal decomposition analysis revealed significant influences on the flame dynamics for changing the load and fuel, but not for adding pilot or central fuel. The energy content distributions of different modes at three conditions: (a) part load (NG) case, (b) base load (NG) case, and (c) base load (H₂) case are shown in Fig. 14 when neither pilot nor central fuel was added. Two dominant modes (first and second) contain about 29%, 30%, and 23% of the total fluctuating variance for the part load (NG), base load (NG), and base load (H₂) cases, respectively. Figure 15 presents modes 0–2 for the three cases, where mode 0 is representing the mean field while subsequent modes represent fluctuations to be added on top of it. The energy content of modes 1 and 2 is almost one order of magnitude larger than the energy of subsequent modes. The scale and sign of the contour plots are arbitrary as the modes are to be multiplied by the time coefficient. Mode 1 contains the axial fluctuation, while mode 2 indicates the rotational movement for the part load (NG) case. For the base load (NG) case, both modes contain axial and rotational movement. Finally, for the base load (H₂) case, mode 1 represents axial fluctuation while mode 2 presents rotational movement.

As the time resolution of acquired data is high enough to capture the evolution of the time coefficients, FFT was performed on time coefficients, $e_1(t)$ and $e_2(t)$, of mode 1 and 2 for the three cases to reveal the frequencies of the modes' oscillations. For every case, both modes were found to oscillate with the same frequencies and therefore, only the frequency spectrum of mode 1 from each of the cases is considered for discussion. The frequency spectrum is plotted in Fig. 16 where frequency is expressed as Strouhal number (St), based on the reference velocity through the burner and the mixing tube diameter. In addition, the spectral

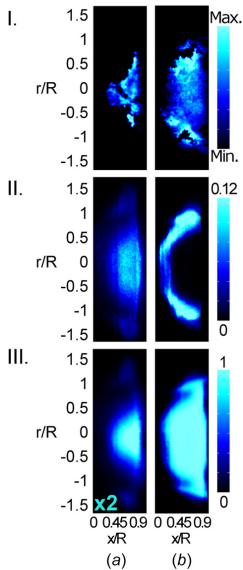


Fig. 9 OH-PLIF results of (a) NG/air and (b) H₂/air flame at base load with PFR = 0 and CFR = 0. I. Single-shots of OH-PLIF; II. PDMs of OH gradient; III. PDMs of single-shots.

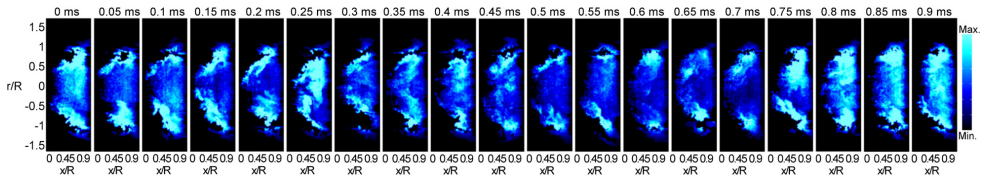


Fig. 10 The intensity fluctuation of the H₂ flame is shown by OH distribution in time sequence. Base load (H₂) case with PFR = 0 and CFR = 0.

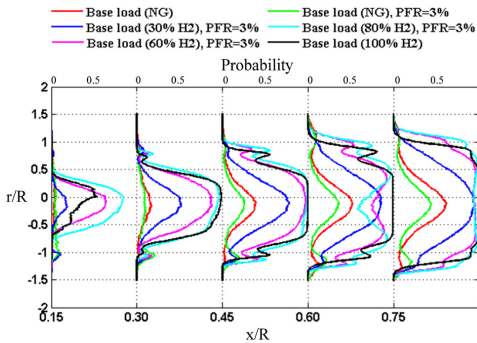


Fig. 11 Radial probability distributions of OH at five different axial positions obtained from OH-PLIF images for NG and H₂-enriched NG flame at base load

intensity is normalized by the maximum intensity value for the base load (NG) case.

For all cases, the frequency band is located at $0.1 < St < 0.2$. A previous study [22] in a similar burner showed the domination of acoustic oscillations in this band of frequencies, which was revealed by the high power spectrum density of the pressure fluctuations. Furthermore, the current study shows that the frequency of instabilities varies with the load and fuel changes. For the part load (NG) case, the axial mode dominates (cf. Fig. 15) over the rotational one and the spectral intensity is the maximum. For increasing the load, the rotational mode dominates, and the peak shifts toward a higher frequency with lower intensity. Combustion of H₂ further enhances the axial mode resulting in the highest frequency with the lowest intensity, which is consistent with the results found in the previous study [17]. The increase in frequency is related to the increase of local temperature which is attributed to higher heat release caused by the higher flame speed. With the temperature increase, the sound speed and by this, the eigenfrequencies of the combustion chamber increase.

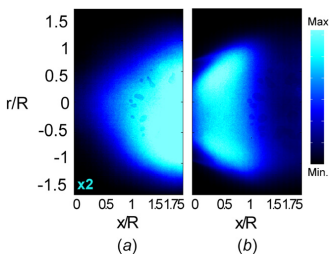


Fig. 12 Time-averaged OH chemiluminescence of (a) NG/air and (b) H₂/air flame at base load with PFR = 0 and CFR = 0

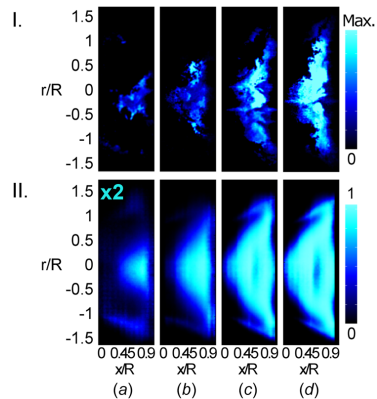


Fig. 13 OH-PLIF results of (a) NG/air, (b) 30 vol%, (c) 60 vol%, and (d) 80 vol% H₂ enriched NG flame at base load with PFR = 3%, CFR = 0 setting. I. Single-shots of OH-PLIF; II. PDMs of single-shots.

Emissions. The effects of load variations, pilot, and central fuel addition, and H₂ enrichment on NO_x production are shown in Fig. 17, even though it is not the main objective of the current study. The values for the NO_x are normalized by the value of NO_{x(0)} at base load (NG) case. For H₂ enrichment of the fuel mixture from 0 to 100 vol %, an increase in NO_x production was observed, which is attributed to the increase in local flame temperature and the size of the postflame zone. By H₂ enrichment, the flame becomes more compact and intense due to the increase in flame speed and consequently, the local flame temperature and the size of the postflame zone increase. Higher temperatures and longer residence time in an extended hot postflame zone promote formation of thermal NO_x. Similar results were also observed previously [17]. For all the base load cases using NG and H₂, it may be seen that the upstream flame position increases NO_x, either it is

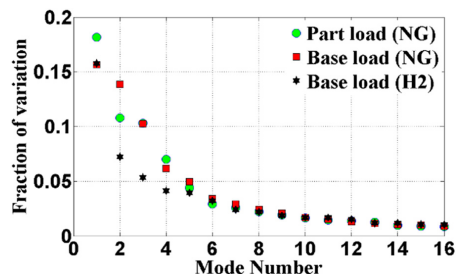


Fig. 14 POD variance distributions of modes 1–16

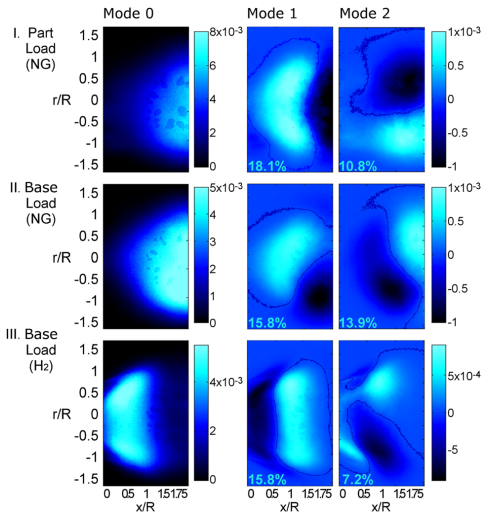


Fig. 15 Mode 0–2 are shown for three cases: I. Part load (NG), II. base load (NG), and III. base load (H₂) with contour plot of the intensity signal

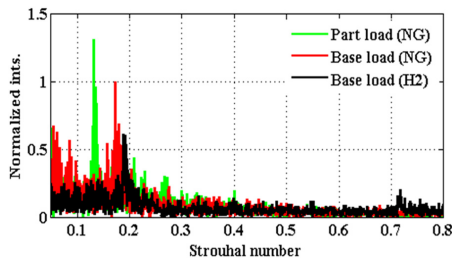


Fig. 16 Intensity versus Strouhal number for three cases: I. part load (NG), II. base load (NG), and III. base load (H₂)

due to CFR or H₂ content. In addition, for the part load (NG) condition, NO_x increased somewhat compared to the base load (NG) using the same PFR and CFR setting that may be due to the slightly higher residence time. In an engine, the reduced pressure

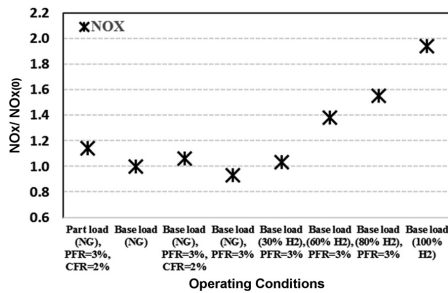


Fig. 17 Relative change in NO_x at different operating conditions

for part load acts to reduce NO_x, which is not captured in an atmospheric rig.

Conclusion

The effects of load and fuel variations on flame structure were investigated in a Siemens standard third generation DLE burner under atmospheric pressure conditions. High-speed kHz OH-PLIF and OH chemiluminescence imaging were employed to study the flame. Temporally resolved investigations of the flame structure revealed insights regarding the flame stabilization and dynamics.

The main flame was observed to be stabilized creating a CRZ. Addition of pilot fuel affected the ORZ significantly by strengthening the reaction process and therefore, the flame was found to be attached to the burner tip. When fuel was added at the central injector, the flame moved upstream without affecting the ORZ. For changing the load from part to base, the CRZ became stronger and more compact. The flame was stabilized close to the burner exit.

The higher reactivity and higher flame speed associated with H₂ affect the flame structure significantly. For H₂ enrichment in NG or replacing pure NG fuel with pure H₂, the CRZ that anchored the flame moved quite close to the burner exit. Without pilot fuel, even though the CRZ and ORZ became quite intense, the flame was not stabilized attaching to burner tip, whereas this attachment of the flame was observed for the pilot fuel addition.

The flame dynamics were affected by the variation of load and fuel type but not by the addition of pilot and central fuel. Application of the proper orthogonal decomposition reveals that the frequency of instability shifts toward higher values with decreasing spectral intensity for increasing the load part to base using NG and substituting fuel from NG to H₂.

In addition, an increase in NO_x was observed with enrichment of H₂ in the fuel mixture while a small change in NO_x was found for addition of pilot or central fuel as well as between part and base load.

Acknowledgment

This research was funded by the Swedish Energy Agency and by Siemens Industrial Turbomachinery AB, within the Centre of Competence in Combustion Science and Technology (KC-CECOST). The authors gratefully acknowledge the work of Arne Irewall and Peter Magnusson at Siemens for the maintenance and operation of the test rig.

Funding Data

- Swedish Energy Agency (Funder ID: 10.13039/501100004527).

Permission for Use Statement

The content of this paper is copyrighted by Siemens Industrial Turbomachinery AB and is licensed to ASME for publication and distribution only. Any inquiries regarding permission to use the content of this paper, in whole or in part, for any purpose must be addressed to Siemens Industrial Turbomachinery AB directly.

Nomenclature

- AFR = air-to-fuel ratio
- CFR = central fuel to total fuel ratio
- CMOS = complementary metal oxide semiconductor
- CRZ = central recirculation zone
- DLE = dry low emission
- f = focal length
- FFT = fast Fourier transform
- H₂ = hydrogen
- HC = hydrocarbon
- ISL = inner shear layer

K = kelvin
 LBO = lean blowout
 MW = megawatts
 NG = natural gas
 NO_x = NO and NO₂ (nitric oxide and nitrogen dioxide)
 OH = hydroxyl
 ORZ = outer recirculation zone
 OSL = outer shear layer
 PDM = probability density map
 PFR = pilot fuel to total fuel ratio
 PLIF = planar laser-induced fluorescence
 POD = proper orthogonal decomposition
 R = burner exit inner radius
 SGT = Siemens gas turbine
 St = Strouhal number
 UV = ultraviolet
 φ = equivalence ratio

References

- [1] Warnatz, J., Maas, P.-D., and Dibble, R. W., 1996, *Formation of Nitric Oxides Combustion*, Springer, Berlin, pp. 219–236.
- [2] Michaud, M. G., Westmoreland, P. R., and Feitelberg, A. S., 1992, "Chemical Mechanisms of NO_x Formation for Gas Turbine Conditions," *Symp. (Int.) Combust.*, **24**(1), pp. 879–887.
- [3] Liewen, T. C., and Yang, V., 2005, *Combustion Instabilities in Gas Turbine Engines: Operational Experience, Fundamental Mechanisms, and Modeling*, American Institute of Astronautics and Aeronautics, Reston, VA.
- [4] Gussak, L. A., Ryabikov, O. B., Politenkova, G. G., and Furman, G. A., 1973, "Effect of Adding Individual Combustion Products on Combustion of Methane—Air Mixture," *Bull. Acad. Sci. USSR, Div. Chem. Sci.*, **22**(9), pp. 2128–2128.
- [5] Lefebvre, A. H., 2010, *Gas Turbine Combustion: Alternative Fuels and Emissions*, CRC Press, Boca Raton, FL.
- [6] Kreutz, T., Williams, R., Socolow, R., Chiesa, P., and Lozza, G., 2003, "Production of Hydrogen and Electricity From Coal With CO₂ Capture," *Greenhouse Gas Control Technologies-Sixth International Conference*, Kyoto, Japan, Oct. 1–4, pp. 141–147.
- [7] Gazzani, M., Chiesa, P., Martelli, E., Sigali, S., and Brunetti, I., 2014, "Using Hydrogen as Gas Turbine Fuel: Premixed Versus Diffusive Flame Combustors," *ASME J. Eng. Gas Turbines Power*, **136**(5), p. 051504.
- [8] Schefer, R. W., Wicksall, D., and Agrawal, A., 2002, "Combustion of Hydrogen-Enriched Methane in a Lean Premixed Swirl-Stabilized Burner," *Proc. Combust. Inst.*, **29**(1), pp. 843–851.
- [9] Dong, C., Zhou, Q., Zhang, X., Zhao, Q., Xu, T., and Hui, S., 2010, "Experimental Study on the Laminar Flame Speed of Hydrogen/Natural Gas/Air Mixtures," *Front. Chem. Eng. China*, **4**(4), pp. 417–422.
- [10] Brower, M., Petersen, E. L., Metcalfe, W., Curran, H. J., Füre, M., Bourque, G., Aluri, N., and Güthe, F., 2013, "Ignition Delay Time and Laminar Flame Speed Calculations for Natural Gas/Hydrogen Blends at Elevated Pressures," *ASME J. Eng. Gas Turbines Power*, **135**(2), p. 021504.
- [11] Venkateswaran, P., Marshall, A. D., Seitzman, J. M., and Liewen, T. C., 2014, "Turbulent Consumption Speeds of High Hydrogen Content Fuels From 1–20 Atm," *ASME J. Eng. Gas Turbines Power*, **136**(1), p. 011504.
- [12] Guiberti, T. F., Durox, D., Scoulaire, P., and Schuller, T., 2015, "Impact of Heat Loss and Hydrogen Enrichment on the Shape of Confined Swirling Flames," *Proc. Combust. Inst.*, **35**(2), pp. 1385–1392.
- [13] Griebel, P., Boschek, E., and Jansohn, P., 2007, "Lean Blowout Limits and NO_x Emissions of Turbulent, Lean Premixed, Hydrogen-Enriched Methane/Air Flames at High Pressure," *ASME J. Eng. Gas Turbines Power*, **129**(2), pp. 404–410.
- [14] Hawkes, E. R., and Chen, J. H., 2004, "Direct Numerical Simulation of Hydrogen-Enriched Lean Premixed Methane-Air Flames," *Combust. Flame*, **138**(3), pp. 242–258.
- [15] Lam, K.-K., and Parsania, N., 2016, "Hydrogen Enriched Combustion Testing of Siemens SGT-400 at High Pressure Conditions," *ASME Paper No. GT2016-57470*.
- [16] Döbbeling, K., Hellat, J., and Koch, H., 2005, "25 Years of BBC/ABB/ALSTOM Lean Premix Combustion Technologies," *ASME Paper No. GT2005-68269*.
- [17] Lantz, A., Collin, R., Aldén, M., Lindholm, A., Larfeldt, J., and Lörstäd, D., 2015, "Investigation of Hydrogen Enriched Natural Gas Flames in a SGT-700/800 Burner Using OH PLIF and Chemiluminescence Imaging," *ASME J. Eng. Gas Turbines Power*, **137**(3), p. 031505.
- [18] Lörstäd, D., Lindholm, A., Barhaghi, D. G., Bonaldo, A., Fedina, E., and Fureby, C., 2012, "Measurements and LES of a SGT-800 Burner in a Combustion Rig," *ASME Paper No. GT2012-69936*.
- [19] Lörstäd, D., Lindholm, A., Pettersson, J., Björkman, M., and Hultmark, I., "Siemens SGT-800 Industrial Gas Turbine Enhanced to 50MW: Combustor Design Modifications, Validation and Operation Experience," *ASME Paper No. GT2013-95478*.
- [20] Moëll, D., Lörstäd, D., and Bai, X.-S., 2016, "Numerical Investigation of Methane/Hydrogen/Air Partially Premixed Flames in the SGT-800 Burner Fitted to a Combustion Rig," *Flow, Turbul. Combust.*, **96**(4), pp. 987–1003.
- [21] Lörstäd, D., Lindholm, A., Alin, N., Fureby, C., Lantz, A., and Collin, R., 2010, "Experimental and LES Investigation of a SGT-800 Burner in a Combustion Rig," *ASME Paper No. GT2010-22688*.
- [22] Moëll, D., Lantz, A., Bengtson, K., Lörstäd, D., Lindholm, A., and Bai, X.-S., 2019, "Large Eddy Simulation and Experimental Analysis of Combustion Dynamics in a Gas Turbine Burner," *ASME J. Eng. Gas Turbines Power*, **141**(7), p. 071015.
- [23] Bechtel, J., and Teets, R., 1979, "Hydroxyl and Its Concentration Profile in Methane-Air Flames," *Appl. Opt.*, **18**(24), pp. 4138–4144.
- [24] Sadanandan, R., Stöhr, M., and Meier, W., 2008, "Simultaneous OH-PLIF and PIV Measurements in a Gas Turbine Model Combustor," *Appl. Phys. B Lasers Opt.*, **90**(3–4), pp. 609–618.
- [25] Donbar, J. M., Driscoll, J. F., and Carter, C. D., 2000, "Reaction Zone Structure in Turbulent Nonpremixed Jet Flames—From CH-OH PLIF Images," *Combust. Flame*, **122**(1–2), pp. 1–19.
- [26] Hellat, J., and Koch, H., 2007, "25 Years of BBC/ABB/Alstom Lean Premix Combustion Technologies," *ASME J. Eng. Gas Turbines Power*, **129**(1), pp. 2–12.
- [27] Coffee, T. P., 1984, "Kinetic Mechanisms for Premixed, Laminar, Steady State Methane/Air Flames," *Combust. Flame*, **55**(2), pp. 161–170.
- [28] Iudiciani, P., Duwig, C., Hussein, S. M., Szasz, R. Z., Fuchs, L., and Gutmark, E. J., 2012, "Proper Orthogonal Decomposition for Experimental Investigation of Flame Instabilities," *AIAA J.*, **50**(9), pp. 1843–1854.
- [29] Berkooz, G., Holmes, P., and Lumley, J. L., 1993, "The Proper Orthogonal Decomposition in the Analysis of Turbulent Flows," *Annu. Rev. Fluid Mech.*, **25**(1), pp. 539–575.
- [30] Smith, T. R., Moehlis, J., and Holmes, P., 2005, "Low-Dimensional Modelling of Turbulence Using the Proper Orthogonal Decomposition: A Tutorial," *Nonlinear Dyn.*, **41**(1–3), pp. 275–307.
- [31] Duwig, C., and Iudiciani, P., 2010, "Extended Proper Orthogonal Decomposition for Analysis of Unsteady Flames," *Flow, Turbulence Combust.*, **84**(1), pp. 25–47.
- [32] Weinberg, F. J., 1986, *Advanced Combustion Methods*, Imperial College of Science and Technology, London, UK.

Paper II



Fiber-based stray light suppression in spectroscopy using periodic shadowing

MIAOXIN GONG,¹ HAISOL KIM,¹  JIM LARSSON,¹ TORSTEN METHLING,¹ MARCUS ALDÉN,¹  ELIAS KRISTENSSON,¹ CHRISTIAN BRACKMANN,¹  TINA ESCHRICH,² MATTHIAS JÄGER,² WOLFGANG KIEFER,^{3,4} AND ANDREAS EHN^{1,*}

¹Division of Combustion Physics, Lund University, Box 118, Lund SE-22100, Sweden

²Leibniz Institute of Photonic Technology, Albert Einstein St. 9, 07745 Jena, Germany

³Institute for Physical and Theoretical Chemistry, University of Würzburg, 97074 Würzburg, Germany

⁴Eisingen Laboratory for Applied Raman Spectroscopy, 97249 Eisingen, Germany

*andreas.ehn@forbrf.lth.se

Abstract: Stray light is a known strong interference in spectroscopic measurements. Photons from high-intensity signals that are scattered inside the spectrometer, or photons that enter the detector through unintended ways, will be added to the spectrum as an interference signal. A general experimental solution to this problem is presented here by introducing a customized fiber for signal collection. The fiber-mount to the spectrometer consists of a periodically arranged fiber array that, combined with lock-in analysis of the data, is capable of suppressing stray light for improved spectroscopy. The method, which is referred to as fiber-based periodic shadowing, was applied to Raman spectroscopy in combustion. The fiber-based stray-light suppression method is implemented in an experimental setup with a high-power high-repetition-rate laser system used for Raman measurements in different room-temperature gas mixtures and a premixed flame. It is shown that the stray-light level is reduced by up to a factor of 80. Weak spectral lines can be distinguished, and therefore better molecular species identification, as well as concentration and temperature evaluation, were performed. The results show that the method is feasible and efficient in practical use and that it can be employed as a general tool for improving spectroscopic accuracy.

© 2021 Optical Society of America under the terms of the [OSA Open Access Publishing Agreement](#)

1. Introduction

Laser-based spectroscopic methods have a wide range of applications in a number of research fields, including fundamental physics, astronomy [1, 2], biomedicine [3–5], materials science [5], combustion science [6], plasma research [7], etc. Among modern optical instruments, fibers have been employed in a variety of spectroscopic applications with several advantages [8]. Fiber-based sampling systems allow the sample to be analyzed remotely from the optical instrumentation, which is especially useful in investigating hostile environments. The chemically reactive flows in combustion with high temperatures and intense heat transfer, for example, result in harsh experimental conditions. Laser-based spectroscopic methods are beneficial tools to investigate such phenomena in-situ and non-intrusively with high accuracy [9].

Stray light in a spectrometer system can be described as light that deviates from the intended path and distorts the spectral characteristics of the detected light [10–12]. Stray light originates from various sources, for example, surface imperfections of the optical components and particles or droplets in the optical path [13]. Stray light can be a severe problem in spectral analysis of signals, especially when the spectral shift from the laser wavelength is small and the signal of interest is weak. Moreover, stray light presents a general experimental challenge for in-situ diagnostics of processes, e.g., for measurements in reactors and/or in the vicinity of surfaces.

Therefore, it is often necessary to eliminate or correct the signal for stray light in the spectroscopic measurements, especially when quantitative analysis is desired. Optical filters provide the traditional solution to suppress background light in a certain wavelength range, such as the spectral width of a laser line, that enters the spectrometer, see for example [14]. In addition to filters based on conventional optical materials, vapor of strongly absorbing atomic species, such as K, Hg, I, Rb, or Na, have been employed as efficient and spectrally narrow filters [15–21]. Another optical solution is provided by double or triple monochromators for stray light reduction [10, 22–24]. Yet, such a method results in the loss of collected light, detrimental for the detection of low signals, and also prevents multiplex spectroscopic measurements as the monochromator requires scanning for registration of a spectrum. In some cases, computer-assisted stray-light correction approaches are feasible, and a method based on analysis of spectrum derivatives is mostly used [25, 26]. However, the ability to remove stray light using the derivative approach is dependent on that the gradients of the stray-light signal and the signal of interest are different, which generally cannot be assumed.

A general experimental solution to the stray-light problem in spectroscopy, referred to as Periodic Shadowing (PS), was presented by Kristensson et al. [27]. The PS concept is the combination of the analog implementation of a periodic pattern onto the signal before reaching the detector, inspired by Structured Illumination Microscopy [28], and the following data processing based on lock-in analysis [29]. The concept was successfully demonstrated for stray-light suppression in a wide range of spectroscopic techniques based on emission, absorption, scattering, and nonlinear coherent optical processes. The experiments were done with optics arranged for open-space collection of light and a transmission grating mounted on the spectrometer entrance slit. The latter is a fundamental part of the PS concept in order to imprint a periodic pattern on the collected signal, which is necessary for further processing. Since the PS concept in this first version proved to be a highly versatile and powerful method for stray-light suppression, a natural next step is to increase its feasibility, strength, and robustness in spectroscopic applications. In this paper, we, therefore, present a novel fiber-based stray-light suppression method based on the PS concept. The fiber-based PS method is implemented with a custom-made array of optical fibers, which enables flexible signal collection combined with stray-light suppression by means of the PS method. The experimental arrangement employs the PS-fiber to deliver the signal light and create the periodic pattern, which is needed for further data processing. A schematic description of the major issues and their corresponding solutions that are addressed in this work is shown in Fig. 1.

The new method is demonstrated with Raman spectroscopy, based on inelastic scattering of laser photons, which is a commonly employed technique for the detection of chemical species in analyses of solid, liquid, and gaseous samples [30]. However, the inherent weakness of the signals from the inelastic scattering makes Raman spectroscopy in the gas phase challenging. Raman spectroscopy is a linear process where more incident photons enhance the signal, and thus a laser of high average power can be used to compensate for weak signals, but then also increases potential interference from stray light. Raman spectroscopy in studies of combustion processes necessitates the detection of species in a gas-phase environment with high background luminosity. While pulsed lasers and gated detection allow for the rejection of continuous background signals, combustion diagnostics nevertheless represents an experimental challenge for Raman spectroscopy. Great care must be taken to distinguish Raman signals from stray light of the laser source and strong Rayleigh and Mie scattering signals, as well as other types of interfering signal contributions [31,32]. The fiber-based PS method has thus been investigated under such conditions by measurements in gases at ambient conditions and in premixed flames. The method has been characterized for suppression of different stray-light levels, and evaluated O₂ mole fractions and temperatures have been assessed to ensure that accurate quantitative information is retrieved from spectra after processing.

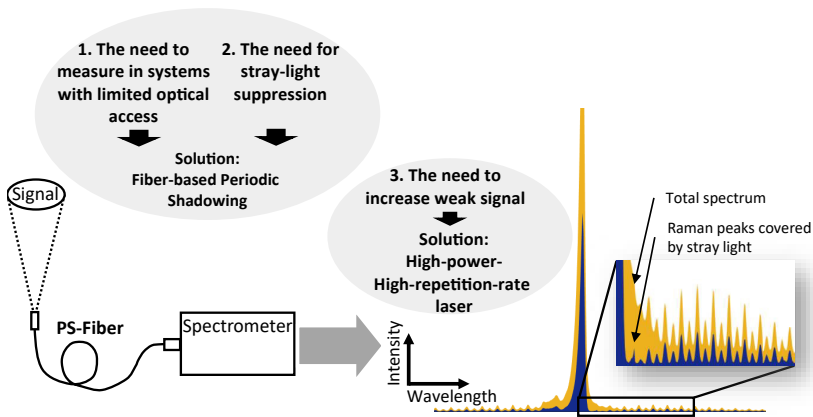


Fig. 1. Schematic diagram illustrating the main challenges and the solutions used in this paper. The experimental arrangement contains the PS-fiber employed to deliver signal light. The spectrum is a typical vibrational Raman spectrum of nitrogen, where the yellow area is the total spectrum, and the blue area is the Raman signal components after rejecting interfering stray light using periodic shadowing.

2. Method

2.1. Fiber based periodic shadowing

The predefined pattern was in the previous study created by a transmissive Ronchi grating placed at the entrance slit of the spectrometer [27], which blocks 50% of the incoming light. Here, as shown in Fig. 2(a), a specialized fiber-optic bundle is used instead. The transmitted light through the Ronchi grating has the modulation of a square wave which is very close to what is achieved with the fiber, as is shown in Fig. 2(b).

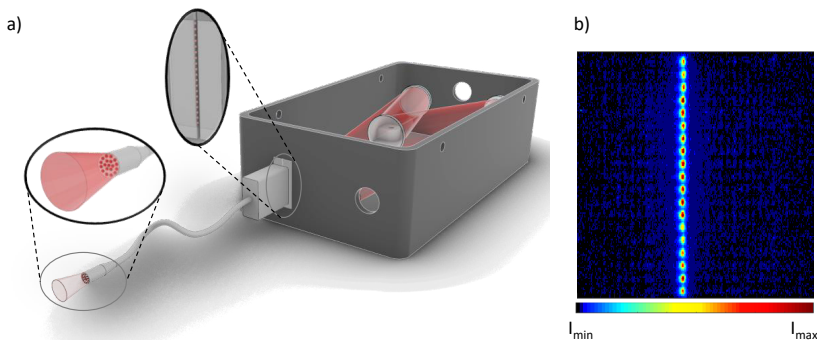


Fig. 2. a) Schematic view of the experimental arrangement. The PS-fiber bundle collects signal light and modulates it into the predefined pattern. b) Unprocessed PS spectrum of vibrational Raman signal of nitrogen at 2331 cm^{-1} in which the predefined pattern of periodic feature can be observed.

The customized silicon fiber manufactured for the PS method is shown in Fig. 3.

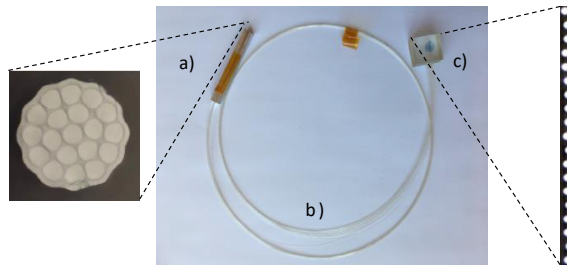


Fig. 3. Illustration and photographs of the custom-made PS fiber. a) and c) show the input end and the output end of the PS fiber with sectional views, respectively. b) shows the extension of the fiber bundle.

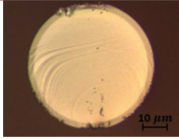
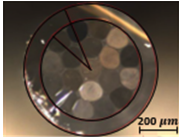
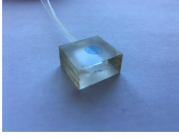
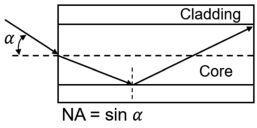
Each PS fiber bundle contains 19 individual and identical multimode fibers, which are arranged into a circular arrangement at the input end and a linear array at the output end. For this purpose, the coatings of the fibers have been stripped on both sides, but the light-guiding in each of the F300 pure silica cores is still provided by the thin fluorine-doped cladding with a numerical aperture of 0.22 (see Table 1 for additional fiber details). The fiber itself has been manufactured at the Leibniz IPHT with the exception of the fluorine-doped cladding (deposited at the Heraeus Comvance company). The round fiber bundle has been inserted into an F300 silica capillary, and the arrangement has been fused together using a Vytran GPX 3200 glass processing machine by applying a vacuum and only gave minor changes in the fiber dimensions. The bundle was finally cleaved to obtain the input facet.

On the output side, the fibers have been arranged in a linear periodic fashion: each active fiber (guidance fiber) is separated by a short piece of identical ‘dead’ fiber (distance fiber) in which no light is transmitted so that a unique pattern with a fixed spatial frequency is created when light is inserted into the input end. The results of such an arrangement, as the fiber is mounted onto the slit, is a periodic pattern that is close to a square wave modulation. Care has been taken to place the central input fiber in the middle of the linear output side. Towards each end of the linear arrangement follow three of the six fibers from the inner input ring and finally the fibers of the outer ring. The individual fibers are bonded using epoxy between two BK7 glass blocks with 130 μm separation. The output facet was obtained by polishing.

The PS fiber transmits the light and forms a predefined spatial modulation pattern at the same time. The introduction of the fiber, in principle, improves the transmission efficiency as it avoids the 50% blockage of light at the slit encountered when using Ronchi gratings. Fiber optics also simplifies the alignment and allows more flexibility in the optical system [8]. In many experiments where optical access is exceedingly limited (e.g., in combustion engines), fiber optics serve as a probe to such environments. The parameters in Table 1 show the dimensions of the optical fibers, which should be related to the spectrometer. The round fiber configuration at the input end assures that the fiber bundle maintains the same numerical aperture (NA) as the individual fibers. In addition, the coupling of the light into the multimode fiber has a considerable effect on its performance. In order to fully utilize the collected signal, the NA of the input light cone has to be less than that of the fiber, i.e., underfilling the fiber.

When the camera registers the light after dispersion, a 2D spectral image is captured that can be further processed in the stray-light removal lock-in algorithm, shown in Fig. 4. Modulated raw input data and the post-processed output data are shown in Fig. 4(i) and 4ii, respectively. The three necessary processing steps, along with a graphical description of the filter function that

Table 1. Important parameters of the PS fiber.

| | Approximate dimensions | Photograph |
|---------------------------------------|-----------------------------------------------------------------------------------------------------------------------|------------------------------------------------------------------------------------|
| Each individual fiber | Fiber core diameter: 114 μm Cladding diameter: 126 μm Coating diameter: 230 μm |  |
| The input end of the PS fiber bundle | Outer diameter: ~ 1610 μm Inner diameter: ~ 1294 μm |  |
| The output end of the PS fiber bundle | LWH of the glass holder: 2.0 × 1.0 × 0.5 cm |  |
| Numerical Aperture (NA) | 0.22 ± 0.02 |  |

is used in the process, is displayed in Fig. 4(a)-(d). The processing of the modulated image is described in detail by Kristensson et al. [27]. In summary, the signal-processing algorithm is carried out by first using fast Fourier transform (FFT) on the modulated spectral image (Fig. 3(i)) column by column, providing a stack of 1D Fourier transforms (Fig. 3(a)). Each column is then multiplied with two reference signals with a 90° relative phase shift, transforming the periodic component into a DC component. This operation will cause the stray light, which originally is a DC component, to shift into higher frequencies, which is shown in the close-up inset in Fig. 3(b). After applying the band-pass filter, shown in Fig. 3(c), the non-modulated stray-light component can be removed, as shown in Fig. 3(d). The final spectrum, with minimal stray light interference, displayed in Fig. 3(ii), is finally obtained by an inverse Fourier transform.

The input data in the periodic shadowing algorithm has to have a periodic modulation, ideally sinusoidal, in order for this demodulation scheme to work. A modulation that deviates from a sinusoidal modulation will have overtone components in its Fourier transform. Such overtones will simply be disregarded in the periodic shadowing processing and will thus not cause any implication for the method except that the signal contribution in these overtones will be lost. These overtones are really small with this fiber arrangement, which is seen in Fig. 4(a) where they are barely visible.

2.2. Raman spectroscopy

An Nd:YAG laser (HD40I-OE, Edgewave, 100 W), operating at 5 kHz with pulses of ~12 ns duration, was used to perform Raman spectroscopy in this investigation. The laser delivered an average power of 25 W, which is 25% of the maximum power, at a wavelength of 532 nm.

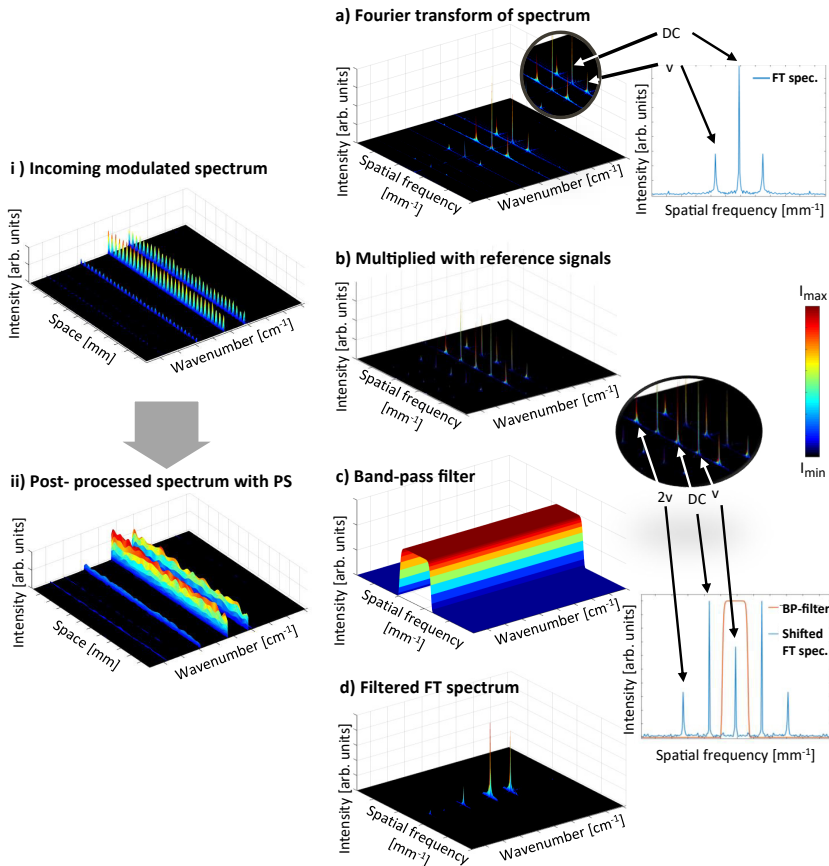


Fig. 4. Data processing of the Periodic shadowing method. i) and ii) illustrate the spectra before and after the PS process, respectively. a)-d). a) Fourier transform of the spectrum; b) multiplication with reference signals to place the fundamental peak at the origin and the DC component to $\pm v$ in the spatial frequency domain; c) application of a band-pass filter to extract the information of the modulation while filtering out components with high spatial frequencies; d) Fourier transformed spectrum after filtering.

A schematic experimental setup is shown in Fig. 5. A multi-pass arrangement, displayed in Ref. [33], was used to increase the laser irradiance in the measurement volume and enhance the Raman signal. The multi-pass optics included a lens (L1) with focal length $f=300$ mm and a cavity with a pair of dichroic multi-pass mirrors (MP) with focal length $f=100$ mm and radius $r=50$ mm. The laser beam was guided into the cavity through a hole on the edge of the first multi-pass mirror and focused at the center of the cavity by the lens. The laser beam was then reflected back and forth between the multi-pass mirrors 32 times, with focal points located at the center of the cavity. This resulted in a probe volume with dimensions of approximately $5 \times 2 \times 1$ mm³.

The Raman scattering signal was collected by a set of two achromatic lenses (L2 and L3) with a focal length of 200 mm each. In addition, a concave aluminum mirror (M4) with a focal length

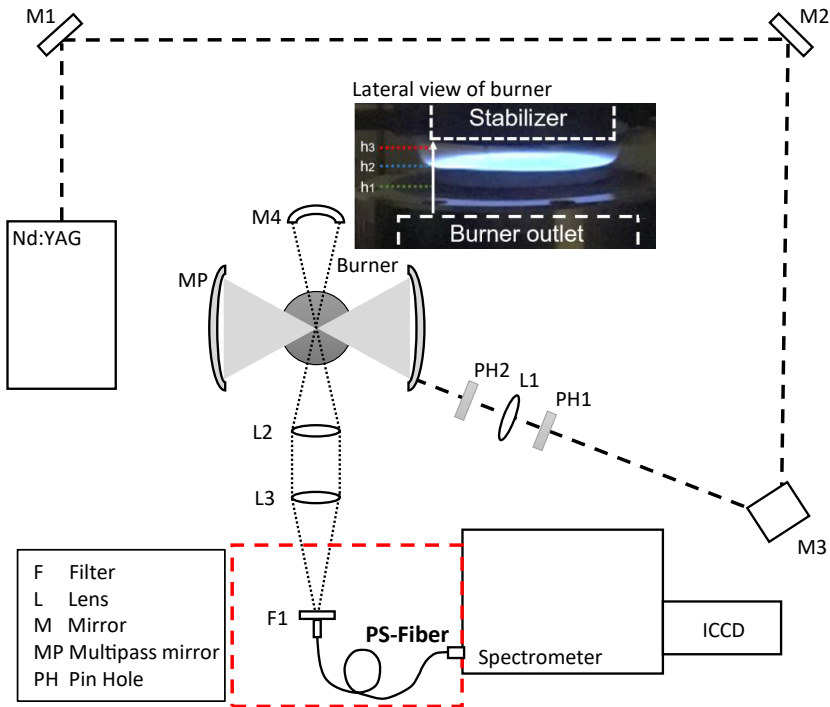


Fig. 5. Schematic of the experimental setup with a 532 nm laser beam employed to measure Raman scattering signals in a porous-plug burner. The burner can be adjusted in the vertical direction for measurements at different heights in the flame. The dashed red box marks out the insertion of the PS fiber in the setup.

of 150 mm was placed on the other side of the spectrometer to reflect signal scattered in this direction back towards the spectrometer, which theoretically increases the signal by a factor of 2. The collected Raman signal was focused onto the input end of the PS fiber, transmitted through the fiber bundle, and formed the PS modulation at the output end, placed at the entrance slit of the spectrometer. The transmitted signal was guided into the spectrometer (Princeton Instruments IsoPlane SCT 320) after a long-pass filter (F1, Semrock EdgeBasic BLP01-532R-25), which reduces light at the laser wavelength. The f-number of the collecting lenses, $f/4$, is selected to approximately match that of the spectrometer, $f/4.6$. However, this slight mismatch will cause a signal loss in the spectrometer since it is slightly overfilled. This corresponds to an NA value of 0.125, i.e., smaller than that of the PS-fiber, which is then underfilled by the light cone. Nevertheless, it was also noted that some imperfection in the manufacture of the PS-fiber prototype leads to some signal loss. For example, slight unevenness on the sizes and spacing of the individual fibers may lead to inaccurate numerical aperture.

The spectrometer was equipped with a grating of groove density 2400 lines/mm for measurements at high spectral resolution. An intensified CCD camera (Princeton Instruments PI-MAX4) was mounted at the output of the spectrometer. The on-CCD accumulation and intensifier gain parameters were set for optimal use of the dynamic range. The number of accumulations varied from 10000 to 300000 in order to achieve adequate photon counts for different measurement

conditions. All the spectra were corrected for a background measured with the laser beam blocked using equal detection settings.

A porous-plug flat-flame McKenna burner was placed at the probe volume in the multi-pass cell with the probe volume located above the burner surface. The burner was placed on a vertical translation stage in order to adjust the height of the probe volume above the burner. The burner was used both for generating room-temperature gas flows of air, nitrogen, and oxygen and for stabilizing a flame. Flame measurements were conducted in a stoichiometric premixed methane/air flame of equivalence ratio of 1.0 at heights above burner (HAB) of 3, 7, and 12 mm. The flame was lifted from the burner surface (cf. Figure 5) by adding an excessive nitrogen flow to the air, and the reaction zone was located approximately 7 mm above the burner surface. Measurements at the flame front are challenging using a multi-pass arrangement due to strong temperature gradients that cause beam steering. These measurements were acquired at stable flame conditions that, with the current measurement setup, minimized the problem of beam steering to slight adjustments of one of the multipass cavity mirrors. A metal plate for stabilizing the flame was placed 19 mm above the burner. The total gas flow rate was set to 22.32 NLPM, and the nitrogen/oxygen ratio was 6.69.

In order to quantitatively analyze the spectra, the software PGOPHER [34] was employed for modeling the theoretical spectra of nitrogen, oxygen, and carbon dioxide, using molecular constants from the literature [9, 35]. Temperature and oxygen mole fraction were evaluated by fitting theoretical spectra to the experimental spectra. The theoretical spectra were calculated for different compositions of $N_2/O_2/CO_2$ and temperature. The evaluated temperature and oxygen mole fraction were retrieved from the theoretical spectrum that gave the best fit of the experimental one.

3. Results and discussion

Raman spectra were recorded in wavenumber ranges $0-500\text{ cm}^{-1}$ and $2000-2500\text{ cm}^{-1}$ to study the effect of the fiber-based PS method. The low-wavenumber region ($0-500\text{ cm}^{-1}$) is where the pure rotational Raman S-branch lines are located, and this spectral range is significantly affected by the laser-induced stray light. Therefore, it is suitable to study the performance of the stray-light suppression process in this region. The region of $2000-2500\text{ cm}^{-1}$ is where the nitrogen ro-vibrational O-, Q-, and S-branches are located and is less affected by stray light.

3.1. Spectral analysis from room-temperature gas mixtures

Raman spectra in the wavenumber range $0-300\text{ cm}^{-1}$ and $2000-2500\text{ cm}^{-1}$ from room-temperature air, oxygen, and nitrogen were investigated. Data are compared before and after they have been processed with the lock-in-based periodic shadowing analysis. The intensity of each spectrum was normalized to the maximum of the after-PS spectrum for better visibility. As shown in Fig. 6, the fiber-based PS method is efficient for stray-light suppression, especially in the low-wavenumber region (a-b) where the pure rotational Raman peaks are located close to the laser line and therefore strongly affected by stray light. The increased level of stray light in this spectral region arises from multiple scattering and reflections of the incident laser light, which are significantly stronger than the Raman signal. The ratio between the signal intensity before and after the PS process is displayed under each spectrum, showing a large improvement in peak contrast where the stray-light interference level is reduced by a factor of up to 80 in the region $0-50\text{ cm}^{-1}$. The PS process also reveals the concealed temperature-dependent intensity distribution of the pure rotational S-branch lines, which indicates the possibility for quantitative temperature evaluation (which will be discussed in section 4.2). An increase of the stray light in the region $2000-2500\text{ cm}^{-1}$ is also caused by the superposition of wings from strong lines nearby [24], in this case, the nitrogen Q-branch at 2331 cm^{-1} (cf. Figure 6(c)). The smaller ro-vibrational S-branch peaks

adjacent to the strong Q-branch peak are revealed with a more accurate intensity distribution after PS processing.

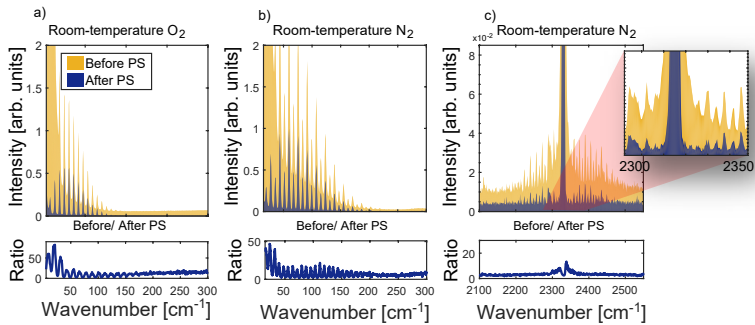


Fig. 6. Raman spectra from room-temperature oxygen and nitrogen at two spectral regions, before (yellow) and after (blue) the PS process. The ratio between the intensity before and after the PS process is plotted below each spectrum. a)-b) pure rotational S-branch spectra of oxygen and nitrogen. c) Q-branch ro-vibrational spectrum of nitrogen.

Figure 7 shows the pure rotational Raman S-branch spectrum of air at room temperature. Similar to the results of Fig. 6, stray light at lower wavenumber values is effectively removed in the PS processing. The spectrum retrieved after PS processing can be well fitted to a theoretical spectrum of temperature 300 K and an O_2 mole fraction of 21%, in agreement with the experimental conditions. This confirms the reliability of the fiber-PS method, as the fit reveals excellent agreement with a correlation value R^2 of 0.99.

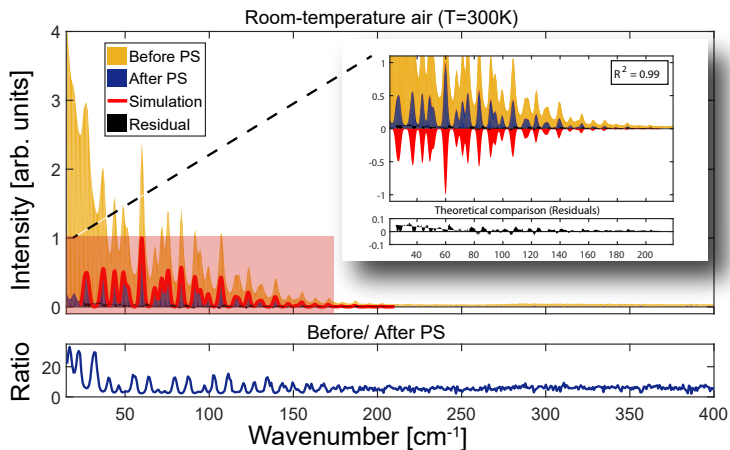


Fig. 7. Pure rotational Raman spectrum from room-temperature air. The theoretical spectrum of temperature 300 K (red) shows excellent agreement with the PS processed spectrum (blue), and the evaluated composition of air agrees well with the actual value (79% nitrogen and 21% oxygen).

3.2. Suppression of different stray-light levels

Different stray-light levels were achieved by placing a scattering object near the probe volume when rotational Raman spectra were acquired. Four sets of 100 spectral images consisting of 2500 on-chip accumulations each, corresponding to an acquisition time of 0.5 s, were recorded for each stray-light level. Averaged data with background levels subtracted are displayed in Fig. 8 for all four cases with different amounts of stray light (Level 1-4). The levels of stray light has a significant impact on the spectra up to about 50 cm^{-1} , where it drops to more moderate levels. Nevertheless, the spectrum that has been processed by periodic shadowing indicates that all levels of stray-light make a significant contribution to the spectrum up to at least 150 cm^{-1} compared to the Raman signal. Data were acquired in these sets in order to investigate the impact of the fiber-PS process on the accuracy and precision of temperature and O_2 mole fractions retrieved from the spectra. Due to severe stray-light interference levels, it was not possible to fit the spectra before the PS process at wavenumber values lower than 50 cm^{-1} . On the other hand, the spectra after PS process could be fitted from 20 cm^{-1} . Thus, the lower limits for fitting were set to 50 cm^{-1} and 20 cm^{-1} for the before- and after- fiber-PS process, respectively.

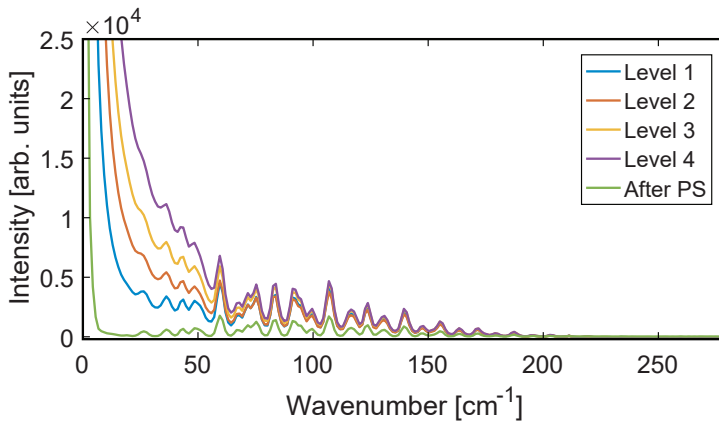


Fig. 8. Pure rotational S-branch Raman spectra measured with different amounts of stray light (Level 1-4). The green curve displays data (the Level 1 case) that has been processed using periodic shadowing where much of the stray light has been suppressed.

The evaluated average oxygen mole fractions and temperatures of each case together with corresponding standard deviations in parenthesis are listed in Table 2. The spectra contain a constant residual baseline that can be accounted for in the fit to evaluate temperature and mole fraction. For the lowest stray-light level, the unprocessed and PS-processed spectra give the same oxygen mole fraction, 20.7%, and the evaluated results then increase with stray-light level. For fiber-PS data, the increase is marginal, and all results are close to the expected value for air, 21%. For the unprocessed data, the increasing trend is stronger, and the values gradually deviate more from the correct value. The spectra were measured at $\sim 295\text{ K}$, and the evaluated temperatures of the PS-processed data are 3-14 K lower. The deviation from the expected temperature shows a slight increase with the stray-light level. However, the unprocessed data result in much lower temperatures that are not realistic for measurements at ambient conditions. This is most likely due to stray-light contribution at the lower wavenumber values of the spectrum, which biases the evaluation towards lower temperature.

Table 2. Evaluated oxygen mole fractions and temperatures with corresponding standard deviations. Expectation values for oxygen mole fraction and temperature is 21% and 295 K, respectively.

| | Evaluated oxygen mole fraction (%) | | Evaluated temperature (K) | |
|--------|------------------------------------|----------------|---------------------------|----------------|
| | Before fiber-PS | After fiber-PS | Before fiber-PS | After fiber-PS |
| level1 | 20.7 | 20.7 (1.4) | 269 | 292 (11) |
| level2 | 21.4 | 20.8 (1.4) | 227 | 287 (11) |
| level3 | 22.0 | 20.9 (1.4) | 211 | 286 (8) |
| level4 | 23.7 | 21.1 (1.2) | - | 281 (9) |

The evaluated temperatures for raw data without periodic shadowing filtering show smaller standard deviations with increased stray-light background levels. This is due to the fact that the raw data is dominated by a rather stable stray-light contribution that does not vary considerably compared with the Raman peaks. Hence, standard deviations for raw data are not presented here to avoid confusion. The standard deviation in O₂ mole fraction and temperatures, evaluated from after fiber-PS data, display small variation for the four different stray-light levels. Thus, the fiber-PS process has a low impact on the accuracy as well as precision of data evaluated from the spectra.

3.3. Temperature measurements in premixed methane-air flame

Temperature evaluation was made for spectra measured at three different heights in a premixed stoichiometric methane/air flame, as shown in Fig. 9. The selected heights above burner ($h_1 = 3$ mm, $h_2 = 7$ mm, $h_3 = 12$ mm) represent the reactant zone (low temperature), the preheat zone (medium temperature), and the post-flame zone (high temperature), respectively. The low-temperature (h_1) case displays pure rotational lines of oxygen and nitrogen from the air. Further, the spectrum at medium temperature (h_2) shows rotational lines from nitrogen, remaining oxygen, and carbon dioxide formed as a result of the combustion. As for the high-temperature (h_3) case, where the oxygen is mostly consumed and carbon dioxide is fully formed, the spectrum mainly consists of nitrogen lines superimposed with carbon dioxide lines.

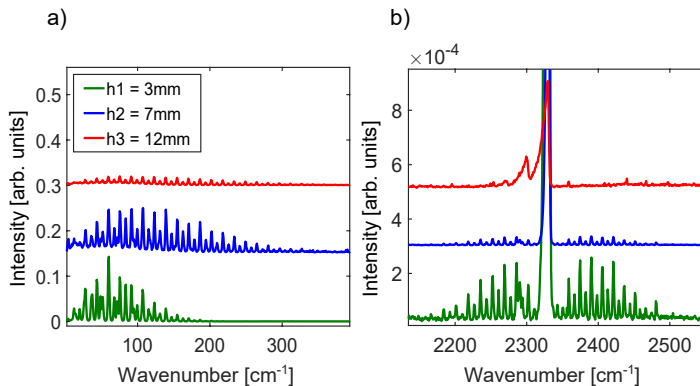


Fig. 9. After PS Raman spectra of a stoichiometric methane/air premixed flame at different heights (h_1 , h_2 , h_3). a) pure rotational S-branch spectra; b) ro-vibrational Q-branch N² spectra. The intensity of each spectrum is normalized by unit acquisition time to illustrate the relative intensity.

The evaluation was performed by fitting experimental spectra with simulated spectra of multi-species (nitrogen, oxygen, and carbon dioxide) pure rotational lines and ro-vibrational nitrogen lines, respectively. For simulations of rotational spectra, the mole fraction of each species at the different heights was estimated in our earlier work [37] by inspection of spectra and calculation of product gas composition. The deduced vibrational temperature is typically higher than the rotational temperature, especially in the high-temperature region. This is caused by the difference in temperature sensitivity of the spectral features used for temperature evaluation in the two cases, the envelope of the pure nitrogen rotational S-branch lines and the Q-branch vibrational hot band. The envelope of the rotational lines becomes less sensitive at higher temperatures, which results in decreased sensitivity, bringing inaccuracy when comparing to the other approach using the vibrational hot band. The evaluated temperatures from the two wavenumber regions are listed in Table 3, where a good agreement between the two approaches is shown at the intermediate temperature where both types of spectra are sensitive, with deviations of the tabulated values around 5%. Temperature measurements can be made with high accuracy for methods based on Raman spectrum analysis, as demonstrated for Coherent Anti-Stokes Raman Spectroscopy (CARS), a well-characterized benchmark method for gas-phase thermometry in combustion diagnostics [6,9]. The CARS method has been employed for studies in flames of the same type as presented here, and temperature uncertainties on the order of a few percent have been reported [36, 38]. Thus, a similar temperature accuracy should be feasible for measurements with Raman spectroscopy as presented here, but calibration is required for the determination of the temperature uncertainty. The product zone temperature, 1519 K, obtained for the stoichiometric flame is rather low. However, the high nitrogen-to-oxygen ratio of the reactants used to obtain a flame lifted from the burner surface resulted in a diluted flame for which rather low temperatures can be expected.

Table 3. Evaluated temperatures at the different heights in the flame.

| | Evaluated temperatures (K) | |
|----|----------------------------------------------------|-------------------------------------------------|
| | From the rotational Raman spectrum of air/nitrogen | From the vibrational Raman spectrum of nitrogen |
| h1 | 292 | 329 |
| h2 | 985 | 1027 |
| h3 | 1294 | 1519 |

The fitted temperatures from the evaluation of the nitrogen vibrational spectra were used as input for the simulations of pure rotational spectra to check the consistency between rotational and vibrational Raman measurements. The calculated rotational spectra show an excellent match with the experimental data, as shown in Fig. 10. Note that the intensity of the simulation in each case is normalized by the maximum of the measured spectrum after PS in order to compare. The excellent agreement between the experimental and theoretical spectra further confirms the feasibility and reliability of the fiber-based PS method. In addition, it needs to be noted that background varies in every measurement due to the uniqueness of each measuring condition. As a result of the spectral resolution of the system, individual carbon dioxide rotational lines cannot be resolved but are observed as a combined broad spectral feature at wavenumber value shifts up to $\sim 150\text{ cm}^{-1}$. Nevertheless, the envelope of the pure rotational CO_2 S-branch lines is exposed after the stray light is removed using the fiber PS method. This envelope is, however, completely concealed by the stray light before the PS process is applied.

3.4. Noise reduction

Frequencies that are not associated with the signal modulation are removed when the band-pass filter is applied. Thus, a ‘cleaner’ spectrum is expected after the PS process with higher

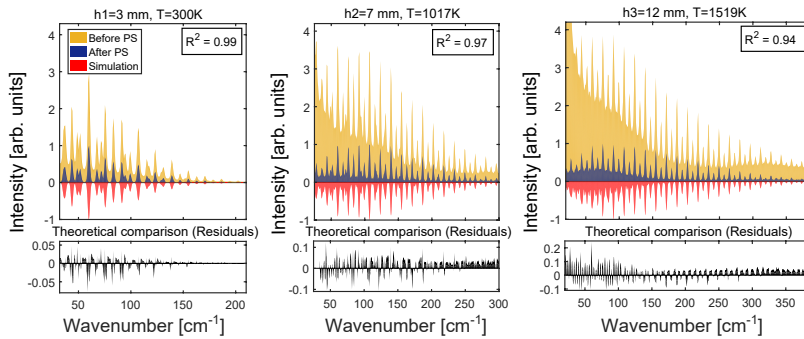


Fig. 10. Comparison between the pure rotational S-branch Raman spectra from three different positions in the methane flame before PS (yellow), after PS (blue), and the corresponding simulation (red). For clarity, the intensity of the simulations is plotted in the reverse direction.

signal-to-noise ratios. This was also confirmed in the previous study by Kristensson et al. [27], where the PS concept was implemented using a Ronchi grating. Figure 11 shows a statistical analysis of a rotational Raman spectral image measured in room-temperature air. The histograms show the intensity distributions of the image background areas indicated by the red rectangles in Fig. 11(a) and (b). A comparison shows that the standard deviation σ , representing the noise level, is reduced by a factor of 4, and the signal-to-noise ratio is then estimated to improve by at least a factor of 2. These results indicate that the implementation of periodic shadowing is beneficial in fiber-based spectroscopy since the technique itself increases the signal-to-noise ratio by the mode-locking-based signal processing. In addition, more light can be collected by the fiber bundle, which also is beneficial from a signal-to-noise point of view. Using a fiber bundle instead of a single fiber does, however, cause a loss in spatial resolution, but the current fiber-bundle input configuration, shown in Table 1 and Fig. 4, displays effective use of the fiber-input area. The presented technique would not give much benefit in measurement situations with strong signals, well-separated spectral features, effective optical filters, and limited stray light interferences, but otherwise, the combination of effective light-collection abilities and suppression of scattered light makes it ideal for Raman spectroscopy.

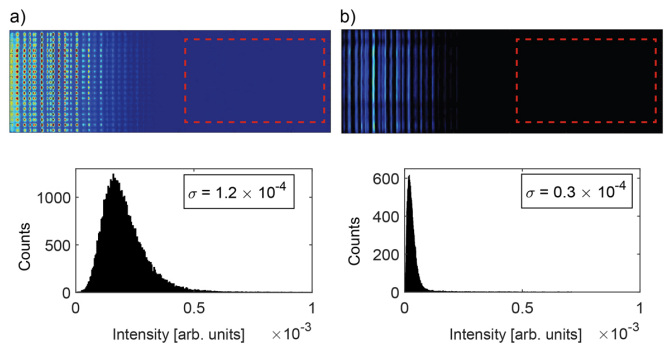


Fig. 11. Improvement of noise level after PS process of a fiber-PS rotational Raman spectrum in room-temperature air. The histograms show the pixel intensity distribution for the image region indicated by the red rectangle and a reduction of the noise level by a factor of 4.

4. Conclusion

In summary, a fiber-based stray-light suppression method for spectroscopic measurements has been presented and demonstrated in Raman spectroscopy of gases. The principle of the method is the implementation of a specialized fiber to perform the Periodic Shadowing method, where the signal light is guided and modulated into a predefined pattern before entering the spectrometer. With further processing algorithms based on spatial lock-in amplification, the stray light can be correctly and efficiently suppressed, in this study by up to a factor of 80. Analysis of Raman spectra showed that correct quantitative information on species mole fractions and temperature could be retrieved from processed data. In addition to the stray-light suppression ability, the fiber-based PS method brings improved flexibility to the detection system. These features together make the concept highly valuable for accurate spectroscopic measurements in experiments with limited optical access.

Funding. Stiftelsen för Strategisk Forskning (ITM17-0313); Energimyndigheten (22538-4); Knut och Alice Wallenbergs Stiftelse (2019.0084); European Research Council (669466, 803634, 852394); Vetenskapsrådet (2015-04056, 2015-05321).

Disclosures. The authors declare no conflicts of interest.

References

1. W. Demtröder, *Laser spectroscopy*. Vol. 2, Springer (1973).
2. C. N. Banwell and E. M. McCash, "Fundamentals of molecular spectroscopy," Vol. 851.: McGraw-Hill New York (1994).
3. A. Downes and A. Elfick, "Raman spectroscopy and related techniques in biomedicine," *Sensors* **10**(3), 1871–1889 (2010).
4. M. Baudelet, "Laser spectroscopy for sensing: fundamentals, techniques and applications," / edited by Matthieu Baudelet. Woodhead publishing series in electronic and optical materials, Amsterdam: Woodhead Publishing, xxiv, 565 pages, 8 unnumbered pages of plates (2014).
5. V. P. Gupta, "Molecular and laser spectroscopy: advances and applications," Elsevier, Amsterdam, Netherlands, xvi, 346 pages (2018).
6. K. Kohse-Höinghaus and J.B. Jeffries, eds. "Applied Combustion Diagnostics," Taylor&Francis: New York (2002).
7. R. Ono, "Optical diagnostics of reactive species in atmospheric-pressure nonthermal plasma," *J. Phys. D: Appl. Phys.* **49**(8), 083001 (2016).
8. S. D. Schwab and R. L. McCreery, "Versatile, efficient Raman sampling with fiber optics," *Anal. Chem.* **56**(12), 2199–2204 (1984).
9. A. C. Eckbreth, "Laser diagnostics for combustion temperature and species," Vol. 3, CRC press. (1996).
10. R. Donaldson, "Stray light in monochromators," *J. Sci. Instrum.* **29**(5), 150–153 (1952).

11. J. K. Pribram and C. M. Penchina, "Stray light in Czerny-Turner and Ebert spectrometers," *Appl. Opt.* **7**(10), 2005–2014 (1968).
12. E. C. Fest, "*Stray Light Analysis and Control*", SPIE Press (2013).
13. A. W. S. Tarrant, "Optical Techniques for Studying Stray Light in Spectrophotometers," *Opt. Acta* **25**(12), 1167–1174 (1978).
14. A. Bohlin and P. E. Bengtsson, "Effective Suppression of Stray Light in Rotational Coherent Anti-Stokes Raman Spectroscopy Using an Angle-Tuned Short-Wave-Pass Filter," *Appl. Spectrosc.* **64**(8), 964–966 (2010).
15. Z. S. Li, M. Afzelius, J. Zetterberg, and M. Aldén, "Applications of a single-longitudinal-mode alexandrite laser for diagnostics of parameters of combustion interest," *Rev. Sci. Instrum.* **75**(10), 3208–3215 (2004).
16. J. Bood, P. E. Bengtsson, and M. Aldén, "Stray light rejection in rotational coherent anti-Stokes Raman spectroscopy by use of a sodium-seeded flame," *Appl. Opt.* **37**(36), 8392–8396 (1998).
17. J. Bood, P. E. Bengtsson, and T. Dreier, "Rotational coherent anti-Stokes Raman spectroscopy (CARS) in nitrogen at high pressures (0.1–44 MPa): experimental and modelling results," *J. Raman Spectrosc.* **31**(8–9), 703–710 (2000).
18. A. P. Yalin and R. B. Miles, "Temperature Measurements by Ultraviolet Filtered Rayleigh Scattering Using a Mercury Filter," *J. Thermophys. Heat Transfer* **14**(2), 210–215 (2000).
19. R. Claps, M. Fink, P. Varghese, and D. Young, "Thermodynamic Studies in Subsonic Gas Flows Using a Laser Diode Raman Spectrometer," *Appl. Spectrosc.* **54**(9), 1391–1398 (2000).
20. R. G. Seasholtz and A. E. Buggele, "Improvement in suppression of pulsed Nd:YAG laser light with iodine absorption cells for filtered Rayleigh scattering measurements," *Proc. SPIE* **3172**, 625–635 (1997).
21. R. B. Miles, L. Qian, and S. H. Zaidi, "Imaging flow structure and species with atomic and molecular filters," *Opt. Lasers Eng.* **44**(3–4), 240–260 (2006).
22. D. Landon and S. Porto, "A tandem spectrometer to detect laser-excited Raman radiation," *Appl. Opt.* **4**(6), 762–763 (1965).
23. A. Walsh, "Multiple Monochromators. II. Application of a Double Monochromator to Infrared Spectroscopy," *J. Opt. Soc. Am.* **42**(2), 96–100 (1952).
24. V. A. Fassel, J. M. Katzenberger, and R. K. Winge, "Effectiveness of interference filters for reduction of stray light effects in atomic emission spectrometry," *Appl. Spectrosc.* **33**(1), 1–5 (1979).
25. W. F. Maddams and M. J. Southon, "III. The effect of band width and band shape on resolution enhancement by derivative spectroscopy," *Spectrochim. Acta* **38**(4), 459–466 (1982).
26. D. G. Cameron and D. J. Moffatt, "A Generalized Approach to Derivative Spectroscopy," *Appl. Spectrosc.* **41**(4), 539–544 (1987).
27. E. Kristensson, J. Bood, M. Aldén, E. Nordström, J. Zhu, S. Hult, P. E. Bengtsson, H. Nilsson, E. Berrocal, and A. Ehn, "Stray light suppression in spectroscopy using periodic shadowing," *Opt. Express* **22**(7), 7711–7721 (2014).
28. M. A. Neil, R. Juškaitis, and T. Wilson, "Method of obtaining optical sectioning by using structured light in a conventional microscope," *Opt. Lett.* **22**(24), 1905–1907 (1997).
29. J. H. Scofield, "Frequency-domain description of a lock-in amplifier," *Am. J. Phys.* **62**(2), 129–133 (1994).
30. E. Smith and G. Dent, "Modern Raman spectroscopy: a practical approach," John Wiley & Sons (2019).
31. K. C. Utsav, J. A. Silver, D. C. Hovde, and P. L. Varghese, "Improved multiple-pass Raman spectrometer," *Appl. Opt.* **50**(24), 4805–4816 (2011).
32. G. Magnotti, K. C. Utsav, P. L. Varghese, and R. S. Barlow, "Raman spectra of methane, ethylene, ethane, dimethyl ether, formaldehyde and propane for combustion applications," *J. Quant. Spectrosc. Radiat. Transfer* **163**, 80–101 (2015).
33. A. Ehn, J. J. Zhu, X. Li, and J. Kiefer, "Advanced laser-based techniques for gas-phase diagnostics in combustion and aerospace engineering," *Appl. Spectrosc.* **71**(3), 341–366 (2017).
34. C. M. Western, "PGOPHER: A program for simulating rotational, vibrational and electronic spectra," *J. Quant. Spectrosc. Radiat. Transfer* **186**, 221–242 (2017).
35. D. Spelsberg and W. Meyer, "Static dipole polarizabilities of N₂, O₂, F₂, and H₂O," *J. Chem. Phys.* **101**(2), 1282–1288 (1994).
36. A. Bohlin, A. Kindeya, E. Nordström, and P.-E. Bengtsson, "Validation of a rotational coherent anti-Stokes Raman scattering model for N₂O at temperatures from 295 K to 796K," *J. Raman Spectrosc.* **43**(5), 604–610 (2012).
37. M. Gong, "Development of Spectroscopic Measurements for Raman and Thomson Scattering Diagnostics - Applications in Combustion and Plasma," M.S. thesis (Department of Physics, Lund University, 2019).
38. L. Martinsson, P.-E. Bengtsson, M. Aldén, S. Kröll, and J. Bonamy, "A test of different rotational Raman linewidth models: Accuracy of rotational coherent anti-Stokes Raman scattering thermometry in nitrogen from 295 to 1850K," *J. Chem. Phys.* **99**(4), 2466–2477 (1993).

Paper III



Suppression of unpolarized background interferences for Raman spectroscopy under continuous operation

HAISOL KIM,  MARCUS ALDÉN,  AND CHRISTIAN BRACKMANN* 

Division of Combustion Physics, Department of Physics, Lund University, P.O. Box 118, Lund 22100, Sweden

**Christian.Brackmann@forbrf.lth.se*

Abstract: A time-resolving filtering technique developed to improve background suppression in Raman spectroscopy is presented and characterized. The technique enables separation of signal contributions via their polarization dependency by the addition of a waveplate to a normal measurement system and data post-processing. As a result, background interferences of broadband laser-induced fluorescence and incandescence, as well as flame luminosity and blackbody radiation, were effectively suppressed from Raman spectra. Experimental setting parameters of the method were investigated under well-controlled conditions to assess their impact on the background-filtering ability, and the overall trend was understood. The fluorescence background was effectively suppressed for all investigated settings of modulation period, number of accumulations, and recording duration, with the spectrum quality preserved after the filtering. For practical application, the method was tested for measurements in a sooting flame accompanied by a strong luminosity and interfering laser-induced background signals. The technique resulted in a 200-fold decrease of the background and allowed for quantitative analyses of concentrations and temperatures from the filtered data. Thus, the method shows strong potential to extend the applicability of Raman spectroscopy, in particular for *in situ* diagnostics under challenging experimental conditions.

© 2021 Optical Society of America under the terms of the [OSA Open Access Publishing Agreement](#)

1. Introduction

Raman spectroscopy is a powerful laser-based diagnostic technique to detect multiple chemical species simultaneously and conduct quantitative analyses of concentrations and temperatures. The inelastic Raman scattering signals appear in a spectrum located relative to the wavelength of the excitation laser, and therefore, it is not required to tune the laser to a specific wavelength, which makes the setup of Raman spectroscopy less complicated than that of many other techniques. For these reasons, Raman spectroscopy is considered an excellent method for studies in various research fields, e.g., combustion, material science, environmental science, and planetary exploration, when it is demanded to detect many kinds of chemical species with quantitative information.

However, Raman spectroscopy has a downside that the signal is weak, which often diminishes all the advantages previously mentioned. In a quantitative comparison for gas, the intensity of Raman scattering is known to be on the order of 0.1% of the Rayleigh scattering intensity, which, in turn, is about 0.1% of the strength of a radiation source [1]. Fortunately, Raman scattering signals are shifted from the wavelength of the laser source and the elastic Rayleigh scattering, so the signals do not interfere with each other if the Raman shift for a target molecule is not too small. However, if there are sources of broadband background signals, e.g., black body radiation and fluorescence, in the measurement volume, the chance of Raman spectroscopy to be successfully employed for measurements is very small. These challenges are particularly

encountered when applying the method for *in situ* diagnostics in different experimental setups and even more so in studies of reactive flows, such as investigations of combustion processes.

In this study, we have developed a technique to overcome the obstacle mentioned above of utilizing Raman spectroscopy due to the unwanted background signals. It is a filtering technique that can suppress polarization-independent signals such as blackbody radiation and most fluorescence. The method is named 'polarization lock-in filtering (PLF)' and was inspired by a spatial lock-in filtering technique previously demonstrated for spectroscopic techniques called 'periodic shadowing' [2] and a polarization-separation method. The PLF technique features a novelty as it can be employed for time-resolved measurements, which was not feasible with most of the existing background suppression methods.

Since the introduction of Raman spectroscopy, there have been a variety of approaches to tackle the limitations of applying the technique. Among them, some similar approaches to this study are selected here and compared with our method. Extensive reviews of the various approaches by Wei et al. and De Luca et al. were helpful for this purpose [3,4]. According to their works, the background suppression methods could be categorized into six kinds: mathematical, polarization gating, time-domain, frequency-domain, wavelength-domain, and modulated Raman spectroscopy. The PLF technique falls into the polarization-gating methods, in accordance with their definition, and other previous works in the same category could be studied. The concept of suppressing luminescence using the polarization characteristics of Raman scattering was first presented by Arguello et al. [5]. Their work suggested a lock-in amplification concept, which resembles the current work but is not providing detailed parameters and applications of the method. While the majority of previous works in the polarization gating category presented improvements in spectral quality and the range of application, the temporal resolution was not considered or had to be compromised [6–9]. The study of Grünefeld et al. is a good example of making Raman spectroscopy possible by overcoming fluorescence interferences for measurements in a spray flame and in a realistic internal combustion engine [10]. They have shifted the laser polarization using an MgF₂ plate, and spectra acquired for the different polarization orientations were compared. However, in order to completely separate two images under different laser polarizations, very accurate control and synchronization of the polarization change and image recording is required for continuous operation. Therefore, keeping temporal information is challenging with the direct subtraction of subsequent spectra. Later, Kojima et al. have introduced a method to realize the concept more conveniently by employing a frame-transfer CCD [11]. Another work in this category, presented by Magnotti et al., introduced an approach of detecting two different polarization components of signals by employing individual detectors for each polarization component [12]. They could obtain interference-free Raman spectra in fuel-rich hydrocarbon flames, and this approach would allow for temporally resolved measurements if the setup is operated continuously. However, the dual detector setup may impose practical limitations. On the other hand, the PLF technique in this study is based on the use of a single detector and has the advantage of conserving temporal resolution while eliminating unwanted signals from the measurement volume with a similar approach to the previous works. The optical arrangement of the method is rather uncomplicated as only one additional component is added to the ordinary setup. Moreover, mathematical post-processing of the data makes acquisition conditions less limited regarding synchronization between the polarization and the recording timing.

The main goals of this study are to validate the PLF concept and present its potential to extend the applicability of Raman spectroscopy for experiments under challenging conditions. This has been achieved with measurements in ambient air, in air seeded with acetone to provide a controlled fluorescence background, and in a luminous sooty flame with background contributions from blackbody radiation and fluorescence. The effects of various experimental parameters were investigated, and the improvements in the quality of Raman spectra were examined. Some

discoveries from the ambient air spectra are included to provide an example of applications in other fields as well.

2. Method

2.1. Polarization Lock-In Filtering (PLF)

As previously mentioned, the PLF technique was largely inspired by the periodic shadowing (PS) technique. For both the PS and PLF methods, modulated signals are utilized to identify the contributions of targeted components and unwanted backgrounds on the recorded signal. The input data for the PS method are spectra acquired as images with the detection wavelength on the x-axis and spatial coordinate along the spectrometer slit on the y-axis. When coupled into the spectrometer, the signal is spatially modulated by a grating element installed on the slit. As a result of a Fourier filtering operation, the spatial resolution of the data is maintained after the post-processing.

The PLF technique utilizes the modulation of signal intensity with time, achieved by having the polarization of the incident laser continuously shifted between vertical and horizontal orientation. Similar to the PS method, the PLF is based on the acquisition of spectral images, but in this case, with temporal modulation registered along the y-axis. As a result, the intensity of polarization-dependent signals oscillate along the y-axis of the image, as shown in Fig. 1(a), and the final data after the filtering maintains temporally varying information like Fig. 1(d). Raman scattering signals are highly polarization-dependent and exhibit a fully toroidal radiation pattern with almost no signal emitted along the dipole axis, i.e., the axis parallel to the incident beam polarization [13]. Therefore, when the laser polarization is shifted from vertical to horizontal orientation, the radiation pattern rotates accordingly, so that a small amount of radiation is collected from the side. On the other hand, depolarized signals, e.g., fluorescence, do not vary with the laser polarization in this way, and therefore, such signals are recorded continuously without the modulation pattern.

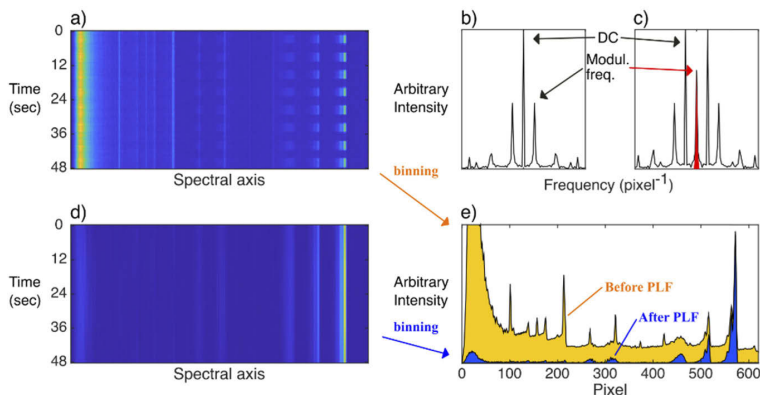


Fig. 1. Two-dimensional a) input and d) output data of the PLF technique. Panel b) shows the Fourier transform of the input data, while panel c) is the Fourier transform of the input data multiplied by a reference signal having the modulation frequency. The red region is selected by a bandpass filter. Panel e) presents intensity-averaged spectra along the image y-axis before and after applying the technique, and polarization-independent backgrounds have been effectively suppressed. The data set is taken from measurements in a sooting flame.

The basic principle of the PLF method is the same as for other polarization-separation methods, but the speciality of the technique is a continuous mode of operation that allows for measurements

under moderately time-varying conditions. The first step of the process is a Fourier transform of the two-dimensional data with periodicity from the modulation [Figs. 1(a) and 1(b)]. At second, a bandpass filter is applied to the transformed data, and a part of information with the periodicity is selected [Fig. 1(c)]. At last, the filtered part of the data is inversely Fourier transformed to reconstruct data where the periodicity is removed, and the temporal resolution is retrieved [Fig. 1(d)]. Theoretically, the temporal resolution after the filtering is half that of the input data before the filtering. In addition, due to the filtering process, it is not required to synchronize the modulation of the laser beam polarization and data recording timing. For more detailed procedures and a mathematical explanation of the filtering process, readers are referred to the previous study by Kristensson et al. [2].

2.2. Experimental

A schematic of the experimental setup is presented in Fig. 2, and it can be separated into a laser part, a detection part, a polarization lock-in filtering (PLF) part, and a measurement volume part. The laser part contains an Nd:YAG laser (HD40I-OE, Edgewave) operated at 532 nm with a repetition rate of 5 kHz and an average power set between 8 and 25 W depending on the objects measured. The laser beam was guided by mirrors and focused by a plano-convex lens with a focal length of 200 mm, and the focal region defined the center of the measurement volume. In order to increase the signal, an additional plano-convex lens and two mirrors were installed after the measurement volume in order to form a double-pass configuration and increase the signal by a factor of 2 (cf., Fig. 2).

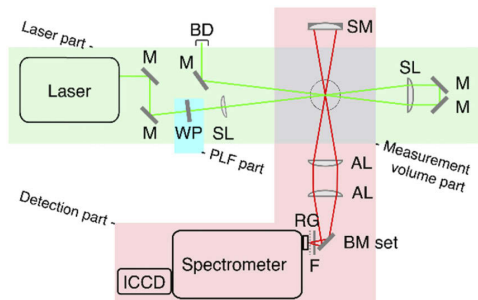


Fig. 2. Schematic of the experimental setup for Raman spectroscopy. M – mirror, WP – half-waveplate on rotation mount, SL – spherical lens, SM – spherical mirror, BD – beam dump, AL – achromatic lens, BM set – a pair of broadband mirrors for image rotation, F – 532 nm longpass filter, RG – Ronchi grating, and ICCD – intensified CCD camera.

The detection part was composed of collection lenses, mirrors, a spectrometer, and an intensified CCD camera. Two achromatic lenses with a focal length of 200 mm were placed to collect the signal, and a pair of aluminum mirrors were installed in front of the spectrometer to rotate the image of the probe volume 90 degrees so that the signal generated along the beam is guided into the vertically oriented slit. A longpass filter (532 nm EdgeBasic, Semrock) was placed in front of the slit in order to minimize background contributions by signals at the laser wavelength, e.g., elastic scattering. A concave aluminum mirror was placed on the opposite side of the measurement volume from the spectrometer to also capture signal scattered toward the other direction. Raman spectra were acquired by a Schmidt-Czerny-Turner type spectrometer (IsoPlane SCT320, Princeton Instruments) with interchangeable gratings of 600 and 1800 lines/mm, and an intensified CCD (PI-MAX 4, Princeton Instruments) connected. The ICCD recorded images in synchronization with the laser, and an on-chip-accumulation function was used to minimize

readout noise. The intensifier gate was set to 100 ns for the air/acetone measurements and to 40 ns for the flame measurements to reject continuous background, e.g., ceiling light and flame emission. The number of on-chip accumulations ranged from 1000-4000, which corresponds to acquisition times of 0.2-0.8 seconds.

A Ronchi grating of 5 lines/mm was installed on the entrance slit of the spectrometer in order to also utilize the PS method. The method is known to effectively suppress effects of stray light inside and outside the spectrometer and would improve the quality of spectra in this study as well [2]. Therefore, in the following, 'Raw spectra' or 'Before the PLF technique' results refer to spectra that have been processed through the PS method. After the PS process, these data were put through the PLF post-processing. The objects measured in this study were operated under steady-state conditions, so the data sets were averaged in time. The intensity of each spectrum was compensated by the wavelength-dependent sensitivity of the camera. The sensitivity along the spectral domain was obtained by utilizing a broadband intensity calibration lamp (IES 1000, Labsphere). A smoothing filter with a span of 5 pixels was applied to each spectrum in the data reduction procedure and following analyses to lower the noise level.

A half-wave plate on a motorized rotation mount (ELL14, Thorlabs) was placed in the laser beam path before the focusing lens, as shown in Fig. 2, to implement the PLF technique. An ideal modulation of the polarization for quantitative analyses requires continuous rotation of the waveplate, resulting in a sinusoidal amplitude modulation. However, due to heating of the rotation mount, an angular oscillation mode was used instead, and therefore, the modulation waveform was closer to a square wave. The modulation period, i.e., the time for changing the polarization from a vertical orientation to horizontal and back to vertical again has been varied to study the effect of this parameter, which will be discussed in section 3.2.

Three different objects were investigated. At first, Raman signals from ambient air were investigated in order to validate the PLF concept. At second, acetone vapor was seeded to an airflow by passing the flow through a reservoir with liquid acetone. The flow was released to the ambient air through a porous-plug McKenna burner to obtain a uniform distribution of the air-acetone mixture across the measurement volume. The center of the burner was positioned at the location where the beams were focused, and the height of the laser beams was set to 3 mm above the burner plug surface. A portion of the incident 532 nm beam was frequency-doubled by inserting a BBO crystal in the path before the beam reached the measurement volume. The generated 266 nm beam induced acetone fluorescence, while the residual 532 nm beam was used for Raman scattering. This arrangement enabled to introduce a well-controlled fluorescence background to the Raman spectrum and allowed to characterize the performance of the PLF method in detail. At last, a sooting ethylene/air flame stabilized on the McKenna burner, as shown in Fig. 3, was investigated. The equivalence ratio of the flame was set to $\Phi=2.0$, where the flame showed luminous blackbody radiation from soot at equivalence ratios higher than 1.7. The height of the burner was adjustable to collect signals from various heights of the flat flame.



Fig. 3. Luminous ethylene/air flame at equivalence ratio $\Phi=2.0$. The flame photo was taken through a 532 nm notch filter to block strong green light from the laser, and the brightness-contrast level has been adjusted to make the burner visible.

3. Results and discussions

3.1. Validation of the PLF technique

Raman spectroscopy with PLF was carried out on ambient air in order to validate the concept and check that the spectral information remains after the data processing. Overall, up to 90% of the already low background level has been removed, and the results are presented in Fig. 4, including spectra retrieved before processing, after PS processing, and after combined PS and PLF processing. Signal intensities were normalized to the maximum intensity of a nitrogen peak for better comparison, and it can be seen that spectral shapes are preserved without distortions.

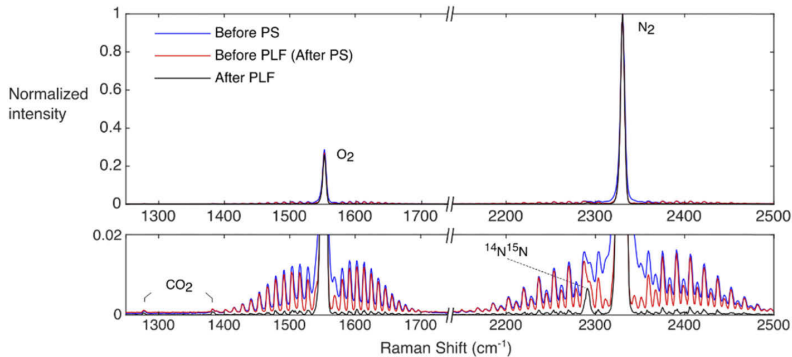


Fig. 4. Raman spectra of O₂, N₂, and CO₂ in ambient air with and without applying the PS and the PLF technique. O- and S-branches of the vibrational Raman peaks are suppressed through the filtering, and therefore, Q-branch vibrational Raman signals of CO₂ and ¹⁴N¹⁵N are clearly observed and separated from signals of O₂ and ¹⁴N₂, respectively.

Some features of the PLF technique are illustrated with this result. At first, the PLF only preserves incident-polarization-dependent signals, and therefore, ro-vibrational O- and S-branches were weakened significantly compared with Q-branch Raman signals due to their large depolarization ratios, i.e., lower polarization dependency. The depolarization ratio of the Q-branch Raman signal is a function of the Placzek-Teller coefficient and polarizability tensor, which gives 0.01 for nitrogen, while that of O- and S-branches is always 0.75 independent of the type of molecule [14]. Therefore, the O- and S-branches of oxygen and nitrogen were suppressed through the filtering process by a factor of 8, as shown in Fig. 4. As a result, the Raman scattering signals from carbon dioxide at 1280 and 1380 cm⁻¹ could be well separated from the O-branch of oxygen. In addition, the Q-branch vibrational Raman signal of a rare stable nitrogen isotope, ¹⁴N¹⁵N, was clearly distinguished at Raman shift 2290 cm⁻¹. The integrated signal of ¹⁴N¹⁵N was 0.7% of the area under the peak of the most abundant ¹⁴N₂ at 2331 cm⁻¹. The value is in good agreement with the known natural abundance of ¹⁴N¹⁵N, which is 0.73% in the ambient air [15]. Considering the importance of investigating ¹⁵N in the field of environmental science and ecology, the PLF combined Raman spectroscopy can be a good candidate for an *in situ* measurement technique for detecting the abundance of nitrogen isotopes, where mass spectrometry of a sample is currently a standard technique [16].

Additionally, since the PLF technique shares the principal concept with polarization-separation by subtraction, background suppression using these two methods are compared in Fig. 5. Spectral data are from the measurements in the sooting flame, which is discussed more in detail in section 3.3. For the direct subtraction method, subsets of data for vertical and horizontal polarization of the laser were retrieved, averaged, and subtracted. As a result, Raman signal strengths are

similar for the two methods, but the direct subtraction result presents a higher noise level and larger errors, e.g., negative values. In addition, rotational Raman lines of hydrogen remain with higher intensity at 596, 821, and 1044 cm^{-1} . The quality of the spectrum obtained from direct subtraction is highly dependent on the quality and noise level of selected data sets. On the other hand, the PLF technique shows an advantage in that the filtering process effectively rejects noise and shot-to-shot deviations that occur out of sync with the modulation frequency. However, some residual background signals coupled to the laser modulation, e.g., C_2 emissions, remain, which will be discussed further in section 3.3.

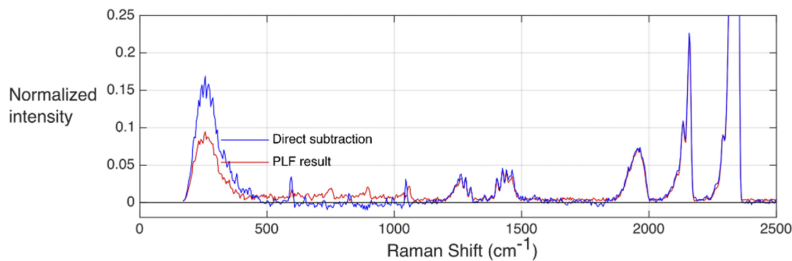


Fig. 5. Comparison between the PLF technique and polarization-separation by direct subtraction. The spectral data are taken from measurements in a sooting flame. Direct subtraction was made for subsets of data acquired with vertical and horizontal polarization of the laser, respectively.

3.2. Investigations of experimental parameters

When the absolute strength of Raman signals is important, it is essential to know how the spectrum is affected by the filtering process. Therefore, the effects of some detection setting parameters on the spectra retrieved after the PLF processing were investigated by introducing a controlled fluorescence background to Raman measurements in air.

By utilizing the previously mentioned acetone-seeded airflow, and simultaneous excitation with 266 nm and 532 nm beams, laser-induced fluorescence of acetone was detected together with Raman signals. Before testing the effects of the experimental setting parameters on the Raman spectrum, the filtering quality for different background levels was investigated. The intensity of the 266 nm beam was varied to change the fluorescence background from zero to a level comparable with the Raman signals, and the result is presented in Fig. 6. For this test, the polarization-modulation period was 7 seconds. In addition, data were recorded with 2500 on-chip accumulations, and it continued for the duration of 7 polarization modulation cycles, i.e., 49 seconds. This set of conditions will be referred to as the 'standard setting' in the following.

Panel a) in Fig. 6 shows the data before applying the PLF technique. A broadband background from acetone fluorescence is observed across the entire wavenumber (Raman shift) range. The intensity of the fluorescence is stronger at smaller wavenumbers, and the longpass filter blocking wavelengths shorter than 540 nm suppressed the background at the lowest Raman shifts. Distinct peaks in the data are Raman signals of acetone (782 cm^{-1}), oxygen (1557 cm^{-1}), and nitrogen (2331 cm^{-1}), while two weaker peaks of acetone are located at 1058 and 1737 cm^{-1} . The identification of the acetone peaks (cf., Fig. 6) refers to the previous work by Bradley and Krech [17].

Panel b) shows the absolute intensity of the signal after the PLF processing, where the fluorescence background has been effectively suppressed. Four spectra originally acquired under different background levels overlap each other very well after the filtering, which implies that the PLF worked well for eliminating the fluorescence background for all the investigated levels.

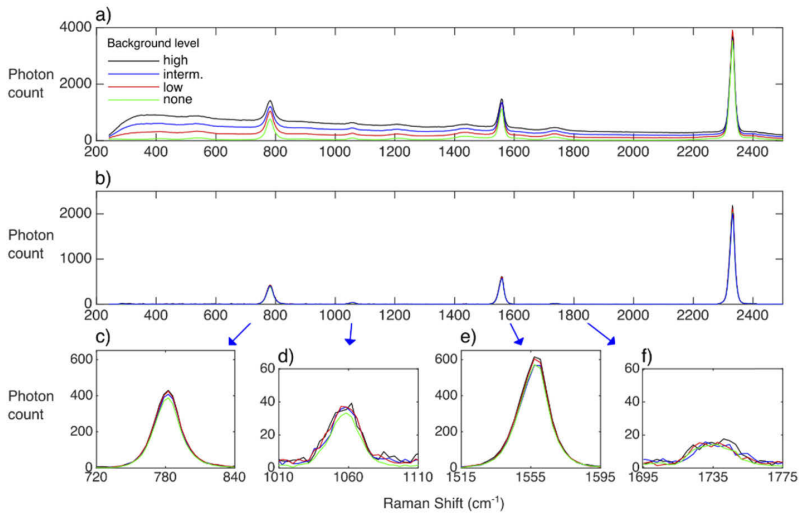


Fig. 6. PLF on Raman spectra of ambient air with acetone fluorescence background. The intensity of the acetone fluorescence has varied from zero to high. a) before applying the PLF, b) after the PLF, c) and d) close-ups of peaks for acetone C-C stretch and C-(C=O)-C breathing motion, e) close-up of oxygen peak, and f) close-up of acetone C=O stretch peak [17].

Panels c) and e) are close-up views of the strong acetone peak and oxygen peak, respectively, and the intensities between the cases vary within 5% of the mean value. The variation in the reconstructed intensity is, possibly, caused by fluctuations of the acetone seeding. The fluctuation can be minimized by normalizing each spectrum to its maximum intensity, i.e., the nitrogen peak, and the results can be compared with each other. Peaks with very weak intensity at 1058 and 1737 cm^{-1} , for which the background is the dominant signal contribution, were also preserved very well through the filtering and became more distinct when free from the background as observed in panel d) and f). The preservation of minor peaks is a great merit of the method for improved detection sensitivity and accuracy since computing the area under these minor peaks for quantification becomes much more accurate by the removal of the background.

The experiments continued with varying the parameters to investigate the preservation of spectral shape and quality under various conditions. Controlled parameters were the period of the polarization modulation, the number of accumulations for one image (recording speed), and the number of images saved (recording duration). From the standard setting, each parameter was changed in turn while keeping the other settings fixed to the standard values. The period of the polarization modulation varied from 3 to 9 seconds with 2 seconds interval where the shortest period was limited by the specification of the rotation mount. The number of accumulations was increased from 1000 to 4000 shots in steps of 500 shots. This parameter is directly affecting the speed of recording, i.e., the frame rate, and 1000 and 4000 accumulations are equivalent to 3.02 and 1.07 frames per second, respectively. The number of images saved was altered to investigate the effect of the modulation phase matching between the first and the last image. Therefore, while 7 cycles of the modulation are equivalent to 49 seconds, the length of the input data was varied from 45 to 53 seconds with an interval of 2 seconds. The variation of the parameters is listed in Table 1.

Table 1. Setting parameters for the polarization lock-in filtering technique investigated to test the impact on spectral quality. Settings written in bold represent the standard condition.

| Controlled Parameters: | Period of Modulation (sec) | Accumulations (# of shots (fps)) | Recording Duration (sec) |
|------------------------|----------------------------|----------------------------------|--------------------------|
| | 3 | 1000 (3.02) | 45 |
| | 5 | 1500 (2.32) | 47 |
| | 7 | 2000 (1.88) | 49 |
| | 9 | 2500 (1.58) | 51 |
| | | 3000 (1.37) | 53 |
| | | 3500 (1.20) | |
| | | 4000 (1.07) | |

Raman spectra of oxygen and nitrogen acquired under the 16 combinations of the conditions are presented in Fig. 7. Different combinations of the parameters affect the absolute intensity of spectra after the Fourier filtering and reconstruction, and therefore, the spectra were normalized to the maximum intensity of the nitrogen signal. As a result, all the spectra show a well-matching shape for baseline level and peak intensities of oxygen and nitrogen Raman signals.

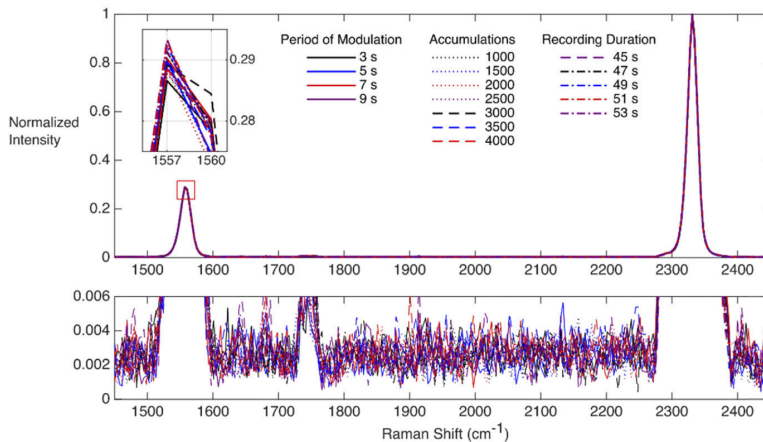


Fig. 7. Raman spectra of air after an acetone fluorescence background has been removed by the PLF method. Raman signals of oxygen and nitrogen at 1557 and 2331 cm^{-1} show good agreement for the 16 different experimental settings investigated. While the standard setting is a modulation period of 7 s, accumulations of 4000 shots, and a recording duration of 49 s, one of these parameters were changed for each case.

The oxygen peak intensities show very good precision with a maximum deviation of 1.3% from their mean value. The baselines at the bottom panel of Fig. 7 are at a similar level, while the deviation from the mean value is minor compared to the noise level of each spectrum. Therefore, it is concluded that the choice of the setting parameters does not affect the quality of the spectrum through the PLF processing. In other words, the PLF method can be applied with the freedom of selecting experimental conditions from slow recording speed with a larger number of accumulations to fast modulation and recording speed, depending on conditions at the measurement volume.

By removing the interfering background, the signal-to-background ratio (SBR) of the spectra has been largely improved. Before the filtering, the ratio of the 782 cm^{-1} acetone peak compared

to the adjacent background level was between 0.9 and 1.6. After the filtering, signals became much more distinct by removing the background, and it resulted in greatly improved SBRs between 32 and 94. Large variations in the SBRs after the filtering is primarily due to the close-to-zero background level obtained after processing, which has a large impact on the calculated ratio.

3.3. Application of PLF for investigating a sooting flame

In order to test the PLF technique under more challenging and practical background conditions, a sooting flame of ethylene/air at equivalence ratio $\Phi=2.0$ was introduced in the setup. The flame was highly luminous as presented in Fig. 4, and a broadband background signal, primarily from laser-induced incandescence (LII) of soot particles, was covering the Raman signals. The position of the measurement was scanned from 1.5 to 19.5 mm above the burner in 1 mm steps, where the flame stabilizer was located at 21 mm. The results are presented in Fig. 8, where the plot at the top shows raw data before applying the PLF technique, the middle one shows data after the filtering, and the bottom one shows the filtered data with an offset to each spectrum for a better illustration. Some heights were excluded from panel c) due to the large similarity between spectra of adjacent heights.

By comparing the spectra in panels a) and b), it is clearly observed that the LII background level up to 20000 counts was effectively filtered with the PLF technique. Therefore, Raman signals of major combustion species, e.g., carbon dioxide (CO_2), oxygen (O_2), acetylene (C_2H_2), carbon monoxide (CO), nitrogen (N_2), ethylene (C_2H_4), water (H_2O), and hydrogen (H_2), were revealed and are labeled in panel c). Strong signals of supplied reactants, i.e., C_2H_4 , O_2 , and N_2 , were clearly observed at the lowest height, but even products, e.g., H_2 and CO_2 , start to appear there. Therefore, it can be expected that a flame front was located at around 1.5 mm above the burner, and this complies with a previous study of similar experimental conditions [18]. At heights above 2.5 mm, only the combustion products and N_2 are detected.

In addition to the Raman peaks, spectra also show residual laser-induced emission peaks of the C_2 Swan bands in the region between 500 and 1000 cm^{-1} that require further discussion for an explanation. For the peak at 1052 cm^{-1} , around 200 out of 2000 counts from the raw data remained after the filtering, even though the C_2 emission signal is unpolarized in general. The appearance of the Swan bands is strongly related to soot sublimation due to the high fluence of the laser utilized in the experiments. The laser fluence in this study was around 60 J/cm^2 at the focus, while it is often set below 0.1 J/cm^2 in soot studies to minimize sublimation [19–21]. The remaining contribution of the Swan bands after the filtering can be explained by the polarization-dependent reflection of the optical components and the resulting laser fluence change. Even though the data were compensated for such effects, sublimation shows a non-linear dependence on laser fluence [22], so a portion of the Swan-band intensity oscillated in phase with the polarization modulation, and thus it remained after the filtering process. If the laser fluence is limited, however, the residue of laser-induced C_2 emission peaks could disappear, and the filtering technique would still be working regardless of the background level.

Spontaneous Raman spectra from sooting flames are rare [6,11,12,23–25], and the spectra at various heights in the flame presented in Fig. 8(c) is already an excellent example of showing how powerful the PLF technique can be. However, straightforward quantification is an important advantage of gas-phase Raman spectroscopy, and therefore, the spectra were converted into a mole fraction plot presented in Fig. 9. The quantification process of Raman spectra consists of calculating the area under each peak in Fig. 8(c) and counting in Raman cross-sections. The integration region for each species is indicated at the bottom of Fig. 8(c). The cross-section values were obtained from the compilation by Eckbreth [13], with a supplement of Gough and Murphy's work for C_2H_2 [26]. Experimental data are presented together with simulation results obtained using the ARAMCO 2.0 kinetic mechanism implemented in the Cantera software

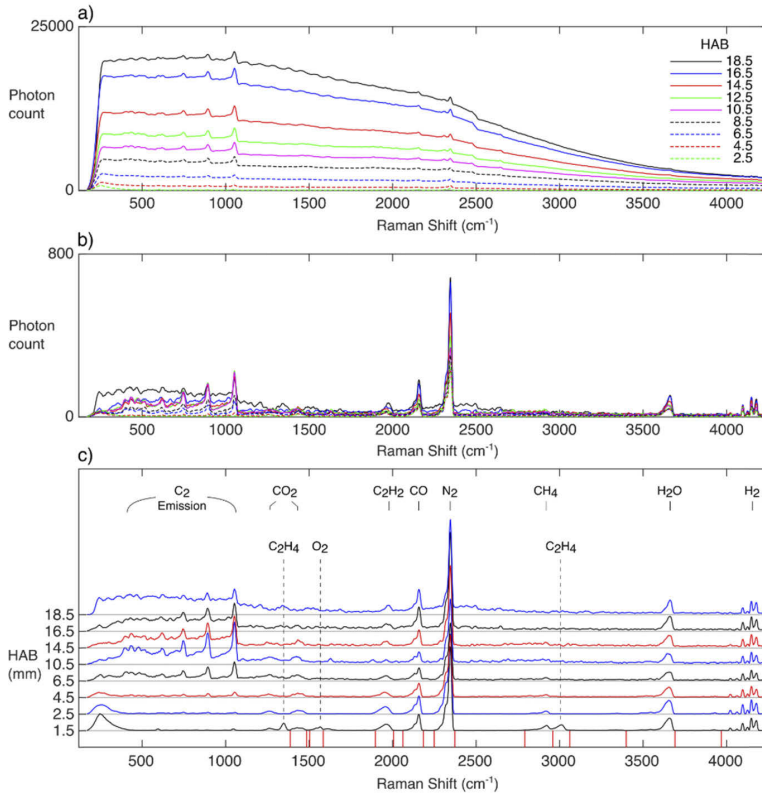


Fig. 8. PLF on Raman spectra of a luminous ethylene/air flame at equivalence ratio $\Phi=2.0$ for various heights above the burner (HAB). a) Spectra before application of PLF show a strong background across the entire wavenumber range. b) Spectra after PLF processing, by which the background has been effectively suppressed. c) Filtered results for some heights plotted with an offset for each HAB for a better illustration. Integration regions for quantitative analyses of species mole fractions are indicated at the Raman-shift axis of panel c).

with the stagnation plane module [27–34]. The simulation had boundary conditions of an inlet temperature of 298 K and a stagnation plane surface temperature of 900 K at 21 mm HAB.

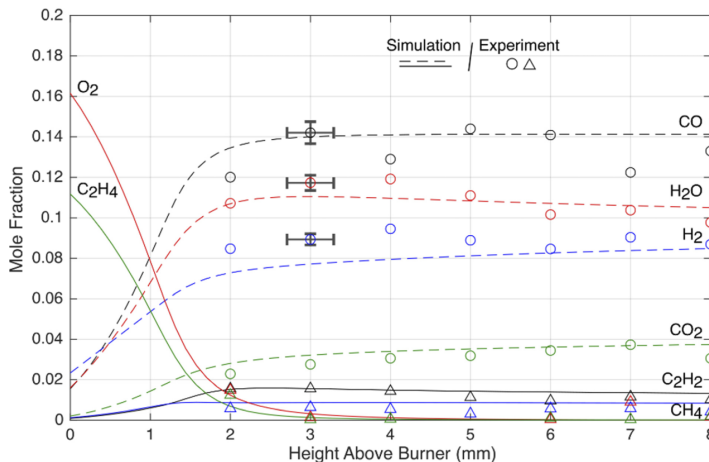


Fig. 9. Mole fractions converted from Raman signals (markers) together with flame simulation results (lines). A 0.5 mm offset in position was added to the experimental data in compliance with the uncertainty estimation. Heights above 8 mm have been excluded due to high noise levels and hence an increase of error. The error bars indicate the range of the largest error estimated from evaluation of the O₂ mole fraction in air and contributions of depolarization ratios (vertical bar), and simulations with 3% variations in inlet conditions (horizontal bar).

The experimental results agree well with the simulation predictions in general. The sublimation was found to add at most 220 ppm of carbon atoms to the flame based on calculations from the soot volume fraction under the given equivalence ratio [35] and has a minor effect on the mole fractions of the species presented in Fig. 9. The hydrogen (H₂) level is overestimated in the experiment, and the error is possibly due to the evaluation of the separated hydrogen Raman peaks that make integration and quantification less accurate. The simulated mole fractions reached plateau levels at heights above 8 mm, but the experimental data showed an increased spread as the height increased. The remaining background level of the filtered spectra for positions above 8 mm was noisier as a result of eliminating a larger background level in the raw data acquired at these positions. In the quantification process, the loss of the Raman signal due to the effect of depolarization was not considered. The maximum error due to the depolarization would be 10% for a depolarization ratio of 0.05; however, all the molecules presented here have lower values than this [36,37]. In addition, some uncertainty could be attributed to crosstalk between spectrally adjacent signals of different species. For example, the overlap between methane and ethylene around 3000 cm⁻¹ [cf., Fig. 8(c)]. Detailed investigations on the effect of crosstalk can minimize the error, but in this study, the integration regions for each species were for convenience set at the local minimum between peaks.

Another quantitative analysis available with Raman spectroscopy is gas-phase thermometry using the nitrogen signal. Therefore, spectra were measured for a narrow wavenumber region centered at the nitrogen Q-branch employing the grating with higher resolution in the spectrometer. The PLF-processed data are presented in Fig. 10(a). The vibrational Q-branch Raman signal of nitrogen and its hot bands are clearly observed around 2300 cm⁻¹, which can be utilized for thermometry.

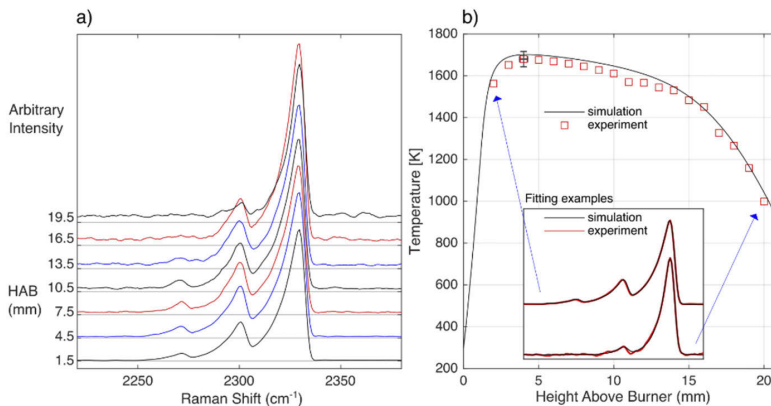


Fig. 10. a) PLF processed spectra of nitrogen in sooting flame plotted with offset values for a better illustration. Fundamental and hot bands of nitrogen are observed. b) Temperature values obtained from the filtered Raman spectra by fitting theoretical spectra in comparison to chemical kinetic simulation results. The insert shows experimental spectra together with the corresponding theoretical spectra obtained by least-squares fitting. A 0.5 mm offset was added to the experimental temperature plot. The error bar indicates the range of the largest error evaluated from the temperature fitting uncertainty and temperature variation in space.

Temperatures at heights between 1.5 mm and 19.5 mm above the burner were evaluated using an in-house developed code. Theoretical spectra simulated with the PGOPHER software [38] were fitted to each experimental spectrum to retrieve the temperature. The values obtained from the spectra at various heights above the burner are presented with square markers in Fig. 10(b). The insert in Fig. 10(b) shows examples of fitted and experimental spectra for the data points indicated by arrows. The maximum temperature of 1680 K from the Raman thermometry is reasonable compared with previous studies under similar flame conditions that reported values between 1680 K and 1790 K [39–41]. However, full profiles of temperatures at various heights of the flame for the specific condition of this study are missing. Temperatures obtained from the previously mentioned simulation are also presented in panel (b). An offset of 0.5 mm added to the height values of the experimental data in Fig. 10(a) gives the best overlap between the profiles. The height offset was reasonable considering the uncertainty of the manual adjustment of the burner position and the errors of the mass flow controller units. From simulations under different flow conditions, a change in the mass flow of 3% was found to shift temperature and mole fraction profiles by 0.3 mm in height. Therefore, the height offset was added to the temperatures and also to the mole fraction data in Fig. 9.

The trends of the temperature from the experiment and the simulation agree well, while the predicted temperatures are higher than the measured ones. The maximum difference is 60 K at a height 11 mm above the burner. The temperature differences might be attributed to the formation of soot that was not included in the simulation. The flame of equivalence ratio $\Phi=2.0$ forms rather low amounts of soot (~ 0.01 ppm in soot volume fraction) [35], so a further discrepancy between simulations and Raman-based thermometry could be expected for even richer flames where a larger amount of soot is formed. However, evaluation of different data sets showed a difference in temperature of ~ 80 K, as indicated by the error bar in Fig. 10(b). Thus, measurements and model predictions agree within the spread observed for the experimental data sets.

Even with the uncertainties addressed here, the PLF technique made it possible to employ Raman spectroscopy to the sooting flame and retrieve quantitative mole fractions and temperatures

with realistic values. This strongly confirms that the technique can be very useful for quantitative Raman spectroscopy under challenging experimental conditions. Here, this has been demonstrated for combustion diagnostics, but the concept should be suitable for application in other research where background interferences are the main obstacle that inhibits the application of Raman spectroscopy.

4. Conclusions

In this study, a polarization lock-in filtering (PLF) technique to extend the applicability of Raman spectroscopy by suppressing polarization-independent background signals has been developed and presented. In order to keep the time-resolved information while eliminating the background interferences, the PLF was devised by combining a temporal lock-in filtering method and a polarization-separation concept. The technique is arranged simply by introducing one additional component to the ordinary Raman measurement system. However, the result is efficient suppression of all polarization-independent signals, e.g., fluorescence and black body radiation, while maintaining polarization-dependent signals, e.g., Q-branch vibrational Raman spectra, under continuous measurement.

Firstly, the feasibility of the technique was validated by ambient air measurements, where vibrational Raman signals of nitrogen, oxygen, and carbon dioxide were clearly separated from rotational Raman signals. Secondly, experimental parameters of the PLF technique have been varied for measurements on air with a controlled background from fluorescence in order to understand optimum settings and the limiting factors. The fluorescence background was effectively suppressed for all investigated settings of modulation period, number of accumulations, and recording duration change that has followed, with the quality of spectrum preserved after the filtering. At last, the technique was employed for practical application in a sooting flame accompanied by a strong luminosity and interfering laser-induced background signals. The PLF technique resulted in a 200-fold decrease of the background and allowed for quantitative analyses of mole fractions and temperatures using the filtered spectra.

Since it is a newly introduced technique, naturally, there exist some limitations and room for improvements. For example, it was observed that suppressing larger backgrounds results in a higher noise level of the background in the processed spectra, which can be problematic when directly comparing results under various conditions that originally had different background levels. In addition, while the technique can eliminate polarization-independent terms in a relatively simple way, some more mathematical procedures would be required if the background and Raman signals are not perfectly depolarized and polarized, respectively. Therefore, in this study, fluorescence and luminosity were assumed to be completely depolarized, and Raman signals were not compensated for the intensity loss due to the depolarization. However, it would be possible to compensate for the effects of depolarization ratios and polarized fluorescence in the results by including known parameters on molecular polarizabilities in the data analysis.

While the main application demonstrated in this study was a flame measurement, we believe that the PLF technique can be easily tailored for applications in any field of interest where Raman spectroscopy would be beneficial but is restricted due to background interference.

Funding. Stiftelsen för Strategisk Forskning (ITM17-0313); European Research Council (TUCLA 669466); Energimyndigheten (CECOST 22538-4).

Acknowledgments. We would like to thank Dr. Torsten Methling for developing the program fitting experimental nitrogen Raman spectra for temperature evaluation.

Disclosures. The authors declare no conflicts of interest.

References

1. D. C. Harris and M. D. Bertolucci, *Symmetry and spectroscopy: an introduction to vibrational and electronic spectroscopy* (Courier Corporation, 1989).

2. E. Kristensson, J. Bood, M. Aldén, E. Nordstrom, J. Zhu, S. Huldt, P. E. Bengtsson, H. Nilsson, E. Berrocal, and A. Ehn, "Stray light suppression in spectroscopy using periodic shadowing," *Opt. Express* **22**(7), 7711–7721 (2014).
3. D. Wei, S. Chen, and Q. Liu, "Review of Fluorescence Suppression Techniques in Raman Spectroscopy," *Appl. Spectrosc. Rev.* **50**(5), 387–406 (2015).
4. A. C. De Luca, K. Dholakia, and M. Mazilu, "Modulated Raman spectroscopy for enhanced cancer diagnosis at the cellular level," *Sensors* **15**(6), 13680–13704 (2015).
5. C. A. Arguello, G. F. Mendes, and R. C. Leite, "Simple technique to suppress spurious luminescence in Raman spectroscopy," *Appl. Opt.* **13**(8), 1731–1732 (1974).
6. J. Egermann, T. Seeger, and A. Leipertz, "Application of 266-nm and 355-nm Nd:YAG laser radiation for the investigation of fuel-rich sooting hydrocarbon flames by Raman scattering," *Appl. Opt.* **43**(29), 5564–5574 (2004).
7. J. J. Kojima and D. G. Fischer, "Multiscalar Analyses of High-Pressure Swirl-Stabilized Combustion Via Single-Shot Dual-Sbg Raman Spectroscopy," *Combust. Sci. Technol.* **185**(12), 1735–1761 (2013).
8. A. Luczak, V. Beushausen, S. Eisenberg, M. Knapp, H. Schluter, P. Andresen, M. Malobabic, and A. Schmidt, "New nonintrusive laser diagnostic tools for design and optimization of technically applied combustion systems," *Combust. Sci. Technol.* **116-117**(1-6), 541–566 (1996).
9. F. Rabenstein and A. Leipertz, "One-dimensional, time-resolved Raman measurements in a sooting flame made with 355-nm excitation," *Appl. Opt.* **37**(21), 4937–4943 (1998).
10. G. Grünefeld, V. Beushausen, P. Andresen, and W. Hentschel, "Spatially resolved Raman scattering for multi-species and temperature analysis in technically applied combustion systems: spray flame and four-cylinder in-line engine," *Appl. Phys. B* **58**(4), 333–342 (1994).
11. J. Kojima, D. Fischer, and Q.-V. Nguyen, "Subframe burst gating for Raman spectroscopy in combustion," *Opt. Lett.* **35**(9), 1323–1325 (2010).
12. G. Magnotti, D. Geyer, and R. S. Barlow, "Interference free spontaneous Raman spectroscopy for measurements in rich hydrocarbon flames," *Proc. Combust. Inst.* **35**(3), 3765–3772 (2015).
13. A. C. Eckbreth, *Laser diagnostics for combustion temperature and species* (CRC press, 1996), Vol. 3.
14. D. A. Long, *Raman spectroscopy* (Mcgraw-Hill, 1977).
15. G. Junk and H. J. Svec, "The Absolute Abundance of the Nitrogen Isotopes in the Atmosphere and Compressed Gas from Various Sources," *Geochim. Cosmochim. Acta* **14**(3), 234–243 (1958).
16. P. A. De Groot, *Handbook of stable isotope analytical techniques* (Elsevier, 2004), Vol. 1.
17. M. S. Bradley and J. H. Krech, "High-pressure Raman spectra of the acetone carbon-carbon stretch in binary liquid mixtures with methanol," *J. Phys. Chem.* **96**(1), 75–79 (1992).
18. C. Brackmann, J. Bood, P. E. Bengtsson, T. Seeger, M. Schenk, and A. Leipertz, "Simultaneous vibrational and pure rotational coherent anti-stokes Raman spectroscopy for temperature and multispecies concentration measurements demonstrated in sooting flames," *Appl. Opt.* **41**(3), 564–572 (2002).
19. H. A. Michelsen, "Understanding and predicting the temporal response of laser-induced incandescence from carbonaceous particles," *J. Chem. Phys.* **118**(15), 7012–7045 (2003).
20. N. E. Olofsson, J. Simonsson, S. Torok, H. Bladh, and P. E. Bengtsson, "Evolution of properties for aging soot in premixed flat flames studied by laser-induced incandescence and elastic light scattering," *Appl. Phys. B* **119**(4), 669–683 (2015).
21. F. Goulay, L. Nemes, P. E. Schrader, and H. A. Michelsen, "Spontaneous emission from C_2 ($d^3\Pi_g$) and C_3 ($A^1\Pi_u$) during laser irradiation of soot particles," *Mol. Phys.* **108**(7-9), 1013–1025 (2010).
22. P.-E. Bengtsson and M. Aldén, "Optical investigation of laser-produced C_2 in premixed sooty ethylene flames," *Combust. Flame* **80**(3-4), 322–328 (1990).
23. G. Grünefeld, V. Beushausen, and P. Andresen, "Interference-free UV-laser-induced Raman and Rayleigh measurements in hydrocarbon combustion using polarization properties," *Appl. Phys. B* **61**(5), 473–478 (1995).
24. W. Meier and O. Keck, "Laser Raman scattering in fuel-rich flames: Background levels at different excitation wavelengths," *Meas. Sci. Technol.* **13**(5), 741–749 (2002).
25. C. Yang, H. Tang, and G. Magnotti, "Picosecond Kerr-gated Raman spectroscopy for measurements in sooty and PAH rich hydrocarbon flames," *Proc. Combust. Inst.* (2020).
26. K. M. Gough and W. F. Murphy, "The Raman-Scattering Intensity Parameters of Acetylene," *J. Mol. Struct.* **224**, 73–88 (1990).
27. A. Kéromnès, W. K. Metcalfe, K. A. Heufer, N. Donohoe, A. K. Das, C.-J. Sung, J. Herzler, C. Naumann, P. Griebel, and O. Mathieu, "An experimental and detailed chemical kinetic modeling study of hydrogen and syngas mixture oxidation at elevated pressures," *Combust. Flame* **160**(6), 995–1011 (2013).
28. W. K. Metcalfe, S. M. Burke, S. S. Ahmed, and H. J. Curran, "A hierarchical and comparative kinetic modeling study of C_1 – C_2 hydrocarbon and oxygenated fuels," *Int. J. Chem. Kinet.* **45**(10), 638–675 (2013).
29. S. M. Burke, W. Metcalfe, O. Herbinet, F. Battin-Leclerc, F. M. Haas, J. Santner, F. L. Dryer, and H. J. Curran, "An experimental and modeling study of propene oxidation. Part 1: Speciation measurements in jet-stirred and flow reactors," *Combust. Flame* **161**(11), 2765–2784 (2014).
30. S. M. Burke, U. Burke, R. Mc Donagh, O. Mathieu, I. Osorio, C. Keesee, A. Morones, E. L. Petersen, W. J. Wang, T. A. DeVerter, M. A. Oehlschlaeger, B. Rhodes, R. K. Hanson, D. F. Davidson, B. W. Weber, C. J. Sung, J. Santner, Y. G. Ju, F. M. Haas, F. L. Dryer, E. N. Volkov, E. J. K. Nilsson, A. A. Konnov, M. Alrefae, F. Khaled, A. Farooq, P.

- Dirrenberger, P. A. Glaude, F. Battin-Leclerc, and H. J. Curran, "An experimental and modeling study of propene oxidation. Part 2: Ignition delay time and flame speed measurements," *Combust. Flame* **162**(2), 296–314 (2015).
31. U. Burke, W. K. Metcalfe, S. M. Burke, K. A. Heufer, P. Dagaut, and H. J. Curran, "A detailed chemical kinetic modeling, ignition delay time and jet-stirred reactor study of methanol oxidation," *Combust. Flame* **165**, 125–136 (2016).
32. C. W. Zhou, Y. Li, E. O'Connor, K. P. Somers, S. Thion, C. Keesee, O. Mathieu, E. L. Petersen, T. A. DeVerter, M. A. Oehlschlaeger, G. Kukkadapu, C. J. Sung, M. Alrefae, F. Khaled, A. Farooq, P. Dirrenberger, P. A. Glaude, F. Battin-Leclerc, J. Santner, Y. G. Ju, T. Held, F. M. Haas, F. L. Dryer, and H. J. Curran, "A comprehensive experimental and modeling study of isobutene oxidation," *Combust. Flame* **167**, 353–379 (2016).
33. Y. Li, C. W. Zhou, K. P. Somers, K. W. Zhang, and H. J. Curran, "The oxidation of 2-butene: A high pressure ignition delay, kinetic modeling study and reactivity comparison with isobutene and 1-butene," *Proc. Combust. Inst.* **36**(1), 403–411 (2017).
34. D. G. Goodwin, R. L. Speth, H. K. Moffat, and B. W. Weber, "Cantera: An object-oriented software toolkit for chemical kinetics, thermodynamics, and transport processes," <https://www.cantera.org>, 2018. (Version 2.4.0).
35. R. Hadeif, K. P. Geigle, W. Meier, and M. Aigner, "Soot characterization with laser-induced incandescence applied to a laminar premixed ethylene-air flame," *Int. J. Therm. Sci.* **49**(8), 1457–1467 (2010).
36. F. Baas and K. Van den Hout, "Measurements of depolarization ratios and polarizability anisotropies of gaseous molecules," *Phys. A* **95**(3), 597–601 (1979).
37. S. Danichkin, A. Eliseev, T. Popova, O. Ravodina, and V. Stenina, "Raman scattering parameters for gas molecules (survey)," *J. Appl. Spectrosc.* **35**(4), 1057–1066 (1981).
38. C. M. Western, "PGOPHER: A program for simulating rotational, vibrational and electronic spectra," *J. Quant. Spectrosc. Radiat. Transfer* **186**, 221–242 (2017).
39. F. Vestin, M. Afzelius, C. Brackmann, and P. E. Bengtsson, "Dual-broadband rotational CARS thermometry in the product gas of hydrocarbon flames," *Proc. Combust. Inst.* **30**(1), 1673–1680 (2005).
40. B. Zhao, Z. W. Yang, Z. G. Li, M. V. Johnston, and H. Wang, "Particle size distribution function of incipient soot in laminar premixed ethylene flames: effect of flame temperature," *Proc. Combust. Inst.* **30**(1), 1441–1448 (2005).
41. Q. Wu, F. Wang, M. Y. Li, J. H. Yan, and K. F. Cen, "Simultaneous In-Situ Measurement of Soot Volume Fraction, H₂O Concentration, and Temperature in an Ethylene/Air Premixed Flame Using Tunable Diode Laser Absorption Spectroscopy," *Combust. Sci. Technol.* **189**(9), 1571–1590 (2017).

Paper IV





Time-resolved polarization lock-in filtering for background suppression in Raman spectroscopy of biomass pyrolysis

Haisol Kim, Miaoxin Gong, Elias Kristensson, Andreas Ehn, Marcus Aldén, Christian Brackmann*

Division of Combustion Physics, Lund University, P.O. Box 118, SE-22100 Lund, Sweden

ARTICLE INFO

Article history:

Received 9 September 2020
Revised 4 December 2020
Accepted 4 December 2020
Available online 21 December 2020

Keywords:

Laser diagnostics
Raman spectroscopy
Polarization lock-in filtering
Biomass pyrolysis

ABSTRACT

Laser-based Raman spectroscopy is a powerful technique for non-intrusive measurements of chemical composition in gas, liquid, and solids. However, weak signals make it challenging to employ the technique for diagnostics under harsh conditions with various background interferences. To overcome such limitations, we have devised a method, polarization lock-in filtering (PLF) based on temporal modulation of the excitation laser polarization, to filter out polarization-independent signals from acquired data. The PLF method applied for continuous Raman spectroscopy measurements of a biomass pyrolysis process showed promising filtering abilities for unwanted background fluorescence signals. A broadband fluorescence background interference was suppressed by up to a factor of 50. Therefore, released species during the biomass pyrolysis process were readily identified with their Raman spectrum signatures and their amounts quantified. In addition, the PLF method provided Raman spectra of low background, from which a gradual change in hydrocarbons released at different stages during the pyrolysis could be observed. Altogether, the efficient background suppression method increases the general applicability of Raman spectroscopy under conditions where interfering signals present a challenge and a limiting factor.

© 2020 The Authors. Published by Elsevier Inc. on behalf of The Combustion Institute. This is an open access article under the CC BY license (<http://creativecommons.org/licenses/by/4.0/>)

1. Introduction

Chemical reaction processes, e.g., combustion, include rapid formation and decomposition of species together with large heat release. Such systems are very complex and sensitive, and thus *ex situ* gas-sampling methods for investigating gas compositions are challenging and associated with uncertainties related to the sampling process itself. On the other hand, laser-based diagnostic techniques can be utilized to investigate processes under harsh conditions with strong gradients without perturbing the studied phenomena. Raman spectroscopy is such a method that can detect multiple chemical species simultaneously, and the signal is proportional to the species concentration, making it quite straightforward to conduct quantitative analysis. However, Raman scattering is a relatively weak process compared to interactions utilized in other laser-based techniques. Therefore, despite its strong points, Raman spectroscopy is often opted out when there are various background sources at the probe volume, e.g., strong elastic scattering of laser light or fluorescence.

Nevertheless, Raman spectroscopy has been employed for combustion diagnostics since the 1970s [1–3], and a review of its development has been presented by Eckbreth [4]. Enhanced sensitivity for Raman spectroscopy can be realized using configurations with multiple passages of the excitation laser beam through the measurement region; an early example of a multipass cell for Raman spectroscopy of gases was presented by Hill and Hartley [5] while a later design demonstrated for studies in flame has been devised by Utsav et al. [6,7]. Raman measurements using continuous-wave lasers can be feasible under conditions with a low level of background light while diagnostics of luminous flames require gated detection and pulsed lasers, which also is necessary for studies under non-stationary conditions, e.g., in turbulent combustion. However, for lasers with high pulse energy operating at a low repetition rate, typically 10 Hz, the high irradiance obtained with a focused beam can induce electric breakdown and plasma formation. The subsequent broadband emission of the plasma then interferes with the acquisition of the weak Raman signal. One way to avoid this problem is to use pulse-stretcher concepts introduced by Nguyen et al. [8] and employed by many research groups [9–14]. The pulse is stretched temporally using multiple optical ring cavities or delay lines, and it was, for example, reported by Kojima and Nguyen that a pulse of duration 8.4 ns (FWHM) was expanded

* Corresponding author.
E-mail address: christian.brackmann@forbrf.lth.se (C. Brackmann).

to over 150 ns while maintaining 82% of its initial energy [9]. However, the downside with this type of setup is increased complexity in the optical arrangement. Alternatively, lasers with high repetition rates, e.g., 5 kHz, and lower pulse energies can be employed to achieve high average power (in the range between 10 and 100 W) and yet avoid problems with laser-induced plasma [15].

The detection sensitivity can also be improved by suppressing the background from stray light and thus achieve a higher signal-to-background ratio. A means to accomplish background suppression was introduced by a method called periodic shadowing (PS) [16]. Installing a Ronchi grating at the entrance slit of the spectrometer and creating an imprinted pattern on the signal, combined with a spatial lock-in filtering in the Fourier domain, results in an efficient suppression of background light that reached the detector from unwanted directions. In the previous study, the PS method was investigated with four different spectroscopic measurement techniques: emission, absorption, laser-induced scattering, and Coherent anti-Stokes Raman Spectroscopy (CARS). Depending on the type of technique and spectral region of interest, an improvement of the signal-to-background ratio by a factor from 20 to 300 was observed. The concept was especially helpful when multiple scattering in the vicinity of the probe volume presented a problem, and therefore, it was also implemented in our Raman spectroscopy setup to improve the detection sensitivity.

Even though the PS method is efficient for reducing the problem with multiple scattering, it, however, cannot filter out interfering laser-induced emission, e.g., fluorescence, originating from the probe volume. These interfering signals follow the same path through the detection system as the Raman signal and will thus not be suppressed with PS. In cases when such undesired background contributions are un-polarized, they can be subtracted from the polarized Raman signal by measurements at orthogonal detection polarizations [13,17–20]. While this can be readily achieved for investigations under static conditions, measurements on time-varying processes are often desirable. Simultaneous acquisition of signals with orthogonal polarizations can then be achieved with dual detection setups, for example, employed in studies of turbulent combustion [13]. As an alternative for studies of moderately time-varying processes, we devised a method, polarization lock-in filtering (PLF), based on a continuous change in polarization of the incident laser beam resulting in Raman signals modulated in time while un-polarized signals such as fluorescence remain unaffected. The acquired data modulated in time are post-processed using lock-in filtering, similar to the PS method. The novelty compared with the previous approach is the continuous mode of operation that allows processes varying on a second-scale to be followed in time with the retrieval of background-free spectra using a single detection system. The method is rather simple to implement experimentally but clearly extends the applicability of Raman spectroscopy for studies of time-varying processes.

This paper presents background suppression using the PS and PLF methods to address the challenges of background interferences in Raman spectroscopy under harsh measurement conditions. The combined PS and PLF methods were employed to investigate gas released from a biomass pyrolysis process, which is accompanied by the release of hydrocarbon volatiles [21] that, upon laser excitation, can result in strong fluorescence swamping Raman signals. This background prohibits analysis of gas composition both in terms of permanent gases, e.g., CO, CO₂, H₂, and CH₄, but also of its content of hydrocarbon volatiles and tars [21,22], which is an indicator of gas quality. Tar composition is dependent on the residence time of the tar-laden gas at high temperature as well as other operational conditions, see, e.g., [23]. While conventional adsorption methods for tar analysis can provide detailed information on their composition, they are time-consuming (~hours), making correlations with process changes and conditions challenging. Therefore,

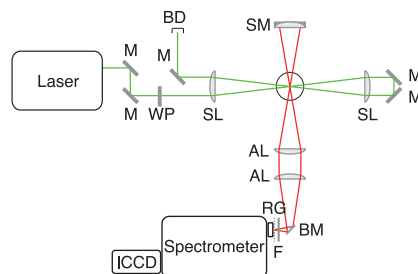


Fig. 1. Schematic of the experimental setup for Raman spectroscopy. The green line represents the laser beam while the red line represents the signal path. A double-pass setup was used to study a biomass pyrolysis process in the measurement volume indicated by a circle. Abbreviations: M – mirror, WP – half-wave plate, SL – spherical lens, SM – spherical mirror, BD – beam dump, AL – achromatic lens, BM – pair of broadband mirrors for image rotation, F = 532 nm long-pass filter, RG – Ronchi grating, and ICCD – intensified CCD camera. (For interpretation of the references to color in this figure legend, the reader is referred to the web version of this article.)

measurement techniques that enable *in situ* on-line measurements are of high value in the characterization of biomass conversion. In such studies, the combined background filtering techniques are very useful to retrieve Raman spectra with significantly reduced background and allow for identification and quantitative analysis of signals of carbon monoxide, hydrocarbons, and water.

2. Methodology

2.1. Raman spectroscopy

An Nd:YAG laser (HD401-OE, Edgewave, 100 W) operating at a repetition rate of 5 kHz was employed for Raman spectroscopy. The operating power of the laser was set to 25 W to prevent damaging optical components. A schematic of the experimental setup is shown in Fig. 1.

A double-pass arrangement consisting of two spherical lenses of $f = 200$ mm focal length and planar dichroic mirrors was used for the laser beam to pass through the measurement volume twice while being focused at the common intersection where the crossing angle between the beams is 8°. A pellet bed, explained more in the following section, was located right below the measurement volume.

A portion of the scattering signal from the probe volume was collected into an $f = 320$ mm spectrometer (IsoPlane SCT 320, Princeton Instruments) using two achromatic lenses of focal length $f = 200$ mm. Between the set of lenses and the spectrometer, a pair of broadband aluminum mirrors was placed in an arrangement that rotates the image of the probe volume by 90° to match the orientation of the slit. The spatially resolved Raman signal for a 6 mm distance along the laser beams was recorded on the CCD sensor, and the spatial resolution was estimated to be 80 μm . A long-pass filter (532 nm EdgeBasic™, Semrock, OD7) was positioned at the slit to suppress elastic scattering and straylight at the laser wavelength, and no appreciable contributions were observed in the spectral regions of the vibrational Raman peaks. The spectrometer was equipped with three different gratings with 600, 1800, and 2400 lines/mm allowing for measurements with different spectral resolution. Depending on the spectral region of interest and purpose of the measurement, different gratings were used to study a particular spectral range in detail or to acquire a full spectrum. The results presented in this paper were recorded with the 600 lines/mm grating, centered at wavelength 627 nm. The

spectrally dispersed signal from the spectrometer was recorded on an intensified CCD camera (PI-MAX 4, GEN III, Princeton Instruments) with an intensifier gate width of 30 ns to suppress continuous background. Raman signals generated by 2000 pulses were accumulated into one image, with an acquisition time of 0.4 s, to enhance the signal-to-noise ratio. Such accumulated images were recorded continuously during measurements with a frame rate of 1.86 fps for 330 s.

2.2. Periodic shadowing and polarization lock-in filtering method

The periodic shadowing (PS) method was implemented by installing a Ronchi grating, denoted RG in Fig. 1, on the entrance slit of the spectrometer. A stripe pattern of 5 lines/mm printed on the grating alternately blocks and transmits signal entering the spectrometer. Only light that has propagated through the entrance slit and followed its intended path inside the spectrometer will preserve the periodic pattern and create a spatially modulated image on the CCD chip. Thus it is possible to filter out stray light by digital lock-in amplification in the post-processing. Subsequent binning of each image vertically results in a Raman spectrum, filtered from interfering stray light, that can be further analyzed in the same manner as an ordinary Raman spectrum. For a more detailed explanation of the PS method, readers are referred to the work of Kristensson et al. [16]. In this study, results were obtained for measurements with combined PS and PLF methods. However, the focus of the discussion is on the PLF method with comparisons of data before and after applying the PLF processing.

For the PLF method, a half-wave plate, denoted WP in Fig. 1, was manually rotated from 0 to 45° and back, which changed the polarization of the incident beam from vertical to horizontal and back to the vertical orientation continuously at a frequency of 0.5 Hz. Therefore, the intensity of polarization-dependent signals, e.g., Raman scattering, varied periodically with time in the set of data. In the two-dimensional data set with the wavelength on the x-axis and time on the y-axis, a periodicity is imprinted along the time direction due to the variation, and it is equivalent to the spatial periodic pattern imprinted on the signal in the PS method. The data with the periodicity was then Fourier filtered to only retain components with the frequency of the modulation. With this filtering method, continuous measurements are possible, and it is not required to precisely synchronize the timing of the polarization shift and the recording. The temporal modulation pattern of the signal resembled a square-wave, and the filtering process resulted in a signal reduction of ~30% while the spectral shape was preserved after processing. Thus, the processed data show a dynamic range equal to ~70% of the detector range.

In this study, it was assumed that Raman signals are completely polarized whereas background signals are assumed to be polarization-independent. However, for more accurate quantification, depolarization ratios of molecules need to be included, and it can result in an error of 10% at a maximum when this is neglected. In addition, background levels are not fully polarization-independent due to the properties of molecules and polarization-dependency of optical components in the measurement setup. For example, the laser power was measured at the end of the beam path for different polarization orientations, and the horizontal polarization showed 2% decrease compared with the vertical polarization. This intensity drop can be compensated for in the data processing when accurate quantification is wanted.

2.3. Biomass pellet and pellet bed

A cylindrical biomass pellet, 20 mm tall and 8.2 mm in diameter, was chosen as a sample in this study. The surface of the pellet was slightly glossy, possibly from the pressing process, and the

density of the pellet was 1174.0 kg/m³. An electric heating coil was devised to heat up the biomass pellet located inside the coil, which in turn was mounted inside a coaxial tube for purging the air out with an argon flow. The argon flow was increased until the Raman signal from nitrogen decreased to lower than 5% of the level for ambient air. Under this condition, no oxygen peak was visible in the Raman spectrum, and the pellet did not ignite during the entire heating process. The temperature development at the center of the coil was reproducible for repeated runs and was recorded with a thermocouple prior to the run with the pellet. The values were later used to assign temperatures to the recording times of the data acquired during the pellet pyrolysis. The initial heating rate was 10.7 °C/s for the first 50 s up to 555 °C, where the heating rate starts to decrease, and the temperature then gradually approached 704 °C for the next 280 s. The recording of Raman data started when the heater was switched on.

3. Results and discussion

The PS and PLF methods were implemented with the Raman spectroscopy setup to filter the strong fluorescence signal generated during the biomass pyrolysis. Each image acquired during the biomass experiments first went through the PS process to suppress background from multiple scattered straylight. With these measurements, the PS method was for the first time utilized for applied spectroscopy under challenging conditions in an environment with dense smoke from condensed pyrolysis products. The PS method improved the quality of spectra by suppressing background from multiple scattering, and about 30% of the background level intensity has been removed across the entire wavenumber range through the process. The processed images were then binned into single spectrum vectors and stacked as rows to form the image of Fig. 2a. Therefore, the images of Fig. 2 display wavenumbers and time along the horizontal and vertical axis, respectively. As mentioned previously, temperatures measured during heating without pellet have been assigned to the recording time, as indicated on the right side of Fig. 2a and b. Strong fluorescence from hydrocarbon volatiles covers the entire range of the spectrum during heating at temperatures between 675 and 696 °C, as shown by the broad bright region covering almost the entire width of the image in Fig. 2a. As a result of the PLF procedure, a periodicity in the overall signal intensity was encoded on Raman signals along the y-axis of the spectral image in Fig. 2a, e.g., for nitrogen at 2331 cm⁻¹, and appears as thin horizontal lines across the image. Figure 2b shows the image after filtering using the PLF method. Polarization-independent fluorescence signals have efficiently been filtered out, and therefore more accurate identification of Raman peaks was achieved.

Spectra at three different temperatures from Fig. 2b are selected and compared in Fig. 3, at temperature 688 °C when the fluorescence signal was increasing (a), at 692 °C when the fluorescence was the strongest (b), and at 697 °C when the tar release was about to finish (c). The broad fluorescence of the tars is suppressed by a factor of 25, 15, and 50 in the spectra of Fig. 3a, b, and c, respectively. Moreover, pronounced interference rejection is achieved for two overlapping peaks at wavenumbers 1818 and 1833 cm⁻¹, which for laser excitation at 532 nm are equivalent to wavelengths 589.0 and 589.5 nm, respectively. Intensities of the peaks together with the background dropped by a factor of 40 compared to the input data as a result of the PLF process, cf. Fig. 3a. The filtered peaks are laser-induced atomic emission of sodium (Na) d-lines [24] due to alkali species in the biomass pellets. The suppression of these peaks serves as a good example of filtering polarization-independent signals using the PLF method.

Additional peaks, located at wavenumbers labeled gray in Fig. 3, disappeared after the filtering. Some of them, positioned

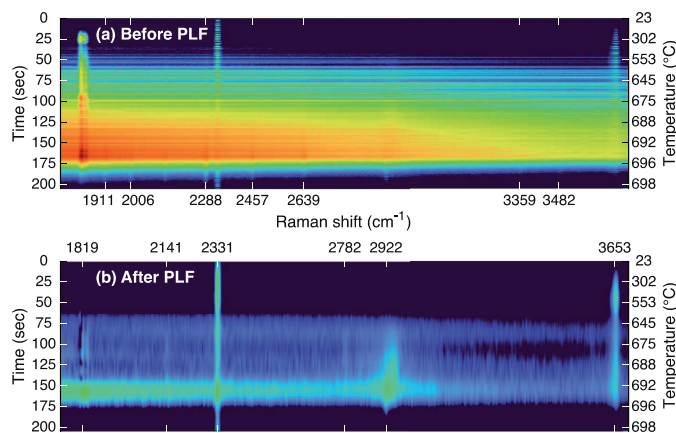


Fig. 2. Images of continuously recorded spectra with temperature increase, (a) before and (b) after polarization lock-in filtering (PLF). The image intensity is presented on a logarithmic scale for clarity. The bright intensity across the entire spectral range in (a) is a background due to fluorescence of hydrocarbon volatiles. This background, as well as some polarization-independent peaks, have efficiently been removed using the PLF filtering in (b).

at wavenumbers 1911, 2006, 2288, 2457, and 2639 cm^{-1} , match the C_2 Swan bands at wavelengths 592.2, 595.6, 605.7, 612.0, and 618.9 nm, respectively [25]. This indicates some photolysis of larger hydrocarbons by the laser. Altogether, the PLF method effectively suppresses fluorescence and laser-induced emission peaks that potentially could be interpreted as false positive Raman signals.

In the spectrum of Fig. 3b, for which the fluorescence contribution was the strongest, a residual fluorescence background of higher intensity at shorter wavenumbers remains after PLF processing, and the spectrum is slightly tilted with a negative slope. In addition to the broad fluorescence contribution of volatiles, the spectrum also shows residual Na peaks at 1881 and 1833 cm^{-1} . Possibly, the release of gases at this stage is too rapid for the PLF method to be able to compensate for the fluorescence background contributions fully. A more rapid modulation might be able to handle this limitation. The residual background was fitted using reference data points where no Raman signal appears, and accounted for in the further quantitative analysis of the Raman peaks.

As a result, Raman signatures of nitrogen, water, hydrocarbons, and carbon monoxide from the biomass pyrolysis were separated from the fluorescence background, and each peak was integrated and converted to an absolute amount using Raman cross-section values obtained from the literature (N_2 : $0.46 \times 10^{-30} \text{ cm}^2/\text{sr}$, H_2O : $0.9 \times 10^{-30} \text{ cm}^2/\text{sr}$, Hydrocarbons: $2.6 \times 10^{-30} \text{ cm}^2/\text{sr}$ for methane, CO : $0.48 \times 10^{-30} \text{ cm}^2/\text{sr}$) [4]. Different classes of hydrocarbons, such as alkanes, oxygenates, and polyaromatic tar compounds, are emitted during pyrolysis [21,22] and contribute to the spectral signature around 2900 cm^{-1} . The composition also varies with time and temperature during the process, which makes the assignment of specific species challenging. Nevertheless, the spectral signature gradually shows a more pronounced peak at 2919 cm^{-1} , indicating increased emission of methane, which is in agreement with the expected trend for the process [21]. Therefore, the cross section of methane was used for the evaluation of the hydrocarbon signal. Since larger hydrocarbons, e.g. higher alkanes, often have higher Raman cross-sections in the CH region [26], the concentration values are likely overestimated. The observed transition of the CH peak indicating a change in the composition of emitted hydrocarbons will be discussed in the last part of this section. Molarities

of the species are plotted with time and temperature increase in Fig. 4. As previously mentioned, an argon flow was introduced to prevent the access of oxygen to the pellet during the process, and the amount of nitrogen at the measurement volume while purging was less than 5% of the level in ambient air. The amount of nitrogen under this condition in the probe volume is observed at time 0 in Fig. 4.

In the early stage of heating, the temperature increased at a rate higher than 10 $^\circ\text{C}/\text{s}$, and a rapid release of nitrogen and water is observed in Fig. 4. Up to 25 s, nitrogen shows a rapid increase above the initial level at $t = 0$ s due to the release of gas from pores of the pellet. Internal gas storage in the pores of wood biomass under ambient conditions has been confirmed in absorption measurements of oxygen to characterize the porosity of such materials [27]. Between ~ 25 and 50 s, the nitrogen concentration shows a drop by $\sim 30\%$, which corresponds to the decrease in molecular number density as the temperature goes up and indicates a rather constant release of nitrogen. The concentration of water increases up to 45 s due to drying of the pellet, and after ~ 50 s, both nitrogen and water follow a similar decrease up to ~ 65 s, indicating the end of the first part of the decomposition. After the first stage of the release, the water concentration in the measurement volume gradually increases again, and it is accompanied by the release of hydrocarbons and carbon monoxide. The former is also confirmed by the appearance of the strong fluorescence signal removed in the PLF processing (cf. Fig. 3a). The release of gases continues for around 100 s, after which the concentrations of water, hydrocarbons, and CO have decreased to zero level, while the nitrogen has returned close to its initial value.

As presented in Fig. 3a, the hydrocarbon signature (around 2900 cm^{-1}) is relatively broad, and a further investigation reveals that it is composed of more than one peak, as discussed in the following. The filtered data was used to zoom in on the hydrocarbon peak, which is presented in Fig. 5. The hydrocarbon Raman signal started to appear at 75 s after the heating when the temperature reached 645 $^\circ\text{C}$. At this moment, the peak intensity of the relatively broad spectrum was located at 2944 cm^{-1} . As time passes, temperature increases, and pyrolysis continues, the position of the maximum-intensity started to move toward the shorter wavenum-

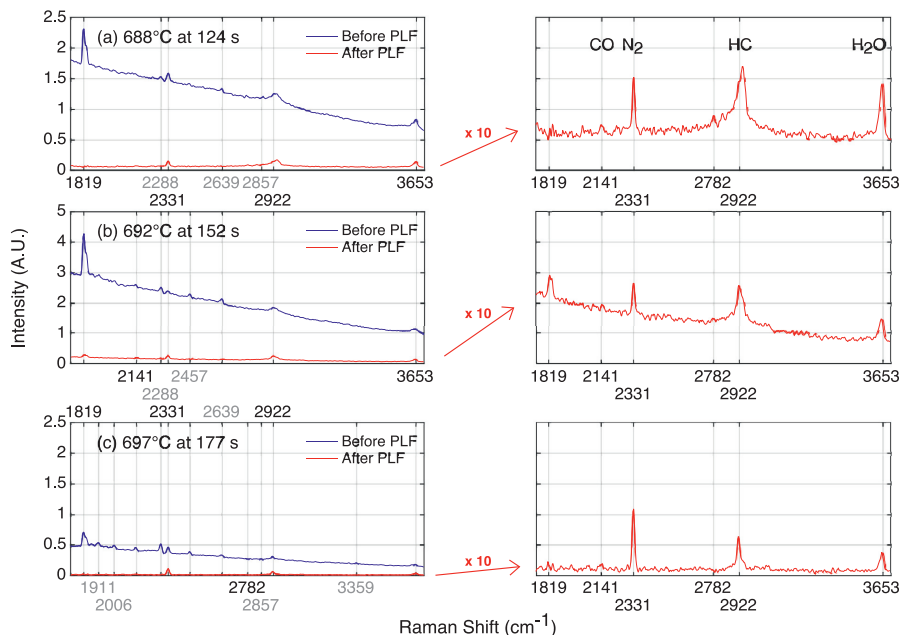


Fig. 3. Spectra of released gas from biomass pyrolysis at a temperature of (a) 688 °C, (b) 692 °C, and (c) 697 °C. The polarization lock-in filtering was utilized to increase the Raman signal-to-background ratio by removing non-Raman signals. Raman peaks of carbon monoxide (CO), nitrogen (N₂), Hydrocarbons (HC), and water (H₂O) are identified.

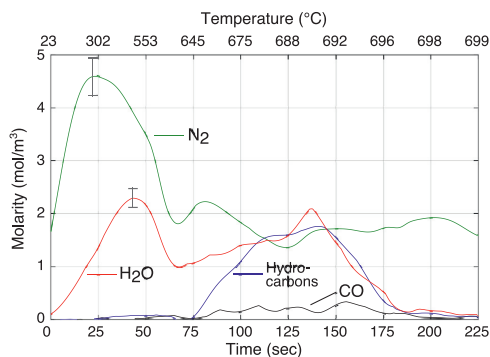


Fig. 4. Absolute amounts of released nitrogen (N₂), water (H₂O), hydrocarbons, and carbon monoxide (CO) during biomass pellet pyrolysis. An argon flow was introduced to the measurement volume to limit the access of oxygen to the biomass pellet. The error bar indicates the range of the largest error in evaluated concentration estimated from repeated Raman concentration measurements in a flame.

ber of 2919 cm⁻¹. After 135 s of heating, when the temperature reached 690 °C, intensities of the two adjacent peaks in the hydrocarbon region were of similar strength. After that, the maximum intensity stayed at 2919 cm⁻¹ until the process ended. The initial Raman spectrum located around wavenumber 2944 cm⁻¹ suggests that the initial release contains larger hydrocarbons. For example, alkanes and oxygenates, see, e.g., [26,28], reportedly released dur-

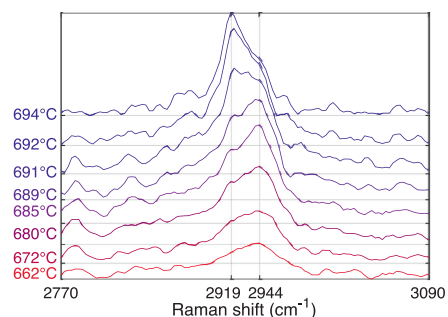


Fig. 5. Change of hydrocarbon Raman spectrum with heating time and temperature increase during pyrolysis. The peak of the hydrocarbon Raman signal located at 2944 cm⁻¹ shifts to 2919 cm⁻¹ as the process continues. The spectra are plotted with offsets for a better visualization.

ing the early stages of pyrolysis [21,22]. An additional indication of the release of oxygenated compounds, such as aldehydes, is the appearance of a small peak at 2780 cm⁻¹, suggesting the release of formaldehyde [26], previously also identified in biomass pyrolysis experiments, see, e.g., [29]. Biomass pyrolysis is also accompanied by the release of tars, primarily consisting of polyaromatic hydrocarbons for which Raman spectra often show prominent peaks in the vicinity of 3050 cm⁻¹ [30]. However, polyaromatic tars are reported to form at higher temperatures than reached in these experiments [22], and, accordingly, the spectra of Fig. 5 show no ap-

parent features around 3050 cm^{-1} . Considering that the peak at 2919 cm^{-1} can be assigned to methane [26], Raman spectra show a shift of release from heavier hydrocarbons to the lightest one, i.e., methane, in agreement with trends for biomass pyrolysis [21].

4. Conclusions

A polarization lock-in filtering (PLF) method was devised to suppress background interferences on weak Raman scattering signals by temporally modulating signals via the polarization of the excitation laser. The technique was demonstrated for *in situ* analysis of gas released from biomass pyrolysis, which is difficult to achieve with conventional Raman spectroscopy due to the presence of substantial fluorescence interference from volatile larger hydrocarbon compounds. The results are very promising, with suppression of un-polarized background contributions, such as fluorescence and laser-induced atomic emission lines, by up to a factor of 50. The accuracy in identifying the Raman peaks has significantly increased, and concentration evaluation of released species was feasible. Also, the background suppression enables a detailed analysis of spectra, demonstrated by the detection of slight changes in the spectral shape of the hydrocarbon CH-stretch signature.

In addition to the application of biomass pyrolysis presented in this paper, the PLF method can be employed with Raman spectroscopy for measurements under any conditions where the background filtering would be beneficial. While the temporal resolution for time-lapse measurements is primarily set by the laser repetition rate and detector performance, the modulation speed of the laser polarization presently limits the method to studies of processes varying on a time-scale on the order of a second. This can potentially be improved with a faster polarization-switching device, but the technique cannot be employed for single-shot measurements. Nevertheless, the additional complexity of the experimental setup is limited to the addition of a rotating wave plate, and the method thus clearly extends the applicability of Raman spectroscopy setups with a single detection system. Quantitative information is preserved after data post-processing, and including additional factors in the evaluation, e.g., the depolarization ratio of molecules, will increase the accuracy of the quantitative analyses. Therefore, the development of the PLF method will be continued to improve its applicability for optimum use in various fields of research.

Declaration of Competing Interest

The authors declare that they have no known competing financial interests or personal relationships that could have appeared to influence the work reported in this paper.

Acknowledgments

This work was supported by the Swedish Energy Agency project (CECOST 22538-4); the European Research Council (Advanced Grant TUCLA 669466); the Swedish Research Council (VR) (Grant 2015-05321); and the Swedish Foundation for Strategic Research (SSF) (ITM17-0313).

References

- [1] M. Lapp, C.M. Penney (Eds.), *Laser Raman gas diagnostics*, Springer-Verlag U.S., New York, 1974.
- [2] W.M. Arden, T.B. Hirschfeld, S.M. Klainer, W.A. Mueller, Studies of gaseous flame combustion products by Raman-spectroscopy, *Appl. Spectrosc.* 28 (1974) 554–557.
- [3] M. Lapp, D.L. Hartley, Raman-scattering studies of combustion, *Combust. Sci. Technol.* 13 (1976) 199–210.
- [4] A.C. Eckbreth, *Laser diagnostics for combustion temperature and species*, Gordon and Breach, Amsterdam, Netherlands, 1996.
- [5] R.A. Hill, D.L. Hartley, Focused, multiple-pass cell for raman-scattering, *Appl. Opt.* 13 (1974) 186–192.
- [6] K.C. Utsav, J.A. Silver, D.C. Howde, P.L. Varghese, Improved multiple-pass Raman spectrometer, *Appl. Opt.* 50 (2011) 4805–4816.
- [7] K.C. Utsav, P.L. Varghese, Accurate temperature measurements in flames with high spatial resolution using Stokes Raman scattering from nitrogen in a multiple-pass cell, *Appl. Opt.* 52 (2013) 5007–5021.
- [8] Q.V. Nguyen, R.W. Dibble, C.D. Carter, G.J. Fiechtner, R.S. Barlow, Raman-LIF measurements of temperature, major species, OH, and NO in a methane-air Bunsen flame, *Combust. Flame* 105 (1996) 499–510.
- [9] J. Kojima, Q.V. Nguyen, Laser pulse-stretching with multiple optical ring cavities, *Appl. Opt.* 41 (2002) 6360–6370.
- [10] W. Meier, O. Keck, Laser Raman scattering in fuel-rich flames: background levels at different excitation wavelengths, *Meas. Sci. Technol.* 13 (2002) 741–749.
- [11] R.S. Barlow, A.N. Karpetis, Measurements of scalar variance, scalar dissipation, and length scales in turbulent piloted methane/air jet flames, *Flow Turbul. Combust.* 72 (2004) 427–448.
- [12] R.S. Barlow, M.J. Dunn, M.S. Sweeney, S. Hochgreb, Effects of preferential transport in turbulent bluff-body-stabilized lean premixed CH_4/air flames, *Combust. Flame* 159 (2012) 2563–2575.
- [13] G. Magnotti, D. Geyer, R.S. Barlow, Interference free spontaneous Raman spectroscopy for measurements in rich hydrocarbon flames, *Proc. Combust. Inst.* 35 (2015) 3765–3772.
- [14] H. Lee, H. Kim, Y. Lee, Y. Yoon, Jet disintegration in supercritical environments, *Exp. Therm. Fluid. Sci.* 115 (2020) 110098.
- [15] X. Zheng, J. Mantzaras, R. Bombach, Kinetic interactions between hydrogen and carbon monoxide oxidation over platinum, *Combust. Flame* 161 (2014) 332–346.
- [16] E. Kristensson, J. Bood, M. Aldén, E. Nordstrom, J.J. Zhu, S. Huld, P.E. Bengtsson, H. Nilsson, E. Berruol, A. Ehm, Stray light suppression in spectroscopy using periodic shadowing, *Opt. Express* 22 (2014) 7711–7721.
- [17] G. Grünefeld, V. Beushausen, P. Andresen, Interference-free uv-laser-induced raman and rayleigh measurements in hydrocarbon combustion using polarization properties, *Appl. Phys. B – Lasers Opt.* 61 (1995) 473–478.
- [18] A. Luczak, V. Beushausen, S. Eisenberg, M. Knapp, H. Schluter, P. Andresen, M. Malobabic, A. Schmidt, New nonintrusive laser diagnostic tools for design and optimization of technically applied combustion systems, *Combust. Sci. Technol.* 116 (1996) 541–566.
- [19] J. Egermann, T. Seeger, A. Leipertz, Application of 266-nm and 355-nm Nd:YAG laser radiation for the investigation of fuel-rich sooting hydrocarbon flames by Raman scattering, *Appl. Opt.* 43 (2004) 5564–5574.
- [20] J.J. Kojima, D.G. Fischer, Multiscalar analyses of high-pressure swirl-stabilized combustion via single-shot dual-Sbg Raman spectroscopy, *Combust. Sci. Technol.* 185 (2013) 1735–1761.
- [21] V. Dhyani, T. Bhaskar, Chapter 9 – pyrolysis of biomass, in: A. Pandey, C. Larroche, C.-G. Dussap, E. Gnansounou, S.K. Khanal, S. Ricke (Eds.), *Biofuels: Alternative Feedstocks and Conversion Processes for the Production of Liquid and Gaseous Biofuels*, 2nd ed., Academic Press (2019), pp. 217–244.
- [22] T.A. Milne, R.J. Evans, N. Abatzoglou, Biomass gasifier “tars”: their nature, formation, and conversion, National Renewable Energy Laboratory, Golden, CO (US, 1998 Report No. NREL/TP-570-25357).
- [23] M. Israelsson, T.B. Vilches, H. Thunman, Conversion of condensable hydrocarbons in a dual fluidized bed biomass gasifier, *Energy Fuel* 29 (2015) 6465–6475.
- [24] L.P. Granath, C.M. Van Atta, The nuclear spin and magnetic moment of sodium from hyperfine structure, *Phys. Rev.* 44 (1933) 0935–0942.
- [25] A. Gaydon, *The spectroscopy of flames*, Springer, Dordrecht, Netherlands, 1974.
- [26] G. Magnotti, K.C. Utsav, P.L. Varghese, R.S. Barlow, Raman spectra of methane, ethylene, ethane, dimethyl ether, formaldehyde and propane for combustion applications, *J. Quant. Spectrosc. Radiat. Transf.* 163 (2015) 80–101.
- [27] J. Larsson, L. Mei, P. Lundin, J. Bood, S. Svanberg, Development of a compact multipass oxygen sensor used for gas diffusion studies in opaque media, *Appl. Opt.* 54 (2015) 9772–9778.
- [28] G. Dellepiane, J. Overend, Vibrational spectra and assignment of acetone $\alpha\alpha$ acetone-D3 and acetone-D6, *Spectrochim. Acta* 22 (1966) 593–614.
- [29] C. Brackmann, M. Aldén, P.E. Bengtsson, K.O. Davidsson, J.B.C. Pettersson, Optical and mass spectrometric study of the pyrolysis gas of wood particles, *Appl. Spectrosc.* 57 (2003) 216–222.
- [30] E. Cloutis, P. Szymanski, D. Applin, D. Goltz, Identification and discrimination of polycyclic aromatic hydrocarbons using Raman spectroscopy, *Icarus* 274 (2016) 211–230.

Paper V



Manuscript submitted for Combustion and Flame

Signal-enhanced Raman spectroscopy with a multi-pass cavity for quantitative analysis of formaldehyde in a one-dimensional laminar DME/air flame

Authors and affiliation:

Mr. Haisol Kim,

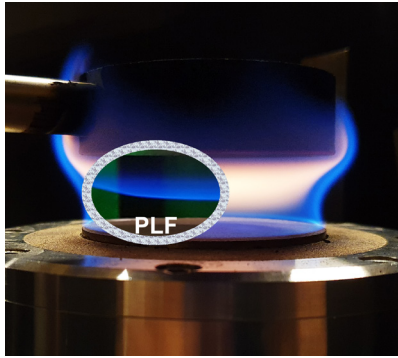
Ms. Alsu Zubairova,

Dr. Marcus Aldén,

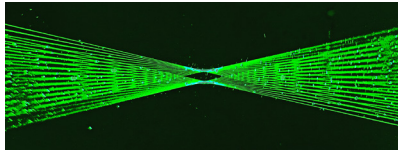
Dr. Christian Brackmann*

Division of Combustion Physics, Lund University, P.O. Box 118, SE-22100 Lund, Sweden

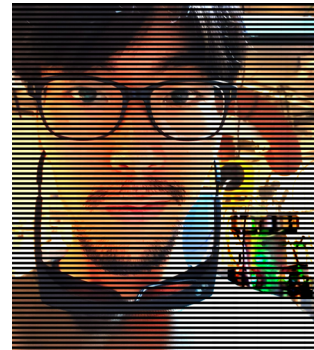
*Corresponding author: christian.brackmann@forbrf.lth.se



A sooting ethylene flame and a methane flame photoshopped to illustrate the Polarization Lock-in Filtering (PLF) technique



Multi-pass alignment (two-point mode)



Author photo with Periodic Shadowing (PS)